AN OBSERVATIONAL AND MODELING STUDY OF THE ENERGY, WATER, AND CARBON CYCLE AT CALHOUN CRITICAL ZONE

A Dissertation
Presented to
The Academic Faculty

by

Yao Tang

In Partial Fulfillment
of the Requirements for the Degree
Doctor of Philosophy in the
School of Civil and Environmental Engineering

Georgia Institute of Technology
May 2019

COPYRIGHT © 2019 BY YAO TANG

AN OBSERVATIONAL AND MODELING STUDY OF THE ENERGY, WATER, AND CARBON CYCLE AT CALHOUN CRITICAL ZONE

Approved by:

Dr. Jingfeng Wang, Advisor
School of Civil and Environmental Engineering
Georgia Institute of Technology

Dr. Satish Bastola
School of Civil and Environmental Engineering
Georgia Institute of Technology

Dr. Aris P. Georgakakos
School of Civil and Environmental Engineering
Georgia Institute of Technology

Dr. Yi Deng
School of Earth and Atmospheric Sciences
Georgia Institute of Technology

Dr. Jian Luo
School of Civil and Environmental Engineering
Georgia Institute of Technology

Date Approved: [December 4, 2018]

To Lucy, my wife, my best friend, and my coadviser.

ACKNOWLEDGEMENTS

First and foremost, I would like to thank my adviser, my mentor, and my counselor, Dr. Jingfeng Wang, who has guided me in study, in research, and in life. I am so fortunate to have the opportunity to learn from him and work with him for the past five years. He is knowledgeable in science, enthusiastic in research, and diligent in work, as well as kind, gracious and compassionate to me in life. Through so many truck rides, field works, and shared meals, I have the privilege to know him not only as my PhD adviser and my funding provider, but also as a mentor and a friend with whom I can share my concerns in career and life. He has made my research life at Georgia Tech such a joyful time and has fired my enthusiasm to always pursuit the unknowns in the broad scientific world. Words cannot express my gratitude to him.

I sincerely appreciate my dissertation committee members, Dr. Aris Georgakakos, Dr. Yi Deng, Dr. Satish Bostola, and Dr. Jian Luo, who have provided critical comments and insightful suggestions that kept me on the right track. My habit of telling jokes before Dr. Georgakakos's classes has equipped me with a lifelong sense of humor in study and research. Dr. Deng is always with a positive attitude towards any results I present. I have benefited greatly through discussions with him and learned to always look at the positive side of my research. Dr. Bostola patiently listened to my confusions about career and shared his wisdom and experience. I have the privilege to stop by Dr. Luo's office in everyday life, have a casual talk with him, and listen to his suggestions. I thank all of their efforts and patience through my PhD study. The dissertation is not possible without their inputs of ideas and insights.

I am fortunate to have worked with many excellent colleagues. Firstly, I would like to thank my big brother and my guide, Dr. Shih-Yu (Steven) Huang. Steven has advised me in course taking, computer programming, and paper writing. I followed his example and obtained two Master's degrees in Civil Engineering and Earth & Atmospheric Sciences. He is the best man in my wedding. Should I say he has made my wedding slightly better!

I sincerely thank Husayn El Sharif, who is one of my coadvisers in the research group. He helped me to sort out the logics between each chapter and improve my outline. I genuinely thank Sai Chen, Sabina Shahnaz, Minjea Kim, Jinge Huo, Na Li, Lijun Chao, Qisheng He, Cheng Yao, and Modi Zhu in Dr. Wang's research group. They have given me many critical suggestions to help me think out of the box. I also thank the CCZO family who have helped me in the field observations and given me many suggestions. To name a few, Dr. Daniel Richter, Zackary Brecheisen, and Will Cook from Duke University, and Dr. Daniel Markewitz at University of Georgia from whom I inherited many car batteries. I sincerely thank Georgia Tech CEE staff Belal Elnaggar, Blake Baklini, Billy Plum, and Andrew Udell, who have greatly helped me in the field observations.

I also had a great time with other graduate students such as Yue Zhao, Ming Liu, Xiao Fu, Saubhagya Singh Rathore, Yiming Chen, Rulan Gong, Yuening Tang, Tongtong Xu, Donghua Cai, Xiufeng Yang, Yibin Liu, Xiaofeng Liu, Irfan Abid, Courtney Di Vittorio, Liao-Fan Lin, Yannis Dialynas, Shawna Mcknight, Jiaying Zhang and many others. My gratitude goes to them for making my research at Georgia Tech so joyful and pleasant. My sincere thanks go to my friends in gym and on basketball court: Huan Yu, Jiasheng Xu, Steven Lustig and many others, who have greatly enriched my life.

Dare I say that my greatest gain in the past five years is not this PhD degree. The Maker of the Heavens and the Earth uses these years to reveal Himself and call me home. My Savior and Lord Jesus Christ pours out His love for me and helps me to reexamine myself. I am loved and treasured even when my grades are not As, my papers are not accepted, and my ideas are not valued. By the grace of Christ, I have the courage to face any difficulties in my PhD research and the opportunity to know so many lifelong friends.

I genuinely thank Neale and Carol Hightower, who open their house to me and share their life with me. Neale is knowledgeable in almost any area, experienced in all engineering, wise in making life decisions, and humble in heart. He perfectly lives out the servant leadership in church and at home. He is always ready to help others in their needs and patient to communicate with Chinese students and scholars. He is the role model whom I look to in workplace, in church, and at home. Carol is a compassionate and caring mom whom everyone wishes to have. Love has overflowed Carol's heart and influenced so many lives around her. They have loved me as a true son and nurtured me in every way to be a real man with integrity. My gratitude to them is beyond words.

I also thank Jason Chen and Jasmine Shi, who are my closest brother and sister, my mentors and counselors. They wholeheartedly served my needs in physical and spiritual life. They have invested much time listening to my concerns and helping me to make career and life plans. I sincerely thank my friends at Westminster Christian Fellowship and North Avenue Presbyterian Church. To name a few, Lynn Bishop, David McCorkle, Renata Dennis, Judy Billings, Frank and Glad Eldridge, Dan and Deborah Lowry, Dun Huang, Xue Zhang, Tingting Wang, Sheng Dai, Siwei Li, Bin Wu, Chenyu Li, Yixing Li, Tutu, Gege, Edwin Goh, Shan Xiong, William Gao, Don and Carolyn Handell, Paul and Judy

Knighten, Barbara Chandler, Paul Hamalian, Tom Mcleod, Edwin Bethea, Stephen Saggus, Kim Goldsmith and many others. They have provided excellent counsels and prepared me to face any challenges in my PhD life.

I sincerely thank my parents, Fulai Tang and Jianhua Song, my sister, Ting Tang, and my brother, Bo Jin. They have graciously supported and encouraged me to run diligently towards the end-mark of the long race in the PhD study. I failed to fulfill my basic responsibilities for attending my sick father and comforting my heartbroken mother. My sister not only took the full burden and looked after my parents in hospital beds, but also comforted and supported me to focus on my study. She is the rock of my family. With her, I never worried about my parents and thus devoted my all in the PhD research. I also would like to thank my in-laws, Changhong Shen and Lijing Zhao. They have been gracious, patient, and supportive as I delayed my graduation repeatedly.

Last, but not least, my genuine gratitude goes to my wife, my best friend, my fellow worker, my helper, and my PhD coadviser, Lu Shen. The good life with Lucy after graduation motives me to work harder than anyone else. She is always with bright ideas to solve my problems in research and in life. She taught me how to communicate with my committee members, how to manage the deadlines, how to interview for jobs, how to give a presentation, and how to apply the OPT. She devoted many endless nights in the editing and proofreading of my thesis. She humbles me when I am proud and encourages me when I am depressed. Without her love, I would never have achieved this monumental goal. This dissertation is dedicated to her.

TABLE OF CONTENTS

LIST OF TABLES

LIST OF FIGURES

LIST OF ABBREVIATIONS

ACS	The Above-Canopy Flux Tower Site
AGL	Above Ground Level
AM	Annual Mean
ASL	Atmospheric Surface Layer
BCS	The Below-Canopy Flux Tower Site
BLR	Bayesian Linear Regression
BR-Sa1	The Santarem-Km67-Pramary Forest Site
BR-Sa3	The Santarem-Km83-Logged Forest Site
BTM	Bulk Transfer Model
CCZ	Cahoun Critical Zone
CCZO	Calhoun Critical Zone Observatory
CEF	Calhoun Experimental Forest
CLR	Classic Linear Regression
CLS	The Cropland Site
CZ	Critical Zone
CZO	Critical Zone Observatory
DFS	Duke Forest Site
DOY	Day Of Year
EC	Eddy-Covariance
ES	Extreme Solution
ET	Evapotranspiration
FIR	Incoming Longwave Far Infrared

GEWEX	The Global Energy And Water Cycle Exchanges
GS	Growing Season
LTSE	Long-Term Soil-Ecosystem Experiment
MDC	Mean Diurnal Cycle
MEP	Maximum Entropy Production
MOSE	Monin-Obukhov Similarity Equations
MOST	The Monin-Obukhov Similarity Theory
NC	North Carolina
NRC	National Research Council
NRMSE	Normalized Rooted-Mean-Square Errors
RE	Relative Error
RMSE	Rooted-Mean-Square Errors
SC	South Carolina
SFT	The Space-For-Time Substitution Approach
US-Br3	The Brooks Fields Site 11-Ames
US-Dk1	The Duke Forest-Open Field Site
US-IB2	The Fermi National Accelerator Laboratory – Batovia (Prairie Site)
US-MRf	The Marys River Fir Site
US-ORv	The Olentangy River Wetland Research Park
US-UMB	The University Of Michigan Biological Station Site
WUE	Water Use Efficiency

LIST OF SYMBOLS

α	Intercept (Linear Regression)
$B(\sigma)$	Reciprocal Bowen Ratio
β	Slopes (Linear Regression)
C	Gas Concentration
C1, C2	Surface Layer Stability Factor (MEP Model)
CH_4	Atmospheric Methane Concentration
CO_2	Atmospheric Co2 Concentration
c_p	The Specific Heat Of Air Under Constant Pressure
Cv	Water Vapor Concentration (Density)
D	Julian Day
D_0	Constant (Friction Velocity Model)
D_c	Eddy-Diffusivity
δ	Declination
E	Latent Heat Flux
EBR	Energy Balance Ratio
e_r	The Saturation Vapor Pressure At An Arbitrary Reference Temperature
Fc	Co2 Flux
FCH_4	Atmospheric Methane Flux
Fv	Water Vapor Flux
G	Soil Heat Flux
g	The Gravitational Acceleration
H	Sensible Heat Flux

$H^{1/3}$	The One-Third Power Of H
H_2O	Water Vapor Concentration
I_0	The Apparent Thermal Inertial Of The Air
I_s	Thermal Inertial Of Soil
κ	The Von Karman Constant
λ	The Latent Heat Of Vaporization Of Liquid Water
ω	Hour Angle
ϕ	Latitude
PREC	Precipitation
P_s	The Surface Atmospheric Pressure
q_s	The Surface Specific Humidity
r	Correlation Coefficients
RH	Relative Humidity
ρ	The Density Of Air
Rn	Net Radiation
R_v	The Gas Constant Of Water Vapor
δ	Dimensionless Parameter (MEP Model)
Sonict T	Sonic Temperature
T_0	A Reference Temperature (MEP Model)
Ta	Air Temperature
θ	Soil Moisture
T_r	An Arbitrary Reference Temperature
Ts	The Surface Temperature
Ts@30cm	Soil Temperature At 30 Cm Deep
u_*	Friction Velocity

WS	Surface Horizontal Wind Speed
w	Vertical Wind Speed
WUE	Water Use Efficiency
z	The Vertical Distance
z_s	The Lower Bound Of The ASL

SUMMARY

This study investigates the evolution of the energy, water, and carbon cycle due to land-use change at Calhoun critical zone (CCZ) using field observations and modeling results of eco-hydro-meteorological variables. Land-use change such as deforestation, cultivation, and reforestation alters the energy, water, and carbon cycle by changing land surface temperature, heat fluxes, evapotranspiration, and carbon storage. CCZ is an ideal platform for investigating this issue as Calhoun has experienced a huge land-use change including severe deforestation in the 18th century, intensive cultivation before the Great Depression in the 1930s, and tremendous reforestation in the 20th century.

This study selects current Duke Forest as Calhoun's pre-agricultural ecosystem before cultivation, current cropland as Calhoun's agricultural ecosystem during the plantation era, and current young pine forest as Calhoun's post-agricultural ecosystem since the reforestation movement, and designs a thorough instrumentation to measure land surface energy, water, and carbon fluxes among other eco-hydro-meteorological variables. Three field sites have been constructed at CCZ from August 2016 to May 2017. The three field sites are the above- and below-canopy flux tower sites at the regrow young pine forest, and the cropland site at a hunting field. The observational system measures more than 300 variables from 7 m below ground to 9 m above ground and records more than 500 GB raw data.

The field observations are used to test three models of land surface fluxes. The first model is the maximum entropy production (MEP) model of heat fluxes. The MEP model is tested

using half-hourly data of more than seven months at CCZ field sites. The MEP model estimates heat fluxes at all sites accurately with the relative errors no greater than 9 %.

The second model is a half-order derivative (HOD) model of gas fluxes that does not use bulk gradient of gas concentration, surface wind speed, or surface roughness. The HOD model is tested using field observations at six field sites with different climate and vegetation types. The results suggest that the HOD model is able to capture the diurnal and seasonal variations of CO_2 fluxes.

The third model is an extreme solution model (ESM) of friction velocity over land surface. The model formulation is based on the extreme solution of the Monin-Obukhov similarity equations relating friction velocity directly to sensible heat flux that may be parameterized using the MEP model. Case studies using half-hourly data validate the model and indicate the possibility for estimating friction velocity and surface wind speed using remote sensing only observations.

The three models are used to fill the data gaps of the eddy-covariance heat and CO_2 fluxes at CCZ field sites. With the MEP model, more than 8000 data gaps of the heat fluxes are filled at the below-canopy flux tower site. With three models together, almost 2000 data gaps of the CO_2 flux are filled at the Duke Forest site. The MEP model is also used to estimate heat fluxes at the cropland site as the eddy-covariance system is not available due to safety concerns.

With the field observations and modeling results of the eco-hydro-meteorological variables at CCZ ecosystems, the evolution of the energy, water, and carbon cycle due to land-use change is quantitatively investigated. The key findings are:

- At long time scale, deforestation increases air temperature (Ta), soil temperature (Ts), sensible heat flux (H), soil heat flux (G), water vapour density (Cv), and evapotranspiration (E), and decreases surface soil moisture (θ). Reforestation decreases Ta, Ts, H, G, Cv, and θ, and increases E. Note that both deforestation and reforestation increase E and decrease θ. The post-agricultural ecosystem has greater Ta, Ts, Rn, H, Cv, E, carbon intake, and water use efficiency (WUE), and smaller G and θ than the pre-agricultural ecosystem. The influence of deforestation on microclimate change is generally greater than that of reforestation.
- At seasonal scale, deforestation increases seasonal variations of Ta, Ts, H, G, Cv, and E, and decreases seasonal variations of θ. Reforestation decreases seasonal variations of Ta, Ts, soil temperature at 30 cm depth (Ts@30cm), H, G, Cv, and E. Land-use change alters Ta, Ts, H, G, and Cv more significantly during the summer than during other seasons. Deforestation alters E more significantly during the summer, and reforestation alters E more significantly during the spring. Land-use change at CCZ alters CO_2 more significantly in winter and CO_2 flux (Fc) more significantly in spring, respectively. The post-agricultural ecosystem has greater seasonal variations of Ta, Ts, Rn, H, G, Cv, E, and CO_2, and smaller seasonal variations of θ and Fc than the pre-agricultural ecosystem.
- At sub-daily scale, deforestation increases diurnal variations of Ta, Ts, H, G, Cv, and E. Reforestation decreases diurnal variations of Ta, Ts, Ts@30cm, and Cv, and increases diurnal variations of H and E. Note that

both deforestation and reforestation increase the diurnal variations of H and E. Land-use change alters almost all variables more significantly during the daytime than during the nighttime. However, throughout the year, land-use change alters daytime and nighttime CO_2 equally strong. The post-agricultural ecosystem has greater diurnal variations of Ta, Ts, Rn, H, G, Cv, E, CO_2 and Fc than the pre-agricultural ecosystem.

- The differences of the pre- and post-agricultural ecosystems in vegetation types and maturity are the major reason for the differences of the two ecosystems in seasonal cycles of H, CO_2, Fc and WUE.

This study draws three conclusions. Firstly, the flux variables such as H, G, E, and Fc are seven times more significantly influenced by land-use change than the corresponding meteorological state variables such as Ta, Ts, Cv, and CO_2. Although the state variables including Ta, Ts, Cv, and CO_2 at pre- and post-agricultural ecosystems are almost identical, the flux variables including H, E, Fc and WUE at the post-agricultural ecosystem are almost twice of those at the pre-agricultural ecosystem. Secondly, deforestation alters land surface variables six times more than reforestation does. Thirdly, land-use change alters soil conditions such as Ts, G, and θ three times more than the corresponding air conditions such as Ta, H, and Cv. Therefore, microclimate change would be underestimated using the most concerned and commonly measured variables such as air temperature, relative humidity, and CO_2 concentration.

CHAPTER 1. INTRODUCTION

1.1 Earth's Critical Zone

The national research council (NRC) defines the Earth's critical zone (CZ) as the thin layer of the Earth's surface and near-surface terrestrial environment from the top of the vegetation canopy (or atmosphere-vegetation interface) to the bottom of the weathering zone (or freshwater-bedrock interface) [*NRC*, 2001]. This zone encompasses the near-surface biosphere, the entire pedosphere, the surface and near-surface portion of the hydrosphere and the atmosphere, and the shallow lithosphere [*Lin*, 2010]. The concept of the CZ provides a unified framework for integrating aboveground-belowground, abiotic-biotic, and time-space in energy and mass flows to comprehensively understand complex terrestrial ecosystems, and offers a fertile ground for interdisciplinary research [*Lin et al.*, 2011]. Thus, the integrated study of the CZ has been recognized as one of the most compelling research fields in Earth and environmental sciences in the 21st century [*NRC*, 2012].

Environmental processes within the CZ, such as energy and mass exchange, soil formation, streamflow generation, and landscape evolution are crucial to sustaining biodiversity and humanity [*Field et al.*, 2015]. The CZ supplies nearly every life-sustaining resources on which life originates, evolves, and thrives; it also provides diverse services to human society and influences human life. Meanwhile, the Earth's CZ is experiencing increasing pressure from growth in human population and wealth. Within the next four decades, demand for food and fuel is expected to double along with a more than 50 % increase in demand for clean water [*SA Banwart et al.*, 2013].

Understanding, predicting, and managing intensification of land-use and associated economic services, while mitigating and adapting to rapid climate change and biodiversity decline, is now one of the most compelling societal challenges of the 21st century. Knowledge of how the CZ forms, functions, and supports humanity is an increasingly important issue raised by both the public and the scientific community. With accelerated socioeconomic development, the CZ is under rising pressure from human perturbations, such as the rapid growth of human and livestock populations, land-use intensification, global environmental changes, and expanding consumption patterns [*IPCC*, 2013]. The rapidly expanding needs for sustainable development demand a special urgency to better understand, predict, and manage the complexity and dynamics within the CZ and its interactions with other environmental systems [*Steve Banwart*, 2011].

To address the challenges, the international CZ scientific community proposed a hypothesis that accelerating changes in land-use, atmospheric composition, and climate are forcing rapid and profound changes in the continental surface, which now requires an exceptional intensity of scientific observations and new knowledge to guide intervention. In 2011, the international workshop at the University of Delaware identified six priority scientific questions. The workshop categorized the six questions into two groups: (1) long-term processes and (2) short-term processes. The first group includes three questions: (1) how has geological evolution established CZ ecosystems? (2) How do molecular scale interactions between CZ processes influence the development of watersheds and aquifers as integrated ecological-geophysical units? (3) How can theory and data be combined from molecular to global scale in order to interpret Earth's surface transformations in the past and forecast CZ evolution in the future? The second group includes three questions: (1)

what controls the resilience, response, and recovery of the CZ and its integrated geophysical, geochemical, and ecological reactions to perturbations such as climate and land-use changes? (2) How can field observations and numerical models be integrated for simulating and forecasting essential terrestrial variables? (3) How can theory, data, and models from natural and social sciences and engineering, be integrated to simulate, evaluate, and manage CZ services? The CZ scientists established multiple Critical Zone Observatories (CZOs) to address the prior questions.

1.2 Calhoun Critical Zone Observatory

The key to CZ science is to use observatories as telescopes to concentrate on the processes and fluxes, and to compare these to the record of the processes in the rock, soil, and sediment—then to use quantitative models parameterized from these observations across spatial and temporal scales to project the future using various scenarios of human behavior. In 2007, the National Science Foundation created the CZO program, to study the Earth's CZ. CZOs are natural watershed laboratories for investigating Earth-surface processes mediated by fresh water. Research at CZO scale seeks to understand these little-known coupled processes through monitoring of streams, soil, canopy, bedrock, and groundwater. CZOs involve teams of cross-disciplinary scientists who enthusiastically investigate the CZ using field observations, theoretical and numerical models. The CZO program established ten observatories across the United States, including the Calhoun CZO (CCZO).

CCZO is located in north central South Carolina (roughly, 34.6° N, 81.7° W), in the Southern Piedmont physiographic province that extends from Virginia to Alabama, a

region with an environmental history that involves serious agricultural land and water degradation. The Calhoun's substrata, topography, vegetation, and land-use history are all closely comparable to conditions across much of the southeastern North America. The Calhoun has a warm temperate climate with mean annual precipitation, potential ET, and temperature 1,300 mm, 850 mm, and 16 °C, respectively. Common soil series at the Calhoun include Cecil, Pacolet, Appling, Cataula, Madison, and Chewacla, which comprise the region's most common soils. These advanced weathering-stage soils are common throughout the world in non-glaciated warm temperate regions and across the lowland tropics, which are experiencing land-use pressure and conversions. Nearly all Piedmont CZs are characterized by: (1) a history of significant human impact, and (2) highly weathered soils and saprolites. During their long natural formation, many Piedmont CZs have lost weatherable primary minerals for many meters in depth, stabilized relatively small contents of organic matter, and become scarce in fertility, all attributes that make these CZs highly vulnerable to human alteration.

In the late 18th century, early settlers in the southeast United States cut down forests for cultivation of cotton, which was critical to economic development. However, inadequate farming practices combined with the region's heavy rainfall and highly erodible landscapes destabilized the soil and severely eroded millions of hectares of land. By the mid-20th century, the Southern Piedmont has eroded the equivalent of about 18 cm of soil, which filled the region's rivers and streams with enormous amounts of sediment. Meanwhile, conventional crops were no longer viable so that millions of farmers left the land, which causes further erosion [*Metz*, 1958].

Yet, throughout the 20th century, the warm temperate climate stimulated regeneration of the old fields abandoned by farmers, and by the second half of the century, the region's farm-dominated landscapes were transformed into secondary forest. Cultivation, land-use change, and land degradation have disrupted and reorganized complex networks of feedbacks between vegetation, soil, and geomorphic evolution, possibly leading ecosystems towards altered states that are different from those pre-disturbance. CCZO provides an opportunity to closely study the dynamics and evolution of highly altered CZs.

CCZO has more than 60 years of research on land and water degradation, and soil change based at the Forest Service's Calhoun Experimental Forest (CEF) in the Sumter National Forest [*Daniel deB. Richter et al.*, 2015]. Calhoun investigators include researchers and educators from Duke University, University of Georgia, Georgia Institute of Technology, University of Kansas, Mississippi State University, Roanoke College, and the USDA Forest Service. The overall goal at CCZO is to marshal the Earth and ecological sciences to understand how critical zones as structures from tree-top to bedrock and as dynamic fluids from the atmosphere to the deepest aquifers are being transformed due to land-use change [*Daniel deB Richter and Billings*, 2015].

CCZO is an ideal platform for investigating how CZs evolve in response to land-use change and how they continue to interact with human communities with land-based livelihoods. CCZO presents an important opportunity to evaluate CZ resilience, and to test a scientifically and socially significant hypothesis: that the Southern Piedmont's impressive post-agricultural reforestation masks persisting alterations in geomorphic, hydrologic, and biogeochemical processes of the region's CZ that have important implications for ecosystem services today.

Research at CCZO is organized into five hypothesis. (1) Ecohydrological recovery hypothesis: in CZs altered by land degradation and soil erosion, restoration of hydrologic functions depends on recoveries of macrospore networks, biodiversity, and biogeochemical processes. (2) Biogeochemical decoupling hypothesis: In CZs altered by land degradation and soil erosion, biogeochemical processes in surficial components become decoupled from those in deep layers. (3) Erosion-Induced carbon dynamics hypothesis: delayed oxidation of eroded soil organic carbon buried in oxygen-deficient alluvial sediments represents a substantial fraction of erosion-induced alterations of soil carbon recycling. (4) Human-critical zone interactions hypothesis: within a physiographic region, historic and contemporary human-forced alterations of the CZ fundamentally shape present and future management and livelihood options. (5) Dynamic persistence of alternative states hypothesis: in CZs altered by land degradation and soil erosion, loss of surficial horizons, and reductions in infiltration, deep rooting, macroinvertebrates, and aggregation, impede redevelopment of forests and CZs with high productivity, standing biomass, and environmental services characteristic of forests never converted to cultivation agriculture.

CCZO is a unique place to study the evolution of the energy, water, and carbon cycle due to land-use change because the Calhoun's land cover changed dramatically from historic forest to agricultural field, and recovered to secondary forest [*Coughlan et al.*, 2017]. Even though energy, water, and carbon variables were not measured through the land-use history, current landscapes such as cropland and forest can represent the landscapes in the past using the Space-For-Time substitution approach. The study of the evolution of the

energy, water, and carbon cycle due to land-use change at CCZ provides valuable references to understand regional and global climatic evolution due to land-use change.

1.3 Objectives and Scope

Deforestation has destroyed 60 % of the original 16 million km^2 of forests. Rainforests once covered 14 % of the Earth's land surface, but now they only cover a mere 6 %. Meanwhile, in many parts of the world, reforestation is increasing the area of forested lands. Asia gained 1 million hectares of forest between 2000 and 2005. Based on the trend, global forest will increase by 10 % by 2050, which is about an area the size of India. Land-use change alters the land surface albedo, evapotranspiration, soil infiltration, runoff, carbon storage, and photosynthesis, and it has significantly influenced the energy, water, and carbon cycle in the ecosystems. This study is motivated by the following scientific question:

How has the land-use change at CCZ including deforestation, cultivation, and reforestation altered the energy, water, and carbon cycle?

The CCZO is an ideal planform for testing on how the energy, water, and carbon cycle evolve due to land-use change as Calhoun has experienced severe deforestation, intensive cultivation, and tremendous reforestation since the 18^{th} century. The CCZO presents an important opportunity to test four scientifically significant hypotheses:

1. Land-use change alters air and soil temperature: deforestation at CCZ increases air and soil temperature, and reforestation decreases them.

2. Land-use change alters the energy cycle: deforestation at CCZ decreases sensible and soil heat fluxes, and reforestation increases them.
3. Land-use change alters the water cycle: deforestation at CCZ increases air humidity and evapotranspiration, and decreases soil moisture; reforestation influences them oppositely.
4. Land-use change alters the carbon cycle: deforestation increases CO_2 concentration, managed reforestation increases carbon intake and water use efficiency.

To test the hypotheses, the Space-For-Time (SFT) substitution approach is applied to reconstruct the eco-hydro-meteorological record through the Calhoun's land-use history. The SFT method takes current ecosystems as historic ecosystems in a chronological order. For example, a current mature forest represents the primary forest before cultivation in the 18^{th} century, a current cropland represents the cropland in the 19^{th} century, and a current young pine forest represents the young pine forest in the 20^{th} century. The evolution of the energy, water, and carbon cycle due to land-use change is quantitatively investigated using field observations and modeling results of the relevant eco-hydro-meteorological variables. Specifically, the research objective and scope are listed as follows:

- Establish instrumentation to measure energy, water, and carbon fluxes among other micrometeorological variables from above-canopy to belowground over cropland and young pine forest at CCZO, and obtain observations over mature forests from Duke Forest Experimental Site. The mature forest, cropland, and young pine forest represent Calhoun's land covers through its land-use history.

- Develop and test models of land surface turbulent fluxes of heat, momentum, water, and carbon using field observations of EC fluxes at young pine forest and Duke Forest, and fill the gaps of the EC fluxes of heat and CO_2 using the new models.
- Study the evolution of the energy, water, and carbon cycle due to land use change at CCZ using the field observations and modeling results.

1.4 Thesis Organization

The thesis is organized as follows: Chapter 1 introduces the Earth's CZ, the CCZO, and the research scope. Chapter 2 reviews literatures relevant to the Earth's energy, water, and carbon cycle; the CZ's energy, water, and carbon cycle; and the research processes at CCZO. Chapter 3 introduces the eco-hydro-meteorological observations at CCZ. Chapter 4 introduces three models of land surface turbulent fluxes, and their applications in gap-fillings and estimation of the heat and CO_2 fluxes at CCZ. Chapter 5 describes the evolution of the energy, water, and carbon cycle due to land-use change at CCZ. Chapter 6 summarizes the dissertation and suggests the future work.

CHAPTER 2. LITERATURE REVIEW

This chapter reviews earlier and contemporary works of the objectives listed above. Section 2.1 reviews the Earth's energy, water, and carbon cycle, 2.2 reviews studies about the energy, water, and carbon cycle across CZOs in the United States, and 2.4 reviews research progresses at CCZO.

2.1 Earth's Energy, Water, and Carbon Cycle

The Earth's energy and water cycle cannot be analyzed separately, as they are linked by many atmospheric and surface processes [*Moustafa T Chahine*, 1992b]. Earth's energy cycle accounts for the balance between the energy Earth receives from the Sun, and the energy Earth radiates back into outer space after having been distributed throughout the five components of Earth's climate system. The five components are earth's water, ice, atmosphere, rocky crust, and all living things. The Earth's water cycle describes the movement of water over, above and below the Earth's surface. By absorbing or releasing energy, water can easily change between any of its three phases: vapor, liquid and ice. The water cycle is all about storing and moving water on, in, and above Earth.

When an energy imbalance occurs in the atmosphere or at the surface, the atmosphere-surface system reacts to re-establish the balance. In the atmosphere, energy balance is most efficiently re-established by means of transport of latent heat through ET and condensation. ET uses energy to break the bonds that hold water molecules together and changes water from a liquid to a water vapor. Condensation, the opposite of ET, releases energy and changes a water vapor to a liquid water.

The first attempt to estimate the Earth's energy cycle can be traced back to 1917 [*Dines*, 1917]. From 1917 to 1986, most of the attempts to estimate the global mean energy budget are severely limited by lack of knowledge of the planetary albedo [*Barkstrom and Smith*, 1986]. In 1990, the global energy and water cycle exchanges (GEWEX) project is founded to investigate Earth's water cycle and energy fluxes at the surface and in the atmosphere [*Moustafa T. Chahine*, 1992a; *Coughlan and Avissar*, 1996; *Energy and Panel*, 1998]. With satellite data, the global energy balance is difficult to estimate, with the uncertainty in longwave radiation about 8 Wm^{-2}, and the shortwave radiation about 25 Wm^{-2} [*Kiehl and Trenberth*, 1997], and with the top-of-atmosphere (TOA) biases in absorbed shortwave radiation, outgoing longwave radiation, and net radiation about 20 Wm^{-2} [*Trenberth et al.*, 2001]. Besides, it is substantially harder to quantify the range of possible changes in the hydrologic cycle than in the global-mean temperature, because the observations are less complete and the physical constraints are weaker [*Allen and Ingram*, 2002]. Maintaining and improving observational capabilities is key to understanding human influences on the large-scale water cycle [*Hegerl et al.*, 2015]. Thus, estimating the global energy and water cycle remains a big challenge.

Land-use change has affected the surface energy and water cycle including the land surface energy balance and runoff ratio in a regional scale [*Pielke et al.*, 2002]. The global surface heat flux differences due to land-use change are on the order of 5-10 Wm^{-2} and the latent heat flux anomalies can reach 40 Wm^{-2} in the tropical central and eastern pacific regions [*Chase et al.*, 2000]. A study of the impact of land-use change on the energy balance over the Mississippi river basin suggests that the conversion from complete forests to crops results in 16% and 19% decreases in the annual average net radiation and ET, respectively,

and a 5 mm day^{-1} (26%) increase in the runoff correspondingly [*Tracy E. Twine et al.*, 2004]. A regional study over the upper Midwest United states indicates that the forest-to-cropland conversion reduces net radiation and sensible heat flux in winter and spring due to effect of albedo, and increases latent heat flux in summer [*Mishra et al.*, 2010]. The impacts of land-use change on energy and water cycle are always investigated using regional or global climate models due to difficulties in observations throughout the land-use history.

The Earth's carbon cycle is the biogeochemical cycle by which carbon is exchanged among the biosphere, pedosphere, geosphere, hydrosphere, and atmosphere of the Earth. The carbon cycle comprises a sequence of events that are key to make Earth capable of sustaining life. Carbon fluxes include photosynthesis, plant and soil respiration, and ocean-atmosphere exchange. The global carbon budget is the balance of the exchange of carbon between the carbon reservoirs.

In the past two centuries, human activities have altered the carbon cycle, most significantly in the atmosphere. Two most important activities that alters the carbon cycle are fossil fuel consumption and land-use change. Before the Industrial Era, atmospheric CO_2 concentration was about 280 ppm for several thousand years. It has risen continuously since then, and surpassed 400 ppm in 2015. The net CO_2 release due to land-use change, mostly deforestation in the tropics, during the 1980s is estimated to be 0.6 to 2.5 petagram of Carbon per year (PgC/yr) (central estimate 1.7 PgC/yr).

The contribution of global deforestation, especially tropical deforestation, to atmospheric CO_2 has been studied since the 1980s [*DETWILER and HALL*, 1988; *Houghton et al.*,

1985; *Woodwell et al.*, 1983]. Changes in land-use between 1850 and 1980 are estimated to have released about 100 PgC to the atmosphere, and transferred about 23 PgC from living vegetation to dead plant material and wood products [*Houghton*, 1995]. Meanwhile, after realizing the damage from deforestation, many countries started to recover forests, which in return absorb carbon from the atmosphere. For example, the reforestation in Northern Hemisphere absorbed 0.5 PgC/yr over 1980s [*David S. Schimel*, 1995b]. The European forest yields a whole tree carbon sink of 0.1 PgC/yr, which is 9.5 % of the European emissions [*Nabuurs et al.*, 1997]. In the United States, the ecosystem absorbs 0.08 PgC/yr based on results from numerical models [*D Schimel et al.*, 2000]. The impacts of land-use change on the carbon cycle are mostly investigated using climate models due to difficulties in observing CO_2 concentration and fluxes throughout land-use history.

2.2 Energy, Water, and Carbon Cycle at Critical Zone

CZOs are natural watershed laboratories distributed globally, so research on the energy, water and carbon cycles at different CZOs varies excessively, although similar models or observations are used.

At the CZOs in cold regions, the snow-related energy and water cycles are of the biggest interest. At Renolds Creek Experimental Watershed in southwestern Idaho, USA, two snow cover energy balance models for estimating surface energy fluxes are developed and evaluated with field measurements [*Kongoli et al.*, 2014; *Reba et al.*, 2014]. At Segehen Creek Watershed in the Central California Sierra, USA, the sensitivity of forest water use to the timing of precipitation and snowmelt recharge is investigated using a coupled hydrological and biogeochemical model [*Tague and Peng*, 2013]. The results suggest that

for a 3 °C warming scenario, the annual actual ET increases in some years due to warmer temperature but decreases by as much as 40% in other years due to an earlier timing of snowmelt. At the Kings River Experimental Watershed in Southern Sierra Nevada, California, USA, two land surface models are tested to estimate the hydrometeorological variables such as net radiation, sensible, latent, and ground heat fluxes at upper and lower meteorological stations along the mountain [*Kim et al.*, 2017]. At the same watershed, ET is measured at four EC towers and extrapolated to the entire basin using remote sensing data, and further analysis of the relationship between mountain runoff and ET predicts that warming projected for 2100 could increase average basin-wide ET by 28% and decrease river flow by 26% [*M. L. Goulden et al.*, 2012; *Michael L. Goulden and Bales*, 2014]. In the Santa Catalina Mountains in southern Arizona, USA, soil evaporation and soil respiration over snow are monitored every two weeks for 15 months, and observations suggest that soil evaporation has a strong relationship with soil moisture and a poor relationship with soil temperature, and soil respiration is the opposite [*Nelson et al.*, 2014].

At CZOs with temperate climates, studies are concentrated on the interactions of the ecosystems, and the energy and water cycle. At the Jemez River Basin—Santa Catalina Mountains CZO, a new term, the coupled effective energy and mass transfer (EEMT) term, is introduced to quantify CZ evolution driven by water, carbon, and energy, and the study indicate that the EEMT is useful at catchment-scale estimate but it has large uncertainties in large scale estimate [*Chorover et al.*, 2011; *C. Rasmussen*, 2012; *C. Rasmussen and Gallo*, 2013; *Craig Rasmussen et al.*, 2011]. At the Susquehanna Shale Hills CZO, a coupled surface-subsurface hydrologic model is developed and tested to estimate the energy, water, and carbon cycle [*Shi et al.*, 2015a; *Shi et al.*, 2014a; *Shi et al.*, 2014b;

2015b; *Yu et al.*, 2014; *Yu et al.*, 2016]. At the Kendall grassland watershed in Arizona, USA, a coupled ecohydrologic model is developed to estimate the energy balance and vegetation dynamics at catchment scale [*Niu et al.*, 2014a; *Niu et al.*, 2014b]. As most of the studies on energy, water, and carbon cycles at CZOs are still limited to the validation of coupled numerical models, studies of this issue based on field observations are urgently needed.

2.3 Research Progresses at CCZO

CCZO is established in the Calhoun Experimental Forest (CEF), which has a long history of research in ecosystems. CEF was established in 1947 for research on Piedmont forest, soil, and water problems, because CEF once represented poorest Piedmont conditions [*Metz*, 1958]. The early research at CEF demonstrated that the Piedmont's land-use history has created a complex of ecological problems that are difficult to recover. Not only were soils often severely eroded and gullied, but also such conditions greatly increased surface and subsurface runoff, increasing sedimentation and endangering soil-water storage [*Hoover*, 1950]. In the 1950s, soil moisture and soil temperature were measured at CEF up to 5-meter depth [*Olson*, 1954], and the measurements demonstrated how contrasting vegetation types utilized soil moisture and altered soil temperature [*Patric et al.*, 1965]. Precipitation and runoff were also measured for 10-15 years at four small watersheds from contrasting land uses including exploitive cropland and restored forest until the Piedmont Research Center and CEF were closed in the early 1960s [*Douglass*, 1972].

After the closure of the Calhoun's Piedmont Research Center, only the experiment of a large-scale loblolly pine spacing study, known as the Calhoun Long-Term Soil-Ecosystem

Experiment (LTSE), remains active today. Meanwhile, a soil scientist, Carol Wells, has sampled soils at four soil-depth within 0-60 cm every 5 years since 1962, and established an extensive sample archive. The LTSE and the soil samples offer scientists the potential to study the relations of the soil's component parts and the functioning of the whole system. The diameters and heights of the pine trees were measured with the growing of the trees, and the data were used to quantify relationships among tree density, volumetric dimensions of tree and stand biomass, and ecosystem productivity. For example, Buford developed and evaluated several sophisticated growth models from the observed density-dependent trajectories of growth [*Buford*, 1991]. DeBell et al. compared the trajectories of growth and mortality at LTSE with those of the identically planted loblolly spacing study in Maui, HI, and develop new ideas about stock ability [*DeBell et al.*, 1989].

During the 1970s and 1980s, acidification of lakes, streams, soils, forests, and even architectural structures was the major concern among scientists and the public. The chemical analyses of the soil samples at CEF demonstrated significant acidification throughout the upper 60 cm of the rooting zone, a soil condition that was probably initiated after the last liming of cotton in 1955. By 1962, the soil's base saturation remained greater than 70 % throughout the upper 60 cm of mineral soil. With forest growth and acid deposition, and without liming, the soil rapidly re-acidified. Binkley et al. compared acidity in the archived soil samples from 1962 and 1982, and estimated that decline in pH was mainly due to reductions in exchangeable base cations [*Binkley et al.*, 1989]. Subsequent studies of Calhoun's soil acidification combined observations of soil chemical change with nutrient-cycling information, and concluded that mineral weathering release of calcium approached zero during the first three decades of forest development [*D. D. Richter et al.*,

1994]. Soil-solution chemistry was analyzed down to 6-m depth and results indicated that up to 40% of the acidification in the upper 60 cm of soil was attributable to acid atmospheric deposition, and below 60 cm, sulfate adsorption effectively reduced cation leaching [*Markewitz and Richter*, 1998]. These observations of soil acidification were featured in national assessments of acid deposition and air pollution, and even were widely reported in the popular press.

CEF also provides significant information of carbon cycling, which meets the national and international demand for quantitative information about soil and ecosystem gains and losses of carbon [*Galik et al.*, 2009; *Daniel D. Richter et al.*, 1999]. CEF is a perfect field site to address both soil and ecosystem carbon gains and losses for two reasons. (1) The long-term Calhoun field experiment is located in a highly eroded landscape, and a major question of carbon cycle in the ecosystem is that whether soil erosion is an atmospheric CO_2 source or sink [*Billings et al.*, 2010; *Van Oost et al.*, 2007]. (2) The long-term field study quantitatively estimates carbon changes in the whole ecosystem aboveground and belowground over nearly five decades [*Mobley et al.*, 2012]. The Calhoun experiment's repeated soil carbon sample archive deep to 60 cm produces valuable knowledge in soil carbon dynamics, as very few of the world's soil carbon change studies have sampled soil deeper than 30 cm [*Daniel deB. Richter and Mobley*, 2009]. A modeling exercise using data from across CEF was developed to provide a range of potential carbon effects associated with soil erosion [*Billings et al.*, 2010]. Overall, the aggrading forest in the Calhoun experiment has been a strong sink for atmospheric carbon from planting to the late 1990s. For example, the forest as a whole has sequestered over 16 kg C m^{-2} in its first

four decades [*Daniel D. Richter et al.*, 1999]. Nearly all of this carbon accumulation is in tree biomass, and secondarily in the soil, i.e., the forest floor and mineral soil.

Since June 2013, research topics at the Calhoun LTSE has expanded greatly from soil science to ecological, hydrological, atmospheric, and geophysical science, as Calhoun LTSE became one of the nation's CZOs. A coupled biogeochemical and hydrological model is tested to estimate the influence of soil and hillslope erosion [*Dialynas et al.*, 2016a; *Dialynas et al.*, 2016b; *Dialynas et al.*, 2017]. A model of three-dimensional topographic stresses is tested to estimate the bedrock fractures, surface processes, and landscape evolution at CCZO [*Moon et al.*, 2017]. Thorough knowledge of CCZ's evolution is urgently needed, but current related studies are limited to testing of numerical models. Therefore, field observations are extremely significant to expand our understanding of CCZ's evolution due to land-use change.

CHAPTER 3. ECO-HYDRO-METEOROLOGICAL OBSERVATIONS AT CALHOUN CRITICAL ZONE

This chapter describes the eco-hydro-meteorological observations at CCZ. Section 3.1 states the motivation of the field observations at CCZ. Section 3.2 describes the three observational sites at CCZ. Section 3.3 describes the major field instruments and their installation instructions. Section 3.4 shows the data samples of a ten-day period and the longest available period. Section 3.5 summarizes the chapter.

3.1 Motivation

The objective of the field observations is to: (1) identify and quantify fundamental eco-hydro-meteorological and biogeochemical processes involved in CZ dynamics and evolution, (2) evaluate integrated process effects especially those altered by human forcing on catchment-scale CZ structure, function, and evolution, and (3) address the five Calhoun-CZO hypothesis in Chapter 1. The study area encompasses CEF's 2057 Ha and adds an adjacent 14,143 Ha of the surrounding Sumter National Forest for a total surface area of 16,200 Ha. The study area is located in the Piedmont plateau physiographic region, bounded by the Appalachian Mountains to the west and uplands at about 205 m above mean sea level that drop steeply down slope into bottomland flood plains at about 95 m above mean sea level. The current land cover is dominated by forests composed of mixed pine-hardwoods. The area receives about 1180 mm of precipitation per year and temperature typically ranges between -2.4 ℃ and 33.1 ℃. We constructed three observational sites measuring eco-hydro-meteorological conditions at CCZO.

3.2 Observational Sites

3.2.1 Above-Canopy Flux Tower Site

Figure 3.1 Above-canopy flux tower site

The above-canopy flux tower site (ACS for short) is in the young pine forest (Figure 3.1), which were planted by Duke University students in the winter of 2008-2009. The canopy height is about 7 m in August 2018. The observational system of the 9-m tower includes above-canopy, below-canopy, and belowground instruments. The main instruments of the above-canopy component are an EC system, a net radiometer, and a temperature and

humidity probe, all mounted at the top of the 9-m tower. The EC system includes a three-dimensional sonic anemometer for measuring high-frequent three-dimensional wind speed and sonic temperature, and an open path gas analyser for measuring high-frequent H_2O and CO_2 concentration. The net radiometer measures upward and downward shortwave and longwave radiation, albedo, and net radiation. The temperature and humidity probe measures air temperature and relative humidity. Both sonic anemometer and the temperature probe measured air temperature, and the accuracies are ± 2 ℃ and ± 0.3 ℃, respectively.

The below-canopy instruments of the 9-m tower include temperature and humidity probes at multiple heights 20 cm, 1 m, 3 m, and 5 m above ground, an infrared thermometer for measuring ground (skin) temperature, and a tipping bucket rain gauge for measuring cumulative rainfall. The belowground instruments include four soil heat flux plates at 80 cm, 40 cm, 15 cm, and 2 cm belowground, six water content reflectometers for measuring soil moisture at 80 cm, 60 cm, 40 cm, 30 cm, 15 cm, and 2 cm belowground, and six temperature probes for measuring soil temperature at the same depth of soil moisture measurements.

The raw data of the EC system are recorded at 10 Hz. EC fluxes of sensible and latent heat, and CO_2 are calculated in a 30-minute time interval. The other eco-hydro-meteorological measurements are recorded every minute. The 9-m tower with its above-canopy instruments was installed in August 2016. The below-canopy and belowground instruments were added gradually until October 2016.

3.2.2 Below-Canopy Flux Tower Site

Figure 3.2 Below-canopy flux tower site

The below-canopy flux tower site (BCS for short) is about 30 m away from the above-canopy flux tower in the young pine forest (Figure 3.2). Below-canopy flux towers are significant for understanding energy and mass exchanges at soil surface. As the soil surface in the young pine forest is mostly covered with dead pine needles, so there is no photosynthesis or transpiration, and the EC system of the below-canopy tower measures energy and mass fluxes over soil. The instruments include an EC system mounted at 2 m above ground, a net radiometer, two temperature and humidity probes at 20 cm and 2 m above ground, an infrared thermometer, a rain gauge, a soil moisture probe at surface, a

soil temperature probe at surface, and a soil heat flux plate at surface. The data of the 3-m tower are recorded and processed in the same way as those of the 9-m tower. The instruments were installed in May 2017, but the eddy fluxes were not available until December 2017 when a new sonic anemometer were added.

3.2.3 Cropland Site

Figure 3.3 Cropland site

The cropland site (CLS for short) is located in Dove Field (Figure 3.3), which is about 1 km away from the flux tower sites in the young pine forest. Dove Field is a hunting ground planted with corns, sunflowers, wheat, beans, and peanuts. The EC system is not allowed during the hunting seasons due to safety concerns. CLS is equipped with instruments measuring soil temperature at surface, 30 cm, 50 cm, 1 m, 2 m, and 7 m below ground, soil moisture at surface, 30 cm, 1.3 m, and 2 m below ground, air temperature and relative humidity at 50 cm above ground, and rainfall. All data are recorded every minute. The

belowground instruments were installed in February 2017, and the aboveground instruments were installed in December 2017.

3.3 Field Instruments

The eco-hydro-meteorological observational system at CCZO includes more than 50 instruments, which can be categorized as ecological, hydrological, and meteorological instruments according to the observed variables.

3.3.1 Ecological Instruments

Ecological instruments include sonic anemometers, gas analyzers, and EC flux software for measuring and processing EC fluxes.

3.3.1.1 Sonic Anemometers

The sonic anemometers at both above- and below-canopy flux tower sites are ultrasonic anemometer Model 81000 vended by R.M. Young company. Model 81000 anemometer measures three dimensional wind velocity and speed of sound based on the transit time of ultrasonic acoustic signals. Sonic temperature is derived from speed of sound that is corrected for crosswind effects. Measurement data are available as serial outputs using RS-232 or RS-485 connections. A variety of serial output formats are available including a custom format that can be easily determined by the user. Four voltage output channels representing sonic temperature and wind in either Cartesian or Polar coordinates are also provided.

Operating parameters may be edited via simplified menus using an ordinary serial communication program like HyperTerminal. All parameters are stored in non-volatile memory. The RS232 cable that connects the sonic anemometer to the computer is made according to the RS232 pinout shown in Figure 3.4. The pinouts and their corresponding wires can be checked by a continuity test using a digital multimeter. After connecting to the computer, set the HyperTerminal at 38400 Baud. Output rate and serial output format are set to 10 Hz and UVW to calculate eddy fluxes. The units of wind speed and temperature are set to m/s and K, respectively. The voltage output format is set to VOLTAGE OUTPUT FORMAT 1 (U V W TEMP). The scaling of wind speed is set to -25 to 25 m/s, and the voltage output full scale is set to 5000 mV. When installing the sonic anemometer, after properly aligned, junction box need to face south.

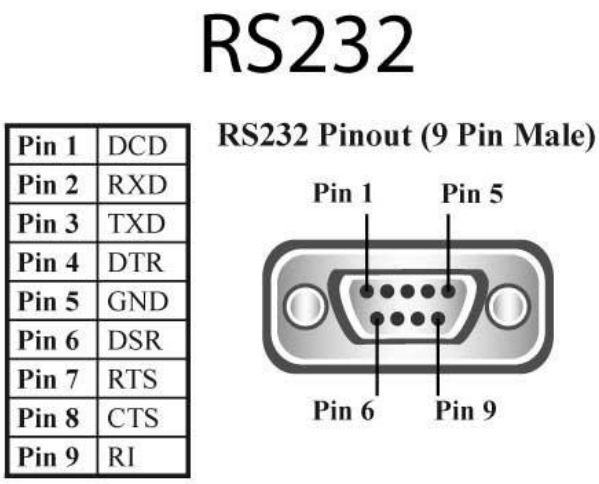

Figure 3.4 RS232 pinout

3.3.1.2 Gas Analyzers

Two models of gas analyzers were installed on the flux towers, a LI-7500 Open Path CO_2/H_2O Analyzer on the 3 m tower, and an improved version LI-7500A on the 9 m tower.

The LI-7500 Analyzer is a high performance, non-dispersive, open path infrared CO_2/H_2O analyzer designed for use in EC flux measurement. The important features of LI-7500 include: (1) simultaneous measurements of CO_2 and H_2O in the free atmosphere; (2) high speed measurements with internal 150 Hz measurements digitally filtered to provide a true 5, 10, or 20 Hz bandwidth; (3) Robust calibrations that withstand exposure to rain or snow without damage or calibration shift.

With the EC technique, high frequency data of CO_2 and H_2O concentration are used in conjunction with sonic anemometer air turbulent data to determine the fluxes of CO_2 and H_2O. The precisions of the CO_2 and H_2O concentration measurements are 0.11 ppm and 0.0047 ppt at 10 Hz, respectively. The raw data of the LI-7500 are recorded to a memory card on a CR3000 data logger.

The LI-7500A improves upon the LI-7500 by providing: (1) High speed analog input channels for auxiliary sensors, such as a sonic anemometer (up to 20 Hz bandwidth); (2) Logs EC data to an internal removable flash drive at up to 20 Hz, which significantly simplifies the data storage; (3) Ethernet for two-way communication / data transfer using standard networking protocols; (4) Reduced energy use in code climates with a low temperature setting for the chopper housing. The LI-7500A model can be connect to a LI-7550 Analyzer Interface Unit. The new interface unit houses the high-speed digital signal processing electronics, and enables the collection of complete data including CO_2 / H_2O concentration, wind speed, and diagnostic data.

The LI-7500A software from LI-COR is used to initialize the gas analyzer. After correctly wired the sonic anemometer to the analyzer interface unit, set the output formats in the LI-

7500A software anemometer section according to the output formats of the sonic anemometer. The output data file combines the gas concentration data and the wind speed data. The 10 Hz data are recorded in a file every 30 minutes. The format of the file is greenhouse gas (.ghg) format, which significantly reduces the size of each file comparing to ASCII files. The .ghg files are converted to ASCII files using the EddyPro software that is introduced in the following.

3.3.1.3 EddyPro Software

With the high-frequent data of wind speed, sonic temperature, CO_2 and H_2O concentration, turbulent fluxes of sensible heat, latent heat, and CO_2 can be calculated following EC method. EddyPro software is used to calculate the fluxes and check the data quality. EddyPro software processes raw EC data to compute biospheric / atmospheric fluxes of CO_2, H_2O, and CH_4, other trace gasses, and energy. EddyPro is customized to efficiently process eddy covariance data logged to LI-COR gas analyzers (.ghg files). It also supports other raw file types, including data stored as ACSII tables, binary files, and SLT formats. The detailed settings of the EddyPro software could be found in EddyPro manual.

3.3.2 Hydrological Instruments

Hydrological instruments include net radiometers, soil heat flux plates, rain gages, and water content reflectometers for measuring radiation, soil heat flux, precipitation, and soil moisture.

3.3.2.1 Net Radiometers

Net radiation is the balance between incoming radiation from the sun and sky, and outgoing radiation from the ground. Shortwave radiation of 0.3 to 3 μm wavelength reaches the Earth's surface, where some is reflected and the rest of the energy is absorbed by the surface. Incoming longwave Far Infrared (FIR) radiation from 4.5 to more than 40 μm is also absorbed by the surface, which heats up and emits FIR back to the sky. The four components of net radiation are the incoming and reflected solar radiation, from which the Albedo can be calculated; and the downward and upward infrared radiation. These parameters can be measured using a pair of pyranometers and a pair of pyrgeometers, but more commonly a net radiometer is used that conveniently combines four sensors into one compact instrument.

CNR 4 net radiometers are used on both the above- and below-canopy flux towers to measure radiation. The CNR 4 net radiometer is a four-component net radiometer for accurate and reliable radiation measurements, and it can be used as the reference instrument for a network of lower performance net radiometers. There are four separate signal outputs and the integrated temperature sensors can be used to calculate the FIR radiation. CNR 4 combines two ISO 9060 Second Class pyranometers for solar radiation with two pyrgeometers for infrared measurements, all integrated into the instrument body. The upper pyrgeometer has a silicon meniscus dome so that water rolls off and the field of view is 180 °. The net radiometers are wired to a data logger to collect data.

3.3.2.2 Soil Heat Flux Plates

Two kinds of soil heat flux plates were installed in the young pine forest, the HFP01 and the HFP01SC. The HFP01 soil heat flux plate uses a thermopile to measure temperature

gradients across its plate. Operating in a completely passive way, it generates a small output voltage that is proportional to this differential temperature. Assuming that the heat flux is steady, the thermal conductivity of the body is constant, and the sensor has negligible influence on the thermal flow pattern, the signal of the HFP01 is directly proportional to the local heat flux. The HFP01's output is in millivolts. To convert this measured voltage to heat fluxes, it must be divided by the plate's calibration constant. A unique calibration constant is supplied with each sensor.

To get the soil heat flux at the surface, use at least two HFP01s to measure soil heat flux at a certain depth; a TCAV averaging soil thermocouple to measure the temporal change in temperature of the soil layer above the HFP01; and a water reflectometer to measure soil water content. The temporal change in soil temperature and soil water content are used to compute the soil storage term.

The location of the heat flux plates and thermocouple should be chosen to be representative of the area under study. If the ground cover is extremely varied, an additional set of sensors is required to provide a valid soil heat flux average. Note that the HFP01 should be installed with the red labelled side facing the sky and the blue labelled side facing the soil. In order for the HFP01 to make quality soil heat flux measurements, the plate must be in full contact with the soil. After locating the sensor properly, bury the sensor leads a short distance back from the hole to minimize thermal conduction on the lead wire. To protect sensor cables from damage caused by rodents, it is recommended to bury them inside of a flexible electrical tubing. In our case, Liquid fence from Amazon is used to keep the rodents away from the experimental area.

The HFP01SC soil heat flux plate consists of a thermopile and an integrated film heater. The thermopile works the same as that in the HFP01. At a regular interval, the film heater is activated to perform a self-test, which results in a verification of sensor contact to the soil and a new sensitivity that is valid for the circumstances at that moment. A self-test is started by switching on HFP01SC's heater, while recording the sensor output signal and the heater power, and finalised by switching the heater off. During the heating interval, a current is fed through the film heater, which generates a known heat flux. The user must interrupt the normal measurement of the soil heat flux during the self-test. The interval between tests is 25 hr, and the duration of the test is 60 s at our sites.

3.3.2.3 Rain Gages

Three TB4 tipping bucket rain gages were installed at the three observational sites. The rain gages funnel rain into a mechanism that tips when filled to the calibrated level. The precision of TB4 is 0.01 inch (0.254 mm). The rain gages should be installed in a relatively level location. Rain gages should be checked every visit as the funnel can be blocked by dirt, pollen, and leaves. Details about the installation and parameters of the rain gage could be found in the manual.

3.3.2.4 Water Content Reflectometers

CS616 water content reflectometers were installed to measure the soil moisture over cropland and young pine forest. The CS616 is designed to measure volumetric water content of soils or other porous media. The water content information is derived from the probe sensitivity to the dielectric constant of the medium surrounding the probe rods. The water content reflectometer consists of two stainless steel rods connected to a printed

circuit board. A shielded four-conductor cable is connected to the circuit board to supply power, enable the probe, and monitor the pulse output. The circuit board is encapsulated in epoxy.

High-speed electronic components on the circuit board are configured as a bistable multivibrator. The output of the multivibrator is connected to the probe rods which act as a wave guide. The travel time of the signal on the probe rods depends on the dielectric permittivity of the material surrounding the rods, and the dielectric permittivity depends on the water content. Therefore, the oscillation frequency of the multivibrator is dependent on the water content of the media. Digital circuitry scales the multivibrator output to an appropriate frequency. The water content reflectometer output is essentially a square wave. The probe output period ranges from about 14 microseconds with rods in air to about 42 microseconds with rods completely immersed in typical tap water. A calibration equation converts period to volumetric water content.

To install the sensor, the probe rods can be inserted vertically into the soil surface or buried at any orientation to the surface. A probe inserted vertically into a soil surface will give an indication of the water content in the upper 30 cm of soil. The probe can be installed horizontal to the surface to detect the passing of wetting fronts or other vertical water fluxes. A probe installed at an angle of 30 degrees with the surface will give an indication of the water content of the upper 15 cm of soil.

The method used for probe installation can affect the accuracy of the measurement. The probe rods should be kept as close to parallel as possible when installed to maintain the design wave guide geometry. The sensitivity of this measurement is greater in the regions

closest to the rod surface than at distances away from the surface. Probes inserted in a manner which generates air voids around the rods will reduce the measurement accuracy. In most soils, the soil structure will recover from the disturbance during probe insertion.

In some applications, installation can be improved by using the CS650G insertion guide tool. The CS650G is inserted into the soil and then removed. This makes proper installation of the water content reflectometer easier in dense or rocky soils.

3.3.3 Meteorological Instruments

Meteorological instruments include air temperature and humidity probes, infrared radiometers, and soil temperature probes to measure air temperature, humidity, skin temperature, and soil temperature.

3.3.3.1 Air Temperature and Humidity Probes

The CS215 temperature and relative humidity probes were installed at the CCZO observational sites. The CS215 probe is designed for general meteorological applications. It utilizes the SDI-12 communications protocol to communicate with any SDI-12 recorder simplifying installation and programming. The CS215 probe uses a single chip element that incorporates both a temperature and an RH sensor. Each element is individually calibrated with the calibration corrections stored on the chip. Sensors should be protected from thermal radiation and adequately ventilated, and thus the chip is protected by a filter at the top. The hydrophobic nature of the filter repels light rain, but driving rain can force itself into the pore structure of the filter and take time to dry out. Therefore, when used in the field, the CS215 must be housed in a radiation shield, which protects the filter at the

top of the sensor from exposure to radiation and liquid water. Radiation shields were purchased from Campbell Scientific or Amazon.

3.3.3.2 Infrared Radiometers

Infrared radiometers are used to measure skin t emperature. All objects with a temperature above absolute zero emit electromagnetic radiation. The wavelengths and intensity of radiation emitted are related to the temperature of the object. Terrestrial surfaces emit radiation in the mid infrared portion of the electromagnetic spectrum (approximately 4-50 μm). Infrared radiometers are sensors that measure infrared radiation, which is used to determine surface temperature without touching the surface. Infrared radiometers are often called infrared thermometers because temperature is the desired quantity, even though the sensors detect radiation.

Apogee instruments SI111 infrared radiometer were installed at the CCZO observational sites. SI111 consist of a thermopile detector, germanium filter, precision thermistor for detector reference temperature measurement, and signal processing circuitry mounted in an anodized aluminium housing, and a cable to connect the sensor to a measurement device. The radiometers come with a radiation shield designed to minimize absorbed solar radiation, but still allowing natural ventilation. The radiation shield insulates the radiometer from rapid temperature changes and keeps the temperature of the radiometer closer to the target temperature. Sensors are potted solid with no internal air space and are designed for continuous temperature measurements of terrestrial surfaces in indoor and outdoor environments. The SI111 sensor output an analog voltage that is directly proportional to the infrared radiation balance of the target and detector, where the radiation balance

between target and detector is related to the temperature difference between the two. Each SI-111 has its own constants that should be included in the program.

3.3.3.3 Soil Temperature Probes

Soil temperature is measured using the 107 temperature probes. The 107 probe is a rugged probe that accurately measures air, soil, or water temperature in a variety of applications. The sensor consists of a thermistor encapsulated in an epoxy-filled aluminium housing. This design allows the probe to be buried or submerged in water to 15 m or 21 psi. The 107 tends to measure the average temperature over its length, so it should generally be buried such that the measurement tip is horizontal to the soil surface at the desired depth. One or two coils of cable should also be buried in a shallow installation. Burial of some cable mitigates the effect of solar heating of the above ground cable on the temperature measurement. Long cable lengths may require longer than normal analog measurement settling times. Settling times are increased by adding a measurement delay to the datalogger program. Details of the installation and programing of the 107 temperature probe could be found in the manual.

3.3.4 Other Devices

Besides the instruments to measure eco-hydro-meteorological variables, other devices to mount the sensors, monitor, collect, and manage data, and provide power supply were also installed at the CCZO sites. These devices are of great importance for accurate and continuous observations.

3.3.4.1 Universal Towers

The above-canopy flux tower is a universal tower UT30 made by Campbell Scientific. The UT30 is a durable and lightweight tower that supports 9 m measurement height for wind sensors as well as sturdy attachment points for antennas, solar panels, environmental enclosures, radiation shields, and crossarms. The detailed description of the tower can be found on Campbell Scientific website. As our project does not allow us to install a concrete base, the RFM18 roof mount base and guy-wires are used in the installation. Guy-wires are connected to earth anchors purchased from Grainger Industry Supply. It is strongly recommended to assemble the tower and install all the sensors in the lab before installation in the field. Installation of the tower includes the following instructions: (1) install sensors at 3 to 10 m; (2) "walk" the tower to its upright position with the help of three people with guy-wires; (3) install the anchor spikes at the bottom; (4) install sensors from surface to 3 m.

3.3.4.2 Tripods

The below-canopy flux tower is a tripod model CM110 vended by Campbell Scientific. The CM110 tripod is a corrosion-resistant stainless steel instrument mounts that support the attachment of sensors, solar panels, and environmental enclosures. A guy-kit is included with the CM110 model. The tripods is much easier to install than the UT30. Details of the tripod can be found on Campbell Scientific website.

3.3.4.3 Data Loggers

CR1000, CR3000, and CR5000 dataloggers from Campbell Scientific are used to collect data at CCZO observational sites.

The CR1000 is the most widely used datalogger, which can be used in a broad range of measurement and control functions. It is robust enough for complex configurations. The CR1000 consists of a measurement and control module, and a wiring panel. The CR1000 uses an external keyboard/display and power supply. The CR1000 suspends execution when primary power drops below 9.6 V, reducing the possibility of inaccurate measurements. Originally, the standard CR1000 has a 2 MB data/program memory, and the optional version, the CR1000-4M, has a 4 MB memory. With a CFM100 CompactFlash Module added to the CR1000 data logger, the memory could be added to 16 GB if the CR1000 is installed with the latest operating system. It is also possible to set up a small local network of CR1000s using conductor cables (Appendix A). Three CR1000s were installed at the CCZO sites. The wiring instructions and programs of the sensors connected to the three CR1000s are in the Appendix B.1 to B.3.

The CR3000 datalogger was installed on the below-canopy flux tower. CR3000 microloggers can support complex applications with many sensors including EC systems with full energy-balance sensors. The CR3000 has a built-in keyboard and display that is convenient for users to monitor data. Multiple CR3000s can be configured as a network or units (Appendix A). Designed for a stand-alone operation in harsh and remote environments, the CR3000 consists of a compact and integrated package with a built-in power supply. It suspends execution when primary power drops below 9.6 V. With a CFM100 CompactFlash Module, the memory of the CR3000 could be added to 16 GB. The wire instructions and program of the sensors connected to the CR3000 are in the Appendix B.4.

The CR5000 data logger was installed to collect data from sensors on above-canopy flux tower. CR5000 is no longer available at Campbell Scientific. It is very similar with CR3000. Our CR5000 is equipped with a 2GB memory card. Unfortunately, the CR5000 can not be added to the logger network as the operating system of CR5000 is no longer updated. The wire instructions and program of the sensors connected to the CR5000 is in the Appendix B.5.

3.3.4.4 LoggerNet Software

LoggerNet from Campbell Scientific is used to compile the programs, monitor, collect, and convert data from the data loggers. LoggerNet supports programming, communication, and data retrieval between dataloggers and a computer. LoggerNet consists of a server application and several client applications integrated into a single product. It can support connection to a single datalogger, but it is especially adept in applications that require telecommunications or scheduled data retrieval used in large datalogger networks. It is strongly recommended to plot all data in the field following instructions in Appendix C.

3.3.4.5 Modem

The RavenXTV digital cellular modem is used to remotely connect the dataloggers to the computer in office to monitor and collect data. The modem is manufactured by Sierra Wireless for use on the Verizon wireless network. The modem is accessed through the Internet using TCP/IP communications protocol using a Static or Dynamic IP address. The model should activate itself automatically. When first powered, the model will check if it has been activated with account data. If there is no account from Verizon for the RavenXTV, the model will not succeed at activating.

3.3.4.6 The Solar Power System

Ten HQST 100 Watt 12 Volt Solar Panels from Amazon were installed in the young pine forest site. The HQST solar panel is made of anti-reflective, high transparent, low iron-tempered glass with enhanced stiffness and impact resistance. It can withstand high winds (2400 Pa) and snow loads (5400 Pa). The idea output of a single solar panel is 500 Wh per day depending on the availability of sunlight. Weighing only 16.5 lbs, the solar panel contains 36 efficient polycrystalline solar cells protected by a thin layer of tempered glass. To parallel connect the solar panels, solar energy panel MC4 T Branch connectors were used. XCSOURCE 30 A 12V/24V Solar Charge Controller Solar Panel Battery Intelligent Regulators were used to control the solar power system. A solar panel controller manages the power going into the battery bank from the solar array. It ensures that the deep cycle batteries are not overcharged during the day, and that the power does not run backwards to the solar panels overnight and drain the batteries. The XCSOURCE controllers have lighting and load control capabilities, but managing the power is their primary job. The detailed installation instructions can be found in the manual.

EverStart Maxx Lead Acid Marine Batteries were installed to store power from the solar panels. The batteries are designed with 30% more cycling capability and longer battery life.. The batteries are placed in Storage Tote from Home Depot. The solar panel frame is constructed using 12-Gauge unistructs.

3.4 Data Samples

More than 200 ecological variables related to EC systems and 100 hydro-meteorological variables are recorded at CCZO observational sites. This section only depicts variables of

special interest. Although the raw data of the observations are recorded at different time resolutions, all data are converted to a half-hourly time resolution in the figures. Figures 3.5 to 3.18 show the observations. Panel (a) shows the data samples during a ten-day period. The ten-day period without rain during April 28 to May 8, 2018 is selected to analyze the sub-daily variations of the observations as rain events significantly affect the accuracy of EC observations. Panel (b) shows all the available data to demonstrate the general trends of the observed variables throughout the periods. The blanks in the long periods are due to power outage, rain events, and sensor malfunctions.

3.4.1 Ecological Variables

Figures 3.5 to 3.12 show the ecological variables including horizontal and vertical wind speed, sonic temperature, sensible heat fluxes, water vapor concentration, latent heat fluxes, CO_2 concentration and fluxes. The long-term mean values of the ecological variables are summarized in Table 3.1.

Table 3.1 Long-term mean values of ecological variables at ACS and BCS

Variables	Unit	ACS	BCS
WS	m/s	0.55	0.12
W	m/s	-0.01	0.01
Sonic T	K	291.03	289.52
H	W/m^2	43.32	10.88
H_2O	g/m^3	21.68	12.96
E	W/m^2	90.43	13.06
CO_2	ppm	375.3	427.77
Fc	$umol/(m^2s)$	-5.91	2.57

3.4.1.1 Wind speed

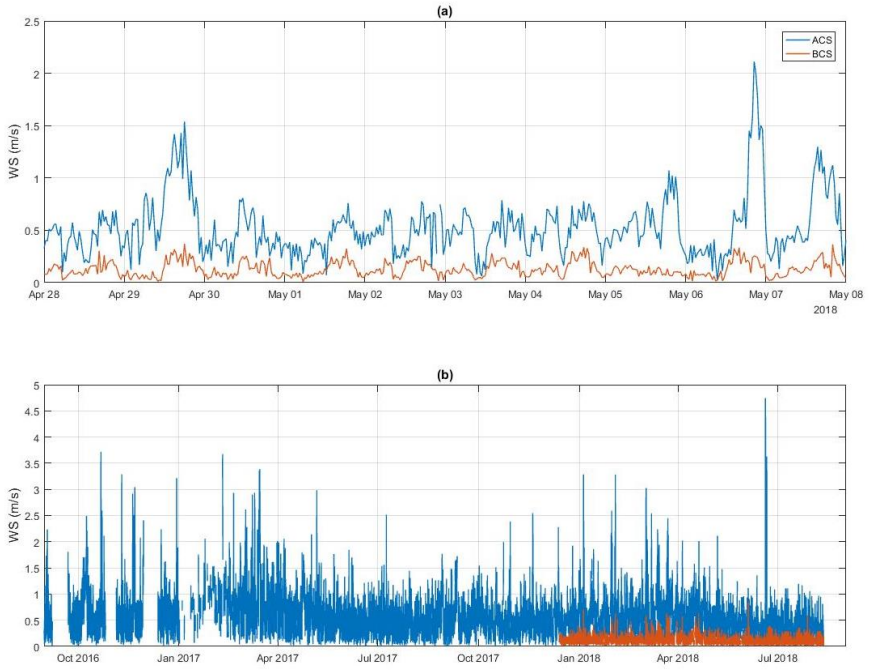

Figure 3.5 Horizontal wind speed during (a) Aril 28 to May 8, 2018, and (b) September 2016 to August 2018

Figures 3.5 and 3.6 show the horizontal and vertical wind speed measured at ACS and BCS. The horizontal wind speed (WS) above canopy is constantly greater than that below canopy (Figure 3.5). The averaged horizontal wind speed above canopy is about 5 times of that below canopy (Table 3.1). The averaged vertical wind speed (w) at ACS and BCS is similar while the fluctuations of vertical wind speed at ACS are greater than at BCS (Figure 3.6). The averaged vertical wind speed above and below canopy is both almost zero, consistent with the assumption that the vertical wind speed is zero very close to the ground [*Lee*, 1998].

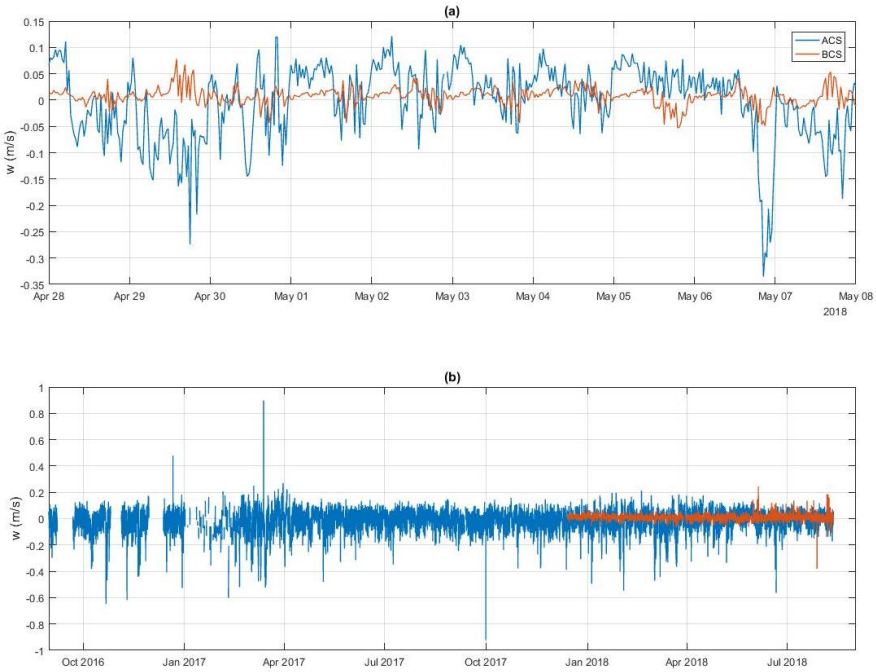

Figure 3.6 Vertical wind speed during (a) Aril 28 to May 8, 2018, and (b) September 2016 to August 2018

3.4.1.2 Sonic Temperature and Sensible Heat Flux

Figure 3.7 shows the sonic temperature (Sonic T) at ACS and BCS. The diurnal variation of sonic temperature below canopy is greater than that above canopy, while the long-term mean sonic temperature at BCS is 1.5 K smaller than at ACS (Table 3.1). Sensible heat flux (H) is calculated as the covariance of the sonic temperature and vertical wind speed. As practical instrumentation cannot fully meet the requirements of the underlying micrometeorological theory, quality control analysis of the EC fluxes must be applied (details in Appendix D). Figure 3.8 shows the sensible heat flux at ACS and BCS. The above-canopy sensible heat flux is constantly higher than the below-canopy one. The sensible heat flux above canopy is about four times of that below canopy, which is consistent with previous studies in an Aspen Forest [*Blanken et al.*, 1998].

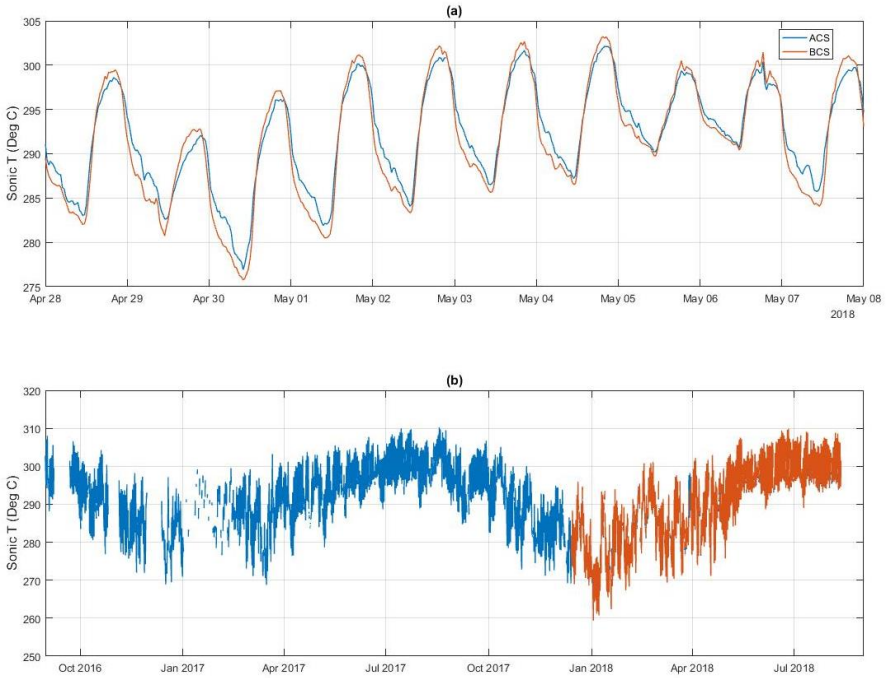

Figure 3.7 Sonic temperature during (a) Aril 28 to May 8, 2018, and (b) September 2016 to August 2018

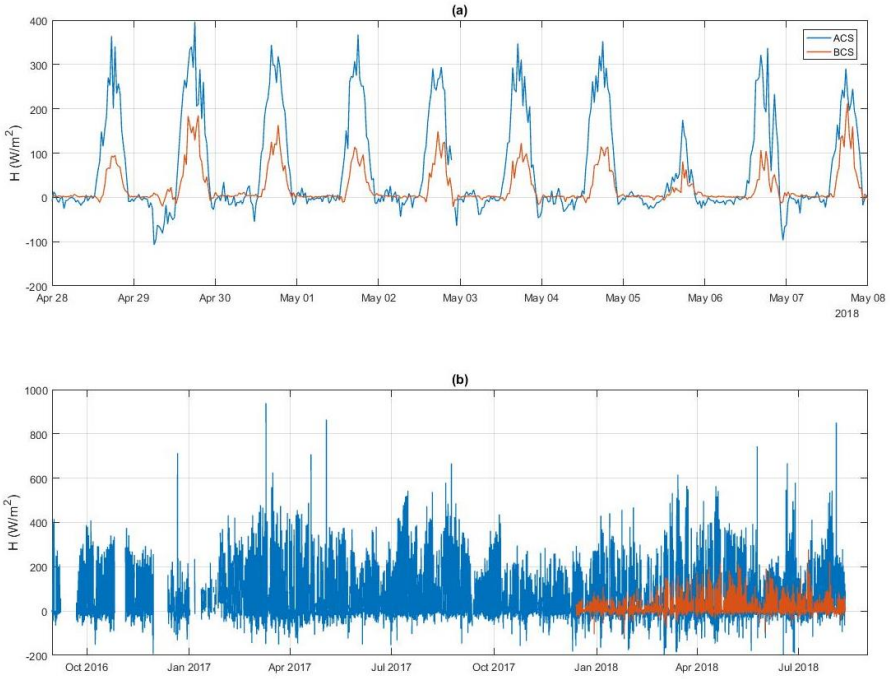

Figure 3.8 Sensible heat fluxes during (a) Aril 28 to May 8, 2018, and (b) September 2016 to August 2018

3.4.1.3 Water Vapor Concentration and Latent Heat Flux

Figures 3.9 and 3.10 show the water vapor concentration (H_2O) and the latent heat flux (E) at ACS and BCS. The water vapor concentration above canopy is constantly greater than that below canopy due to transpiration of the pine trees, while there is no obvious diurnal cycle of the water vapor concentration. The long-term mean water vapor concentration above canopy is nearly doubled that below canopy. The latent heat flux above canopy is also constantly greater than that below canopy. The mean latent heat flux below canopy is about 14 % of that above canopy (shown in Table 3.1), consistent with previous study stating that evaporation from the canopy floor generally accounted for 10 to 40% of total evaporation [*Dennis D. Baldocchi et al.*, 1997].

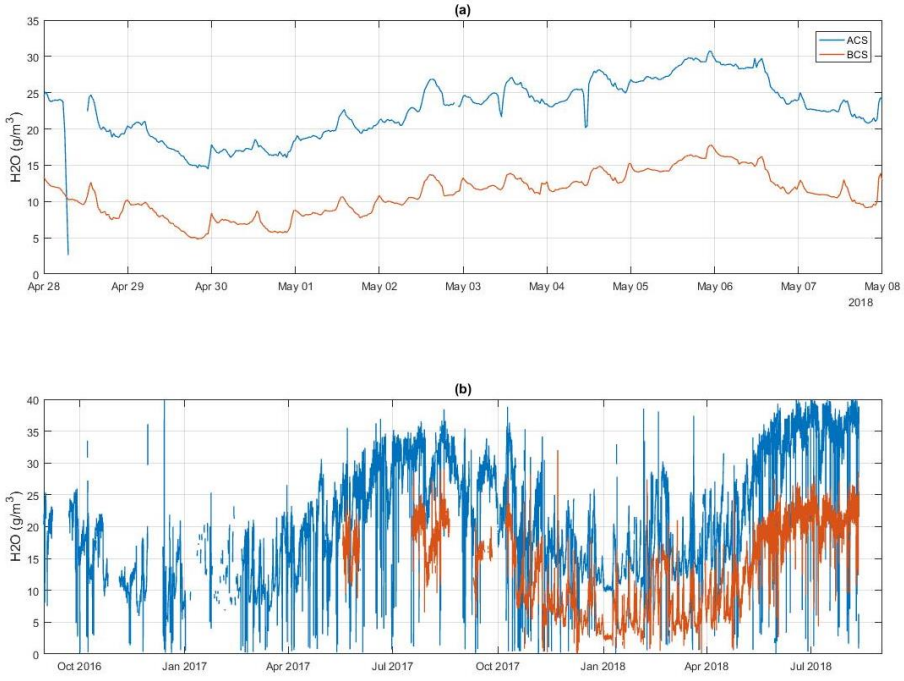

Figure 3.9 Water vapor concentration during (a) Aril 28 to May 8, 2018, and (b) September 2016 to August 2018

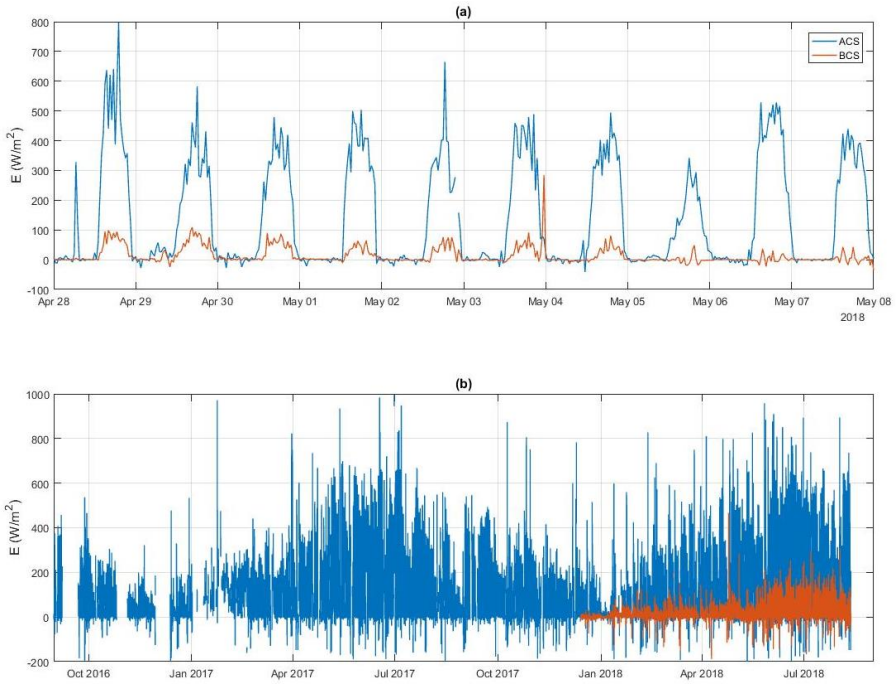

Figure 3.10 Latent heat fluxes during (a) Aril 28 to May 8, 2018, and (b) September 2016 to August 2018

3.4.1.4 CO_2 Concentration and Flux

Figures 3.11 and 3.12 show the CO_2 concentration (CO_2) and flux (Fc), respectively. The CO_2 concentration is high during nighttime and low during daytime due to respiration at all time and photosynthesis during daytime. The CO_2 concentration below canopy is constantly higher than that above canopy due to soil respiration, and the difference is greater during nighttime than daytime due to photosynthesis. The mean CO_2 concentration below canopy is about 52 ppm above canopy. The CO_2 flux above canopy is positive during nighttime, and negative during daytime, while the CO_2 flux below canopy is always positive with a greater magnitude during daytime. The CO_2 flux above canopy is much greater than below canopy. The mean CO_2 flux below canopy is about 50% of that above

canopy (shown in Table 3.1), indicating the soil respiration is about 50 % of the total net primary production of the ecosystem.

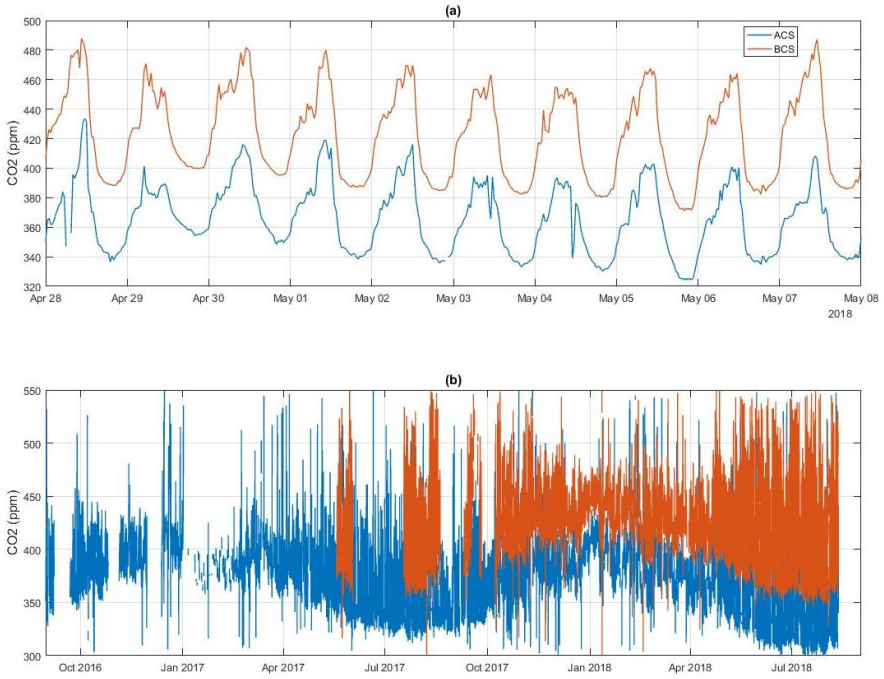

Figure 3.11 CO_2 concentration during (a) Aril 28 to May 8, 2018, and (b) September 2016 to August 2018

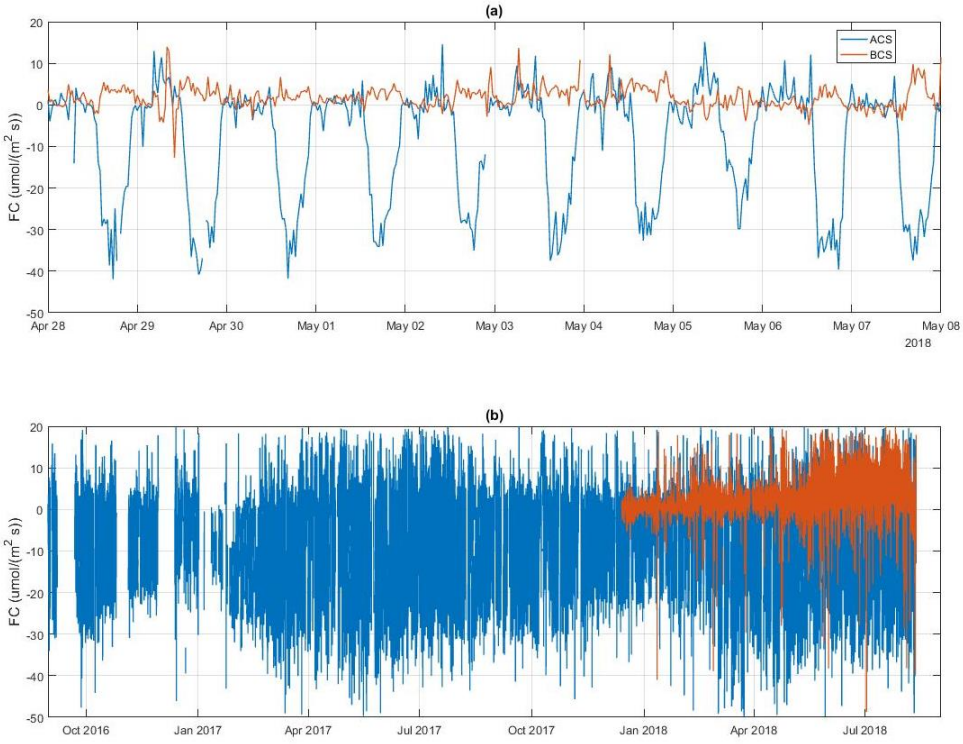

Figure 3.12 CO_2 fluxes during (a) Aril 28 to May 8, 2018, and (b) September 2016 to August 2018

3.4.2 Hydrological Variables

The hydrological variables include net radiation, soil heat flux, and soil moisture. The half-hourly data are shown in Figures 3.13 to 3.15. The long-term mean values of the hydrological variables at ACS, BCS, and CLS are summarized in Table 3.2.

Table 3.2 Long-term mean values of hydrological variables at ACS, BCS, and CLS

Variables	Unit	Depth	ACS	BCS	CLS
Rn	W/m2	NA	132.15	33.76	NA
G	W/m2	surface	0.63	-0.6	NA
		15 cm	-0.41	NA	NA
		40 cm	-0.25	NA	NA
		80 cm	0.28	NA	NA
		Mean	0.0625	-0.6	NA
θ	m^3/m^3	surface	0.0995	0.069	NA
		2 cm	0.1208	NA	0.1341
		15 cm	0.1443	NA	NA
		30 cm	0.1417	NA	0.1234
		40 cm	0.1805	NA	NA
		60 cm	0.2143	NA	NA
		80 cm	0.3314	NA	NA
		1.3 m	NA	NA	0.1772
		2 m	NA	NA	0.2204
		Mean	0.1761	0.069	0.1638

3.4.2.1 Net Radiation

Figure 3.13 shows the net radiation (Rn) at ACS and BCS. The diurnal variation of net radiation above canopy is much greater than that below canopy. The net radiation above canopy is greater (smaller) than that below canopy during the daytime (nighttime). The fluctuations of the net radiation below canopy are mainly due to the shadings of the trees. The long-term observations of net radiation show obvious seasonal cycles with large (small) net radiation during summer (winter) above and below canopy. The long-term mean net radiation above canopy is about four times of that below canopy (Table 3.2).

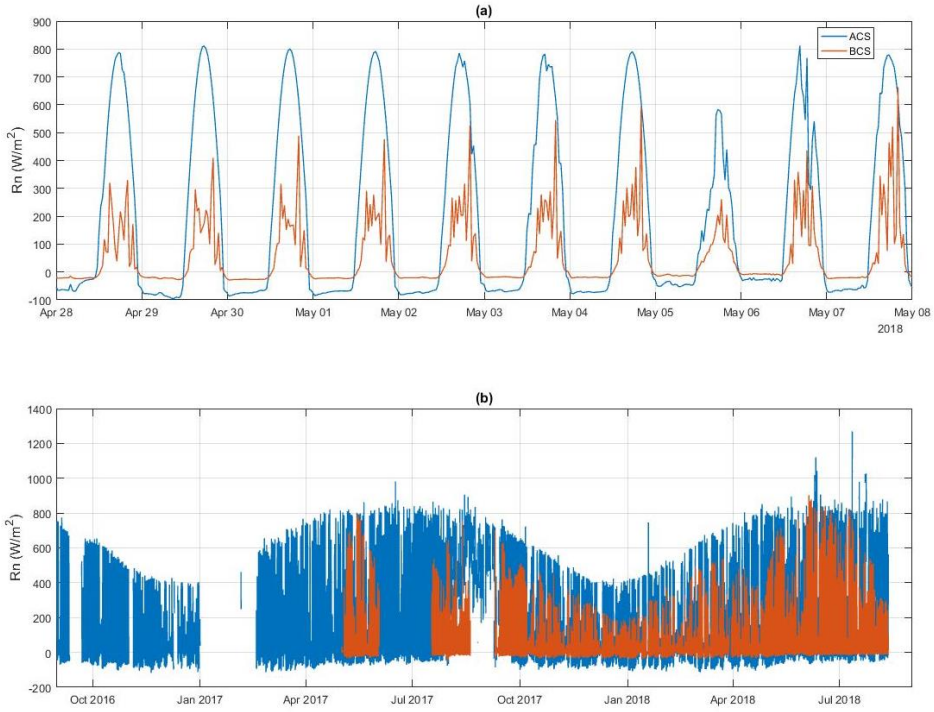

Figure 3.13 Net radiation during (a) Aril 28 to May 8, 2018, and (b) September 2016 to August 2018

3.4.2.2 Soil Heat Flux

The soil heat flux (G) is measured at multiply levels at the ACS, and at the surface at BCS. Figure 3.14 shows the half-hourly data of soil heat fluxes at ACS and BCS. The surface soil heat flux reaches 200 W/m^2 as the young pine forest is not dense enough to block the sunlight reaching to the soil. The diurnal variations of soil heat flux at surface are much greater than that in deeper soil. And there is a phase shift of the diurnal cycle between deeper soil and surface. The soil heat flux at 15 cm depth reaches to maximum two hours after the surface soil heat flux. The long-term mean values of soil heat fluxes at ACS and BCS are both almost zero, indicating that the soil heat fluxes over young pine forest are negligible.

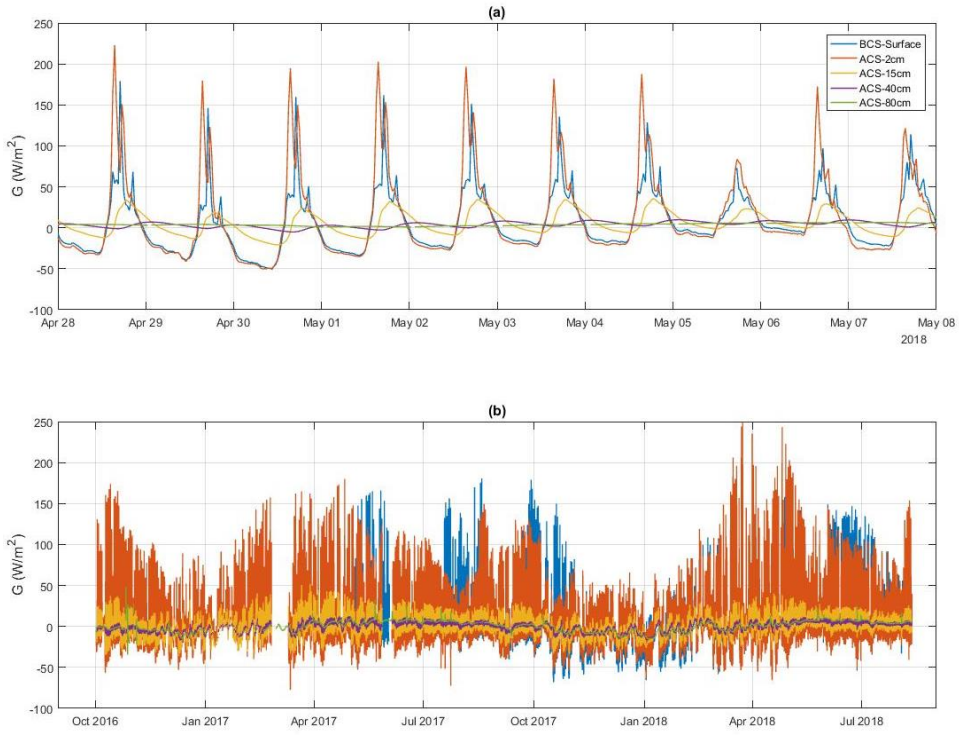

Figure 3.14 Soil heat fluxes during (a) Aril 28 to May 8, 2018, and (b) October 2016 to August 2018

3.4.2.3 Soil Moisture

Figure 3.15 shows the soil moisture (θ) measured at multiple depths at ACS, BCS, and CLS. The half-hourly precipitation data are added in Figure 3.15 (b). For the ten-day period without rain events, soil moisture at deeper soil is generally greater than that at shallower soil. Figure 3.15 (b) indicates that the change of soil moisture is consistent with the rain events. The long-term mean values of soil moisture are summarize in Table 3.2. At each site, the soil moisture generally increases with the depth. At the surface, soil moisture at cropland is greater than that at young pine forest, while at 30 cm depth the soil moisture at young pine forest is greater than that at cropland. At the deepest level at ACS and CLS,

soil moisture at 80cm at ACS is 50 % more than that at 2 m at CLS. Detailed analysis of the soil moisture is introduced in Chapter 5.

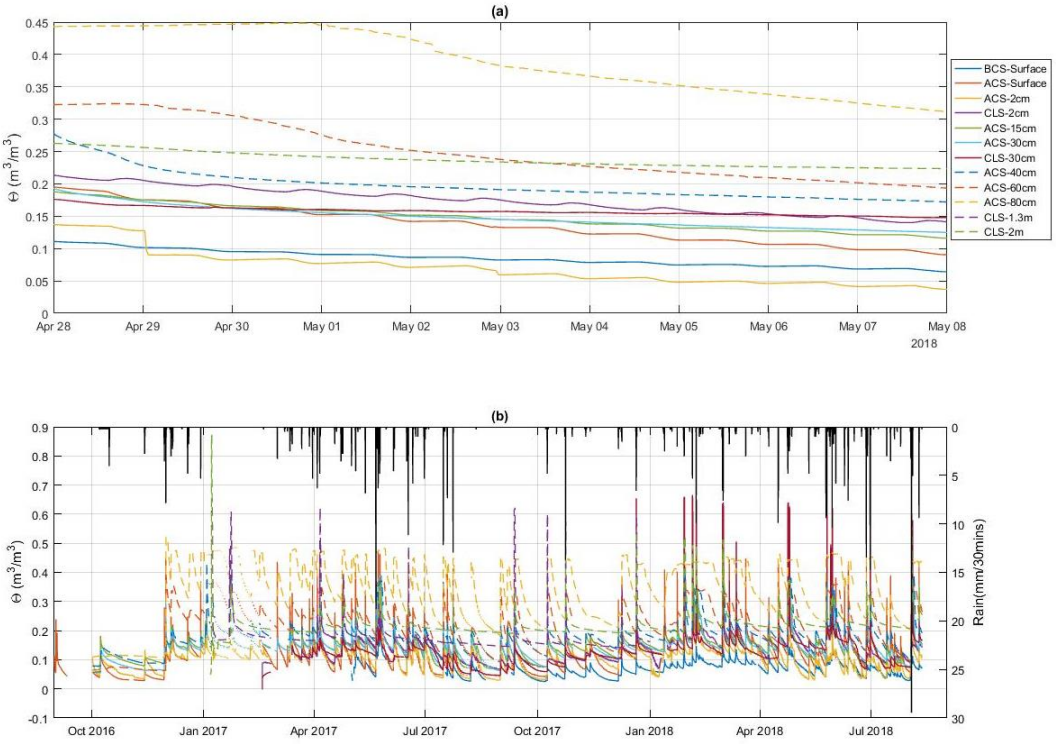

Figure 3.15 Soil moisture and precipitation during (a) Aril 28 to May 8, 2018, and (b) September 2016 to August 2018

3.4.3 Meteorological Variables

Meteorological variables include air temperature, relative humidity, and soil temperature at multiple levels at ACS, BCS, and CLS. The long-term mean values of the meteorological variables are summarized in Table 3.3.

Table 3.3 Long-term mean values of meteorological variables at ACS, BCS, and CLS

Variables	Unit	Height	ACS	BCS	CLS
Ta	℃	Skin	16.546	16.4523	NA
		20cm	17.4673	16.7093	NA
		50cm	NA	NA	16.5041
		1m	15.8248	NA	NA
		2m	NA	16.3611	NA
		3m	16.1209	NA	NA
		5m	16.6398	NA	NA
		9m	17.0181	NA	NA
		Mean	16.61418	16.5352	16.5041
RH (%)	%	20cm	72.8601	80.525	NA
		50cm	NA	NA	74.0088
		1m	77.7181	NA	NA
		2m	NA	76.2985	NA
		3m	76.3099	NA	NA
		5m	73.6348	NA	NA
		9m	72.0162	NA	NA
		Mean	74.50782	78.41175	74.0088
	Unit	Depth	ACS	BCS	CLS
Ts (℃)	℃	surface	16.391	16.856	20.7076
		15 cm	16.4945	NA	NA
		30cm	16.4988	NA	19.7405
		40cm	16.5292	NA	NA
		50cm	NA	NA	18.5142
		60cm	17.0287	NA	NA
		80cm	16.6782	NA	NA
		2m	NA	NA	17.768
		7m	NA	NA	17.9654
		Mean	16.6034	16.856	18.94

3.4.3.1 Air Temperature

Figure 3.16 shows the air temperature (Ta) at ACS, BCS, and CLS including the skin temperature measured by infrared thermometer. The air temperature of different heights at the same location is almost identical. The skin temperature at noon is slightly higher than the air temperature. As the pine trees grow, the leaves of the trees block more sunlight and

the skin temperature at noon in May 2018 is not as high as that in May 2017. The long-term mean air temperature at ACS, BCS, and CLS are almost identical. At the same site, the mean air temperature near surface is slightly higher than at a higher level. The mean air temperature at CCZO is 16.5 °C according to our measurement.

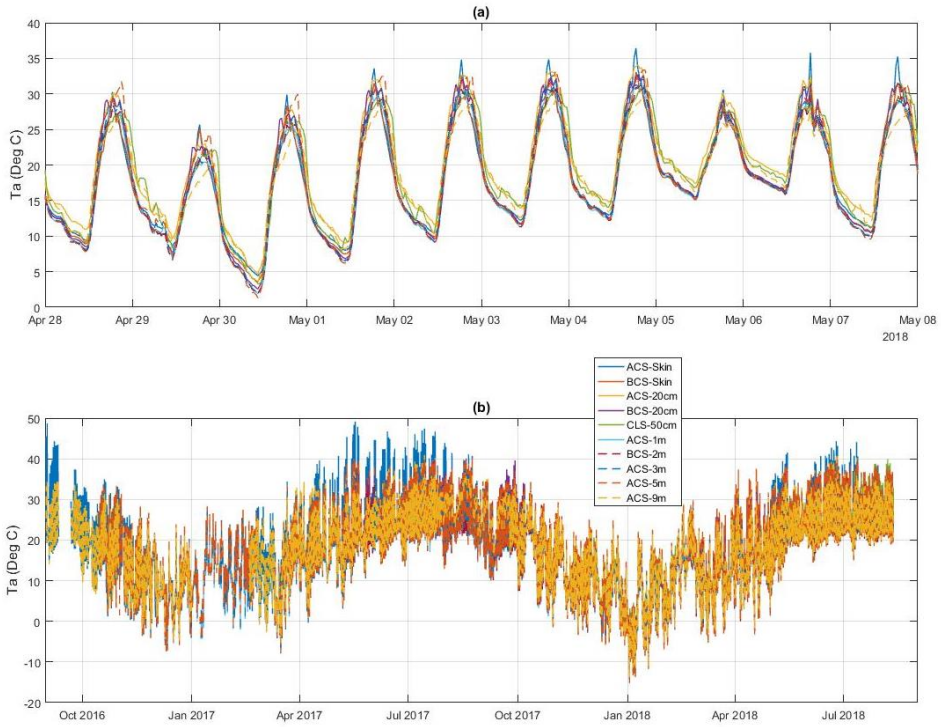

Figure 3.16 Air temperature during (a) Aril 28 to May 8, 2018, and (b) September 2016 to August 2018

3.4.3.2 Relative Humidity

Figure 3.17 shows the relative humidity (RH) at multiple levels at ACS, BCS, and CLS. During nighttime, the relative humidity at surface is about 80 %, that at 1 m to 5 m is almost 100 %, and that above canopy at 9 m is about 95 %. There is no obvious seasonal cycle of the long-term relative humidity. The mean relative humidity at CCZO is about 75 % according to our measurement.

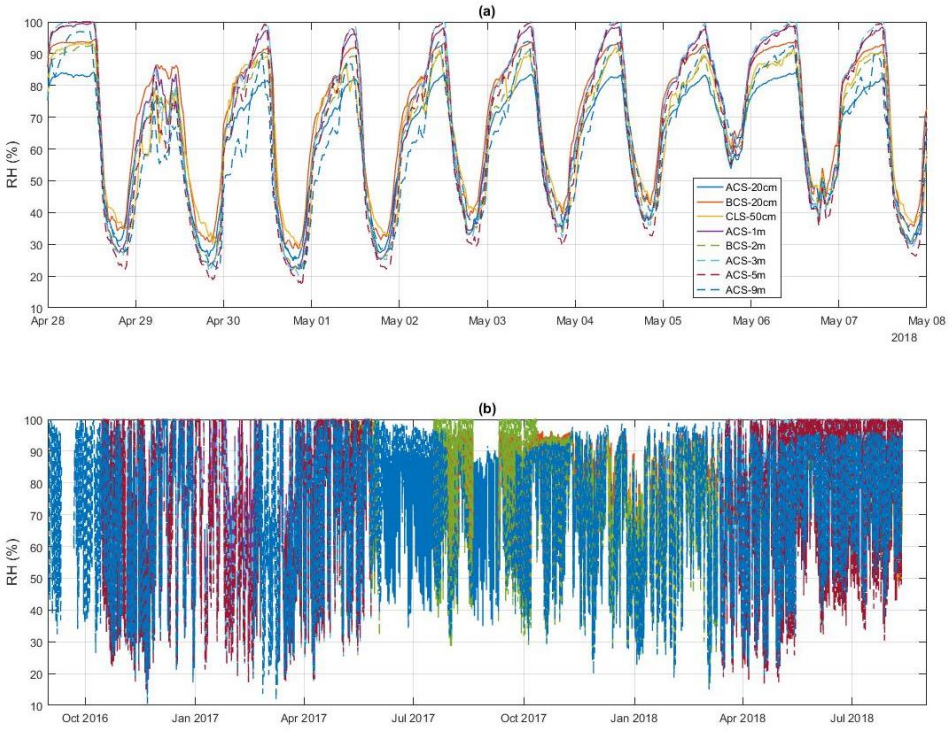

Figure 3.17 Relative humidity during (a) Aril 28 to May 8, 2018, and (b) September 2016 to August 2018

3.4.3.3 Soil Temperature

Figure 3.18 shows the soil temperature (Ts) measured at multiple depths at ACS, BCS, and CLS. The diurnal variation of surface soil temperature at CLS is greatest as the soil is exposed to the sun. The diurnal variations of soil temperature decrease with the depth, and down to 50 cm (40 cm) at CLS (ACS), the diurnal variation is not obvious. The diurnal cycles at deeper soil have a phase shift relevant to that at the surface. The seasonal cycle of the soil temperature is clearly observed until 2 m in depth, while at 7 m, the soil temperature remains approximately 18.0 °C. In the long-term, the mean surface soil temperature at cropland is greater than that at young pine forest. At the young pine forest, the long-term mean temperature at different depths is almost identical, while at cropland,

the long-term mean temperature decreases with depth, indicating there is no significant heat flux from surface to deep soil over young pine forest but a long-term positive heat flux from surface to deep soil over cropland. The mean soil temperature is almost identical to the mean air temperature over young pine forest, while the mean soil temperature is 2.4 °C higher than the mean air temperature over cropland.

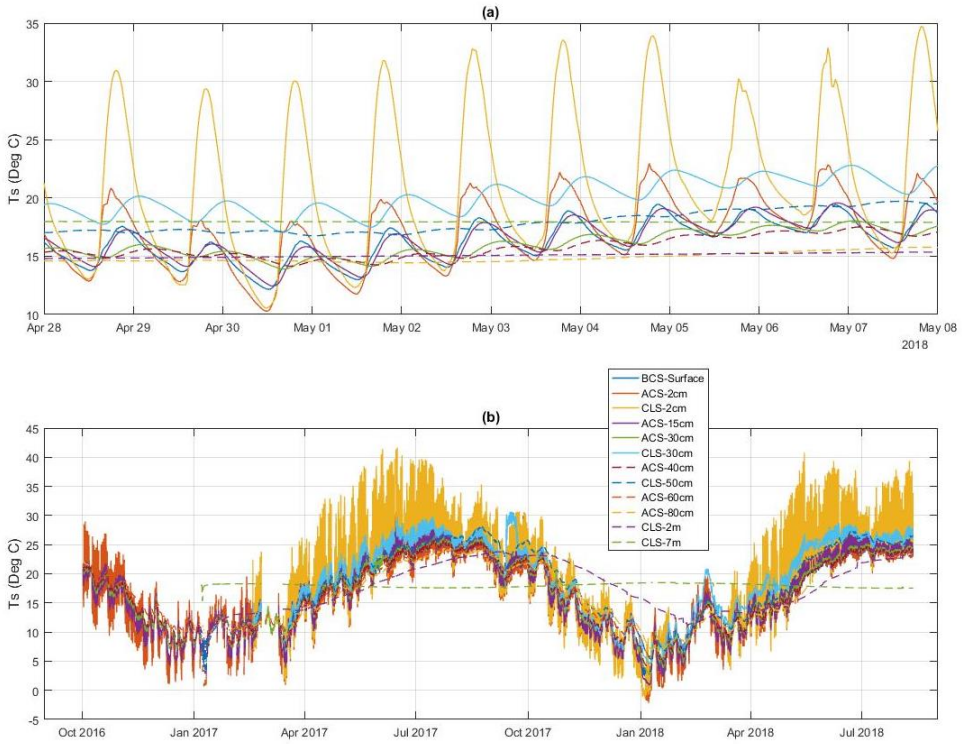

Figure 3.18 Soil temperature during (a) Aril 28 to May 8, 2018, and (b) September 2016 to August 2018

3.5 Summary

This chapter describes the eco-hydro-meteorological observations at CCZ. Three field observational sites were constructed and sensors were added from August 2016 to December 2017. The above-canopy flux tower site was constructed in the young pine forest at CCZ in August 2016. The observational system of the 9-m flux tower includes above-

canopy, below-canopy, and belowground instruments. Eco-hydro-meteorological variables including EC fluxes, CO2 concentration, water vapor concentration, net radiation, wind speed, air temperature, air humidity, soil heat flux, soil temperature, soil moisture, and precipitation are measured. The below-canopy flux tower site was constructed in the same young pine forest in May 2017. The observational system of the 3-m flux tower measures EC fluxes, CO2 concentration, water vapor concentration, net radiation, wind speed, air temperature, air humidity, soil heat flux, soil temperature, soil moisture, and precipitation. The cropland site was constructed in February 2017. Due to safety issues, EC system is not installed at this site. Soil moisture is measured from the surface to 2 m deep and soil temperature is measured from surface to 7 m deep. Air temperature, humidity, and precipitation are also measured at the cropland site since December 2017.

Major field instruments and their installation instructions are deliberately described in this Chapter. More than 200 ecological variables related to the EC fluxes and 100 hydro-meteorological variables are recorded at all three sites. The total raw data are more than 500 GB. Variables essential to the energy, water, and carbon cycle of the local ecosystem are converted to a half-hourly time resolution. Data samples during a typical sunny ten-day period are plotted to exhibit the ordinary diurnal cycles and amplitudes of the variables of interest. All available field data are also plotted to exhibit the long-term seasonal cycles and amplitudes of essential variables and the total observational time span.

The observational systems at CCZ measure eco-hydro-meteorological variables from 9 m above ground to 7 m below ground at both the young pine forest and cropland. The observations are valuable and essential not only to test and improve the existing models of land surface processes, but also to understand the evolution of the energy, water, and

carbon cycle due to land-use change at CCZ. Chapter 4 introduces tests of three new land surface models and a new gap-filling strategy using the theoretical models with field observations at CCZ. Chapter 5 discusses the evolution of the energy, water, and carbon cycle due to land-use change at CCZ using the field observations and modeling results.

CHAPTER 4. MODELS OF LAND SURFACE ENERGY, WATER, AND CARBON EXCHANGE

This chapter describes three models of land surface processes and their applications in gap-fillings of the EC fluxes at CCZ. Section 4.1 states the motivation of the chapter. Section 4.2 describes the tests of the maximum entropy production model of heat fluxes. Section 4.3 describes the tests of the friction velocity model. Section 4.4 describes the tests of the half-order derivative model of gas fluxes. Section 4.5 states the results of gap-fillings of the EC fluxes at CCZ field sites using the three models. Section 4.6 summarizes this chapter.

4.1 Motivation

Land surface models play a significant role in numerical simulations of weather, climate, and greenhouse gas emissions. However, modeling land surface fluxes remains a major challenge in the study of energy, water, and carbon cycles. Current land surface models mainly use the bulk-transfer method to estimate heat, water, and carbon fluxes [*Sellers et al.*, 1997]. As the bulk-transfer model requires input variables such as surface wind speed , roughness length, and bulk gradient that are subject to large uncertainties, this chapter desires to develop more robust land surface models to accurately estimate the land surface fluxes of energy, water, and carbon.

EC flux measurement is considered as the most direct measurement of land surface turbulent fluxes. However, EC fluxes usually have many data gaps and unreasonable spikes due to rain events, condensation, power outage, sensor malfunction, fast changes in

turbulent conditions among other reasons. The data gaps are commonly filled using a look-up table based on experience and statistics. This chapter proposes to fill the data gaps using the theoretical models that have been tested applicable at CCZ. Comparing with the conventional gap-filling method, the new gap-filling models have stronger physical backgrounds and apply more accurately measured variables to fill the gaps of the EC fluxes.

4.2 Model of Surface Heat Fluxes

4.2.1 Introduction

A good understanding of surface heat fluxes is essential for improving regional and global weather and climate models. Turbulent fluxes of heat, including sensible and latent heat fluxes in the field, are usually measured using EC systems. Considered as the most direct method to measure turbulent fluxes of heat, EC systems have been implemented at more than 400 field sites worldwide [*D Baldocchi*, 2014]. However, the heat fluxes measured by the EC systems are subject to large uncertainties caused by power fluctuations, rainfall, contaminations on the sensors among others [*Hollinger and Richardson*, 2005]. One method of independently evaluating turbulent heat fluxes from EC systems is energy balance closure. However, a lack of closure at EC sites is typical in all land-surface types and under all environmental conditions, and energy imbalance is commonly cited as being on the order of 20 % [*K Wilson et al.*, 2002]. The lack of energy balance conservation among measured terms could be caused by landscape heterogeneity, error in flux observations, averaging periods, coordinate systems, horizontal advection, instrument bias, and a combination of several issues [*Reed et al.*, 2018].

The use of surface flux data to validate land surface models requires that conservation of energy be satisfied; therefore, the measured energy budget must be closed by some method. Assuming that the measured available energy (net radiation minus soil heat flux) is accurate enough [*T. E. Twine et al.*, 2000], two methods are used to force energy balance closure. The first method is to assume that sensible heat flux is accurately measured, and solve for latent heat flux as a residual to the energy balance equation, referred as 'residual-E closure'[*Stannard et al.*, 1994]. The second method is to assume Bowen ratio is correctly measured so that individual values of H and E can be adjusted to energy balance, referred to as 'Bowen-ratio method' [*Alan G. Barr et al.*, 1994]. However, these two methods are problematic as recent studies suggest that G can be subject large errors and necessary to be corrected [*Ochsner et al.*, 2007; *T Sauer and Horton*, 2005]. Therefore, a method to close the energy budget and estimate three heat fluxes is needed.

This study proposes to analyze the energy balance closure using the maximum entropy production (MEP) model of land surface heat fluxes. Based on non-equilibrium thermodynamics, information theory, and atmospheric turbulence theory, the MEP model predicts surface fluxes automatically balance the surface energy budget at all time and space scales without explicit use of near-surface temperature and humidity gradient, wind speed, or surface roughness data. Comparing with the classic methods, the MEP model not only estimates the extent of the lack of energy balance closure, but also identifies the fluxes that are most uncertain.

4.2.2 Methodology

4.2.2.1 Energy Balance Closure

The most straightforward method to evaluate energy balance closure is to cumulatively sum available energy (Rn - G) including net radiation (Rn) and soil heat flux (G) and turbulent fluxes of heat (E+H) including latent (E) and sensible (H) heat fluxes over specified time periods and calculated the energy balance ratio (EBR) [*J Gu et al.*, 1999]

$$\boldsymbol{EBR \equiv \frac{\sum(E+H)}{\sum \mathrm{Rn}-G} = \frac{\sum E+\sum H}{\sum \mathrm{Rn}-\sum G} = \frac{n\bar{E}+n\bar{H}}{n\overline{\mathrm{Rn}}-n\bar{G}} = \frac{\bar{E}+\bar{H}}{\overline{\mathrm{Rn}}-\bar{G}}} \qquad \textbf{4.1}$$

where n is the sample size, $\bar{E}$, $\bar{H}$, $\overline{Rn}$, and $\bar{G}$ the mean values of E, H, Rn, and G at *n*, respectively.

The advantage of EBR is that it gives an overall evaluation of energy balance closure at longer time scales by averaging over random errors in the half-hour mean measurements. A disadvantage of EBR is the potential to overlook biases in the half-hourly data, such as the tendency to overestimate positive fluxes during the day and underestimated the negative fluxes at night.

Another method to evaluate energy balance closure is to use linear regression coefficients (slope and intercept) from ordinary least squares relationship between the half-hourly estimates of the dependent flux variables (E + H) against the independently measured available energy (Rn - G) when the energy balance equation is rewritten as

$$\boldsymbol{E + H = Rn - G} \qquad \textbf{4.2}$$

Ideal closure is represented by an intercept of zero and slope of one. The ordinary least square regression is typically valid only if there is no random error in the independent variable, which would incorrectly imply that the measurements of Rn and G contain no random errors.

As all observations of energy components are subject to measurement errors and uncertainties, Bayesian linear regression is used to estimate the slope in addition to the ordinary linear regression. Bayesian linear regression is used to find the straight line slope β and intercept α, given data points (x_i, y_i), i = 1, …, n, where both x and y are subject to errors. Assuming we have the following models,

$$\boldsymbol{y_i = \alpha + \beta X_i + e_i, e_i \sim N(0, \sigma_y)} \qquad \textbf{4.3}$$

$$\boldsymbol{x_i = X_i + \eta_i, \eta_i \sim N(0, \sigma_x)} \qquad \textbf{4.4}$$

where X_i are unknown "true" values of x_i, and σ_x and σ_y are given (known) measurement errors of x_i and y_i, the likelihood function of x, y = (x_i,y_i), i =1,…, n, is

$$L(x, y|\alpha, \beta, \sigma_x, \sigma_y, X) = L(y|\alpha, \beta, \sigma_y, X)L(x|\sigma_x, X)$$

$$= \prod_{i=1}^{n} \frac{1}{2\pi\sigma_x\sigma_y} \exp\left\{-\frac{(y_i-\alpha-\beta X_i)^2}{2\sigma_y^2} - \frac{(x_i-X_i)^2}{2\sigma_x^2}\right\} \qquad \textbf{4.5}$$

$$= \frac{1}{(2\pi\sigma_x\sigma_y)^n} \exp\left\{-\frac{1}{2\sigma_y^2}\sum_{i=1}^{n}(y_i - \alpha - \beta X_i)^2 - \frac{1}{2\sigma_x^2}\sum_{i=1}^{n}(x_i - X_i)^2\right\}$$

The exponent in the above exponential functions may be re-written as

$$\frac{(y_i-\alpha-\beta X_i)^2}{2\sigma_y^2} + \frac{(x_i-X_i)^2}{2\sigma_x^2} = \frac{AC-B^2}{C} + \left(\frac{B}{\sqrt{C}} - \sqrt{C}X_i\right)^2 \qquad \textbf{4.6}$$

with

$$A = \frac{(y_i-\alpha)^2}{2\sigma_y^2} + \frac{x_i^2}{2\sigma_x^2}, B = \frac{\beta(y_i-\alpha)}{2\sigma_y^2} + \frac{x_i}{2\sigma_x^2}, C = \frac{\beta^2}{2\sigma_y^2} + \frac{1}{2\sigma_x^2}$$

$$\frac{AC - B^2}{C} = \frac{(y_i - \alpha - \beta x_i)^2}{2(\sigma_y^2 + \beta^2 \sigma_x^2)}$$

Using the equation

$$\int_{-\infty}^{\infty} \mathbf{exp}\left\{-\left(\frac{B}{\sqrt{C}} - \sqrt{C}X_i\right)^2\right\} dX_i = \sqrt{\frac{\pi}{C}} \qquad \mathbf{4.7}$$

to marginalize the nuisance variables Xi assuming uniform prior of Xi, we obtain,

$$\boldsymbol{L(x, y|\alpha, \beta, \sigma_x, \sigma_y)} = \frac{1}{(2\pi)^{\frac{n}{2}}(\sigma_y^2+\beta^2\sigma_x^2)^{\frac{n}{2}}} \mathbf{exp}\left\{-\frac{1}{2(\sigma_y^2+\beta^2\sigma_x^2)}\sum_{i=1}^{n}(y_i - \alpha - \beta X_i)^2\right\} \quad \mathbf{4.8}$$

The author uses the following notations,

$$\bar{x} = \frac{1}{n}\sum_{i=1}^{n} x_i \,, \bar{y} = \frac{1}{n}\sum_{i=1}^{n} y_i,$$

$$s_{xx} = \frac{1}{n}\sum_{i=1}^{n}(x_i - \bar{x})^2 \,, s_{yy} = \frac{1}{n}\sum_{i=1}^{n}(y_i - \bar{y})^2 \,, s_{xy} = \frac{1}{n}\sum_{i=1}^{n}(x_i - \bar{x})(y_i - \bar{y})$$

Assuming uniform prior of $-\infty < \alpha < \infty$,

$$L(x, y|\beta, \sigma_x, \sigma_y) = \int_{-\infty}^{\infty} L(x, y|\alpha, \beta, \sigma_x, \sigma_y) d\alpha$$

$$= \frac{1}{(2\pi)^{\frac{n-1}{2}}(\sigma_y^2+\beta^2\sigma_x^2)^{\frac{n-1}{2}}} \mathbf{exp}\left\{-\frac{n(s_{yy}-2\beta s_{xy}+\beta^2 s_{xx})}{2(\sigma_y^2+\beta^2\sigma_x^2)}\right\} \qquad \mathbf{4.9}$$

If we use maximum likelihood estimate of α and β assuming known σ_x and σ_y,

$$\frac{\partial L}{\partial \alpha} = 0, \frac{\partial L}{\partial \beta} = 0 \rightarrow$$

$$\hat{\alpha} = \bar{y} - \hat{\beta}\bar{x}$$

$$\boldsymbol{\hat{\beta}^3 + \frac{s_{xy}}{\sigma_x^2}\hat{\beta}^2 + \left(\frac{\sigma_y^2 - s_{yy}}{\sigma_x^2} + \frac{\sigma_y^2}{\sigma_x^2}\frac{s_{xx}}{\sigma_x^2}\right)\hat{\beta} - \frac{\sigma_y^2}{\sigma_x^2}\frac{s_{xy}}{\sigma_x^2} = 0} \qquad \textbf{4.10}$$

It can be shown that the 3rd order algebraic equation for solving $\hat{\beta}$ has only one real positive root if $s_{xy} > 0$ and only one real negative root when $s_{xy} < 0$. The measurement errors of Rn, E, H, and G are approximately 60 Wm^{-2}, 35 Wm^{-2}, 20 Wm^{-2}, and 35 Wm^{-2}, respectively [*F Thomas*, 2008]. Therefore, the measurement error of y is 55 Wm^{-2}, and the measurement error of x is 95 Wm^{-2}.

4.2.2.2 MEP Model of Surface Heat Fluxes

The MEP model [*J Wang and Bras*, 2011] predicts the surface heat fluxes by partitioning net radiation flux into the surface turbulent and conductive heat fluxes,

$$\boldsymbol{E + H + G = Rn} \qquad \textbf{4.11}$$

Following the MEP formalism, the heat fluxes over land surfaces are expressed as

$$G = \frac{B(\sigma)}{\sigma}\frac{I_s}{I_0}H|H|^{-\frac{1}{6}}, \qquad E = B(\sigma)H,$$

$$I_0 = \rho c_p\sqrt{C_1 \kappa z}\left(C_2\frac{\kappa z g}{\rho c_p T_0}\right)^{\frac{1}{6}}, \qquad \textbf{4.12}$$

$$B(\sigma) = 6\left(\sqrt{1 + \frac{11}{36}\sigma} - 1\right), \sigma = \frac{\lambda^2}{c_p R_v}\frac{q_s}{T_s^2}$$

where $B(\sigma)$ is recognized as the reciprocal Bowen ratio, σ a dimensionless parameter characterizing the surface thermal and moisture condition on the partition of surface net

radiation into heat fluxes, I_s is the thermal inertia of soil, I_0 the "apparent thermal inertia of the air" parameterized based on the Monin-Obukhov similarity theory (MOST), ρ the density of air, c_p is the specific heat of air under constant pressure (10^3 J kg^{-1} K^{-1}), C_1 and C_2 the parameters related to the universal constant in the empirical functions characterizing the atmospheric stability of the surface layer [*Businger et al.*, 1971]

$$C_1 = \begin{cases} \frac{\sqrt{3}}{\alpha}, unstable \\ \frac{2}{1+2\alpha}, stable \end{cases}$$

and

$$C_2 = \begin{cases} \frac{\gamma_2}{2}, unstable \\ 2\beta, stable \end{cases}$$

$$\alpha \sim 0.75, \beta \sim 4.7, \gamma_1 \sim 15, \gamma_2 \sim 9$$

κ the von Karman constant ~0.4, z the vertical distance (m) from the material surface above which the MOST holds, g the gravitational acceleration (m s^{-2}), T_0 a reference temperature (K) set to be 300 K in this study, λ (2.5×10^6 J kg^{-1}) the latent heat of vaporization of liquid water, R_v (461 J kg^{-1} K^{-1}) the gas constant of water vapor, q_s (kg kg^{-1}) the surface specific humidity, and T_s (K) the surface temperature.

Over land surfaces covered with dense canopy $I_s \approx 0$, Eq. (4.12) reduce to

$$\boldsymbol{H = \frac{Rn}{1+B(\sigma)}, E = \frac{Rn}{1+B^{-1}(\sigma)}} \qquad \textbf{4.13}$$

Over the canopy without water stress, q_s is a function of T_s according to the Clausius-Clapeyron equation,

$$q_s(T_s) = 0.622 \frac{e_r}{P_s} \exp\left[\frac{\lambda}{R_v}\left(\frac{1}{T_r} - \frac{1}{T_s}\right)\right] \qquad 4.14$$

where e_r is the saturation vapor pressure at (an arbitrary reference) temperature T_r, the surface atmospheric pressure P_s ($\approx 10^5$ Pa). e_r = 611 Pa at T_r = 273 K.

4.2.3 Data

Except for the above-canopy flux tower site (ACS) and below-canopy flux tower site (BCS) in the CCZ young pine forest, Duke Forest site (DFS) is also selected to test the MEP model. Owned and managed by Duke University, the Duke Forest consists of over 7,000 acres of forested land and open fields in Durham, Orange, and Alamance counties. The hardwood forest flux tower is located in Durham, North Carolina (36.0°N, 79.1°W, 168 m above sea level). The hardwood forest is classified as an uneven-aged (90-110 year old) oak-hickory forest, which has not been managed after establishment. The mean canopy height is 25 m, with the upper canopy reaching over 35m. EC instrumentation is positioned at 39.8 m on a 42 m tower. Peak leaf area index at this site is 6.3 m^2 m^{-2}. The hardwood ecosystem has little topographic variation and the long-term mean annual temperature and precipitation are 15.5°C and 1,146mm, respectively. The sensible and latent heat fluxes, CO_2 concentration and flux, and net radiation among other micrometeorological variables were measured half-hourly from 2001 to 2008. Soil heat flux was measured from 2006 to 2008.

4.2.4 Results

4.2.4.1 Observed Energy Balance Closure

Energy balance closure of the observations at ACS, BCS, and DFS is evaluated using bulk *EBR*s and regression lines. The mean values of *H*, *E*, *G*, *Rn*, and *EBR* are summarized in Table 4.1. The statistics of the regression lines of the observed turbulent fluxes of heat and available energy including sample size (n), intercepts (α) and slopes (β) of classic linear regression (CLR) and Bayesian linear regression (BLR), and correlation coefficients (r) are summarized in Table 4.2. Figure 4.1 shows the scatter plots of the observed turbulent fluxes of heat and available energy at half-hourly time scale that demonstrate the energy balance closure.

The effective sample sizes (Table 4.1) of the fluxes at ACS, BCS, and DFS are 24301, 10713, and 131788, respectively, indicating effective fluxes data of approximately 17 months, 7 months, and 7.5 years. The long-term mean values of observed G are all approximately zero. The available energy (Rn - G) at all sites is slightly higher than the turbulent fluxes of heat (E + H), consistent with previous study across 22 sites and 50 site years in FLUXNET [*K Wilson et al.*, 2002]. The *EBR* of the observed fluxes at ACS, BCS, and DFS are 0.98, 0.64, and 0.84, respectively, indicating a good energy balance closure at ACS and a poor energy balance closure at BCS and DFS.

The α of the regression analysis are all within the estimated measurement uncertainties (55 W m^{-2} for E+H), indicating a reasonable good quality of the EC measurements at all sites. The energy balance is well closed at ACS as the slopes of both CLR and BLR are no less than 0.82, and r of the turbulent fluxes of heat and available energy is 0.92. A lack of energy balance closure is identified at BCS as the slopes are no greater than 0.31 and r is only 0.58. A reasonable energy balance closure is reached at DFS as the slopes are greater than 0.63, and r is 0.86.

Results from the bulk EBR and statistical analysis both indicate a good energy balance closure at ACS, a lack of energy balance closure at BCS and a reasonable energy balance closure at DFS. Plausible reasons for the observed lack of energy balance closure include footprint differences between radiometers and EC-measured fluxes, instrument bias, neglected storage sinks, high frequency losses, and advection [*C. et al.*, 2006].

Table 4.1 Mean values of OBS and MEP modeled heat fluxes at ACS, BCS, and DFS including sample size (*n*) and *EBR*s

Site	Method	*n*	*H*	*E*	*G*	*Rn*	*E* + *H*	*Rn* - *G*	*EBR*
ACS	OBS	24301	46.67	94.48	0	144.35	141.15	144.35	0.98
	MEP	24301	63.30	81.05	0	144.35	144.35	144.35	1.00
BCS	OBS	10713	10.94	13.06	0.18	37.76	23.99	37.57	0.64
	MEP	10713	12.42	17.43	7.91	37.76	29.84	29.84	1.00
DFS	OBS	131788	25.06	56.78	0	97.37	81.83	97.37	0.84
	MEP	131788	46.74	50.64	0	97.37	97.37	97.37	1.00

Table 4.2 Statistics of the regression lines of the observed half-hourly turbulent fluxes of heat and avaiable energy at ACS, BCS, and DFS

		CLR		BLR		
Site	*n*	α (W m^{-2})	β	α (W m^{-2})	β	*r*
ACS	24301	17.66	0.86	21.54	0.83	0.92
BCS	10713	12.49	0.31	16.77	0.19	0.58
DFS	131788	19.91	0.64	20.28	0.63	0.86

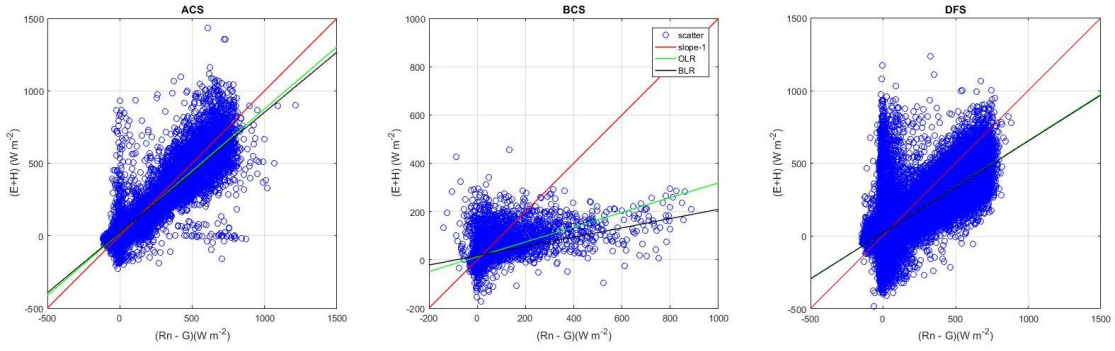

Figure 4.1 Energy balance closure at ACS, BCS, and DFS

4.2.4.2 MEP Modeled Heat Fluxes

The MEP model over dense canopy is used to estimate *H* and *E* in terms of available energy, air temperature, and humidity at ACS and DFS. The MEP model over grassland is used to estimate *H*, *E*, and *G* in terms of *Rn*, air temperature, and humidity at BCS. Soil thermal inertial (1194 tiu) used in the MEP model is estimated using the half-order derivative model in terms of soil heat flux and soil temperature at the same level. The MEP model is tested for all time steps as long as input variables are available. The MEP results are compared with the EC measured fluxes, and the statistics of the MEP modeled heat fluxes including sample size *n*, rooted-mean-square errors (RMSE), normalized RMSE (NRMSE, defined as the RMSE divided by the range of the flux), and the correlation coefficient *r* are summarized in Table 4.3. The sample sizes at ACS, BCS, and DFS are no less than 24320, 10713, and 132936, respectively, meaning approximately more than 17 months', 7 months', and 7.6 years' heat fluxes are compared at ACS, BCS, and DFS, respectively.

Table 4.3 Statistics of the MEP heat fluxes including sample size *n*, RMSE (W m^{-2}), NRMSE (%), and correlation coefficient *r*.

Site	Variable	*n*	RMSE	NRMSE	*r*
ACS	H	25500	54	5	0.88
	E	24320	86	7	0.82
BCS	H	10788	26	7	0.63
	E	10713	42	6	0.50
	G	19084	23	9	0.70
DFS	H	134430	63	6	0.86
	E	132936	83	7	0.73

Figures 4.2 to 4.4 show the scatter plots of the available MEP modeled and EC observed heat fluxes at ACS, BCS, and DFS at half-hourly time scale, respectively. The MEP modeled fluxes generally agree well with the EC observed ones as the NRMSEs are no

greater than 9 % for all fluxes. The MEP modeled *H* agree more closely with the EC measured *H* than *E* as the component to calculate *H* (sonic temperature) is more accurately measured than that to calculate *E* (water vapor concentration). Discrepancies of MEP modeled and EC observed *H* and *E* are large when the modeled *H* or *E* is approximately zero, as the MEP model estimated *H* and *E* are constrained by the available energy or *Rn* which is nearly zero during rain events, sunrises and sunsets, when the EC observed H and E are subject to large uncertainties [*Aubinet et al.*, 2012]. *r* of the MEP heat fluxes at BCS are smaller than those at ACS and DFS, indicating a poorer agreement of MEP and OBS heat fluxes at BCS than ACS and DFS. The discrepancies of MEP modeled and EC observed heat fluxes at BCS are due to the fluctuations of *Rn* at BCS caused by shading.

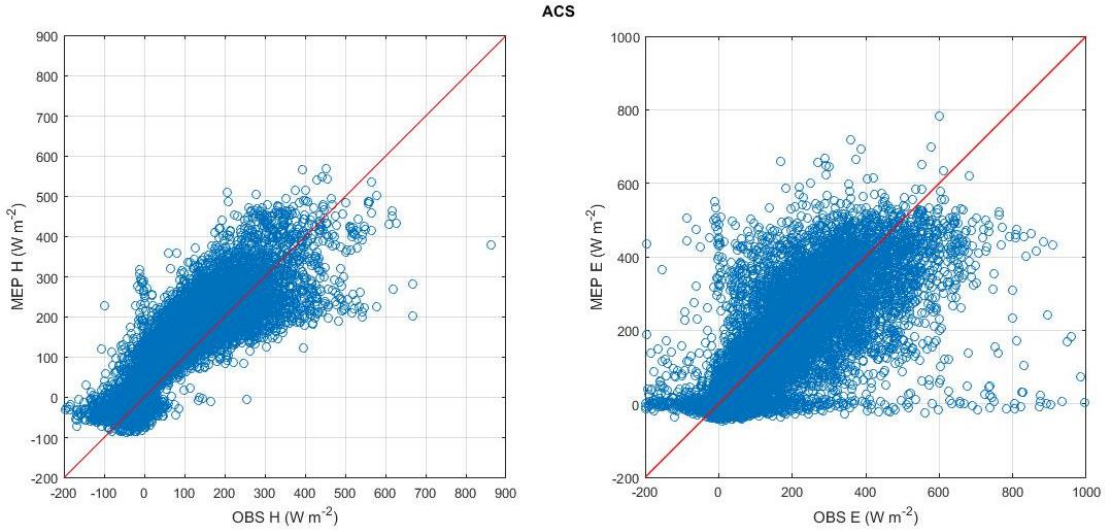

Figure 4.2 MEP modeled heat fluxes at ACS

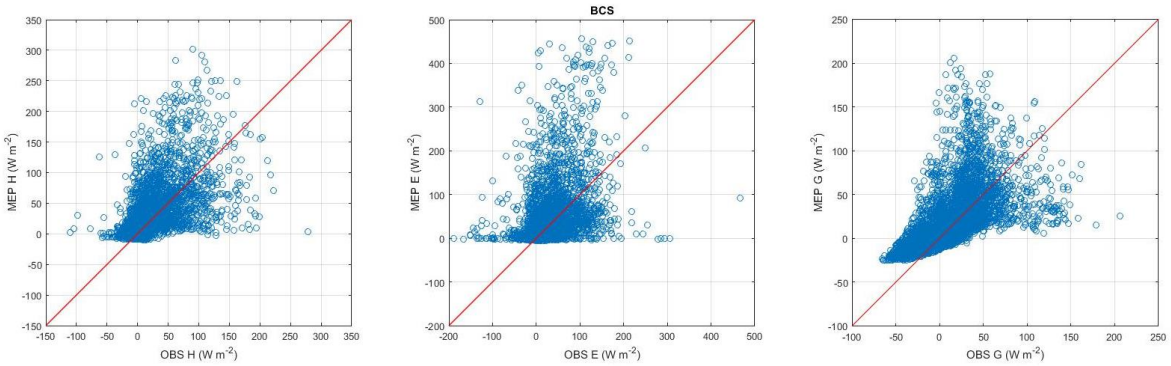

Figure 4.3 MEP modeled heat fluxes at BCS

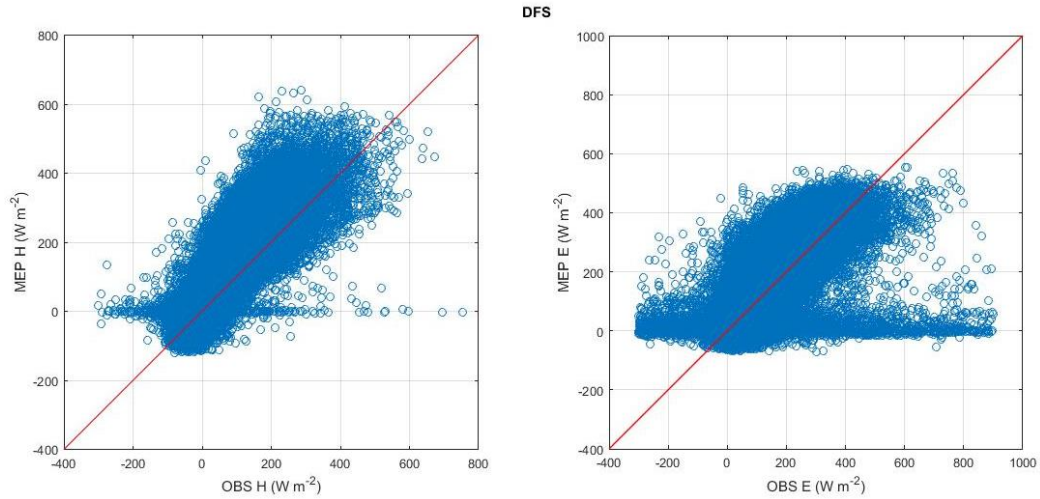

Figure 4.4 MEP heat fluxes at DFS

Figures 4.5 to 4.7 show the mean diurnal cycles of the MEP modeled and EC observed heat fluxes at ACS, BCS, and DFS, respectively. At ACS, the mean MEP *H* is almost identical to the OBS one during nighttime, is slighter higher than the OBS one during daytime. The mean MEP *E* is negative during nighttime, while the OBS *E* is positive, inconsistent with the negative *Rn* during nighttime. During daytime, the MEP modeled and EC observed E are almost identical. At BCS, the MEP modeled *H*, *E*, and *G* agree well with the OBS heat fluxes except when the daytime *Rn* has large fluctuations due to the shading of trees. At DFS, nighttime MEP modeled and EC observed *H* are almost identical, and daytime MEP

modeled *H* is about 30 % more than the EC observed one. Nighttime MEP modeled E are negative, consistent with the negative *Rn*, while the nighttime EC observed E are positive. During daytime, MEP modeled *E* are approximately 30 % more than the EC observed one. As the lack of energy balance closure of the observed fluxes at BCS ad DFS is identified and the energy balance closure of the MEP modeled fluxes are perfect (Table 4.1), the MEP is proved useful in estimating and filling the gaps of the observed data.

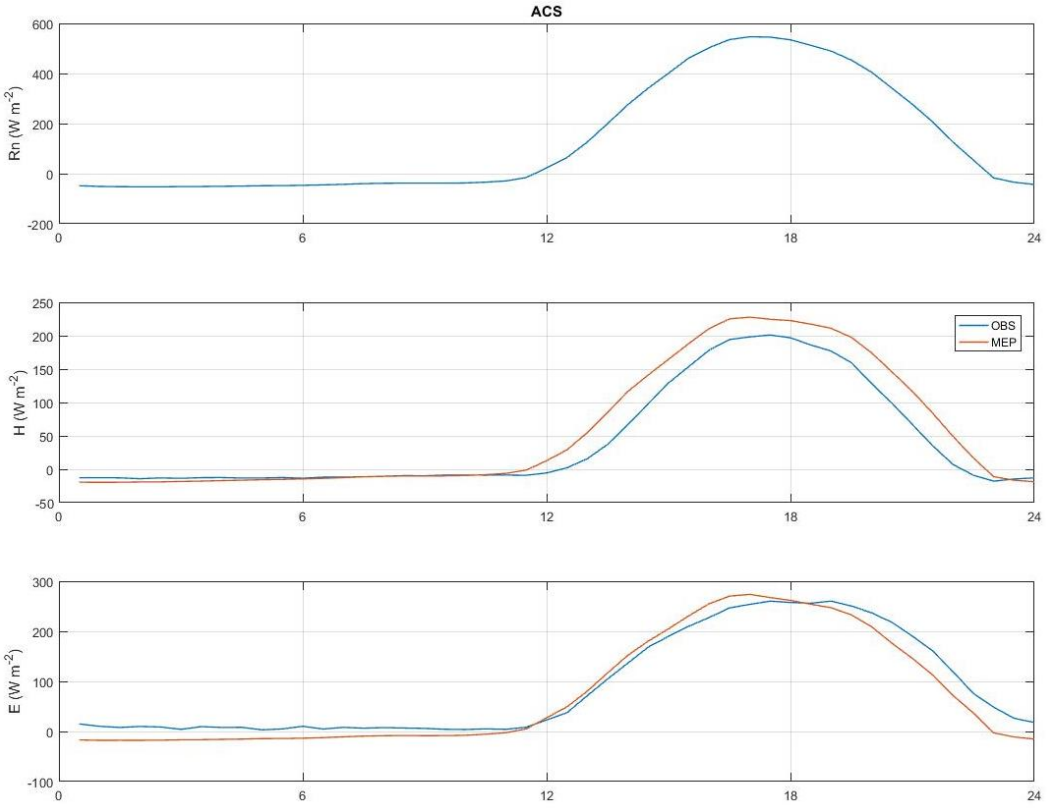

Figure 4.5 Mean diurnal cycles of heat fluxes at ACS

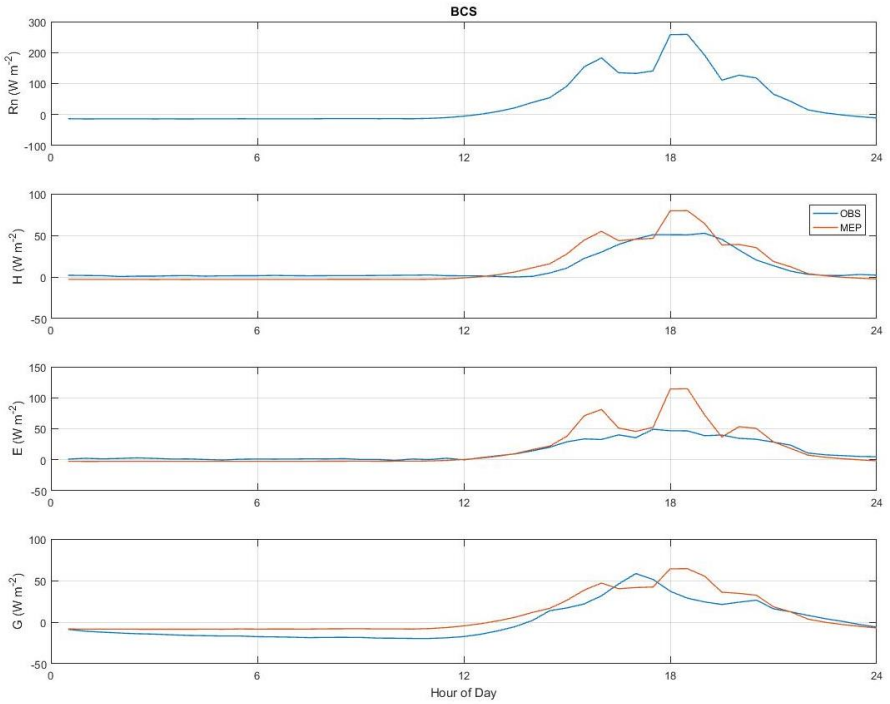

Figure 4.6 Mean diurnal cycles of OBS and MEP heat fluxes at BCS

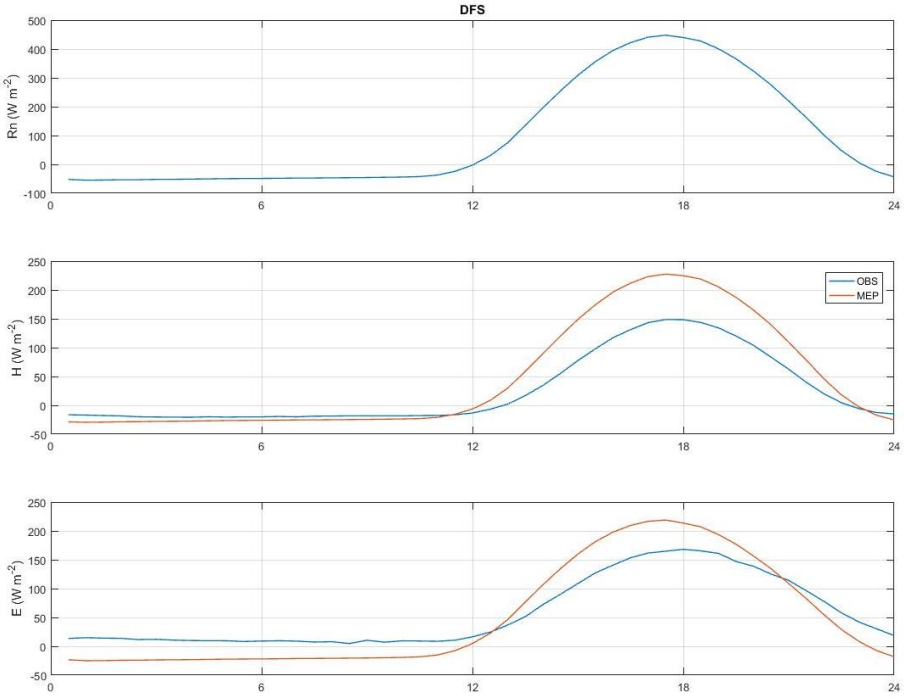

Figure 4.7 Mean diurnal cycles of heat fluxes at DFS

4.2.5 Conclusion

The MEP model is tested using field observations at ACS, BCS, and DFS with most available data, of which the time periods are 17 months, 7 months, and 7.6 years. The energy balance closure of the observed heat fluxes at ACS is much better than those at BCS and DFS. The MEP model generally estimates the heat fluxes at all sites accurately with NRMSEs no greater than 9%. The large discrepancies of the MEP modeled and EC observed heat fluxes appear during rain events, sunrise, and sunset, when the dews on the EC instruments cause large uncertainties of the measurements. The mean diurnal variations of the MEP heat fluxes agree well with the OBS ones at ACS and DFS, and the differences of the MEP and OBS heat fluxes at BCS are caused by the shading of trees. The good agreement of the MEP modeled and EC observed fluxes, and the perfect closure of the energy balance of the MEP modeled fluxes justify the applicability of the MEP model in data-fillings of the EC observations.

4.3 Model of Surface Gas Fluxes

4.3.1 Introduction

Fluxes of greenhouse gases such as water vapor and CO_2 over land surface are commonly estimated using the bulk transfer model (BTM) [*Sellers et al.*, 1997; *K C Wang and Dickinson*, 2012]. A bulk flux, according to the BTM, is expressed as the bulk gradient of gas concentration (measured at two levels separated by a short distance) multiplied by a transfer coefficient, which is often parameterized in terms of wind speed and surface roughness [*Arya*, 2001]. The BTM is suitable for estimating gas fluxes when multiple-level gas concentration and wind speed data are available. Multiple-level observations of water

vapor concentration (air humidity) are abundant while multiple-level measurements of other greenhouse gases such as CO_2 and methane are less common from field observation networks in the US including AmeriFlux (http://ameriflux.lbl.gov/) or around the world such as FLUXNET (http://fluxnet.fluxdata.org/). Although the AmeriFlux Tech team has started building portable profile systems to measure CO_2 concentration at multiple levels since 2013, the new systems have only been tested at around 30 sites out of 300 sites in the AmeriFlux network. The estimation of gas fluxes at regional scales using the BTM require remote sensing data of bulk gradient of gas concentration and wind speed. Yet, the (near-surface) bulk gradients of gas concentration cannot be measured remotely. To our knowledge, remote sensing data of surface wind speed over lands, contrary to oceans [*Cox and Munk*, 1954; *Garrison et al.*, 1998; *Garrison et al.*, 2002], do not exist. Surface roughness is even more difficult to measure remotely at regional scales especially for vegetated surfaces [*Beven*, 1979; *Kondo and Watanabe*, 1992]. Therefore, an alternative method for modeling gas fluxes is desirable for the estimation of regional gas fluxes over land surfaces.

In this study, we formulate and test an innovative model of gas fluxes that does not use bulk gradient of gas concentration, surface wind speed, or surface roughness. The half-order derivative (HOD) model based on fractional calculus [*Miller and Ross*, 1993] was first proposed for modeling sensible and ground heat flux derived from single-level temperature data [*J Wang and Bras*, 1998; 1999]. We propose to generalize the HOD model to estimating turbulent gas fluxes over land surfaces from single-level gas concentration data. The model formulation follows the concept that a spatial gradient variable may be expressed in terms of the time-history of the corresponding scalar variable

when the transport process is described by a diffusion equation. A novel parameterization of eddy-diffusivity in terms of sensible heat flux based on the Monin-Obukhov similarity theory [*J Wang and Bras*, 2010] characterizes the effect of turbulent mixing under both unstable (daytime) and stable (nighttime) conditions. The MEP model [*J Wang and Bras*, 2011] may be used for deriving sensible heat flux from surface radiation and temperature data to facilitate remote sensing applications of the proposed model at regional and global scales.

4.3.2 Model Formulation

The distribution of a non-reactive gas in the atmospheric surface layer is often described by a one-dimensional diffusion equation assuming that the gas transport is predominantly vertical [*Nieuwstadt*, 1980],

$$\frac{\partial C}{\partial \mathrm{t}} = \frac{\partial}{\partial \mathrm{z}}\left[D_c(z,t)\frac{\partial C}{\partial z} \right] \qquad \textbf{4.15}$$

where C (kg m^{-3}) is the gas concentration (density), D_c (z, t) (m^2 s^{-1}) the variable eddy-diffusivity, and z (m) the distance above the ground or canopy surface. Theoretically, C and D_c could be the averaged values at any time scales, and for testing the model, data with finest time resolution (half-hourly or hourly) are used. In this study, a new parameterization of D_c based on the Monin-Obukhov similarity theory [*J Wang and Bras*, 2010] is adopted assuming that the turbulent flow in the boundary layer responsible for heat transfer is also responsible for the transport of passive tracers such as water vapor and CO_2 [*Monteith and Unsworth*, 2013],

$$D_c(z,t) = D_0 z^{\frac{4}{3}} |H(t)|^{\frac{1}{3}} \qquad \textbf{4.16}$$

where H (W m^{-2}) is sensible heat flux (defined as positive when heat is transferred from the land surface into the atmosphere), and D_0 an empirical constant (Eq. (E1)) related to the coefficients in the Monin-Obukhov similarity equations [*Businger et al.*, 1971]. As EC measured H is unreliable during rainy periods [*Aubinet et al.*, 2012], H in Eq. 4.16 may be parameterized using the MEP model in terms of surface net radiation and air temperature. Tests of the MEP model have been reported previously [*Huang et al.*, 2016; *Nearing et al.*, 2012; *Shanafield et al.*, 2015; *H L Wang et al.*, 2017; *J Wang and Bras*, 2009; 2011; *J Wang et al.*, 2014; *Yang and Wang*, 2014].

It can be shown (Appendix E) that gas flux F_c (kg m^{-2} s^{-1}), defined as positive when transferred from the land surface into the atmosphere, is expressed as

$$F_c(z,t) \equiv -D_c(z,t)\frac{\partial C}{\partial z} = \frac{D_c(z,t)}{\sqrt{\pi}} \int_0^t \frac{\partial C(z,\tau)}{\partial \tau} \left[\int_\tau^t D_c(z,\zeta) d\zeta \right]^{-\frac{1}{2}} d\tau \qquad \textbf{4.17}$$

where τ, ζ are the integration (dummy) variables. Theoretically, the starting time (t = 0) is the time when C is constant in z corresponding to zero flux to allow an analytical solution of F_c as in Eq. 4.17. This assumption turns out to be not restrictive since the sensitivity of F_c to the initial condition of C, measured by the RMSEs of the modeled CO_2 fluxes, is limited due to the fact that the effect of the initial value of C on F_c decays rapidly with time. As shown in Figure 4.8, a 12-hour time-series is sufficient to obtain accurate F_c using Eq. 4.17.

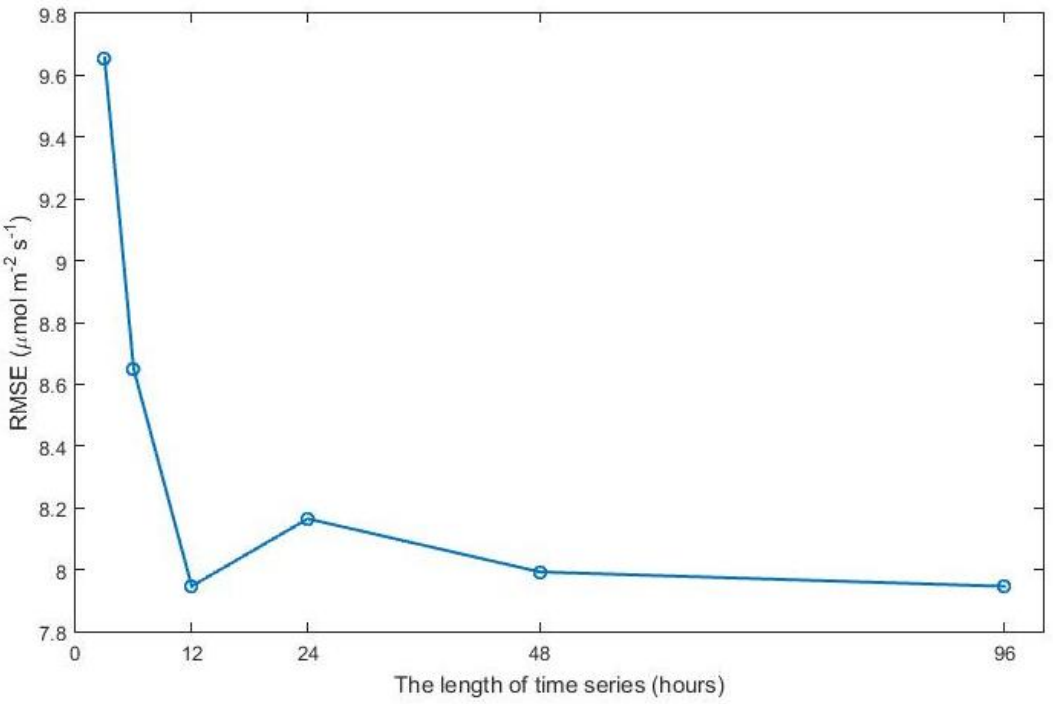

Figure 4.8 The effect of the length of time series on the RMSEs of the modeled CO_2 fluxes calculated using one-year's data at Santarem-Km67-Pramary Forest site in 2003

The proposed model allows a surface gas F_c to be derived from a weighted average of the single-level time-series data of gas concentration C. In fact, F_c over the entire period (0 to t) is obtained from the time-series data of C and D_c (or H) over the same period. Calculation of F_c using Eq. 4.17 involves a numerical integration of a singular convolution with a removable singularity of the integrand at $\tau = t$. A numerical algorithm for computing F_c is given in Appendix F. F_c in Eq. 4.17 does not require uniform sampling interval of C data, but large data gaps will affect the accuracy of F_c. Figure 4.9 demonstrates the dependence of RMSEs of the modeled F_c on the integration time step or sampling interval of C. It is evident that hourly C data are sufficient to capture the diurnal variations of F_c with reasonable accuracy.

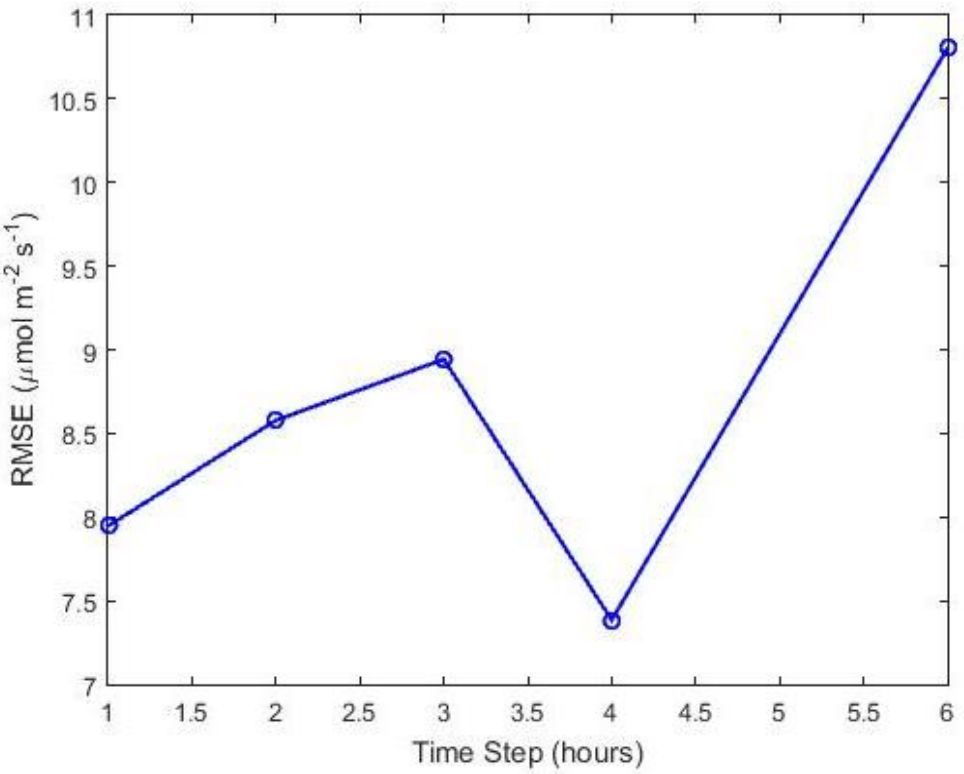

Figure 4.9 Dependence of RMSE of the modeled CO_2 fluxes, according to numerical algorithm as in Eqs. (F3)- (F4), to the integration time step calculated using one-year's data at Santarem-Km67-Pramary Forest site in 2003

The proposed non-gradient model has several advantageous properties. First, the model uses single-level gas concentration data instead of gas concentration gradient data that are rarely available and subject to larger measurement and/or modeling errors. Second, the model is parameter parsimonious as it requires fewer inputs than BTM models. The HOD model does not use near-surface wind speed, surface roughness, or vegetation specific data. Third, the modeled gas fluxes are not sensitive to the uncertainties of sensible heat flux due to the one-sixth power dependence of F_c on H. For example, when the uncertainty of H is 20%, the corresponding uncertainties of the eddy-diffusivity and the modeled fluxes are only 6% and 3%, respectively. Fourth, the parameterization of H in terms of surface net radiation and temperature using the MEP model facilitates the application of the HOD

model at regional and global scales. These advantageous properties result in part from the new parameterization of eddy-diffusivity.

4.3.3 Data

4.3.3.1 Site Descriptions

Test sites with diverse and contrasting climates, geography, land covers, and vegetation types from the AmeriFlux network are selected to evaluate the model's performance [*Allison et al.*, 2005; *Kwon et al.*, 2018; *Morin et al.*, 2017; *Saleska et al.*, 2003; *T J Sauer et al.*, 2007]. The Santarem-Km67-Pramary Forest site (BR-Sa1 for short, 2.9 °S, 55.0 °W) is located in evergreen broad leaf Amazon rainforest with mean canopy height of 45 m in Pará, Brazil. The tropical climate is strongly influenced by the monsoon with annual mean air temperature 26 °*C* and precipitation 2,075 mm. Latent heat fluxes (W m^{-2}), CO_2 flux (μmol m^{-2} s^{-1}), CO_2 concentration (μmol mol^{-1}), air temperature (°C), and relative humidity (%) are recorded hourly at 58 m above ground level (AGL). Net radiation (W m^{-2}) is measured at 64.1 m AGL. The available percentages of CO_2 concentration, CO_2 fluxes, and latent heat fluxes at BR-Sa1 in 2003 are 93 %, 88 %, and 88 %, respectively. The Marys River Fir site (US-MRf for short, 44.6 °N, 123.6 °W) is located in an evergreen needle leaf forest with mean canopy height of 30 m in Oregon, United States. The climate is Mediterranean with annual mean temperature 10 °*C* and precipitation 1,819 mm. Half-hourly EC fluxes, CO_2 concentration, and other meteorological variables are measured at 38.3 m AGL. Net radiation is measured at 37 m AGL. The available percentages of CO_2 concentration, CO_2 fluxes, and latent heat fluxes at US-MRf in 2007 are 94 %, 77 %, and

84 %, respectively. These two forest sites are selected to test the model for estimating gas fluxes at diurnal and seasonal scales.

Calhoun Critical Zone Observatory site (CCZO for short, 34.6 °N, 81.7 °W) is located in a young pine forest with canopy height of 6 m in South Carolina, United States. CCZO has a warm temperate climate with annual mean temperature 16 °*C* and precipitation 1,300 mm. Half-hourly EC fluxes and other meteorological variables are measured at 9 m AGL. CCZO data are not used for seasonal analysis due to incomplete coverage of EC fluxes data.

The Brooks Fields Site 11-Ames (US-Br3 for short, 42.0 °N, 93.7 °W) is located in a corn/soybean agricultural region in Iowa, United States. The climate is humid continental (cold winter, hot summer, and no dry season) with annual mean temperature 8.9 °*C* and precipitation 847 mm. Half-hourly EC fluxes and other meteorological variables are measured at 2.4 m AGL in 2007. The growing season of soybean in Iowa is from May to October.

The Fermi National Accelerator Laboratory – Batovia (Prairie site) (US-IB2 for short, 41.8 °N, 88.2 °W) is located in a restored prairie in Illinois, United States. The climate is humid continental with annual mean temperature 9 °*C* and precipitation 930 mm. Half-hourly EC fluxes and other meteorological variables are measured at 3.76 m AGL.

The Olentangy River Wetland Research Park (US-ORv for short, 40.0 °N, 83.0 °W) is located in a 21-ha large-scale, long-term wetland campus facility in Ohio, United States. The climate is humid subtropical with annual mean temperature 11.6 °*C* and precipitation 1,500 mm. Half-hourly EC fluxes and other meteorological variables are measured at 9.6 m AGL. Growing seasons at these four sites with different land covers are selected to test

the proposed model. Data are recorded in local time zone at all sites, except for CCZO, where data are recorded in Coordinate Universal Time. These sites (summarized in Table 4.4) represent major land covers where water vapor and CO_2 fluxes are strong.

Table 4.4 Site information [a]

Site name	Coordinate	Vegetation	Climate	Annual mean T_a (°C)	Annual mean *PREC*(mm)
BR-Sa1	2.9 °S, 55.0 °W	Evergreen broadleaf Amazon rainforest	Tropical monsoon	26.0	2,075
US-MRf	44.6 °N, 123.6 °W	Evergreen needle leaf forest	Mediterranean	10.2	1,819
CCZO	34.6 °N, 81.7 °W	Young pine forest	Humid subtropical	16.0	1,300
US-Br3	42.0 °N, 93.7 °W	Cropland	Humid continental	8.9	847
US-IB2	41.8 °N, 88.2 °W	Grassland	Humid continental	9.0	930
US-ORv	40.0 °N, 83.0 °W	Permanent wetland	Humid subtropical	11.6	1,499

[a] T_a = air temperature, *PREC* = precipitation.

4.3.3.2 EC measurement errors

EC fluxes are subject to substantial measurement errors caused by the inherent variability of turbulence, sampling errors, uncertainties of the mean variables in the calculation of covariance of vertical wind and the scalar, instrument calibration errors among others [*Aubinet et al.*, 2012]. The EC measurement errors generally vary with land covers, and increase with the magnitude of fluxes. The measurement errors over forest are generally larger than over grassland or cropland [*Richardson et al.*, 2006]. Daytime relative flux uncertainty, defined as the ratio of standard deviation of random errors to hourly mean fluxes, is 20% at maize site, and 40% at forest sites [*D. Vickers et al.*, 2010]. Nighttime

EC fluxes are more uncertain than daytime fluxes due to intermittent turbulence, low wind speed, and temperature inversion [*Aubinet*, 2008; *D. D. Baldocchi*, 2003]. At forest sites, the relative uncertainty of EC water vapor fluxes could reach 84% during nighttime compared to 45% during daytime [*D. Vickers et al.*, 2010]. Hence, nighttime fluxes are often rejected in the analysis of model simulations [*A. G. Barr et al.*, 2006]. Similarly, the EC fluxes during winters are more uncertain than during summers due to lower EC data quality caused by weak turbulence, strong stability, and liquid water in gas analyzer path [*Post et al.*, 2015]. EC fluxes during rainy periods are especially problematic due to instrumental malfunctions. Raindrops and ice may block the transducer path, attenuate the sound pulse of sonic anemometer, and degrade the three-dimensional wind speed measurements [*Aubinet et al.*, 2012]. Water drops on the sapphire windows of infrared gas analyzer head can weaken sensor signals, leading to unrealistic gas concentration readings. In this study, growing season data are selected to test the model at diurnal time scale with rainy periods excluded as suggested [*Hollinger and Richardson*, 2005; *K B Wilson et al.*, 2001].

4.3.4 Water Vapor Fluxes

4.3.4.1 Diurnal scale analysis

The HOD model requires observations of net radiation, air temperature, and relative humidity for calculating water vapor fluxes according to Eq. 4.17. Eddy-diffusivity in Eq. 4.17 are parameterized according to Eq. 4.16 in terms of H calculated from net radiation, air temperature, and/or relative humidity using MEP model. The modeled water vapor fluxes are compared with the EC measured latent heat fluxes.

Figures 4.10 to 4.15 show the modeled (HOD) vs. observed (OBS) diurnal surface water vapor fluxes (F_v) during growing season at the six test sites. Panel (a) shows the canopy surface and observed near-surface water vapor concentration (C_v) for calculating water vapor fluxes. Measurements of surface soil moisture (θ) are also included in Panel (a) when available. Since canopy surface humidity is not directly measured, daytime canopy surface water vapor concentration is calculated as the saturation water vapor density at canopy surface temperature assumed equal to near-surface air temperature (Appendix G). Vegetation at the test sites during the growing season is mostly not water-stressed under the condition of relatively high soil moisture. Open stomata of plants under no water stress make leaf surface humidity equal or close to saturation. Nighttime canopy surface water vapor concentration is obtained from the observed near-surface water vapor concentration (calculated from the measured near-surface air temperature and relative humidity) since condensation of water vapor during nighttime (or negative water vapor flux) is controlled by air humidity. This inference of canopy surface water vapor concentration is confirmed by the close agreement of the HOD modeled water vapor fluxes with the observations at all test sites. Panels (b) and (c) compare the HOD and OBS diurnal variations of water vapor fluxes (F_v). Rainfall data when available are shown in Panel (b). Panels (d) and (e) compare the mean diurnal cycles of the HOD and OBS water vapor fluxes. The RMSEs, normalized RMSEs (NRMSE, defined as the RMSE divided by the range of the OBS fluxes), and correlation coefficients (r) of the HOD vs. OBS water vapor fluxes are summarized in Table 4.5.

Table 4.5 Statistics of HOD vs. OBS water vapor fluxes in diurnal and seasonal scale analyses including Period (day), RMSE (mmol m^{-2} s^{-1}), NRMSE (%), *r*

Diurnal Scale Analysis							
Site name	Period	RMSE[a]	NRMSE[a]	r^a	RMSE[b]	NRMSE[b]	r^b
BR-Sa1	10	1.44	13	0.90	0.63	8	0.98
US-MRf	10	0.82	13	0.87	0.47	13	0.95
CCZO	10	1.01	7	0.88	0.45	10	0.98
US-Br3	14	1.07	8	0.90	0.47	9	0.98
US-IB2	20	2.39	19	0.81	0.86	10	0.98
US-ORv	10	2.24	11	0.81	1.08	12	0.95
Seasonal Scale Analysis							
Site name	Period	RMSE[c]	NRMSE[c]	r^c	RMSE[d]	NRMSE[d]	r^d
BR-Sa1	365	0.64	7	0.97	0.35	5	0.99
US-MRf	365	0.43	10	0.95	0.31	12	0.97

[a] calculated using hourly or half-hourly results, [b] calculated using mean diurnal cycles in diurnal scale analysis, [c] calculated using monthly mean diurnal cycles, [d] calculated using annual mean diurnal cycles.

The HOD model estimates water vapor fluxes accurately (Table 4.5) at all sites given that the relative uncertainties of the EC latent heat fluxes are 20% over cropland, 40% over pine forest during daytime, and nearly doubled over pine forest during nighttime [*D. Vickers et al.*, 2010]. Discrepancies between the HOD and OBS fluxes occur during relatively dry and rainy days. During dry days, the HOD water vapor fluxes tend to be overestimated due to the overestimation of water vapor concentration. The actual leaf surface water vapor concentration is lower than saturation water vapor concentration due to partial or complete stomatal closure caused by high atmospheric evaporative demand (high temperature with dry air) or soil water limitation (dry soil) [*Tombesi et al.*, 2015]. For example, on DOY 221 at US-MRf site, high air temperature with relatively low air humidity (Figure 4.16), and low soil moisture (Figure 4.11 (a)) cause stomatal closure, leading to leaf surface water vapor substantially below saturation level. Better parameterization of leaf surface water

vapor concentration under low soil moisture has been proposed [*Hajji et al.*, 2018]. The issue of large EC measurement errors during rainy days is discussed in Section 4.4.3.2.

It is evident that the mean diurnal cycles of the HOD water vapor fluxes shown in Panels (d) and (e) of Figures 4.10 to 4.15 agree closely with the EC measured fluxes. All correlation coefficients of the mean diurnal cycles of HOD and OBS water vapor fluxes are above 0.95, indicating good performance of the model at diurnal time scale. Note that positive mean nighttime OBS water vapor fluxes at all sites excluding wetland site are inconsistent with the land surface energy balance and the Fick's law of mass transfer [*Arya*, 2001]. Earlier studies have shown that the EC measured water vapor fluxes are subject to large uncertainties, especially when wind is weak during night times [*Novick et al.*, 2009]. In contrast, the HOD model provides realistic nighttime water vapor fluxes, mostly negative (condensation) except for the case of permanent wetland, where water vapor fluxes are positive throughout the night [*South et al.*, 1998].

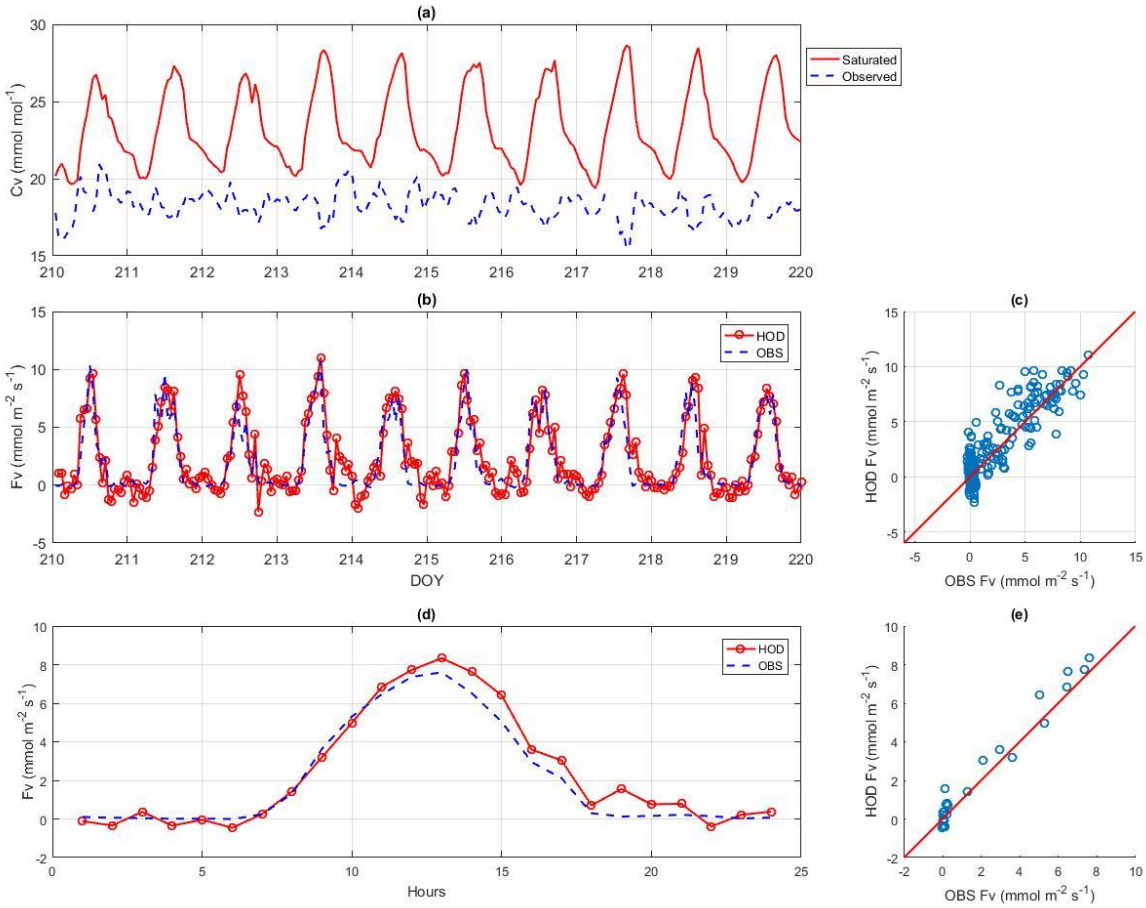

Figure 4.10 Evergreen broadleaf Amazon rainforest: (a**) saturated and observed water vapor concentration (*C_v*), (**b**) modeled (HOD) vs. observed (OBS) water vapor flux (*F_v*), (**c**) HOD vs. OBS *F_v*, *r* = 0.90,** (d) **mean diurnal cycles of HOD vs. OBS *F_v*, and** (e) **mean diurnal cycles of HOD vs. OBS *F_v*, *r* = 0.98, at BR-Sa1, Jul. 29- Aug. 8, 2003.**

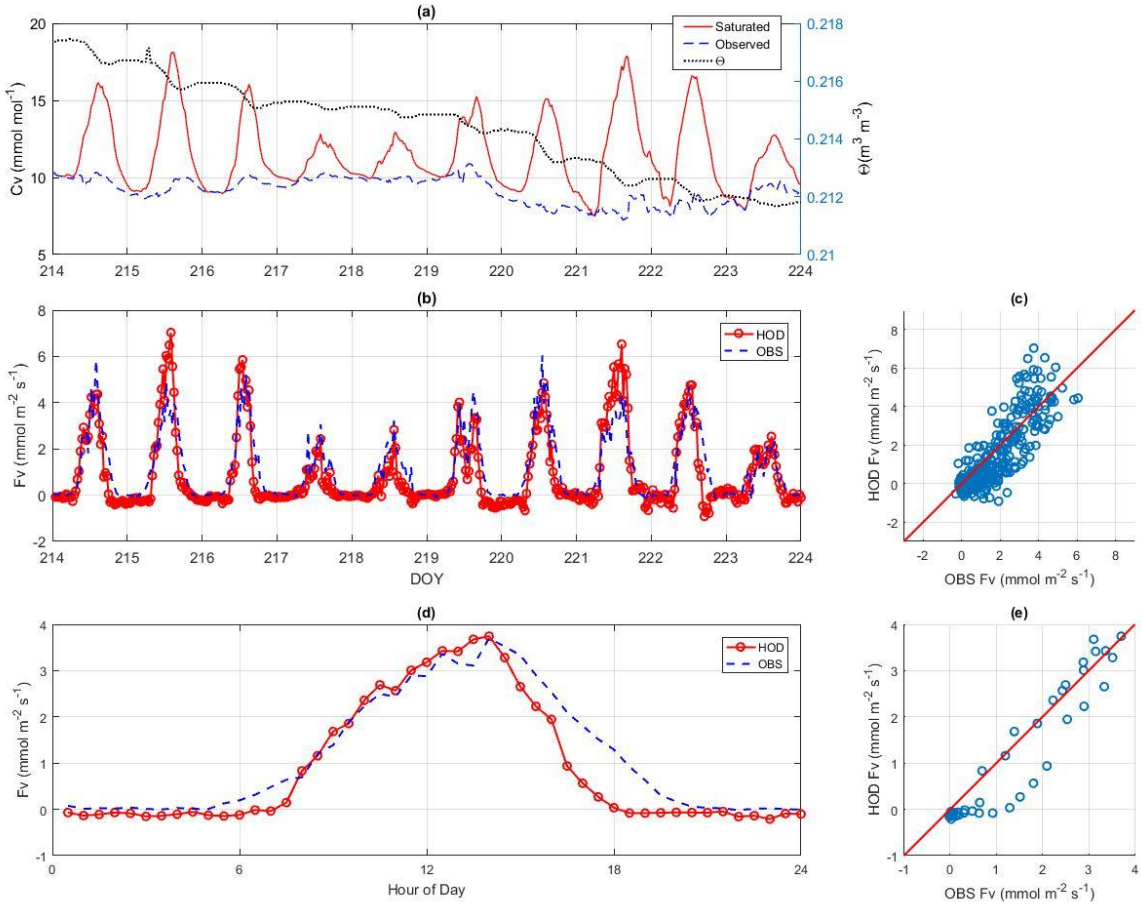

Figure 4.11 Evergreen needle leaf forest: (a**) saturated and observed C_v, and θ, (**b**) HOD vs. OBS F_v, (**c**) HOD vs. OBS F_v, r = 0.87,** (d) **mean diurnal cycles of HOD vs. OBS F_v, and** (e) **mean diurnal cycles of HOD vs. OBS F_v, r = 0.95, at US-MRf, Aug. 2- Aug. 12, 2007.**

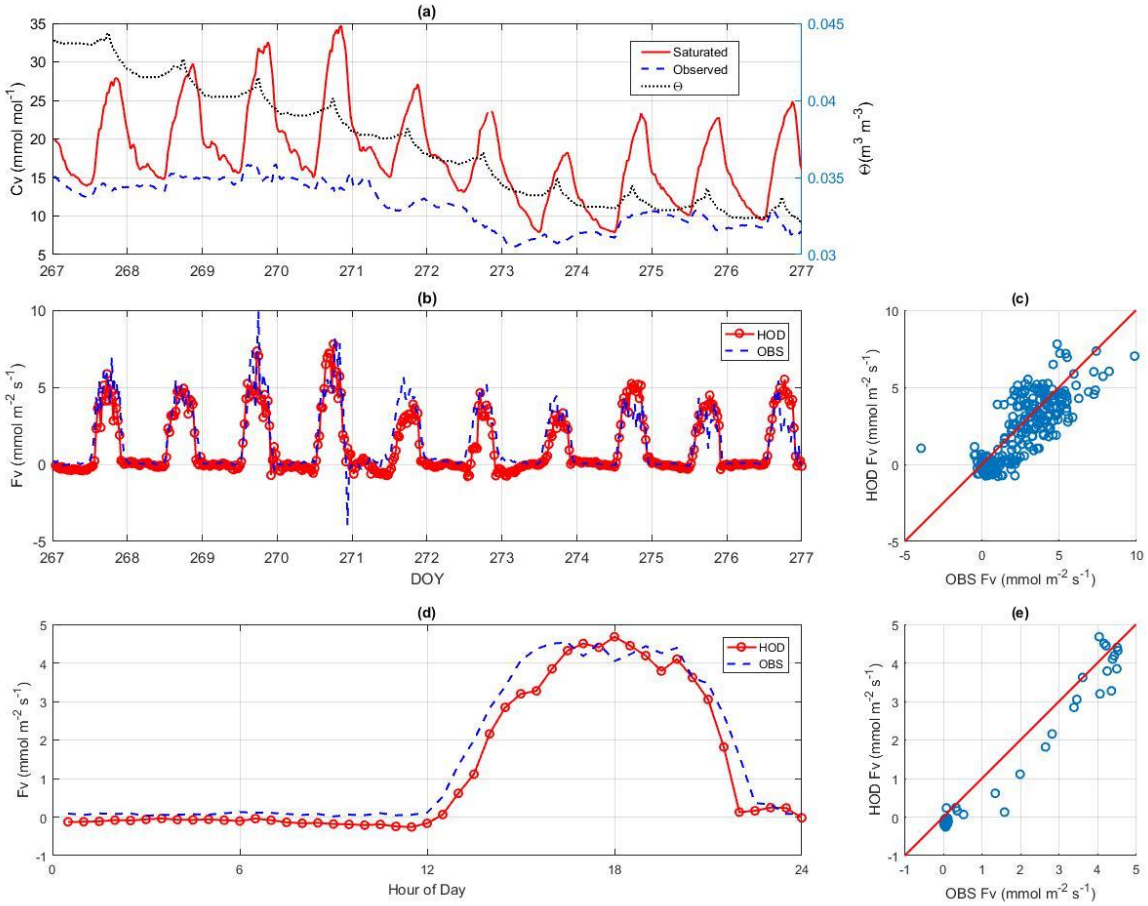

Figure 4.12 Young pine forest: (a**) saturated and observed C_v, and θ, (**b**) HOD vs. OBS F_v, (**c**) HOD vs. OBS F_v, r = 0.88, (**d**) mean diurnal cycles of HOD vs. OBS F_v, and (**e**) mean diurnal cycles of HOD vs. OBS F_v, r = 0.98, at CCZO, Sep. 24- Oct. 4, 2017.**

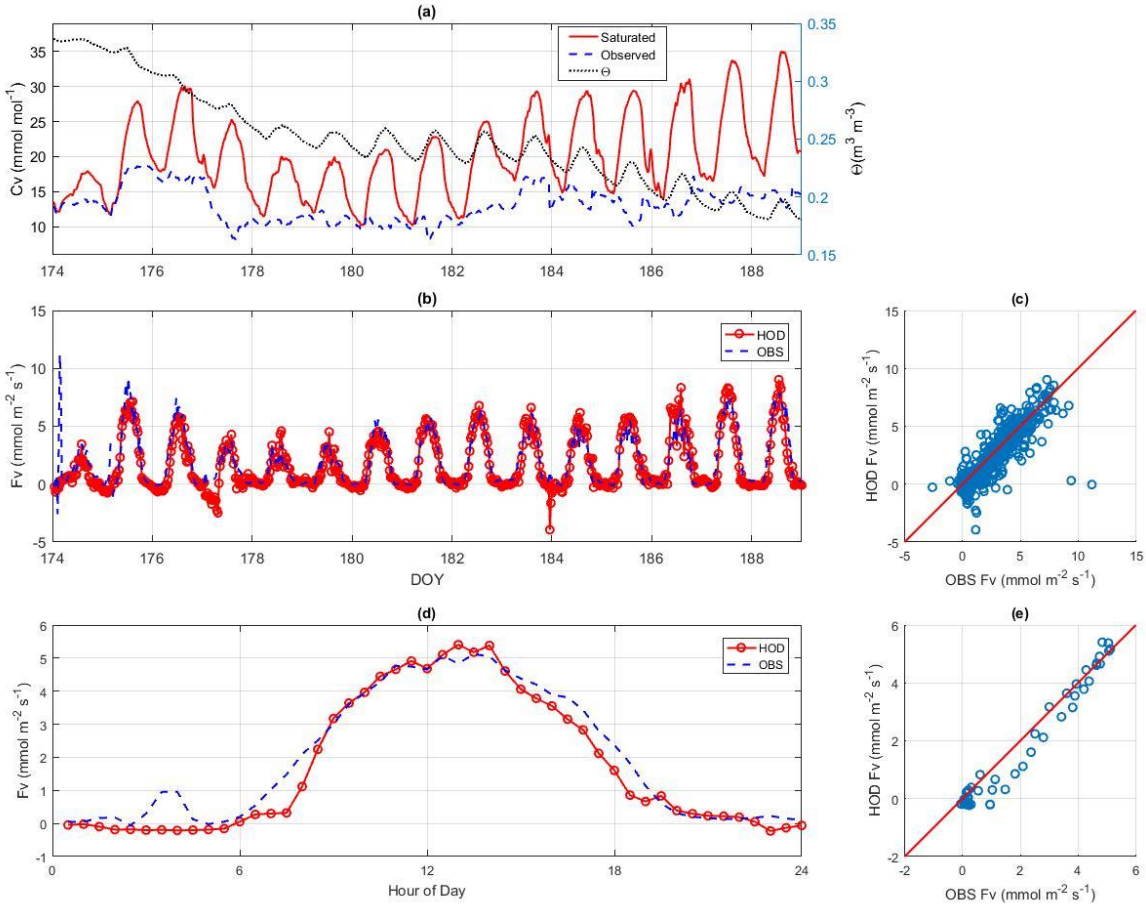

Figure 4.13 Cropland: (a**) saturated and observed C_v, and θ, (**b**) HOD vs. OBS F_v, (**c**) HOD vs. OBS F_v, r = 0.90,** (d) **mean diurnal cycles of HOD vs. OBS F_v, and** (e) **mean diurnal cycles of HOD vs. OBS F_v, r = 0.98, at US-Br3, Jun. 23- Jul. 8, 2007.**

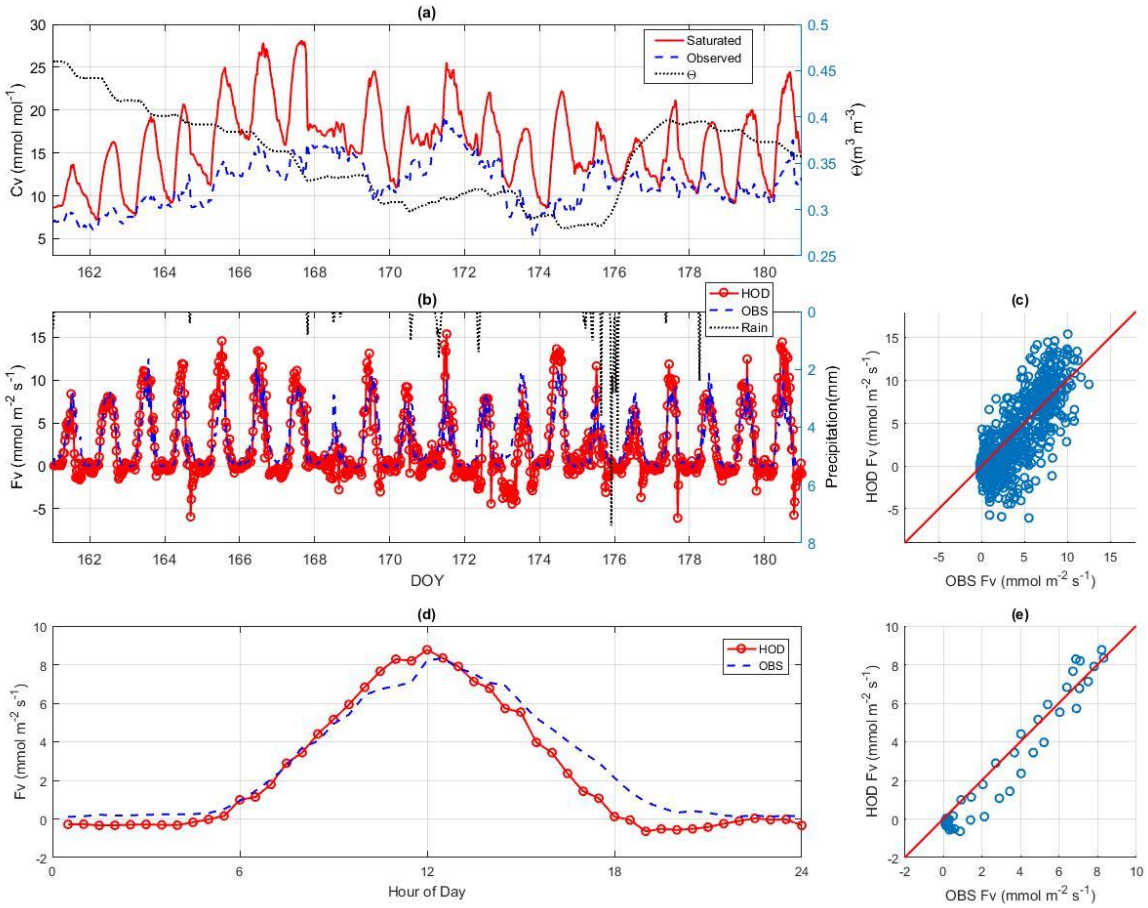

Figure 4.14 Grassland: (a) saturated and observed C_v, and θ, (b) HOD vs. OBS F_v, and precipitation, (c) HOD vs. OBS F_v, r = 0.81, (d) mean diurnal cycles of HOD vs. OBS F_v, and (e) mean diurnal cycles of HOD vs. OBS F_v, r = 0.98, at US-IB2, Jun. 10 - Jun. 30, 2006.

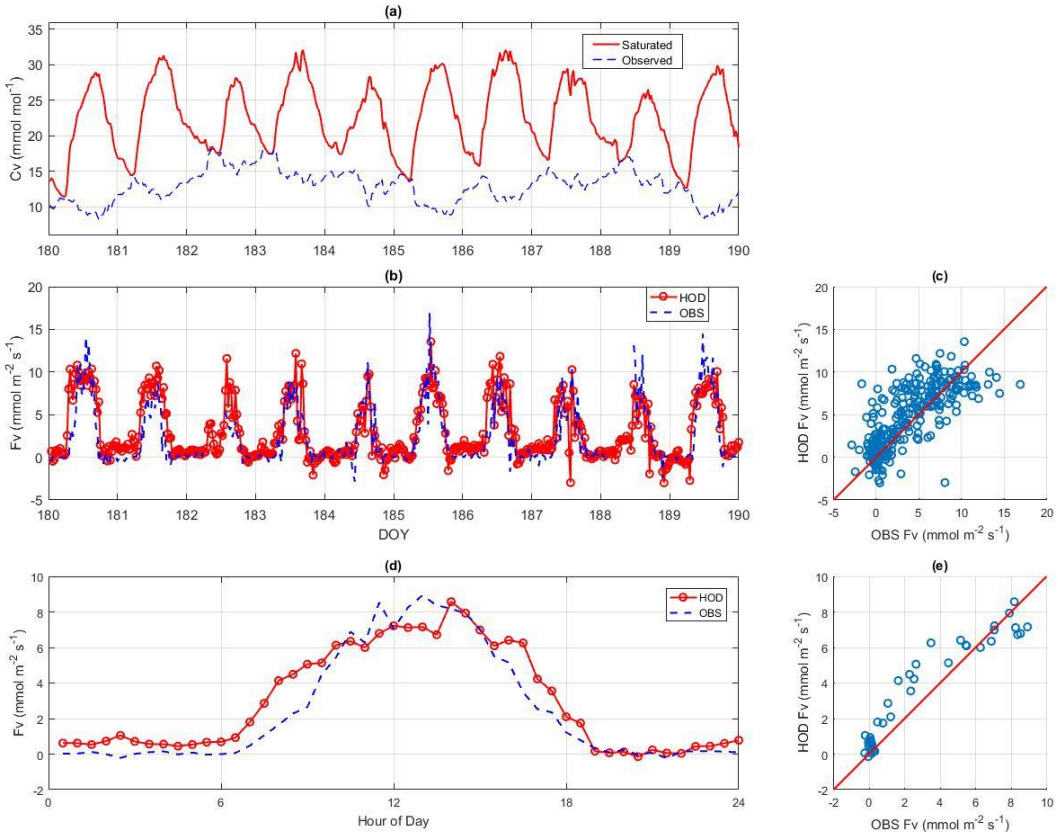

Figure 4.15 Permanent wetland: (a) saturated and observed C_v, (b) HOD vs. OBS F_v, (c) HOD vs. OBS F_v, r = 0.81, (d) mean diurnal cycles of HOD vs. OBS F_v, and (e) mean diurnal cycles of HOD vs. OBS F_v, r = 0.95, at US-ORv, Jun. 29 - Jul. 9, 2011.

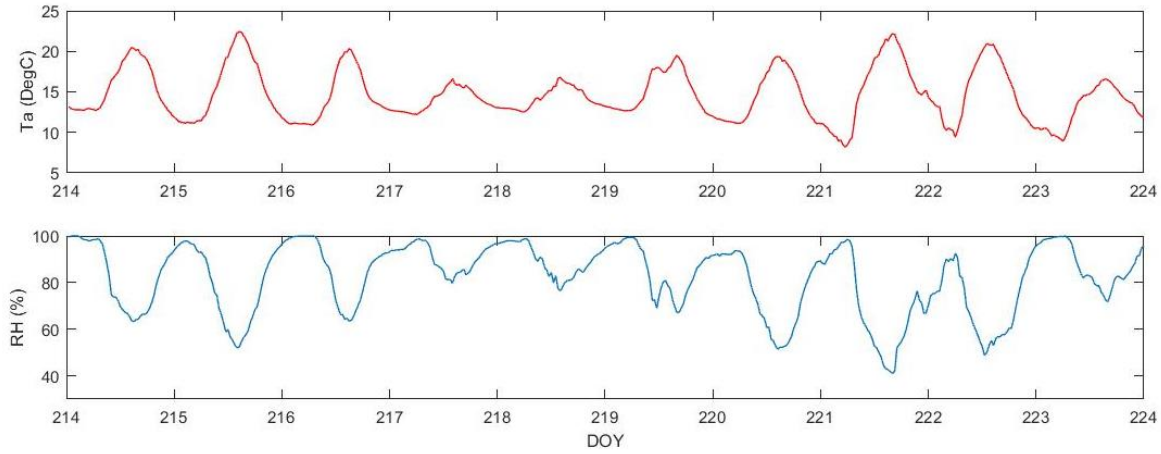

Figure 4.16 Evergreen needle leaf forest: air temperature (T_a) and relative humidity (RH), at US-MRf, Aug. 2- Aug. 12, 2007.

4.3.4.2 Seasonal scale analysis

Monthly accumulations and diurnal cycles are calculated from sub-daily results as shown in Figures 4.17 and 4.18. The monthly and annual accumulative fluxes are calculated from the corresponding monthly and annual mean diurnal cycles. Panel (a) shows the monthly accumulative daytime (6 AM to 6 PM), nighttime (6 PM to 6 AM), and all-day HOD and OBS water vapor fluxes. Panels (b) and (c) compare the monthly mean diurnal cycles of the HOD and OBS water vapor fluxes. Panels (d) and (e) compare the annual mean diurnal cycles of the HOD and OBS water vapor fluxes. The statistics of annual accumulative water vapor fluxes including daytime, nighttime, and all-day annual accumulations and corresponding relative errors, defined as the absolute error divided by the magnitude of the OBS fluxes, are summarized in Table 4.6.

Table 4.6 Statistics of annual accumulative daytime (6 AM to 6 PM), nighttime (6 PM to 6 AM), and all-day HOD and OBS fluxes of water vapor (F_v) and CO_2 (F_c) including relative error (σ)

F_v (mm year^{-1})									
	Daytime			Nighttime			All-Day		
Site name	HOD	OBS	σ	HOD	OBS	σ	HOD	OBS	σ
BR-Sa1	1127	1071	5 %	-5	28	118 %	1122	1099	2 %
US-MRf	414	478	13 %	-15	31	148 %	399	509	22 %
F_c (gC m^{-2} year^{-1})									
	Daytime			Nighttime			All-Day		
Site name	HOD	OBS	σ	HOD	OBS	σ	HOD	OBS	σ
BR-Sa1	-1199	-1280	6 %	922	920	0.2 %	-277	-360	23 %
US-MRf	-1681	-1898	11 %	913	229	298 %	-768	-1669	54 %

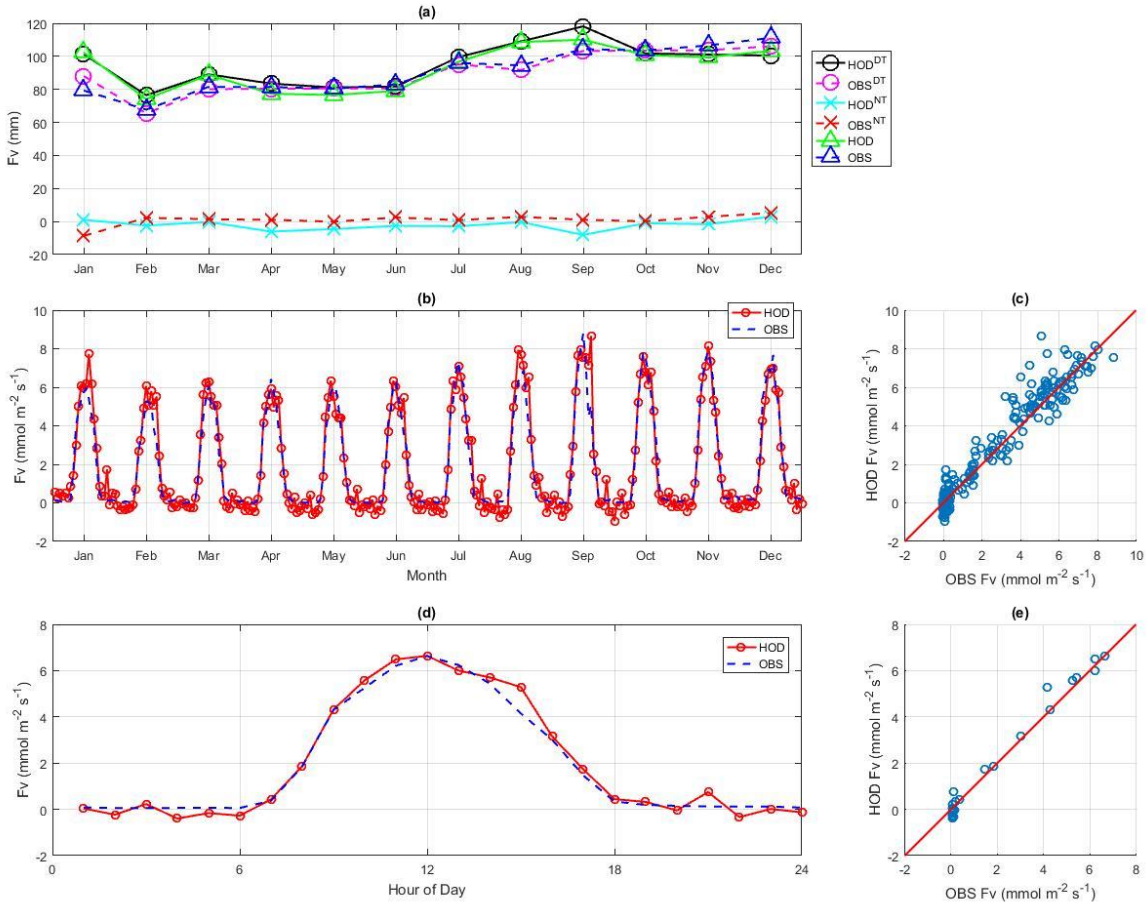

Figure 4.17 Evergreen broadleaf Amazon rainforest: (a**) monthly accumulative daytime (^DT, circle), nighttime (^NT, cross), and all-day (triangle) HOD (solid line) vs. OBS (dash line) F_v, (**b**) monthly mean diurnal cycles of HOD vs. OBS F_v, (**c**) monthly mean diurnal cycles of HOD vs. OBS F_v, r = 0.97, (**d**) annual mean diurnal cycles of HOD vs. OBS F_v, and** (e) **annual mean diurnal cycles of HOD vs. OBS F_v, r = 0.99, at BR-Sa1, 2003.**

Figure 4.17 (a) shows that the HOD model estimates the monthly (daytime, nighttime, and total) accumulative water vapor fluxes accurately at BR-Sa1. The monthly and annual mean diurnal cycles of the HOD and OBS water vapor fluxes are in close agreement as shown in Figures 4.17 (b) to (e) with correlation coefficients 0.97 and 0.99, respectively. The annual accumulative daytime HOD and OBS water vapor fluxes are 1127 and 1071 mm year^{-1}, respectively, with 5 % relative error. Both the OBS and HOD annual mean

nighttime water vapor fluxes are close zero. The annual accumulative nighttime HOD and OBS water vapor fluxes are -5 and 28 mm $year^{-1}$, respectively. The negative HOD water vapor fluxes are consistent with negative nighttime net radiation (-21 W m^{-2} on average) over land surfaces. The annual accumulative HOD water vapor fluxes (evapotranspiration or ET) at BR-Sa1 in 2003 is 1122 mm $year^{-1}$ with annual precipitation 1920 mm, which is consistent with the reported ET (1281 mm $year^{-1}$ with annual precipitation 2200 mm in 2001) at a site 23 km from BR-Sa1 [*da Rocha et al.*, 2004]. The encouraging results demonstrate that the model is suitable for estimating daily, monthly and annual ET over tropical rainforest.

Figure 4.18 presents the same seasonal analysis for US-MRf site. The HOD model captures the seasonal and diurnal variations of the OBS water vapor fluxes. The half-hour phase shift of the HOD and OBS fluxes as shown in Figure 4.18 (d) is likely caused by the half-hour time shift of net radiation and EC flux records. The annual accumulative daytime HOD and OBS water vapor fluxes are 414 and 478 mm $year^{-1}$, respectively, with 13% relative error given that the daytime relative uncertainty of latent heat fluxes at a mature pine forest site (MP for short) 150 km from US-MRf is 45 % [*D. Vickers et al.*, 2010]. The annual accumulative nighttime HOD and OBS water vapor fluxes are -15 and 31 mm $year^{-1}$, respectively. The positive OBS nighttime fluxes appear erroneous based on the land surface energy balance (with the average nighttime net radiation -32 W m^{-2}) given that the uncertainty of EC water vapor fluxes at MP is 84 % during nighttime [*D. Vickers et al.*, 2010]. The annual ET estimated by the HOD model (399 mm $year^{-1}$) is consistent with the reported annual ET (478 mm $year^{-1}$, http://terraweb.forestry.oregonstate.edu/marys-river-

fir-ameriflux-site-us-mrf) and the annual ET (430 mm year^{-1}) at MP site [*Anthoni et al.*, 1999].

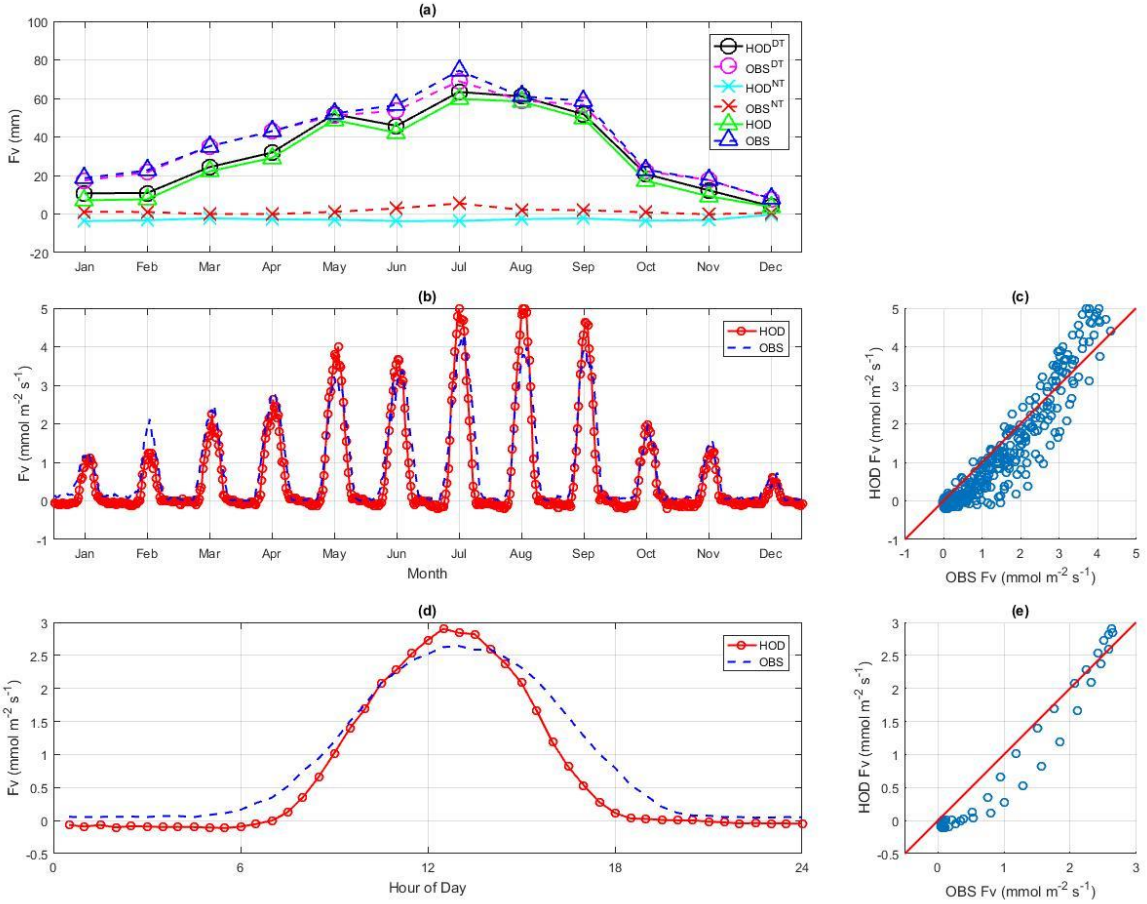

Figure 4.18 Evergreen needle leaf forest: (a**) monthly accumulative daytime (**^{DT}**, circle), nighttime (**^{NT}**, cross), and all-day (triangle) HOD (solid line) vs. OBS (dash line) F_v, (**b**) monthly mean diurnal cycles of HOD vs. OBS F_v, (**c**) monthly mean diurnal cycles of HOD vs. OBS F_v, r = 0.95, (**d**) annual mean diurnal cycles of HOD vs. OBS F_v, and (**e**) annual mean diurnal cycles of HOD vs. OBS F_v, r = 0.97, at US-MRf, 2007.**

The discrepancies of the HOD and OBS fluxes in February 2007 as shown in Figure 4.18 (b) are mainly caused by the malfunctions of EC sensors due to rain. Figure 4.19 shows that the EC fluxes are overestimated during rainy periods, while the HOD fluxes are realistic, being positive during daytime and negative during nighttime. Too many missing

data points of input variables during rainy periods are partially responsible for the discrepancies of the HOD and OBS fluxes. The sensitivity test in Figure 4.9 demonstrates that input data with coarse time resolution increase modeling errors, indicating that large input data gaps may affect the modeling accuracy. In the dry season of the Mediterrannean climate (July, August, and September), the noontime HOD water vapor fluxes are higher than the OBS fluxes as shown in Figure 4.18 (b) when assuming canopy surface water vapor concentration remains at saturation level. Yet under dry and hot condition, partial closure of stomata reduces leaf surface water vapor concentration. Parameterization of stomatal response to water or temperature stress is beyond the scope of this study. Nonetheless, the test results reported here imply that the HOD modeled fluxes would be more accurate using improved leaf surface water concentration data especially under the condition of water and temperature stress.

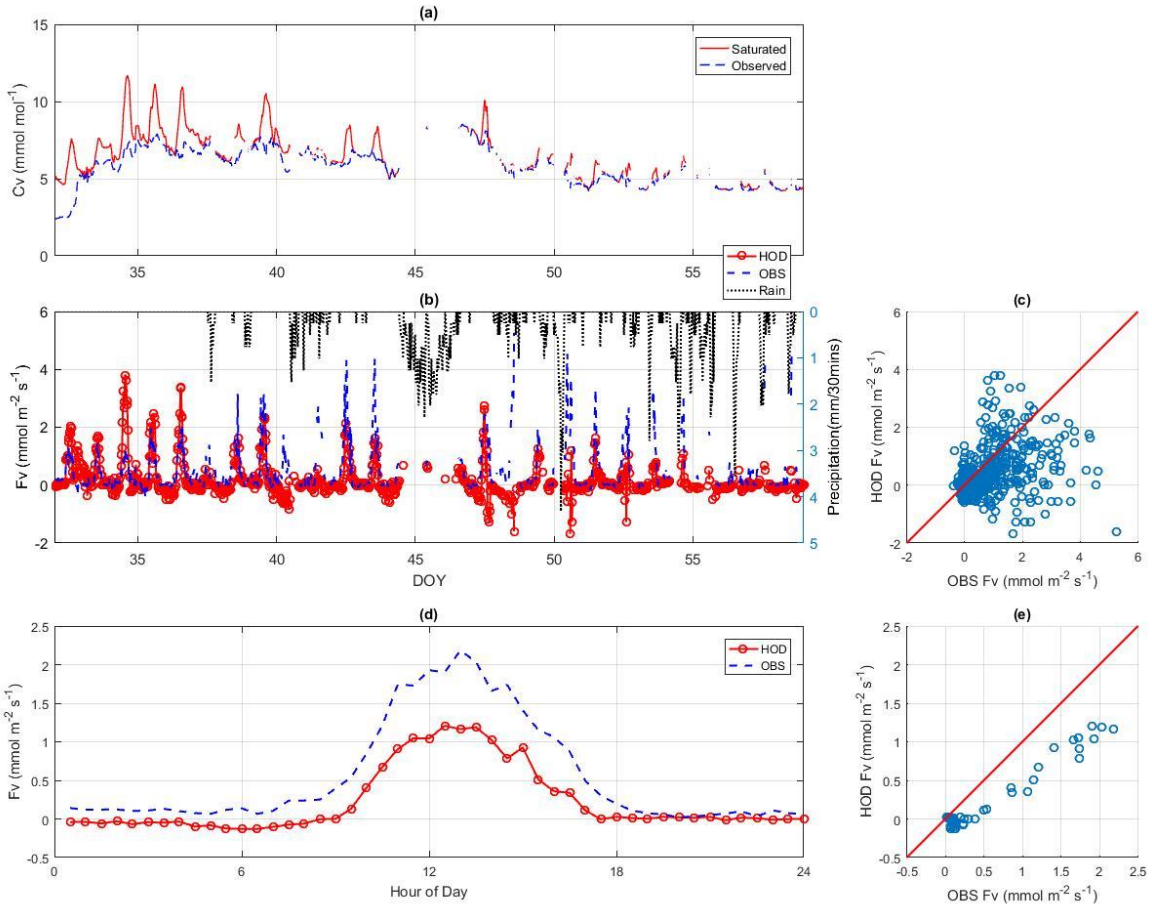

Figure 4.19 Evergreen needle leaf forest: (a**) saturated and observed C_v, (**b**) HOD vs. OBS F_v, (**c**) HOD vs. OBS F_v, r = 0.44,** (d) **mean diurnal cycles of HOD vs. OBS F_v, and** (e) **mean diurnal cycles of HOD vs. OBS F_v, r = 0.98, at US-MRf, February, 2007.**

4.3.5 CO_2 Fluxes

4.3.5.1 Diurnal scale analysis

Figures 4.20 to 4.25 show the model tests of CO_2 fluxes for the same periods as for the case of water vapor fluxes at the same sites. Panel (a) shows CO_2 concentration (C) data. The CO_2 concentration data are subject to large measurement errors due to dews or raindrops as discussed in Section 4.3.3.2. As CO_2 concentration is unlikely higher than 450 μmol mol^{-1} (ppm) over active vegetation (see Figure 3 in [*Franks et al.*, 2014]), periods

with CO_2 higher than 450 μmol mol^{-1} over cropland and grassland in Figures 4.23 (a) and 4.24 (a) are excluded in the analysis. Panels (b) and (c) compare the HOD and OBS CO_2 fluxes (F_c). Panels (d) and (e) compare the mean diurnal cycles of HOD and OBS CO_2 fluxes. The RMSEs, NRMSEs, and *r*s of the HOD vs. OBS CO_2 fluxes are summarized in Table 4.7.

Table 4.7 Statistics of HOD vs. OBS CO_2 fluxes in diurnal and seasonal scale analyses including Period (day), RMSE (μmol m^{-2} s^{-1}), NRMSE (%), *r*

Diurnal scale analysis							
Site name	Period	RMSE[a]	NRMSE[a]	r^a	RMSE[b]	NRMSE[b]	r^b
BR-Sa1	10	6.02	12	0.66	3.0	14	0.89
US-MRf	10	7.5	18	0.80	3.65	13	0.98
CCZO	10	8.00	17	0.89	6.20	21	0.95
US-Br3	14	5.93	11	0.60	1.63	11	0.96
US-IB2	20	20.37	24	0.59	7.51	22	0.95
US-ORv	10	7.36	10	0.47	3.77	16	0.82
Seasonal scale analysis							
Site name	Period	RMSE[c]	NRMSE[c]	r^c	RMSE[d]	NRMSE[d]	r^d
BR-Sa1	365	3.9	14	0.89	2.33	10	0.95
US-MRf	365	4.34	19	0.90	3.1	18	0.99

[a] calculated using hourly or half-hourly results, [b] calculated using mean diurnal cycles in diurnal scale analysis, [c] calculated using monthly mean diurnal cycles, [d] calculated using annual mean diurnal cycles.

The HOD model captures accurately the magnitudes and the diurnal variations of CO_2 fluxes as shown in Figures 4.20 to 4.25. The discrepancies in the HOD and OBS CO_2 fluxes are likely caused by unrealistic overmeasure of nighttime CO_2 concentration due to dews. The formation and vaporization of dews produce rapid fluctuations of measured CO_2 concentration, leading to unrealistic HOD CO_2 fluxes as shown in DOY 210 in Figure 4.20 (b), DOY 215 in Figure 4.21 (b), DOY 270 in Figure 4.22 (b), and DOY 186 in Figure 4.23

(b). Rain events also cause large fluctuations of CO_2 concentration as shown in Figure 4.24 (b), leading to amplified fluctuations of the HOD CO_2 fluxes. Panel (d)s in Figures 4.20 to 4.25 indicate the good agreement of daytime HOD and OBS CO_2 fluxes. During nighttime, the HOD CO_2 fluxes, which are higher than the OBS fluxes, appear to be more realistic as many studies have suggested that the EC system underestimates the nighttime CO_2 fluxes under stably stratified atmospheric conditions [*Aubinet*, 2008; *D. D. Baldocchi*, 2003; *Falge et al.*, 2001; *M. L. Goulden et al.*, 1996; *L H Gu et al.*, 2005; *Hollinger and Richardson*, 2005]. Overall, the HOD model estimates CO_2 fluxes accurately at sub-daily scale with NRMSEs under 20 % at all sites except for US-IB2 where the measurements are unreliable due to frequent rain. All correlation coefficients of the mean diurnal cycles of the HOD and OBS CO_2 fluxes are higher than 0.82. The major uncertainty of the HOD fluxes is due to the measurement errors of CO_2 concentration. The proposed model would estimate CO_2 fluxes more accurately using improved CO_2 concentration data.

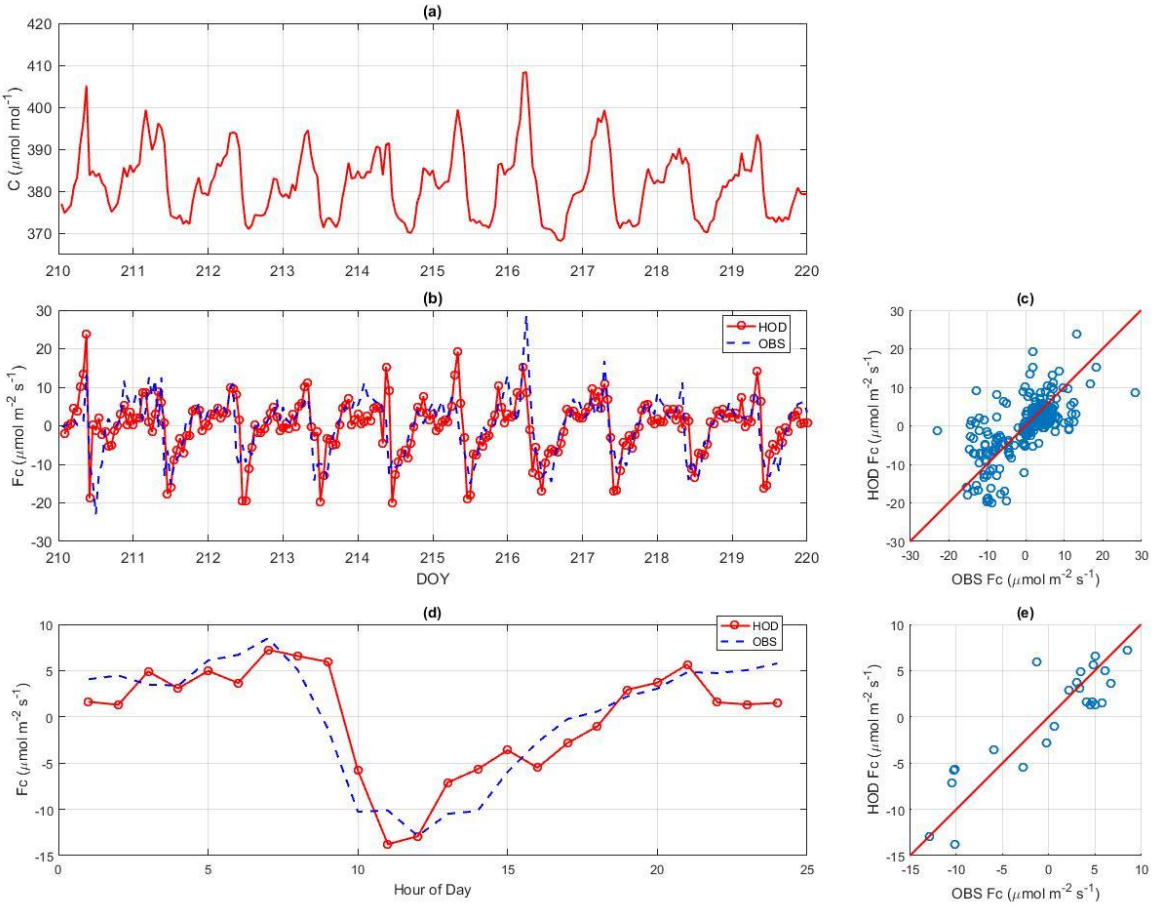

Figure 4.20 Evergreen broadleaf Amazon rainforest: (a**) CO_2 concentration (*C*), (**b**) HOD vs. OBS CO_2 flux (F_c), (**c**) HOD vs. OBS F_c, r = 0.66,** (d) **mean diurnal cycles of HOD vs. OBS F_c, and** (e) **mean diurnal cycles of HOD vs. OBS F_c, r = 0.89, at BR-Sa1, Jul. 29 - Aug. 8, 2003.**

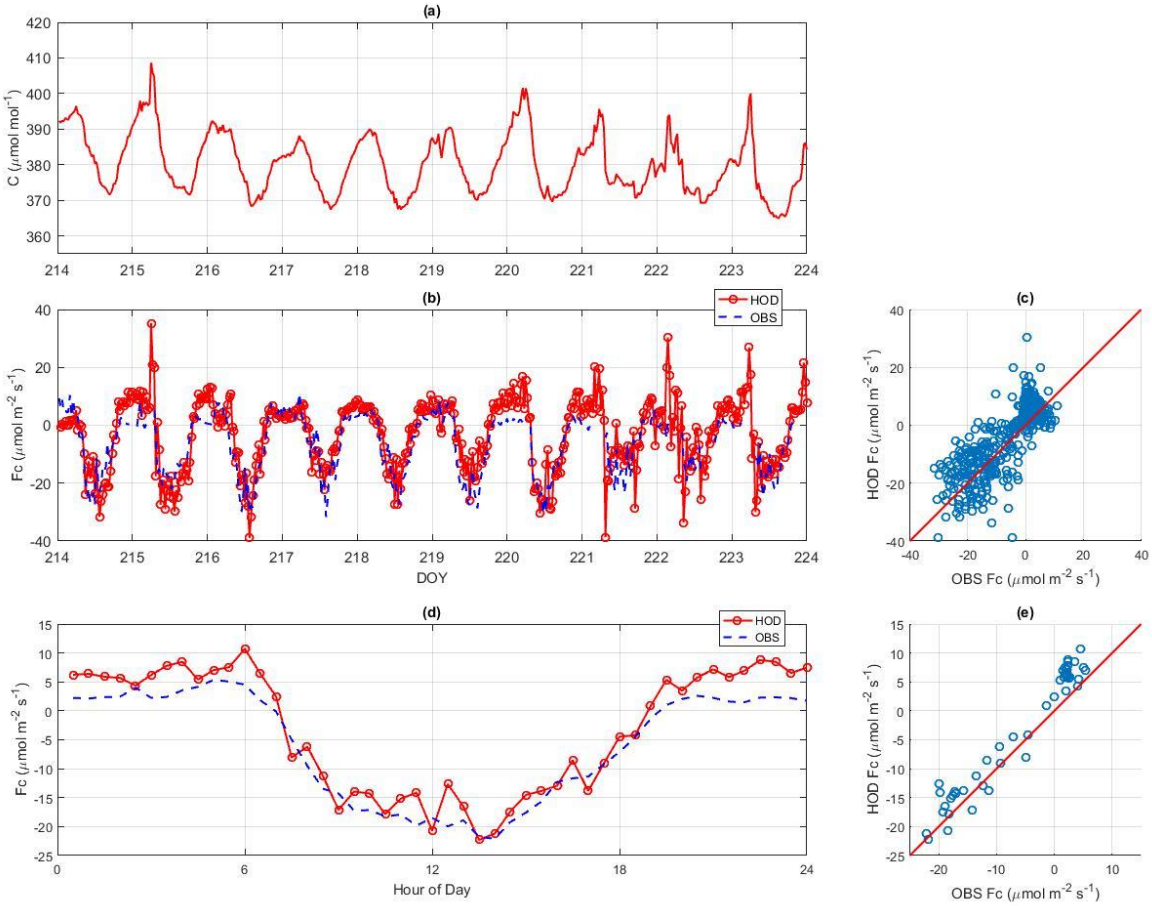

Figure 4.21 Evergreen needle leaf forest: (a**) *C*, (**b**) HOD vs. OBS F_c, (**c**) HOD vs. OBS F_c, r = 0.80,** (d) **mean diurnal cycles of HOD vs. OBS F_c, and** (e) **mean diurnal cycles of HOD vs. OBS F_c, r = 0.98, at US-MRf, Aug. 2- Aug. 12, 2007.**

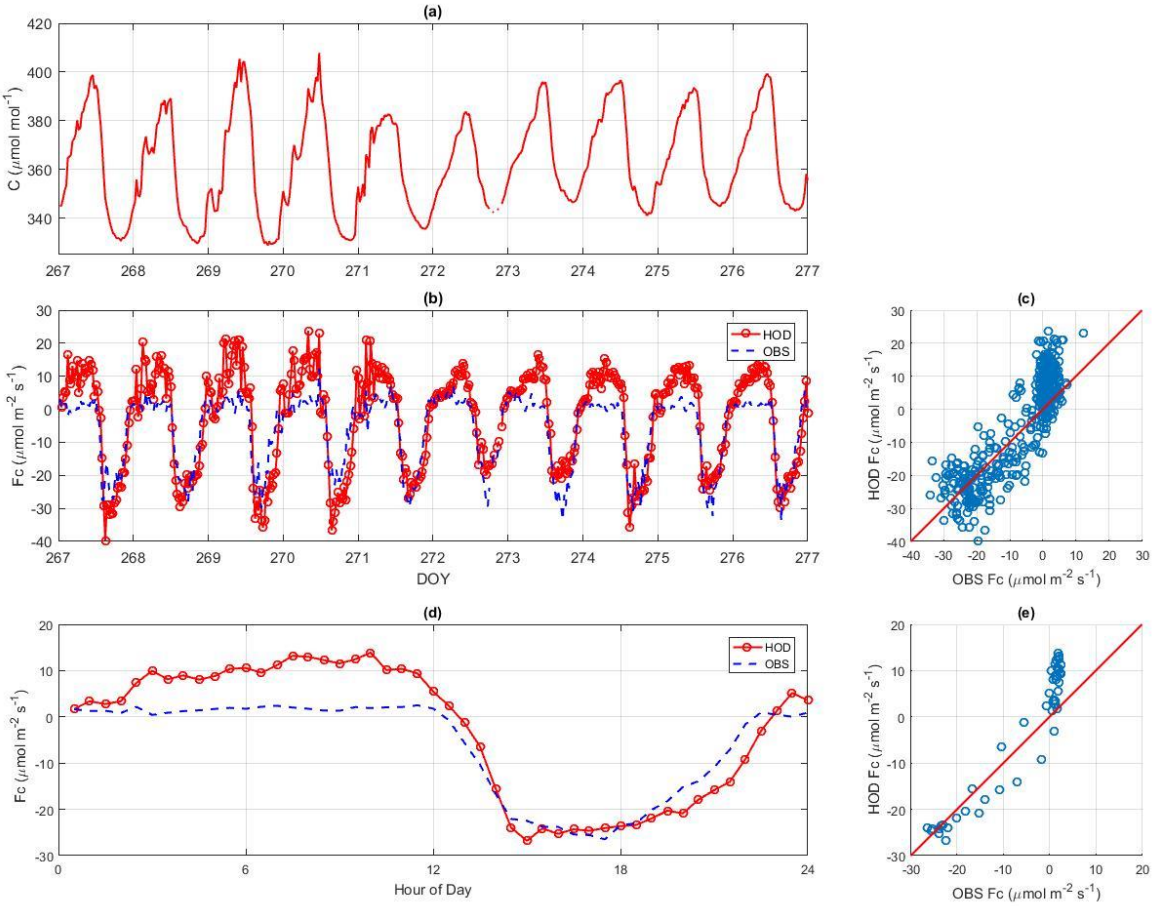

Figure 4.22 Young pine forest: (a**) *C*, (**b**) HOD vs. OBS F_c, (**c**) HOD vs. OBS F_c, r = 0.89,** (d) **mean diurnal cycles of HOD vs. OBS F_c, and** (e) **mean diurnal cycles of HOD vs. OBS F_c, r = 0.95, at CCZO, Sep. 24 – Oct. 4, 2017.**

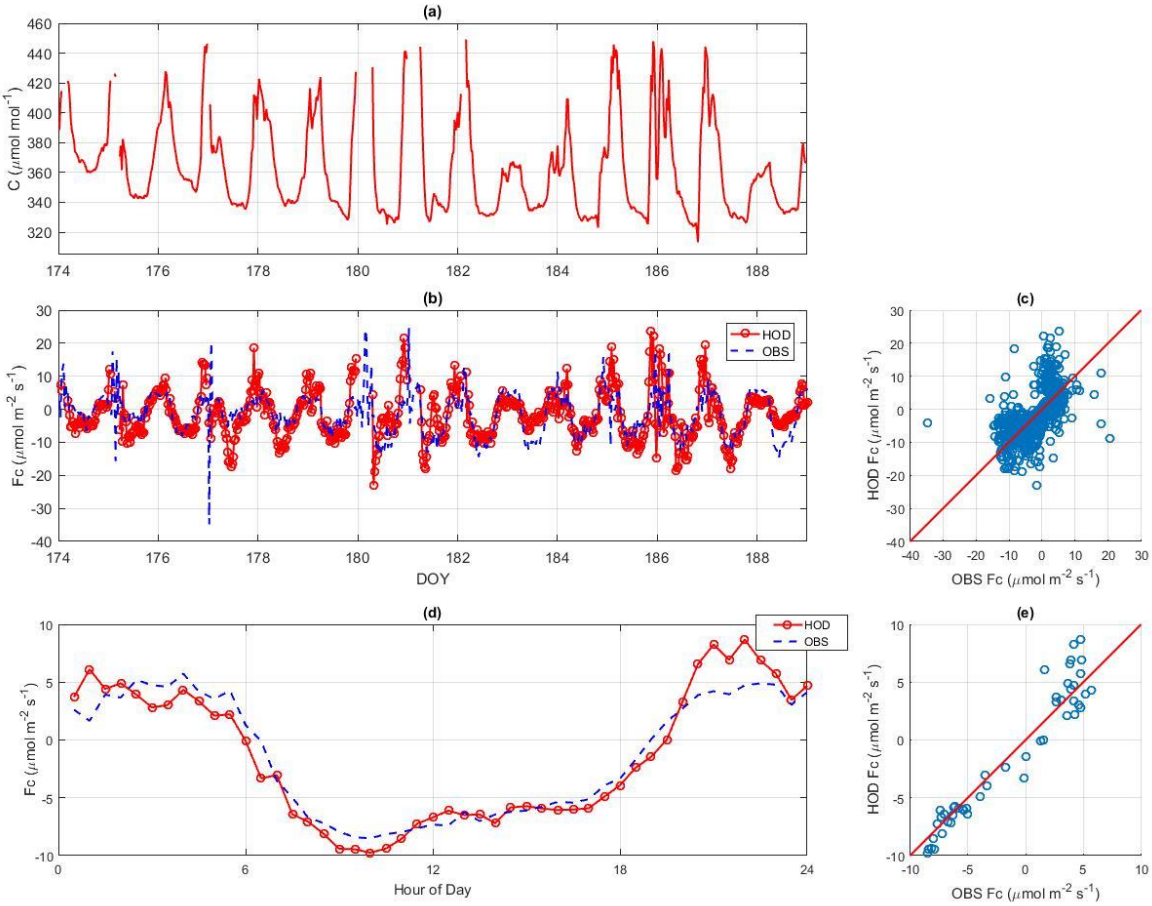

Figure 4.23 Cropland: (a) ***C*****,** (b) **HOD vs. OBS F_c,** (c) **HOD vs. OBS F_c, r = 0.60,** (d) **mean diurnal cycles of HOD vs. OBS F_c, and** (e) **mean diurnal cycles of HOD vs. OBS F_c, r = 0.96, at US-Br3, Jun. 23- Jul. 8, 2007.**

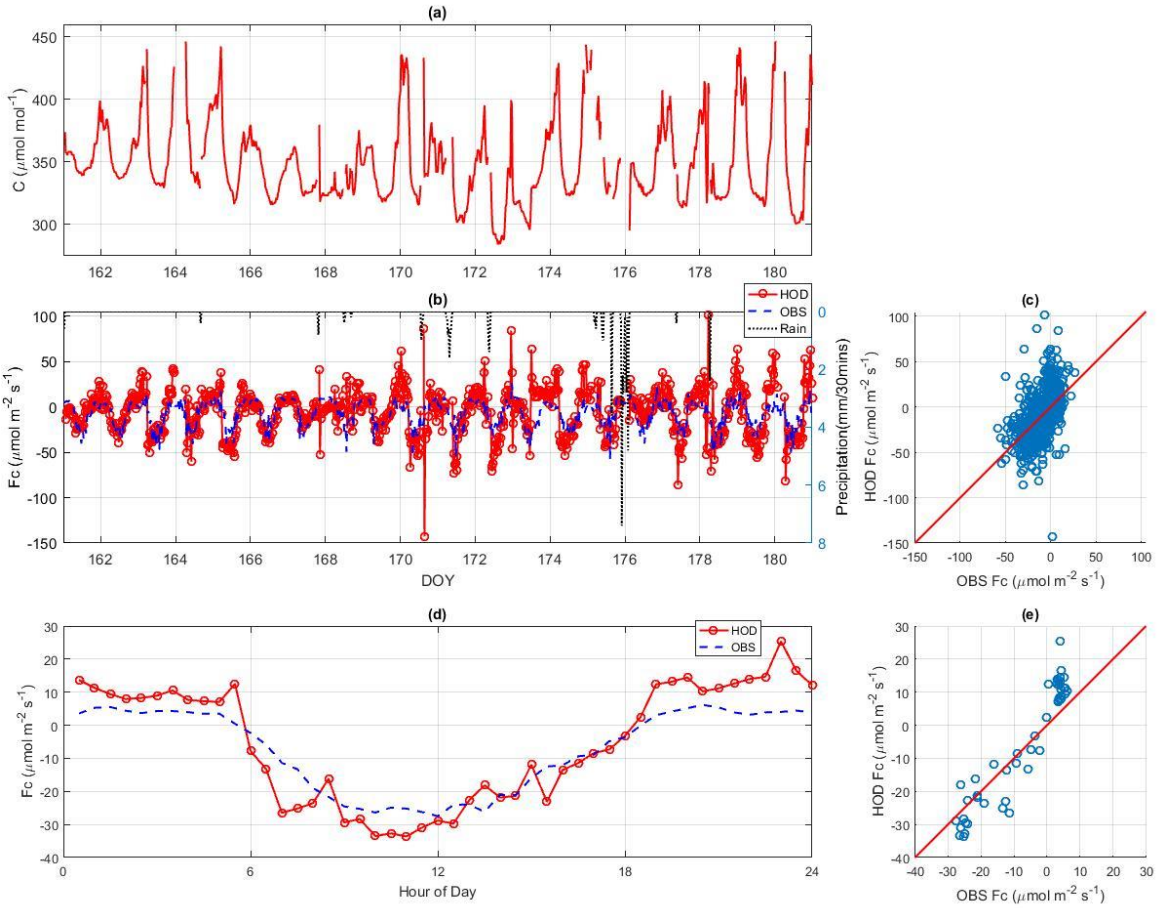

Figure 4.24 Grassland: (a**) *C*, (**b**) HOD vs. OBS F_c, (**c**) HOD vs. OBS F_c, r = 0.59,** (d) **mean diurnal cycles of HOD vs. OBS F_c, and** (e) **mean diurnal cycles of HOD vs. OBS F_c, r = 0.95, at US-IB2, Jun. 10 - Jun. 30, 2006.**

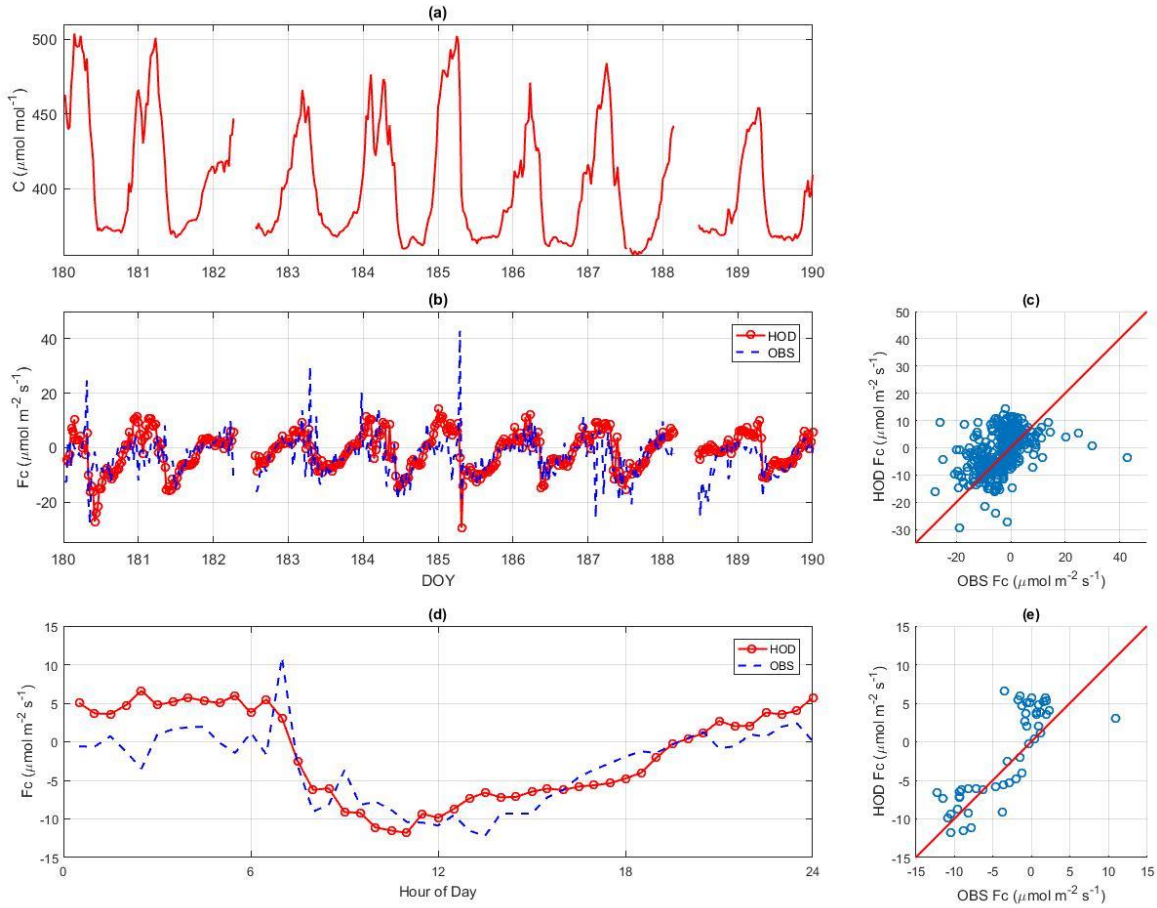

Figure 4.25 Permanent wetland: (a**) *C*, (**b**) HOD vs. OBS F_c, (**c**) HOD vs. OBS F_c, r = 0.47,** (d) **mean diurnal cycles of HOD vs. OBS F_c, and** (e) **mean diurnal cycles of HOD vs. OBS F_c, r = 0.82, at US-ORv, Jun. 29 - Jul. 9, 2011.**

4.3.5.2 Seasonal scale analysis

The HOD model of CO_2 fluxes is also tested at seasonal scale at BR-Sa1 and US-MRf as shown in Figures 4.26 and 4.27. Panel (a) shows the monthly accumulative HOD and OBS CO_2 fluxes. Panels (b) and (c) show the monthly mean diurnal cycles of the HOD and OBS CO_2 fluxes. Panels (d) and (e) show the annual mean diurnal cycles of the HOD and OBS CO_2 fluxes. The statistics of annual accumulative CO_2 fluxes are summarized in Table 4.6.

At BR-Sa1, the monthly accumulative HOD and OBS CO_2 fluxes are in good agreement (Figure 4.26 (a)) with smaller discrepancies for dry months (June to September) than wet months (November to January) due to large measurement errors in rainy season. It is evident that the HOD model estimates accurately the magnitudes and the diurnal variations of CO_2 fluxes at monthly scale with a correlation coefficient of 0.89. The overestimations of the HOD CO_2 fluxes in the early mornings in Figure 4.26 (b) are likely caused by spurious fluctuations of measured CO_2 concentration due to dew formation. The annual mean diurnal cycles of the HOD and OBS CO_2 fluxes agree closely with a correlation coefficient of 0.95, implying that the HOD is capable of estimating annual CO_2 fluxes over rainforest.

Numerous efforts over the past decades have been made to assess the Amazon carbon budgets and address the issue that whether the Amazon rainforest is a carbon source or sink [*Brienen et al.*, 2015; *Gatti et al.*, 2014; *Phillips et al.*, 2009; *Saleska et al.*, 2003; *Tian et al.*, 1998]. The uncertainties in the current CO_2 fluxes data are arguably responsible for the unbalanced carbon budget at regional and global scales, causing the missing carbon sink problem [*D. S. Schimel*, 1995a]. According to the analysis of EC data at BR-Sa1 from 2001 to 2003, Amazon forests change from a carbon sink to a carbon source when more than 50 % of EC flux data are rejected and refilled using gap filling methods [*Saleska et al.*, 2003]. Our study uses more than 90 % of CO_2 concentration data to calculate the HOD CO_2 fluxes, and more than 88 % of EC CO_2 flux data to calculate the annual mean diurnal cycles and accumulative fluxes in 2003. The annual accumulative daytime HOD and OBS CO_2 fluxes at BR-Sa1 are -1199 and -1280 gC m^{-2} $year^{-1}$, respectively, with 6 % relative error. The annual accumulative nighttime HOD and OBS CO_2 fluxes are 922 and 920 gC m^{-2} $year^{-1}$,

respectively, with 0.2 % relative error. The net ecosystem exchange (NEE) estimated using the HOD model (annual accumulative all-day CO_2 flux in Table 3) at BR-Sa1 is -277 g C m^{-2} $year^{-1}$, indicating that the rainforest at BR-Sa1 is a carbon sink in 2003. Our conclusion is consistent with a recent study based on the field biometric observations at up to 321 location across mature forest from 1983 to 2011 [*Brienen et al.*, 2015]. The proposed model is shown to be a promising new modeling tool for the assessment of the Amazon carbon budgets.

Figure 4.27 shows the seasonal analysis of the HOD model of CO_2 fluxes over evergreen needle leaf forest at US-MRf. The HOD model captures accurately the magnitudes and seasonality of the monthly accumulative daytime CO_2 fluxes as shown in Figure 4.27 (a). The monthly mean diurnal cycles of the HOD and OBS fluxes (Figures 4.27 (b) and (c)) are in good agreement except for some discrepancies in June 2007 due to the measurement errors of CO_2 concentration during rainy periods (see Figure 4.28) when 15% of CO_2 concentration data are missing. The annual mean diurnal cycles of the HOD and OBS fluxes agree better during daytime than during nighttime. The annual accumulative daytime HOD and OBS CO_2 fluxes are -1681 and -1898 gC m^{-2} $year^{-1}$, respectively, with 11% relative error given the 45 % relative flux uncertainty of daytime CO_2 fluxes at the nearby MP site [*D. Vickers et al.*, 2010].

Underestimation of nighttime CO_2 fluxes by the EC system has been reported based on chamber measurements over mid-latitude forests [*M. L. Goulden et al.*, 1996]. As respiration tends to be underestimated by the above-canopy EC system at US-MRf, a sub-canopy EC system was added to obtain a more accurate estimate of NEE [*C Thomas et al.*, 2008]. The HOD modeled NEE (-768 gC m^{-2} $year^{-1}$) from single-level above canopy CO_2

concentration is consistent with that (-563 gC m^{-2} $year^{-1}$) from two levels (above-canopy and below-canopy) of EC fluxes and seven levels of CO_2 mixing ratio, which is more accurate than that (-1258 gC m^{-2} $year^{-1}$) calculated from above-canopy EC fluxes [*C K Thomas et al.*, 2013]. A study on carbon fluxes at MP site also confirms the HOD NEE [*Dean Vickers et al.*, 2012]. The HOD modeled CO_2 fluxes have comparable or better accuracy compared to those obtained using existing methods but using fewer input data. As only limited field sites are equipped with multi-level EC measurements and CO_2 profile measurements, the HOD model provides a new opportunity for improving quantitative evaluation of the carbon budgets over forest in the mid-latitudes.

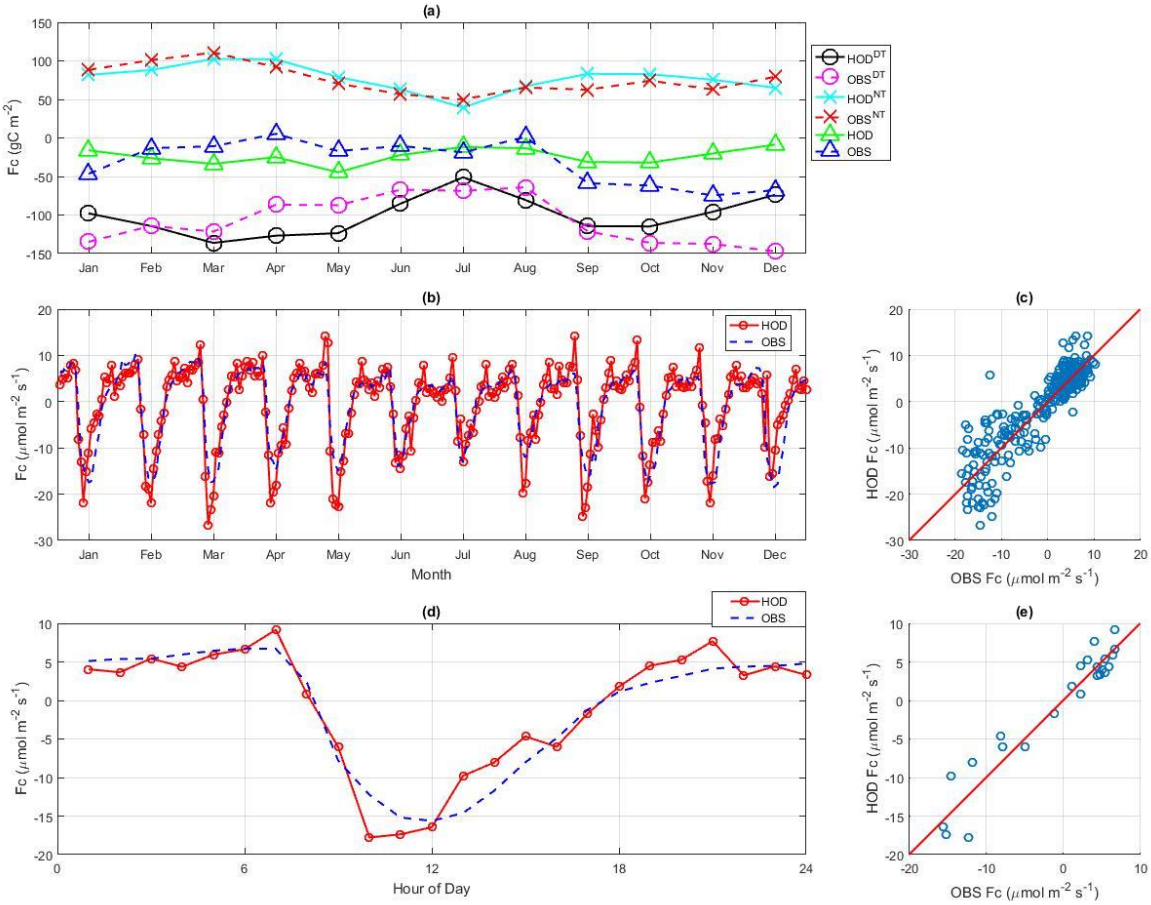

Figure 4.26 Evergreen broadleaf Amazon rainforest: (a**) monthly accumulative daytime (^{DT}, circle), nighttime (^{NT}, cross), and all-day (triangle) HOD (solid line) vs. OBS (dash line) F_c, (**b**) monthly mean diurnal cycles of HOD vs. OBS F_c, (**c**) monthly mean diurnal cycles of HOD vs. OBS F_c, r = 0.89, (**d**) annual mean diurnal cycles of HOD vs. OBS F_c, and** (e) **annual mean diurnal cycles of HOD vs. OBS F_c, r = 0.95, at BR-Sa1, 2003.**

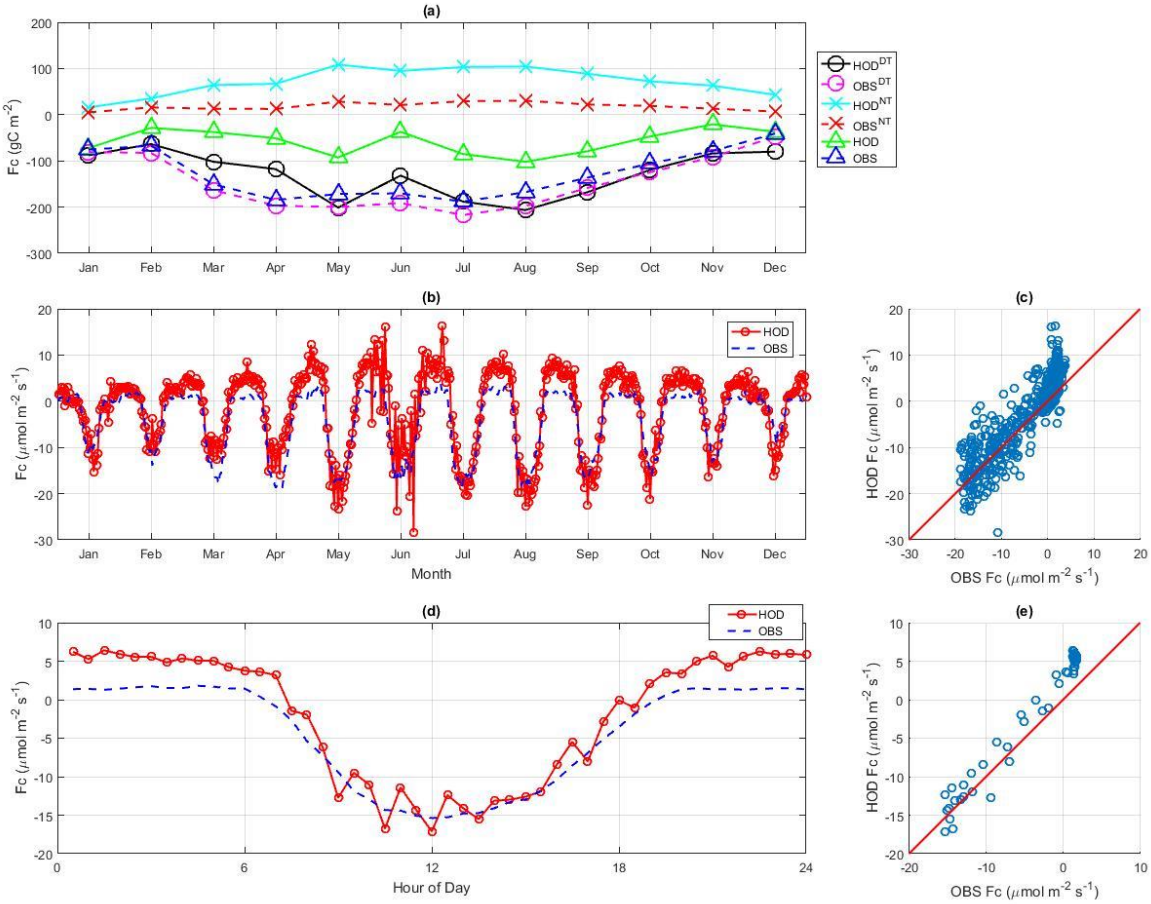

Figure 4.27 Evergreen needle leaf forest: (a) monthly accumulative daytime (^{DT}, circle), nighttime (^{NT}, cross), and all-day (triangle) HOD (solid line) vs. OBS (dash line) F_c, (b) monthly mean diurnal cycles of HOD vs. OBS F_c, (c) monthly mean diurnal cycles of HOD vs. OBS F_c, r = 0.90, (d) annual mean diurnal cycles of HOD vs. OBS F_c, and (e) annual mean diurnal cycles of HOD vs. OBS F_c, r = 0.99, at US-MRf, 2007.

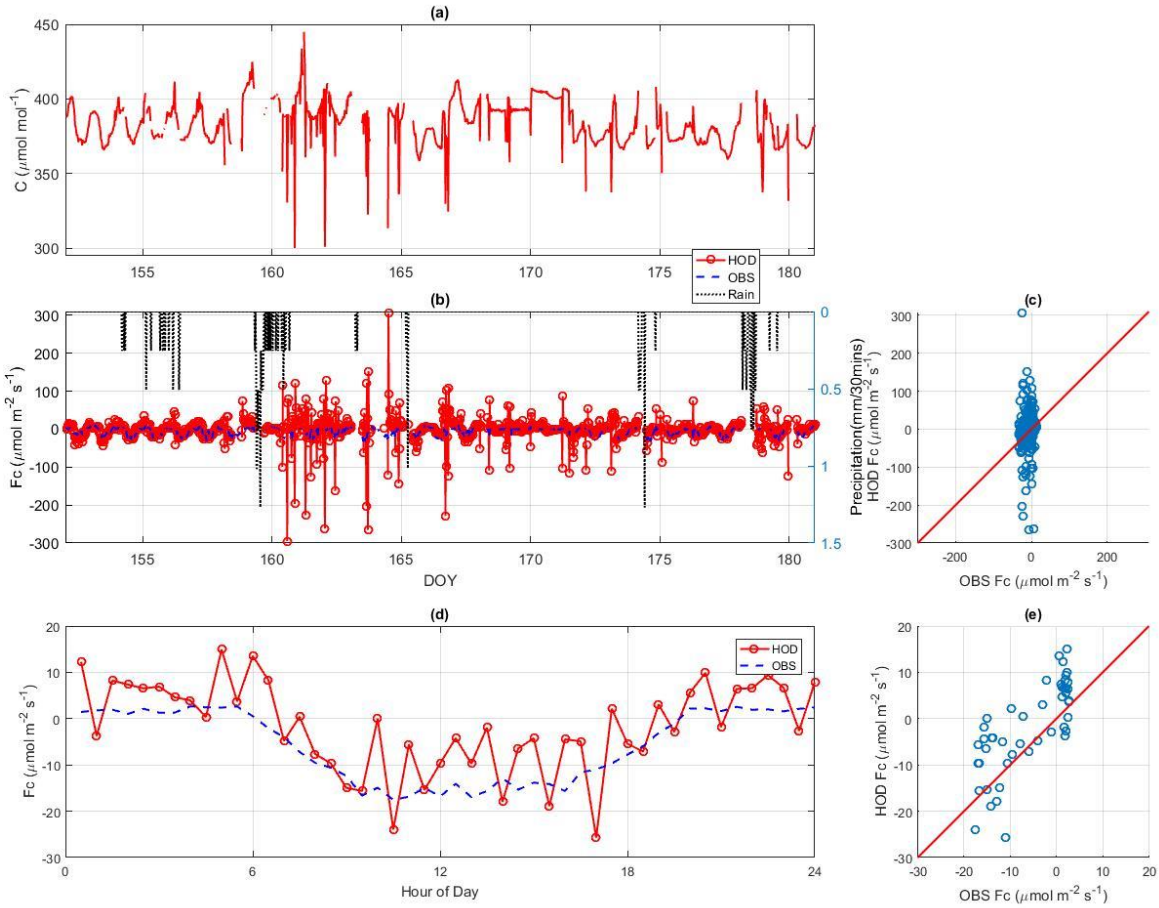

Figure 4.28 Evergreen needle leaf forest: (a**) *C*, (**b**) HOD vs. OBS F_c, (**c**) HOD vs. OBS F_c, r = 0.24,** (d) **mean diurnal cycles of HOD vs. OBS F_c, and** (e) **mean diurnal cycles of HOD vs. OBS F_c, r = 0.76, at US-MRf, June, 2007.**

4.3.6 Methane Fluxes

A preliminary test of the HOD model for estimating methane (CH_4) fluxes is conducted at the Sherman Island site, California, United States (US-Snd for short, 38.04 °N, 121.75 °W) [*Hatala et al.*, 2012]. The US-Snd site is located in a mid-latitude peatland pasture in the west of the California Delta. The canopy height is over 0.3 m during summer. The climate is Mediterranean with annual mean temperature 16 °*C*, and precipitation 358 mm. Half-hourly EC fluxes and other meteorological variables are measured at about 3 m AGL. Due

to technical difficulties, only limited methane concentration and flux data are available. Figure 4.29 shows that the modeled methane fluxes are in reasonable agreement with the observed fluxes given that the uncertainties of the EC methane fluxes ranging from 20 % to 300 % [*Kroon et al.*, 2010]. When CH_4 concentration increases rapidly, the HOD model captures a large CH_4 flux on DOY 120. The RMSE, NRMSE, and *r* of the modeled methane fluxes are 41 nmol m^{-2} s^{-1}, 14 %, and 0.52, respectively. Considering that multi-level methane data are sparse at best, the HOD model is a promising new tool for monitoring and modeling methane fluxes at local, regional, and global scales.

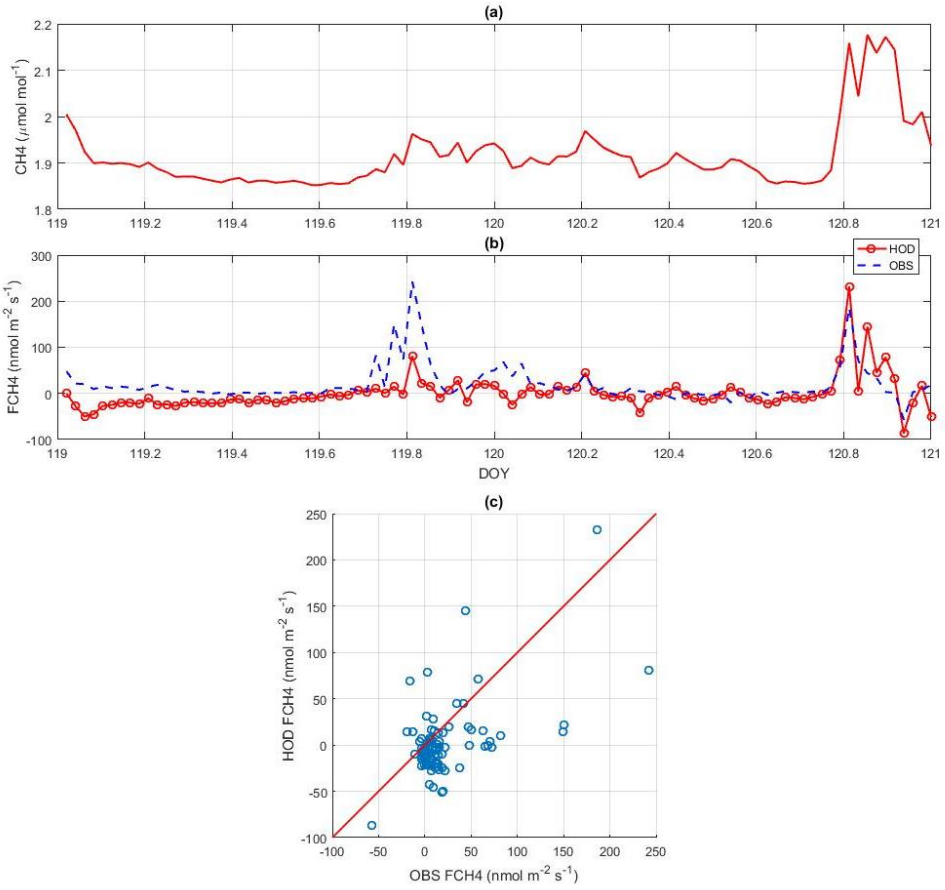

Figure 4.29 (a**) Methane concentration (*CH4*), (**b**) HOD vs. OBS methane flux (*FCH4*), and (**c**) HOD vs. OBS *FCH4*, *r* = 0.52, at US-Snd, Apr. 29 - May 1, 2007.**

4.3.7 Conclusion

This proof-of-concept study demonstrates the feasibility of surface gas fluxes derived from single-level near-surface gas concentration data. The case studies suggest that the proposed non-gradient model is able to capture the diurnal and seasonal variations of gas fluxes using fewer input variables and model parameters than conventional models. The new parameterization of the eddy-diffusivity based on the Monin-Obukhov similarity theory combined with the MEP model of surface heat fluxes facilitates its applications to modeling (greenhouse) gas fluxes at regional and global scales using remote sensing observations. More independent tests of the proposed model are anticipated to further evaluate its performance. On-going work includes using the proposed model as an alternative method for retrieving gas emission using historical gas concentration observations, and monitoring regional and global greenhouse gas fluxes budgets using satellite remote sensing data. The proposed model may also be used as an alternative algorithm of gas exchange over the land surface in the Earth system models.

4.4 Model of Friction Velocity

4.4.1 Introduction

The Monin-Obukhov similarity equations (MOSE) are the theoretical basis of parameterizing turbulent momentum and heat fluxes within the atmospheric surface layer (ASL) [*Monin and Obukhov*, 1954]. The original goal of the MOSE is to derive friction velocity (momentum flux) and turbulent heat flux from mean wind speed and temperature profiles. With the development of the eddy-covariance (EC) technology in the 1970s for direct measurements of turbulent fluxes [*Dyer and Hicks*, 1970], the MOSE have been used

mainly as a physical parameterization of boundary layer turbulence. At regional and global scales, friction velocity is commonly estimated using ASL models [*Hari Prasad et al.*, 2016; *S-Y Hong and Pan*, 1996; *Mellor and Yamada*, 1982; *Zhang and Anthes*, 1982] as in-situ measurements of surface wind speed are limited. However, the current models of boundary layer turbulence do not allow friction velocity and surface wind speed to be parameterized independently [*Grell et al.*, 1994; *Jimenez et al.*, 2012]. Remote sensing algorithms have been developed for the estimation of wind speed over ocean surfaces from sea surface roughness measurements [*S Hong and Shin*, 2013]. Methods for the retrieval of friction velocity and surface wind speed over land surfaces using remote sensing data do not exist. Wind profiles in the atmospheric boundary layer may be estimated using Doppler LIDAR technology [*Baker et al.*, 2014]. Yet, even with the most advanced satellite, the Atmospheric Dynamics Mission Aeolus to be launched in August 2018, wind profile retrievals using current technology can only reach 500 m above the surface layer [*Stoffelen et al.*, 2005].

In this study, we propose a novel model of friction velocity over land surfaces. The model formulation is based on the extreme solution of the MOSE [*J Wang and Bras*, 2010] relating friction velocity directly to sensible heat flux, which may be parameterized using the MEP model in terms of net radiation, surface temperature and humidity [*J Wang and Bras*, 2009; 2011]. The proposed model is tested using field observations over diverse geographic and climatic conditions at diurnal and seasonal time scales. As the MEP model has demonstrated successes in estimating global heat fluxes [*Huang et al.*, 2016], the new model of friction velocity combined with the MEP model facilitates the estimation of

friction velocity over land surfaces at regional and global scales using remote sensing observations and reanalysis products.

4.4.2 Methodology

Equilibrium thermodynamics of physical processes is often represented as extremum principles [*Kondepudi*, 2008]. The MOSE may also be associated with extremum principles as the MOSE generally hold when wind shear and buoyancy are in equilibrium [*Cheng et al.*, 2005]. Wang and Bras [*J Wang and Bras*, 2010] proposed an extremum hypothesis about the turbulence structure of the ASL described by the MOSE. The extremum hypothesis states that the momentum flux would reach certain values to minimize heat flux and mean wind shear (temperature) under stable (unstable) conditions. Based on the extremum hypothesis, a unique extreme solution of the MOSE linking friction velocity and sensible heat flux to wind shear and temperature gradient is obtained. According to the extreme solution, friction velocity is expressed in terms of sensible heat flux (Appendix H) as,

$$\boldsymbol{u_* = D_0 |Hz|^{\frac{1}{3}}, D_0 = \begin{cases} 0.047, H < 0 \\ 0.037\,, H > 0 \end{cases}'} \qquad \textbf{4.18}$$

where u_* (m s^{-1}) is friction velocity, H (W m^{-2}) sensible heat flux, and z (m) the height above surface. Eq. 4.18 is a wind speed independent model of u_*. H in Eq. 4.18 may be obtained from net radiation, surface temperature, and humidity using the MEP model, which is also independent of wind speed.

u_* in Eq. 4.18 appears to be a function of z even though the ASL is defined as the layer of fluxes varying by less than 10 % [*Stull*, 1988]. In fact, u_* according to Eq. 4.18 is a weak

function of z due to its one-third power dependence on z and H, which decreases with z [*J Wang and Bras*, 2001]. Since the MOSE are only valid for a limited range of z, z in Eq. 4.18 is assumed to be the lower bound of the ASL, z_s [*J Wang and Bras*, 2009]. Theoretically, the surface layer depth under stable condition is approximately 10 % of that under unstable condition [*Arya*, 2001]. Therefore, z ($=z_s$) in Eq. 4.18 under stable condition is approximately 10 % of that under unstable condition. The case studies suggest that z in Eq. 4.18 under unstable condition is approximately equal to the distance between anemometer and canopy top on the order of 3-5 m.

4.4.3 Data

The proposed model of friction velocity as in Eq. 4.18 is tested at four selected sites (Table 4.8) with diverse climates, geography, and vegetation types from the AmeriFlux network (http://ameriflux.lbl.gov/). The Santarem-Km83-Logged Forest site (BR-Sa3 for short, 3.0 °S, 55.0 °W) is located in the evergreen broadleaf Amazon rainforest in Para, Brazil [*Rocha et al.*, 2004]. The average tree height is approximately 40 m. The climate is tropical monsoon with annual mean temperature 26.1 °*C* and precipitation 2,044 mm. Friction velocity (m s^{-1}), sensible heat flux (W m^{-2}), net radiation (W m^{-2}), air temperature (°C), and relative humidity (%) are measured half-hourly at 64 m above ground level (AGL). The available percentages (defined as the ratio of the number of usable data points to that of total data points in a year) of sensible heat flux, friction velocity, net radiation, air temperature, and relative humidity in 2001 are 75%, 86%, 92%, 93%, and 71%, respectively.

The University of Michigan Biological Station site (US-UMB for short, 45.6 °N, 84.7 °W) is located in a deciduous broadleaf forest in Michigan, United States [*Nave et al.*, 2011]. The average tree height is approximately 20 m. The climate is warm summer continental with annual mean temperature 5.8 °*C* and precipitation 803 mm. Friction velocity and other meteorological variables are measured half-hourly at 46 m AGL. The available percentages of sensible heat flux, friction velocity, net radiation, air temperature, and relative humidity in 2007 are 87%, 95%, 98%, 98%, and 96%, respectively.

The Brooks Fields Site 11-Ames (US-Br3 for short, 42.0 °N, 93.7 °W) is located in a corn/soybean agricultural region in Iowa, United States [*T J Sauer et al.*, 2007]. The crop in 2007 is soybean and the average height of soybean is approximately 0.4 m during growing season (May to October). The climate is humid continental (cold winter, hot summer, and no dry season) with annual mean temperature 8.9 °*C* and precipitation 847 mm. Friction velocity and other meteorological variables are measured half-hourly at 2.4 m AGL. The available percentages of sensible heat fluxes, friction velocity, net radiation, air temperature, and relative humidity in 2007 are 97%, 97%, 99%, 99%, and 99%, respectively.

The Duke Forest-open field site (US-Dk1 for short, 36.0 °N, 79.1 °W) is located in a grassland in North Carolina, United States [*Katul et al.*, 2003]. The average height of grass is approximately 0.2 m. The climate is humid subtropical with annual mean temperature 14.4 °*C* and precipitation 1,170 mm. Friction velocity and other meteorological variables are measured half-hourly at 2.8 m AGL. The available percentages of sensible heat flux, friction velocity, net radiation, air temperature, and relative humidity in 2004 are 91%, 100%, 100%, 100%, and 100%, respectively.

Table 4.8 Site list [a]

Site	Coordinate	Vegetation	Climate	T_a (°C)	*PREC* (mm)	z_m (m)	z_c (m)
BR-Sa3	3.0 °S, 55.0 °W	EBF	Am	26.1	2,044	64	40
US-UMB	45.6 °N, 84.7 °W	DBF	Dfb	5.8	803	46	20
US-Br3	42.0 °N, 93.7 °W	CRO	Dfa	8.9	847	2.4	0.4
US-Dk1	36.0 °N, 79.1 °W	GRA	Cfa	14.4	1,170	2.8	0.2

[a] Vegetation is categorized according to the International Geosphere-Biosphere Programme (IGBP): EBF (Evergreen Broadleaf Forest), DBF(Deciduous Broadleaf Forest), CRO (Cropland), and GRA (Grassland). Climate is categorized according to the Koppen climate classification: Am (tropical monsoon), Dfb (warm summer continental), Dfa (humid continental), and Cfa (humid subtropical). T_a is the annual mean air temperature. *PREC* is the annual mean precipitation. z_m is the measurement height. z_c is the canopy height.

4.4.4 Results

4.4.4.1 Tests of Eq. 4.18

The linear relationship of friction velocity (u_*) and the one-third power of sensible heat flux ($H^{1/3}$) as in Eq. 4.18 is evaluated using the EC flux observations. Nighttime data ($H < 0$) are excluded in the test as the nighttime EC signals are often too noisy under stable conditions [*Aubinet et al.*, 2012]. Figure 4.30 shows one-year long half-hourly data of $H^{1/3}$ and u_* at the four sites with the corresponding classical linear regression (CLR), Bayesian linear regression (BLR) and extreme solution (ES) lines (The measurement errors of $H^{1/3}$ and u_* are in Appendix I. The linear relationship is evident at BR-Sa3, US-Br3, and US-Dk1, but not as strong at US-UMB. Table 4.9 summarizes the parameters of the CLR, BLR, and ES including the number of samples (n_s), the interception (α), the slope (β), and the

relative error (σ) of β, defined as the difference between βs of the regression and the ES divided by the β of the ES. The errors of both αs and βs of the BLR are consistently smaller than those of the CLR at all sites. The averaged α (σ)s of CLR and BLR are 0.14 m s^{-1} (19 %) and 0.12 m s^{-1} (12 %), respectively. Given $\geq 20\%$ uncertainties of the EC measurements at all sites [*Oren et al.*, 2006; *Pressley et al.*, 2006; *Rocha et al.*, 2004; *D. Vickers et al.*, 2010], the close agreement of the regression equations and the extreme solution supports the validity of the linear relationship of u_* and $H^{1/3}$ as in Eq. 4.18.

Table 4.9 Regression results of the function $u_* = \beta H^{\frac{1}{3}} + \alpha$ under unstable conditions

		CLR			BLR			ES	
Site Name	n_s	α_{CLR}	β_{CLR}	$\sigma(\beta_{CLR})$	α_{BLR}	β_{BLR}	$\sigma(\beta_{BLR})$	α_{ES}	β_{ES}
BR-Sa3	5369	0.0687	0.1033	3.2%	0.0554	0.1070	0.2%	0	0.1067
US-UMB	6494	0.3116	0.0765	30.2%	0.2803	0.0844	23.0%	0	0.1096
US-Br3	7231	0.1469	0.0524	29.2%	0.1284	0.0583	21.3%	0	0.0740
US-Dk1	7536	0.0493	0.0543	14.3%	0.0303	0.0601	5.0%	0	0.0633

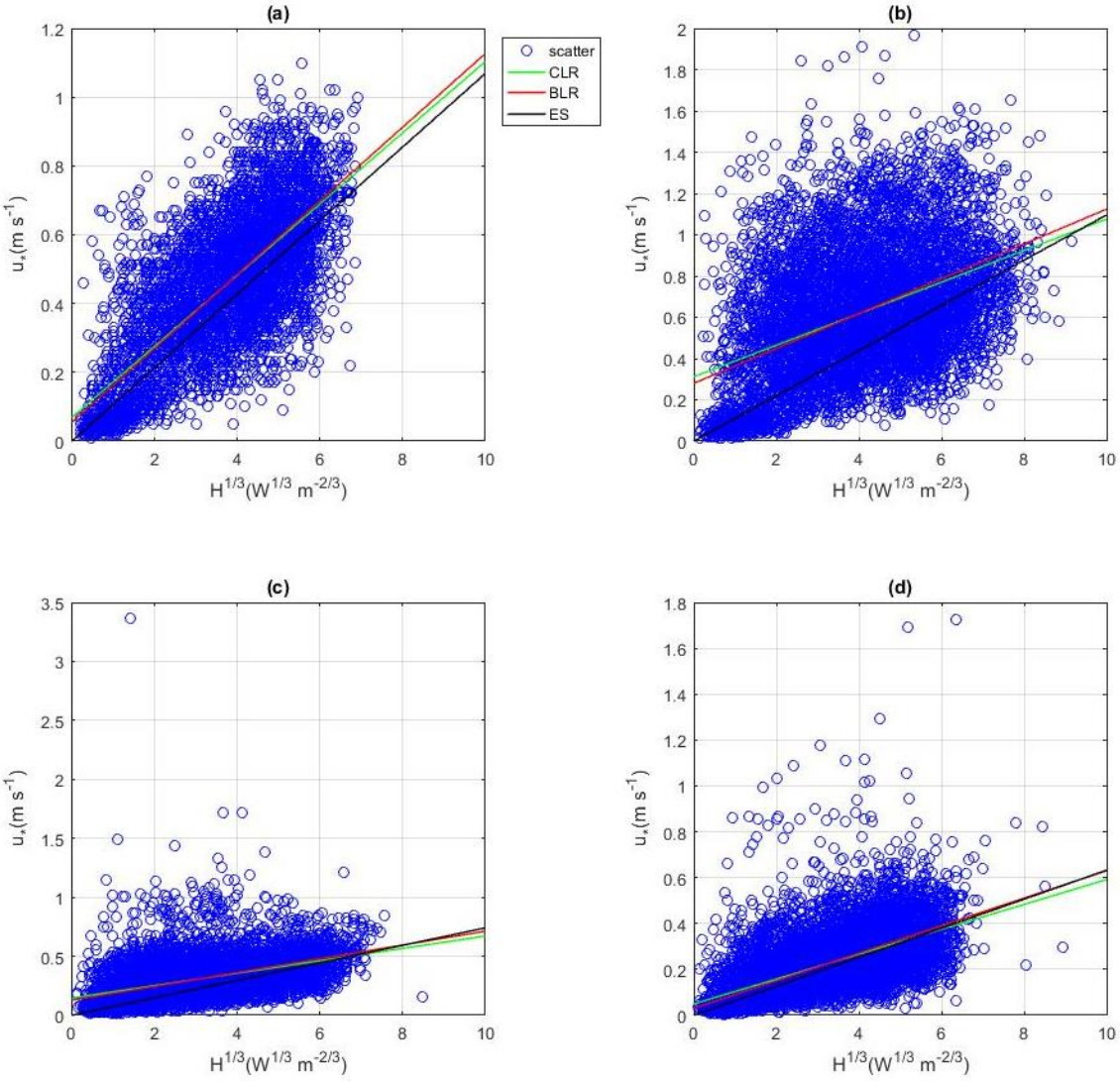

Figure 4.30 Half-hourly observations of $H^{1/3}$ and u_* under unstable condition (daytime) with CLR, BLR, and ES lines, (a) at BR-Sa3 in 2001, (b) at US-UMB in 2007, (c) at US-Br3 in 2007, and (d) at US-Dk1 in 2004.

4.4.4.2 Estimation of u_* at diurnal scale

Eq. 4.18 is tested for estimating sub-daily friction velocities using observed and modeled sensible heat fluxes during a ten-day period at the four sites. The modeled sensible heat fluxes are obtained from the MEP model with observations of net radiation, air temperature, and humidity. The observations at raining times are excluded as EC fluxes

during rainy periods are known to be erroneous [*Aubinet et al.*, 2012]. The diurnal variations of observed and modeled friction velocities and sensible heat flux are displayed in Figures 4.31 to 4.35 where rainfall data are shown in Panel (a) whenever available and half-hourly wind speed observations are in Panel (c). Panels (e) and (f) compare the mean diurnal cycles of the observed and modeled friction velocities. Mean diurnal cycles of wind speed are shown in Panel (e). Although not required by the model, wind speed data are added in the figures to explain the uncertainties of the modeled friction velocity as friction velocity is directly related to surface wind shear in the MOSE. Tables 4.10 and 4.11 summarize the statistics of the modeled sensible heat fluxes and friction velocities including the root-mean-square errors (RMSE, with respect to the observed variables), the normalized RMSEs (NRMSE, defined as the RMSE divided by the range of the observed variables), and the correlation coefficients (r).

The MEP modeled sensible heat fluxes without using wind speed data agree closely with the observations at all sites (Figures 4.31 to 4.35 (a) and (b)), given that the uncertainties of the EC sensible heat fluxes are at least 20 % [*Oren et al.*, 2006; *Pressley et al.*, 2006; *Rocha et al.*, 2004; *D. Vickers et al.*, 2010]. The modeled friction velocities using sensible heat fluxes agree with the observations in both magnitude and diurnal variations (Figures 4.31 to 4.35 (c) and (d)). The observed friction velocities is greater than the modeled ones when wind speed suddenly strengthens, e.g. on DOY 264, 267, and 269 in Figure 4.31(c), DOY 199 in Figure 4.32(c), DOY 184 in Figure 4.33(c), DOY 318 in Figure 4.34(c), and DOY 185 and 189 in Figure 4.35(c). The modeled friction velocity agrees more closely with the observation during growing season (summer) than during dormant season (winter)

at US-Br3 as background wind speed during winter is twice as strong as that during summer.

The mean diurnal cycles of the modeled and observed friction velocities are in good agreement at all sites with all *r*s greater than 0.9 and NRMSEs smaller than 20 %. The discrepancies between the modeled and observed friction velocities occur under the condition of strong wind (> 3 m s^{-1} at BR-Sa3 as shown in Figure 4.31(e)) and weak sensible heat flux (< 20 W m^{-2}) near sunset times (Figures 4.32 (e), 4.33(e), 4.34(e), and 4.35(e)).

Table 4.10 Statistics of modeled vs. observed sensible heat fluxes in diurnal and seasonal scale analyses including Days/Period, RMSE (W m^{-2}), NRMSE (%), *r*

Diurnal Scale Analysis				
Site Name	Days	RMSE	NRMSE	*r*
BR-Sa3	10	28	9	0.91
US-UMB	10	43	9	0.89
US-Br3 (growing season)	10	19	8	0.96
US-Br3 (dormant season)	10	19	7	0.94
US-Dk1	10	27	9	0.95
Seasonal Scale Analysis				
Site Name	Period	RMSE	NRMSE	*r*
BR-Sa3	One year	21	10	0.94
US-UMB	One year	35	10	0.97
US-UMB (May to August)	May to August	41	12	0.96
US-Dk1	One year	12	6	0.97

Table 4.11 Statistics of modeled vs. observed friction velocities in diurnal and seasonal scale analyses including RMSE (m s^{-1}), NRMSE (%), and *r*

Diurnal Scale Analysis													
Site Name	Days	RMSE[a]	NRMSE[a]	r^a	RMSE[b]	NRMSE[b]	r^b	RMSE[c]	NRMSE[c]	r^c	RMSE[d]	NRMSE[d]	r^d
BR-Sa3	10	0.13	13	0.88	0.10	15	0.94	0.13	13	0.86	0.07	11	0.96
US-UMB	10	0.15	16	0.76	0.07	15	0.93	0.17	18	0.70	0.09	18	0.92
US-Br3 (growing)	10	0.07	14	0.85	0.04	14	0.96	0.08	16	0.80	0.03	12	0.96
US-Br3 (dormant)	10	0.09	16	0.66	0.03	12	0.94	0.10	17	0.57	0.04	17	0.91
US-Dk1	10	0.07	13	0.73	0.03	14	0.93	0.07	14	0.68	0.03	14	0.94
Seasonal Scale Analysis													
Site Name	Time	RMSE[e]	NRMSE[e]	r^e	RMSE[f]	NRMSE[f]	r^f	RMSE[g]	NRMSE[g]	r^g	RMSE[h]	NRMSE[h]	r^h
BR-Sa3	One year	0.08	11	0.94	0.07	15	0.96	0.07	10	0.93	0.04	8	0.99
US-UMB	One year	0.25	35	0.78	0.22	58	0.96	0.22	31	0.74	0.18	48	0.95
US-UMB	May - August	0.13	21	0.94	0.13	27	0.95	0.09	15	0.93	0.08	18	0.95
US-Dk1	One year	0.04	16	0.87	0.03	20	0.96	0.05	17	0.87	0.03	20	0.98

[a] calculated from half-hourly results using extreme solution with H_{OBS},
[b] calculated from mean diurnal cycles using extreme solution with H_{OBS},
[c] calculated from half-hourly results using extreme solution with H_{MEP},
[d] calculated from mean diurnal cycles using extreme solution with H_{MEP},
[e] calculated from monthly mean diurnal cycles using extreme solution with H_{OBS},
[f] calculated from annual mean diurnal cycles using extreme solution with H_{OBS},
[g] calculated from monthly mean diurnal cycles using extreme solution with H_{MEP},
[h] calculated from annual mean diurnal cycles using extreme solution with H_{MEP}.

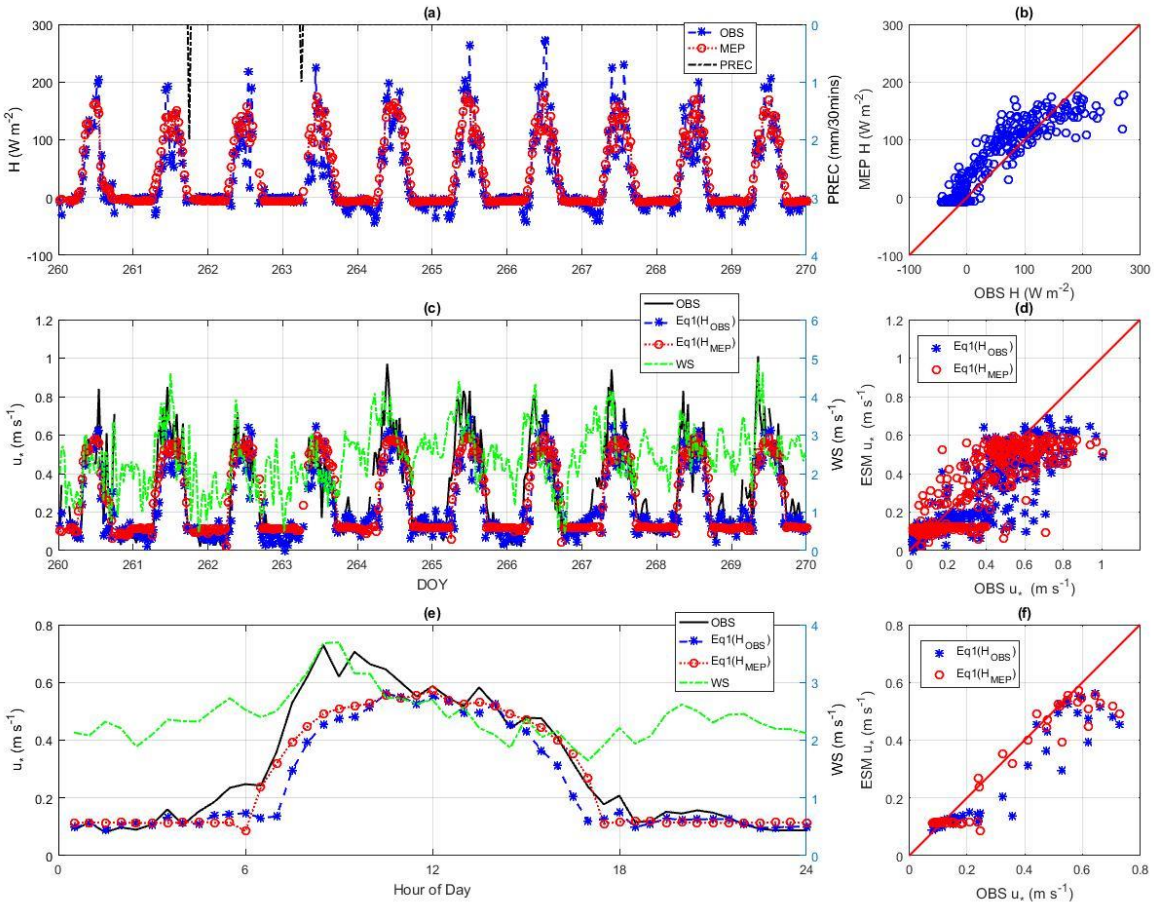

Figure 4.31 (a) (b) MEP modeled (MEP) and observed (OBS) sensible heat fluxes (*H*), and precipitation (PREC), (c) (d) extreme solution modeled (ESM) u_* using Eq. (1) with OBS *H* (Eq1(H_{OBS})) and MEP *H* (Eq1(H_{MEP})), OBS u_*, and observed wind speed (WS), and (e) (f) mean diurnal cycles of ESM and OBS u_*, and WS at BR-Sa3, Sep. 17 – 27, 2001.

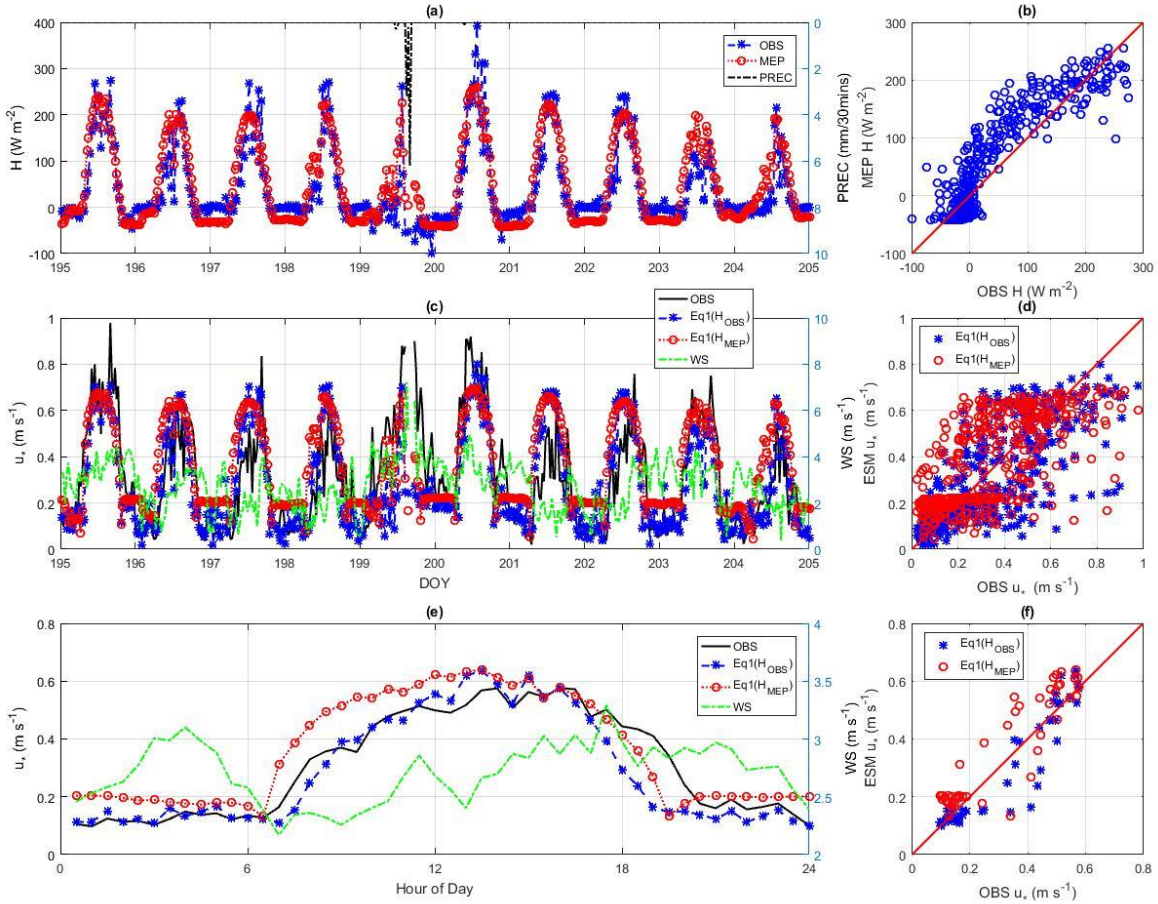

Figure 4.32 (a) (b) MEP and OBS *H*, and PREC, (c) (d) ESM and OBS u_*, and WS, and (e) (f) mean diurnal cycles of ESM and OBS u_*, and WS at US-UMB, Jul. 14 – 24, 2007.

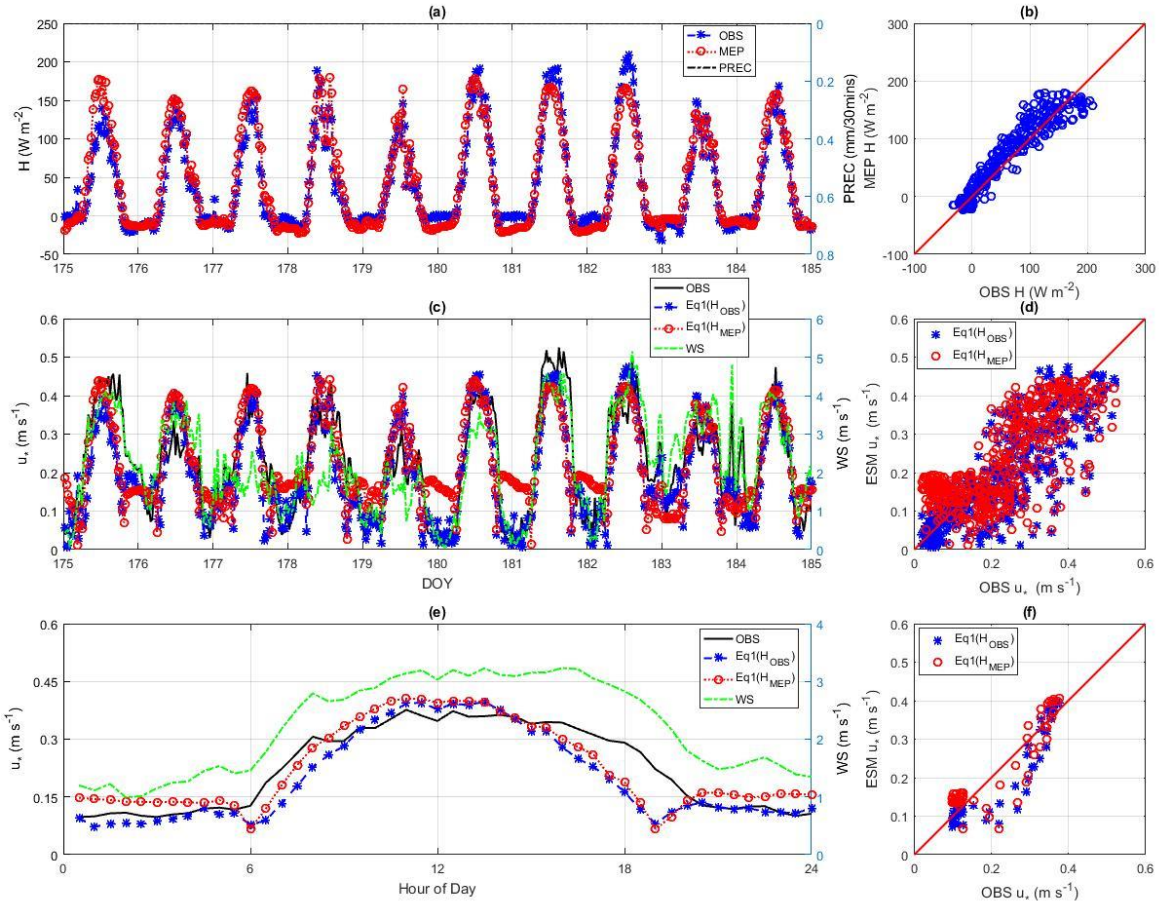

Figure 4.33 (a) (b) MEP and OBS *H*, and PREC, (c) (d) ESM and OBS u_*, and WS, and (e) (f) mean diurnal cycles of ESM and OBS u_*, and WS at US-Br3, Jun. 24 – Jul. 4, 2007 (growing season, soybean).

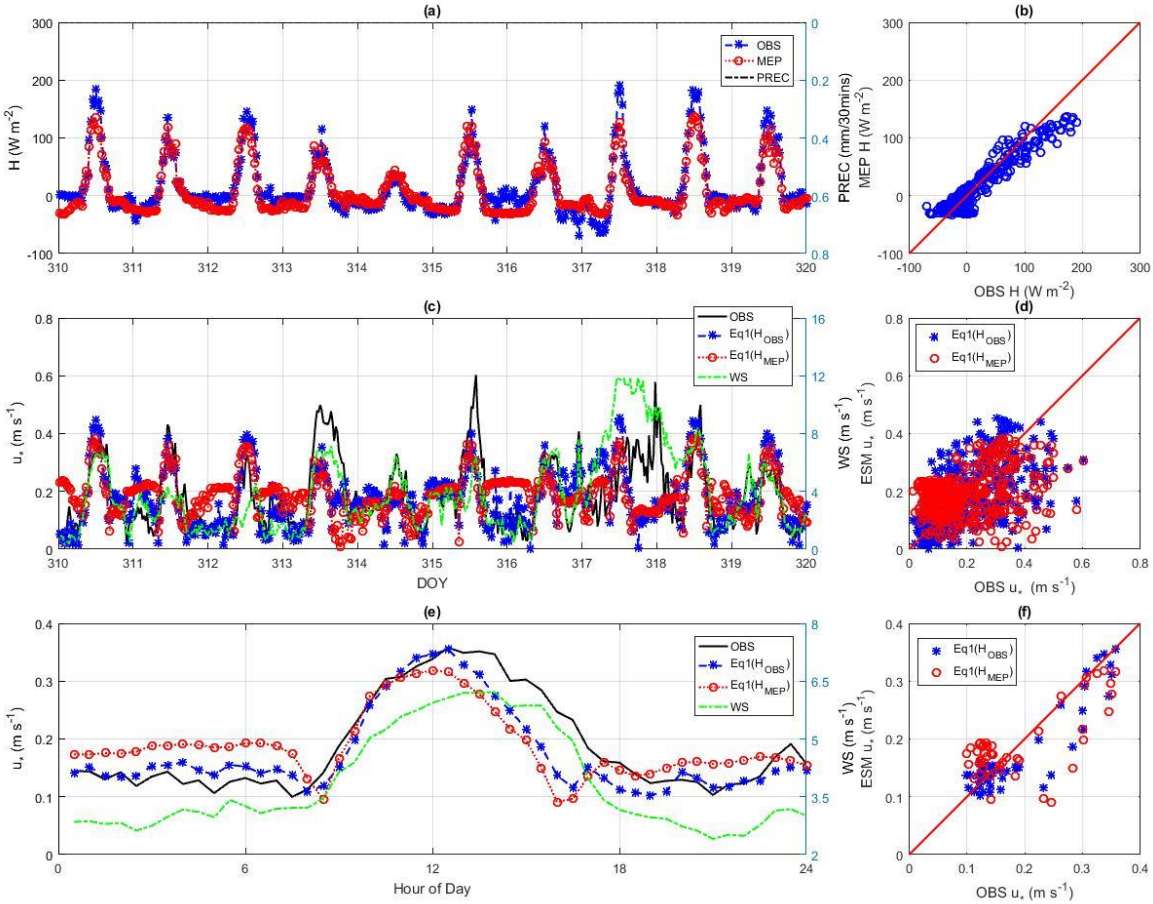

Figure 4.34 (a) (b) MEP and OBS *H*, and PREC, (c) (d) ESM and OBS u_*, and WS, and (e) (f) mean diurnal cycles of ESM and OBS u_*, and WS at US-Br3, Nov. 6 – 16, 2007(dormant season, bare soil).

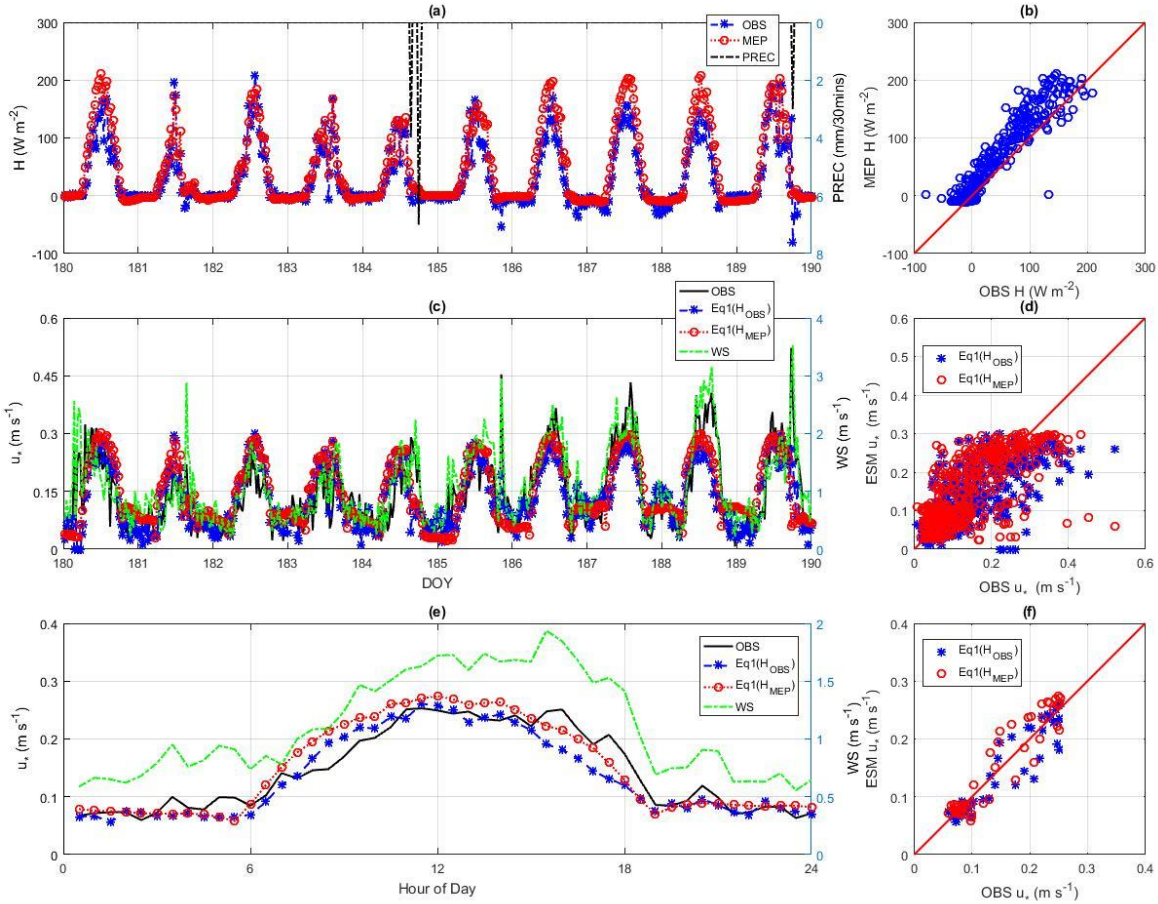

Figure 4.35 (a) (b) MEP and OBS *H*, and PREC, (c) (d) ESM and OBS u_*, and WS, and (e) (f) mean diurnal cycles of ESM and OBS u_*, and WS at US-Dk1, Jun. 28 – Jul. 8, 2004.

4.4.4.3 Estimation of u_* at seasonal scale

Monthly and annual mean diurnal cycles calculated from half-hourly data are analyzed to understand the model's performance at seasonal scales at BR-Sa3, US-UMB, and US-DK1 as shown in Figures 4.36 to 4.39. Cropland site US-Br3 is not included in the seasonal scale analysis as human activities such as planting and harvesting significantly influence the land surface processes while diurnal scale tests in growing and dormant seasons have demonstrated the model's effectiveness over cropland. Panels (a) and (b) compare the

monthly mean diurnal cycles of the MEP modeled and observed sensible heat fluxes. Panels (c) and (d) compare the monthly mean diurnal cycles of the modeled and observed friction velocities. The monthly mean diurnal cycles of wind speed is also included in Panel (c). Panels (e) and (f) compare the annual mean diurnal cycles of the modeled and observed friction velocities. The annual mean diurnal cycles of wind speed are shown in Panel (e). Although not included in the model, wind speed in shown to explain the behavior of the proposed model. The statistics of sensible heat fluxes and friction velocities are summarized in Tables 4.10 and 4.11, respectively.

The MEP modeled and EC observed sensible heat fluxes are in good agreement with NRMSEs less than 12 % and *r*s greater than 0.94 at all test sites. The modeled friction velocities agree closely with the observations at all-times except for the winter at US-UMB. When mean wind speed is stronger (> 4 m s^{-1}) during November as shown in Figure 4.37 (c), the modeled friction velocities are significantly smaller than the observation at US-UMB. Figure 4.38 compares the modeled and observed friction velocities at US-UMB when wind speed is weak (< 4 m s^{-1}) from May to August in 2007. It is evident that Eq. 4.18 estimates friction velocities at seasonal scale with high accuracy when wind is weak with all *r*s of mean diurnal cycles greater than 0.87.

The proposed model as Eq. 4.18 performs well except for neutral ASL when friction velocity is decoupled from sensible heat flux. The ASL tends to become neutral with strong wind, weak sensible heat flux, and within one hour after sunrise or before sunset [*Davies and Singh*, 1985; *Pasquill*, 1961; *Sutherland et al.*, 1986], causing the discrepancies between the modeled and observed friction velocities discussed previously. Nonetheless,

Eq. 4.18 estimates the annual mean friction velocities accurately at all sites, indicating the effect of neutral stability conditions is negligible at annual time scales [*Arya*, 2001].

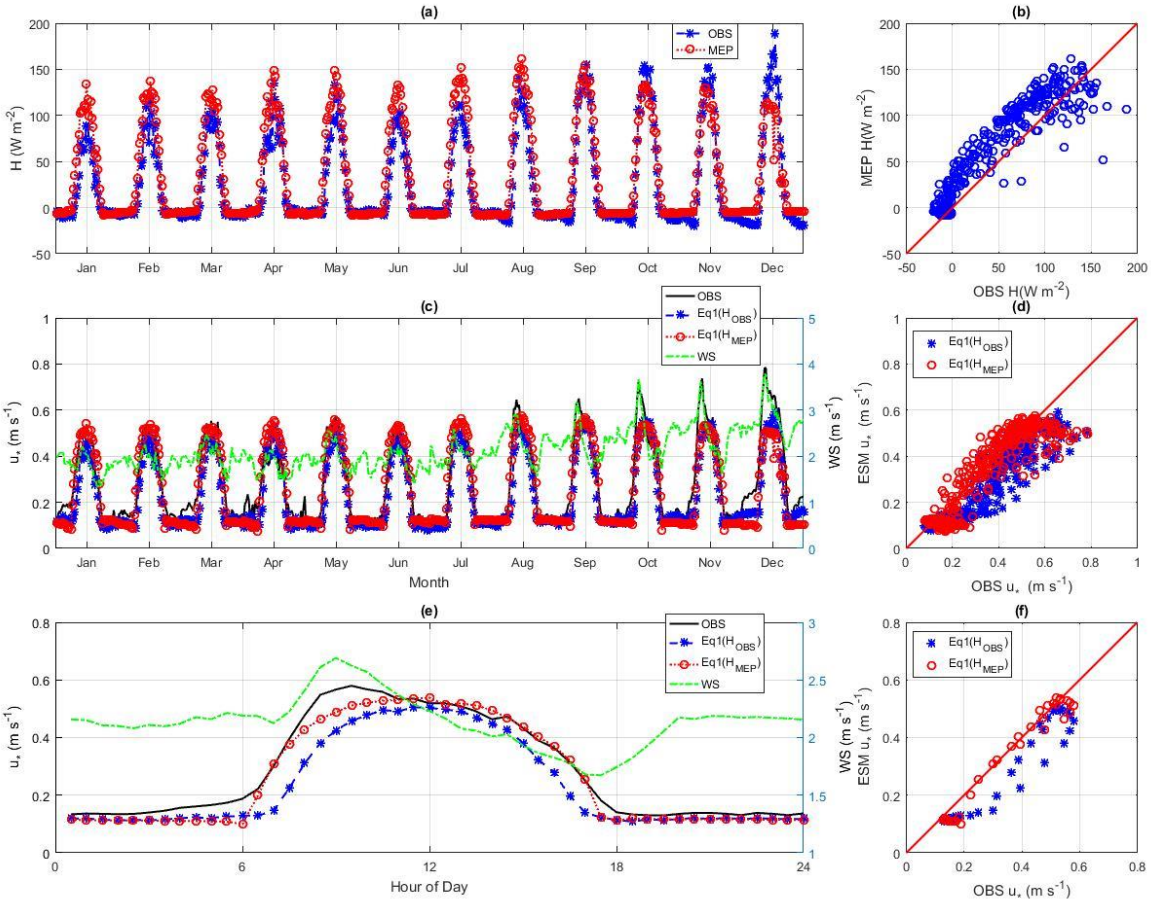

Figure 4.36 Monthly mean diurnal cycles of (a), (b) MEP and OBS *H*; (c), (d) ESM and OBS u_*. Annual mean diurnal cycles of (e), (f) ESM and OBS u_*, and WS at BR-Sa3 in 2001.

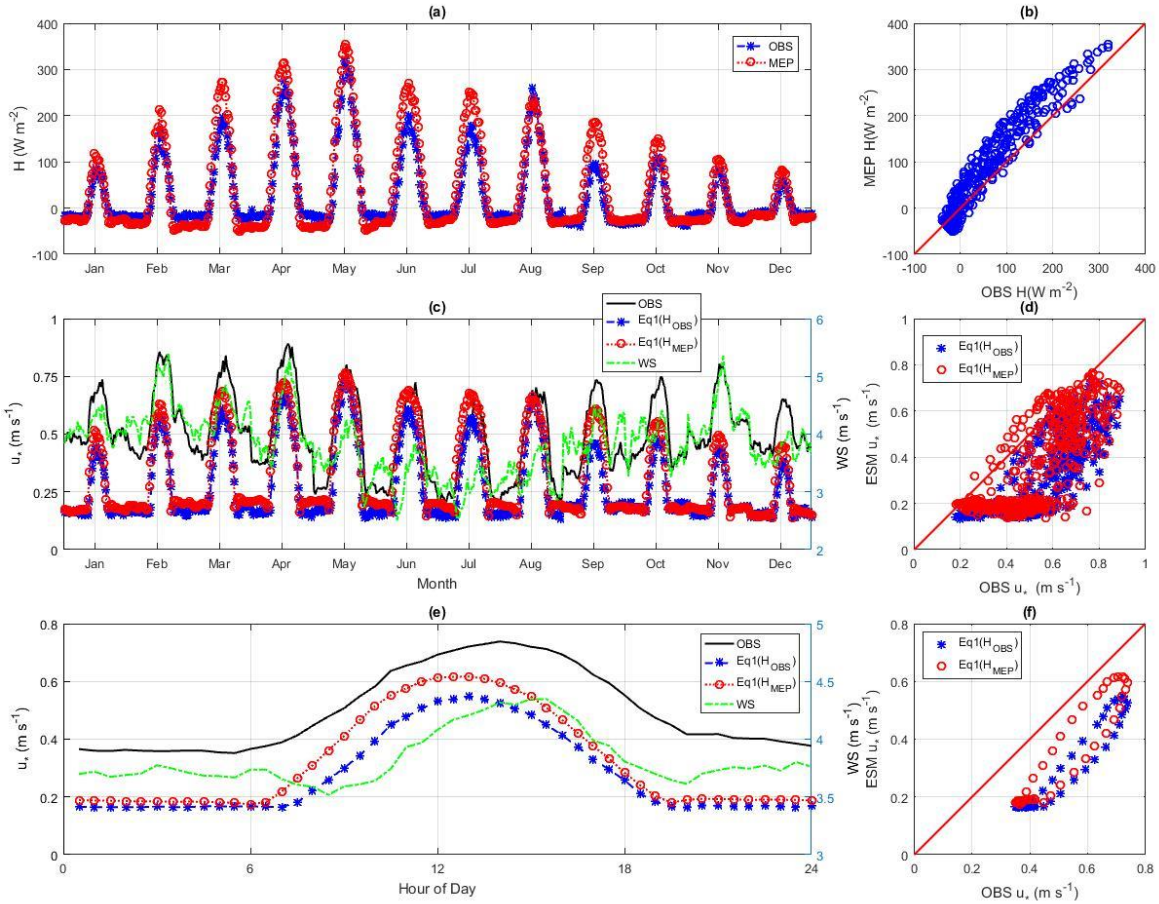

Figure 4.37 Monthly mean diurnal cycles of (a), (b) MEP and OBS *H*; (c), (d) ESM and OBS u_*. Annual mean diurnal cycles of (e), (f) ESM and OBS u_*, and WS at US-UMB in 2007.

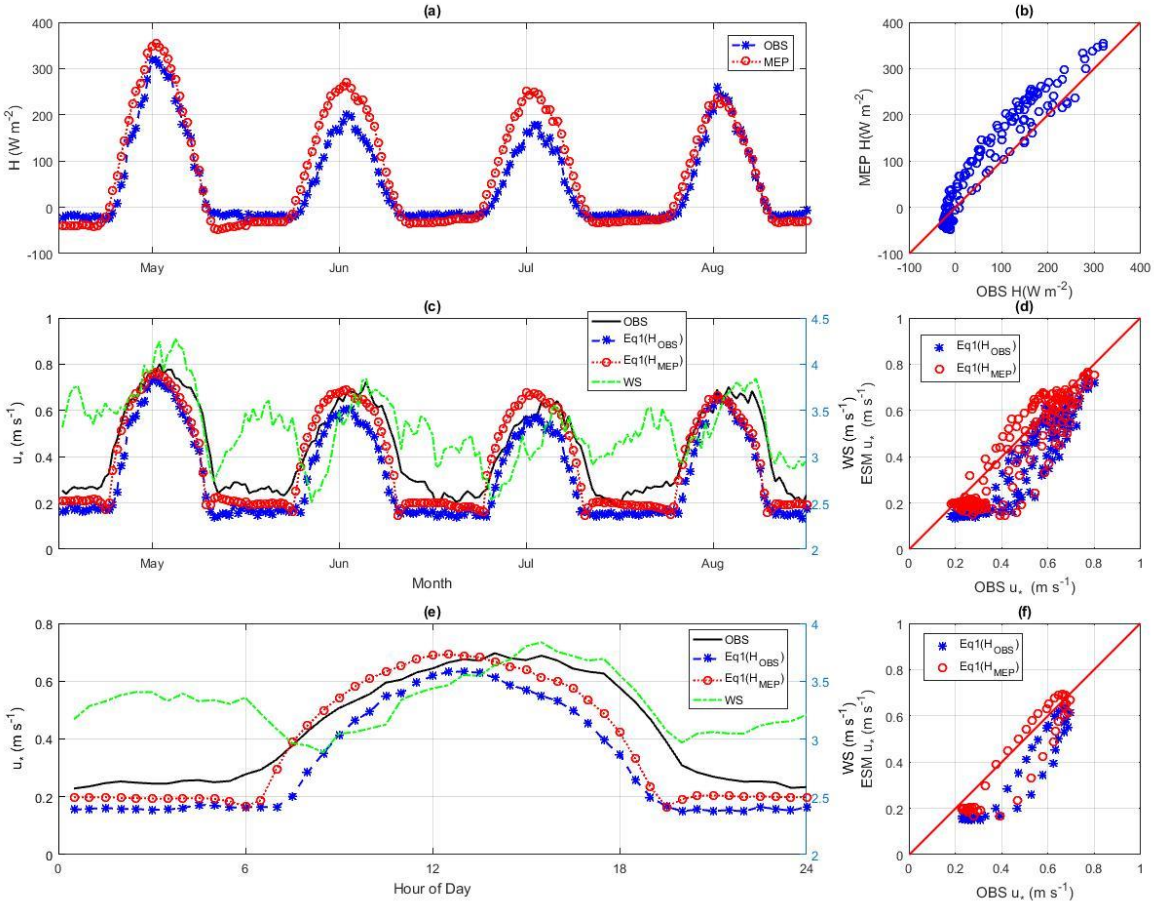

Figure 4.38 Monthly mean diurnal cycles of (a), (b) MEP and OBS *H*; (c), (d) ESM and OBS u_*. Mean diurnal cycles of (e), (f) ESM and OBS u_*, and WS at US-UMB from May to August in 2007.

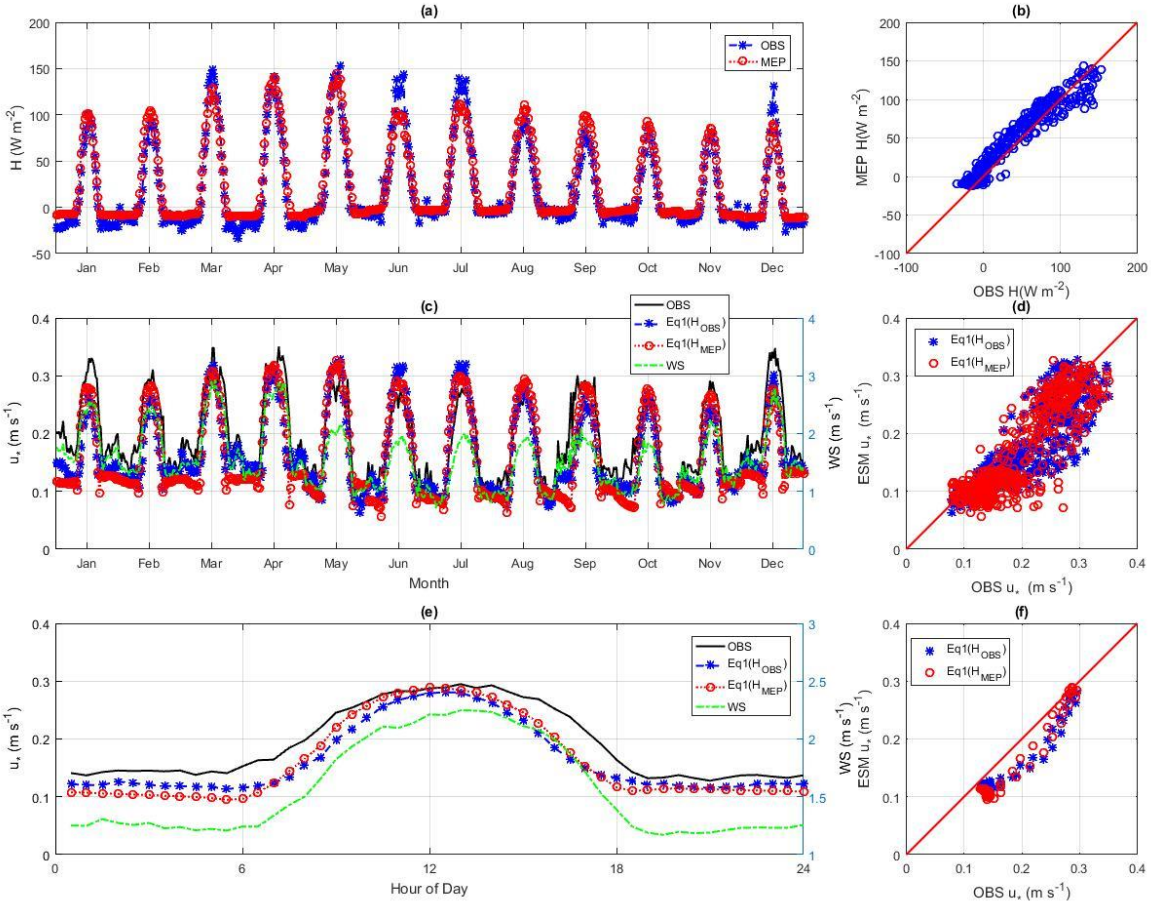

Figure 4.39 Monthly mean diurnal cycles of (a), (b) MEP and OBS *H*; (c), (d) ESM and OBS u_*. Annual mean diurnal cycles of (e), (f) ESM and OBS u_*, and WS at US-Dk1 in 2004

4.4.4.4 Estimation of u_* using daily data

Time-averaged Eq. 4.18 becomes,

$$\overline{u_*} = 0.042\sqrt[3]{|\bar{H}|z} \qquad 4.19$$

where $\overline{u_*}$ (m s^{-1}) is the daily mean friction velocity and $\bar{H}$ (W m^{-2}) the daily mean sensible heat flux. The coefficient 0.042 is the mean of D_0 in Eq. 4.18. The nonlinearity of Eq. 4.18 due to the one-third power of *H* is tested using field observations. Figure 4.40 shows daily $\bar{H}^{1/3}$ vs. $\overline{H^{1/3}}$ calculated using one-year long half-hourly data at the four sites. The

statistics of $\bar{H}^{1/3}$ in respect to $\overline{H^{1/3}}$ are summarized in Table 4.12. Although $\overline{H^{1/3}}$ is consistently smaller than $\bar{H}^{1/3}$, the average NRMSE and *r* are 18 % and 0.93, respectively, indicating the nonlinearity of Eq. 4.18 is weak and Eq. 4.19 is a reasonable time-average of Eq. 4.18.

Eq. 4.19 is tested using daily input data for a 50-day period with least missing records as shown in Figure 4.41. The blanks in Figure 4.41 are the missing records due mostly to rain events. The magnitudes of the modeled friction velocities are consistent with those of the observations at daily scale at all sites. Table 4.13 summarizes the statistics of the daily friction velocities including the mean friction velocity $\widetilde{u_*}$, the error (E, defined as absolute difference of the mean modeled and observed u_*), and the relative error (RE, defined as E divided by the observed u_*). The average Es (REs) of modeled $\widetilde{u_*}$ using daily observed and modeled *H* are 0.03 m s^{-1} (9 %) and 0.04 m s^{-1} (14 %), respectively. Given that the measurement errors of u_* are ~ 20% at the test sites [*Oren et al.*, 2006; *Pressley et al.*, 2006; *Rocha et al.*, 2004; *D. Vickers et al.*, 2010], the close agreement of the modeled and observed friction velocities demonstrates the usefulness of Eq. 4.19 for estimating friction velocity from sensible heat flux at daily scale without using wind speed.

Table 4.12 Statistics of $\bar{H}^{1/3}$ vs. $\overline{H^{1/3}}$ including Days, Mean $\bar{H}^{1/3}$($W^{1/3}\,m^{-2/3}$), Mean $\overline{H^{1/3}}$ ($W^{1/3}\,m^{-2/3}$) RMSE ($W^{1/3}\,m^{-2/3}$), NRMSE (%), and *r*

Site Name	Days	Mean $\bar{H}^{1/3}$	Mean $\overline{H^{1/3}}$	RMSE	NRMSE	*r*
BR-Sa3	365	3.16	2.56	0.64	21	0.93
US-UMB	365	3.63	3.11	0.60	20	0.93
US-Br3	365	3.01	2.64	0.43	14	0.97
US-Dk1	366	3.20	2.59	0.66	16	0.90

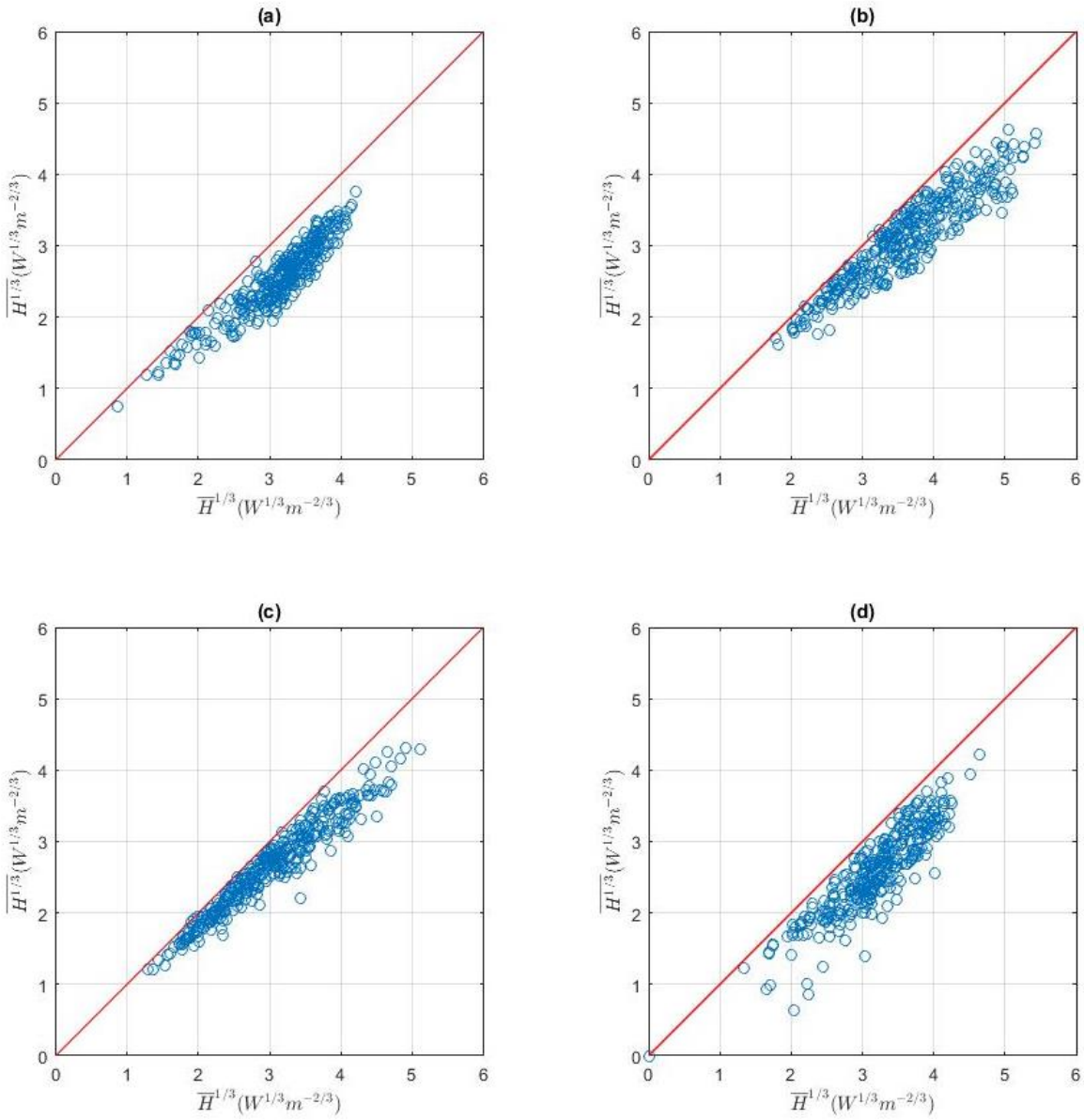

Figure 4.40 $\overline{H}^{1/3}$ and $\overline{H^{1/3}}$ at daily scale at (a) BR-Sa3 in 2001, (b) US-UMB in 2007, (c) US-Br3 in 2007, and (d) US-DK1 in 2004.

Table 4.13 Statistics of modeled friction velocities using daily inputs including mean friction velocity $\widetilde{u_*}$ (m s^{-1}), E (m s^{-1}), and RE (%) for the 50-day periods

Site Name	Days	$\widetilde{u_*}^a$	E^a	RE^a	$\widetilde{u_*}^b$	E^b	RE^b	$\widetilde{u_*}^o$
BR-Sa3	50	0.32	0.02	5	0.34	0.04	13	0.30
US-UMB	50	0.35	0.05	13	0.35	0.05	13	0.40
US-Br3	50	0.19	0.02	11	0.19	0.02	11	0.21
US-Dk1	50	0.19	0.01	8	0.20	0.03	17	0.17

[a] calculated using daily mean observed *H*,
[b] calculated using MEP modeled *H* with daily inputs,
[o] calculated from half-hourly observation.

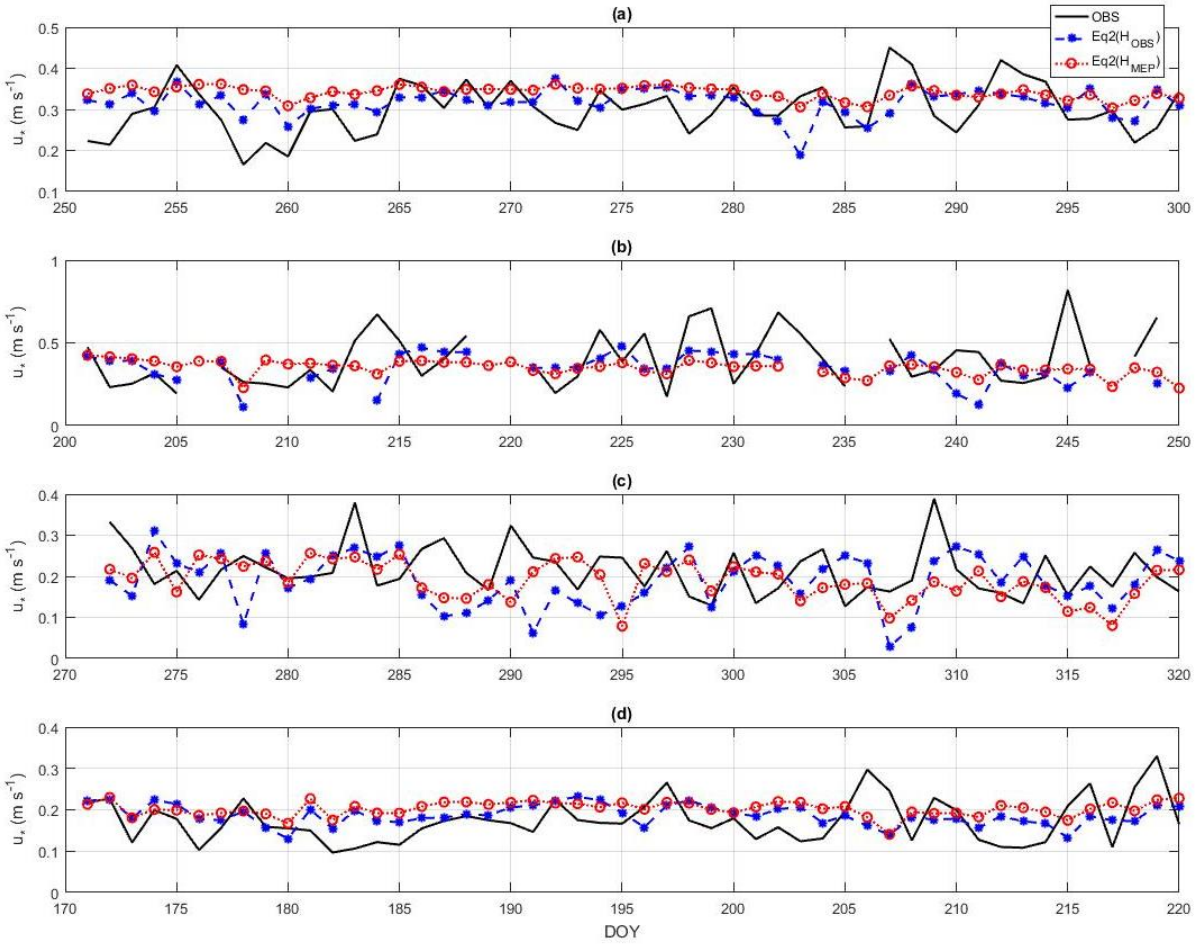

Figure 4.41 Observed (OBS) and modeled daily friction velocities using Eq. (2) with daily OBS (Eq2(H_{OBS})) and MEP *H* (Eq2(H_{MEP})) at (a) BR-Sa3, Sep. 7 – Oct. 27, 2001, (b) US-UMB, Jul. 19 – Sep. 7, 2007, (c) US-Br3, Sep. 27 – Nov. 16, 2007, and (d) US-DK1, Jun.18 – Aug.7, 2004.

4.4.5 Conclusion

This proof-of-concept study demonstrates the possibility of estimating the friction velocity from the sensible heat flux without using wind speed data based on the extremum solution of the MOSE. The case study further confirms the extremum solution of the MOSE at sub-daily and seasonal time scales. The proposed model is also able to estimate the daily friction velocity directly using daily data if sub-daily data are not available. As land surface wind speed at regional and global scales is difficult to measure, the proposed model combined with the MEP model opens an opportunity of estimating the land surface friction velocity and wind speed at regional and global scales using remote sensing observations, ground-based observations, and reanalysis products. On-going research explores the retrieval of the friction velocity and wind speed over land surfaces at regional and global scales.

4.5 Gap-Fillings and Estimations of EC Heat and CO_2 Fluxes

4.5.1 Introduction

The half-hourly EC turbulent fluxes of heat and CO_2 are derived from high-frequency measurement of wind speed and direction together with measurements of air scalar characteristics such as temperature, water vapor and CO_2 concentration. Typical post-processes of the EC data include data quality checks and quality assessment. Through the data quality check, no more than 2 % of the turbulent fluxes measured at ACS and BCS are with low quality (Appendix D). However, the quality check could not identify the unreasonable spikes due to reasons both bio-physical (changes in the footprint or fast changes in turbulence conditions) and instrumental (water drops on sonic anemometer or on open path IRGA) [*Papale et al.*, 2006]. Moreover, although the EC data are usually

recorded half-hourly or hourly, the average data coverage during a year is only 65% due to system failures or data rejection [*Falge et al.*, 2001]. Therefore, gap-filling procedures need to be established for providing complete datasets.

The most widely used method for gap-filling of EC fluxes is the u_* correction method, which uses friction velocity as a criterion to discriminate EC data during low and well-mixed periods [*Aubinet et al.*, 1999]. However, the u_* correction method has many drawbacks. Firstly, the threshold of u_* is specific for each season of a site year, causing one of the largest uncertainty components in the post-processing of EC fluxes [*Wutzler et al.*, 2018]. Secondly, the uncertainty of the u_* correction method significantly depends on the operator's subjectivity [*Papale et al.*, 2006]. Finally, the hypotheses underlying the u_* correction are still debatable. The u_* correction method supposes that measurements made during turbulent periods are free of errors, which is questioned by many experiment results [*Cook et al.*, 2004; *Wohlfahrt et al.*, 2005].

This study proposes to fill the data gaps of turbulent heat fluxes using MEP model and of CO_2 fluxes using HOD model. Comparing with u_* correction method, the MEP and HOD models have several advantages. Firstly, they are based on the physical processes of land surface energy and gas transport rather than merely statistics. The MEP model is based on the land surface non-equilibrium thermodynamics, and the HOD model is based on the land surface turbulent diffusive gas transport. Secondly, the variables used by the MEP and HOD model to estimate turbulent fluxes are easily and accurately measured. The MEP model uses net radiation, air temperature, and humidity to estimate turbulent heat fluxes and the HOD model uses an extra CO_2 concentration measurement. The uncertainties of net radiation, air temperature, humidity, and CO_2 concentration are 5%, 1%, 4%, and 1%,

respectively, according to the sensor manuals. Therefore, the data-filling method using MEP and HOD models is an improvement of the classic u_* correction method.

4.5.2 Methodology

As EC fluxes are available at ACS, BCS, and DFS sites, the MEP and HOD models are used to fill the data gaps of turbulent fluxes in the existing time records as follows. Firstly, estimate turbulent fluxes using MEP and HOD models with available observations of net radiation, air temperature, humidity, and CO_2 concentration. Secondly, find the data gaps in the existing time records of turbulent fluxes. Finally, fill the data gaps with estimated turbulent fluxes. As EC fluxes and net radiation are not available at CLS due to safety concerns in the hunting ground, the MEP model is used to estimate turbulent heat fluxes with net radiation data from the ACS site.

4.5.3 Results

4.5.3.1 Gap-Fillings of Turbulent Heat Fluxes using MEP model

As EC fluxes are available at ACS, BCS, and DFS sites, the MEP model is used to fill the data gaps of turbulent heat fluxes in the existing time records. To fill the data gaps, turbulent heat fluxes are firstly estimated with available observations of net radiation, air temperature, humidity, and CO_2 concentration. Secondly, data gaps in the observations of the turbulent heat fluxes are filled with the MEP modeled heat fluxes. Figures 4.42 to 4.44 show the results of the filled data records at ACS, BCS, and DFS, respectively. The blue lines are the original observed turbulent heat fluxes, and the read dash lines are the filled turbulent heat fluxes. The blanks in the filled records are due to absence of the input data

required by the MEP model. The statistics of gap-fillings at ACS, BCS, and DFS are summarized in Table 4.14.

Table 4.14 Statistics of Gap-Fillings at ACS, BCS, and DFS

	Variable	OBS	Modeled	Filled	Available	Percentage (%)
ACS	H	28146	28465	2965	31111	9.53
	E	26828	28465	4145	30973	13.38
	FC	26121	24769	314	26435	1.19
BCS	H	10788	19085	8297	19085	43.47
	E	10713	19085	8372	19085	43.87
	G	19084	19085	1	19085	0.00
DFS	H	134430	140256	5826	140256	4.15
	E	132936	140256	7320	140256	5.22
	FC	131061	128414	1542	132603	1.16

At ACS and DFS, upto 7000 data gaps of turbulent heat fluxes are filled. The filled blanks are mainly caused by unreasonable spikes in the observations due to rain events or malfunctions of the EC systems. At BCS, almost 44 % of the turbulent heat fluxes are filled by the MEP modeled fluxes. The large absence of EC fluxes at BCS are due to a failure of an old anemometer.

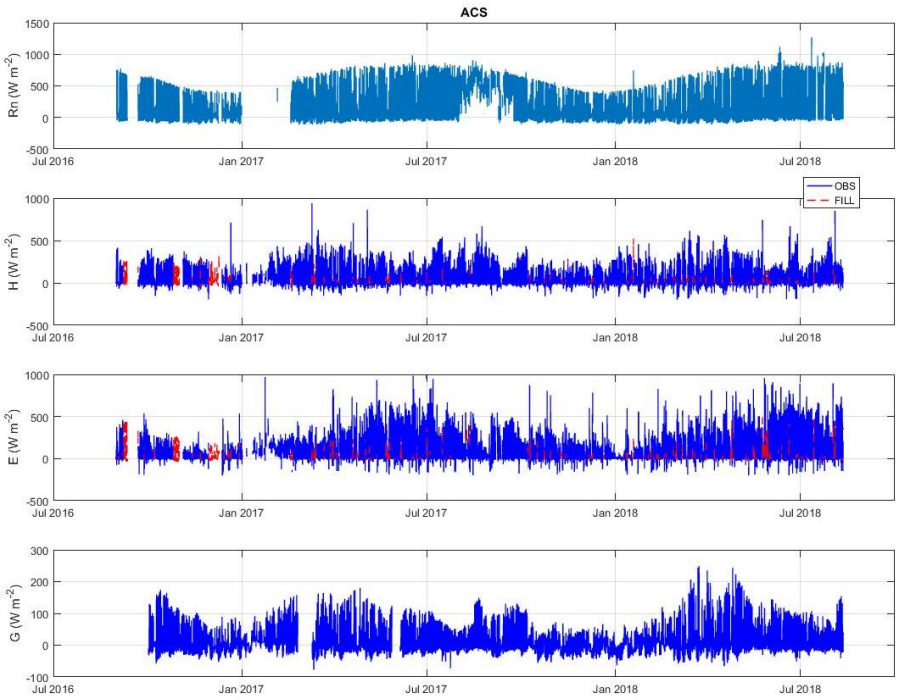

Figure 4.42 Filled data of heat fluxes at ACS

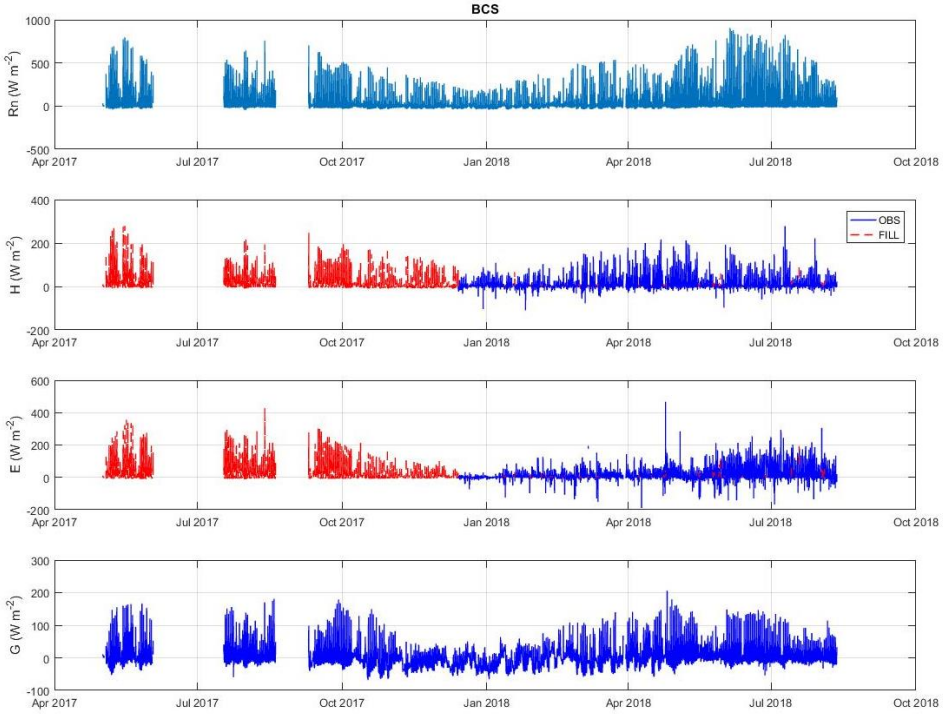

Figure 4.43 Filled data of heat fluxes at BCS

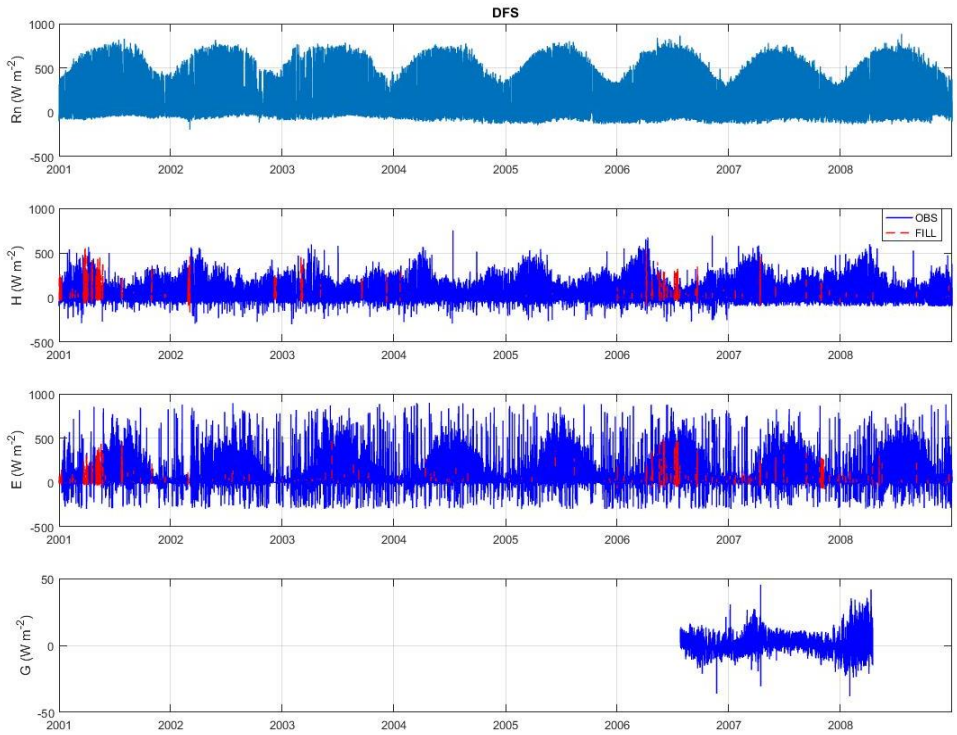

Figure 4.44 Filled data of turbulent heat fluxes at DFS

4.5.3.2 Estimations of Heat Fluxes at CLS using the MEP model

As the EC system is not installed at CLS, the MEP model is used to estimate surface heat fluxes. As the MEP model requires net radiation, air temperature, and humidity to calculate heat fluxes, and net radiation is not measured at CLS, net radiation at ACS is assumed to be the same as that at CLS. The assumption that net radiation over different land covers at nearby geographic locations is the same is tested using field observations over grassland, pine forest, and mature forest at three Duke experimental sites.

Duke Forest Open Field site (USDk1 for short) is approximately 480 × 305 m, dominated by the C3 grass. The site was burned in 1979 and is mowed annually during the summer for hay according to local practices. The net radiometer for measuring net radiation is

installed at 3.3 m above ground level [*Lai and Katul*, 2000]. Data at USDk1 are available from 2001 to 2008. Duke Forest Hardwoods site (USDk2 for short) is introduced in Chapter 3. The net radiometer is installed 39.8 m above the ground level [*Novick et al.*, 2009]. Data at USDk2 are available from 2001 to 2008. Duke Forest Loblolly Pine site (USDk3 for short) was established in 1983 following a clear cut and a burn. Pine seedlings were planted at 2.4 m by 2.4 m spacing and ecosystem development has not been managed after planting. Canopy height increased from 16 m in 2001 to 18 m in 2004. The flux tower lies upwind of the CO2-enriched components of the free atmosphere carbon enrichment (FACE) facility located in the same pine forest. Net radiometer instrumentation is at 20.2 m on a 22 m tower. Data at USDk3 are available from 1998 to 2008. USDk1 and USDk3 are similar to cropland site and young pine forest site at CCZO, respectively.

Field observations of net radiation, air temperature, and relative humidity during June 15 to June 25, 2005 from USDK1, USDK2, and USDK3 are compared in Figure 4.45. The net radiation, air temperature, and relative humidity at the three sites are almost identical. Though net radiation over forests are slightly greater during noontime, the differences are within 20 W m^{-2}, which is the measurement uncertainty of a net radiometer [*T. E. Twine et al.*, 2000]. Figure 4.46 compares the net radiation at three sites in 2005. Net radiation over pine forest is slightly greater than that over grassland. Given the pine trees at USDk1 are more mature than those at ACS, the net radiation measurement at ACS logically is less different from that at CLS. Therefore, net radiation at ACS is a good substitute of that at CLS.

With field observations of air temperature and humidity at CLS and net radiation at ACS, surface heat fluxes at CLS are estimated using the MEP model as shown in Figure 4.47.

The modeled heat fluxes at CLS are used to study the evolution of energy and water cycles due to land-use change at Calhoun critical zone in next chapter.

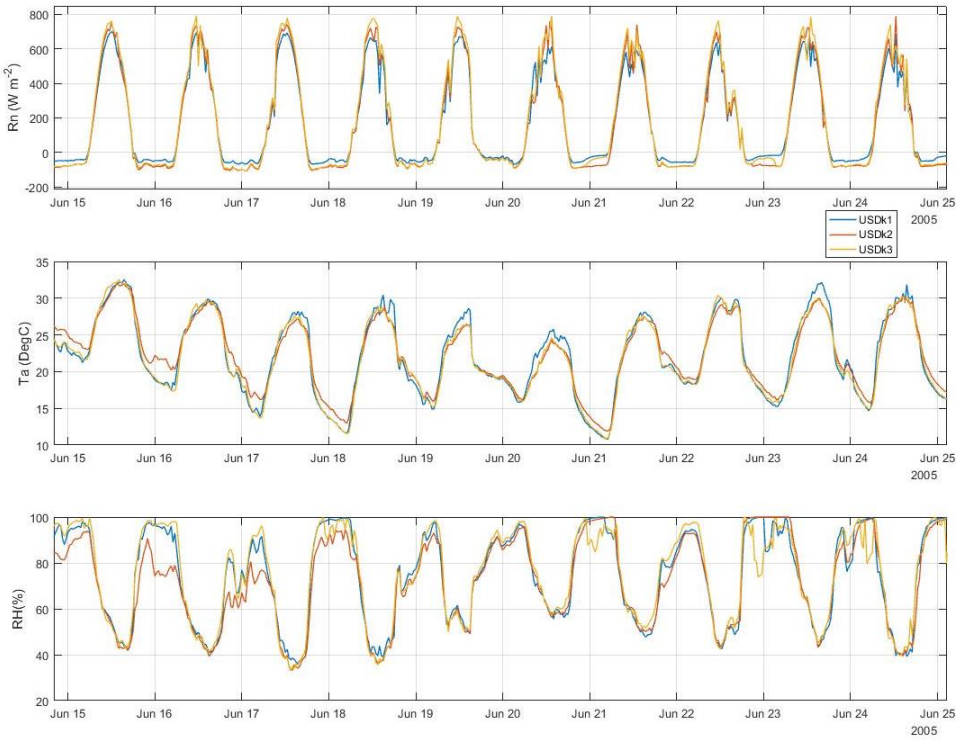

Figure 4.45 Rn, Ta, and RH at USDK1, USDK2, and USDK3 on June 15 to 25, 2005

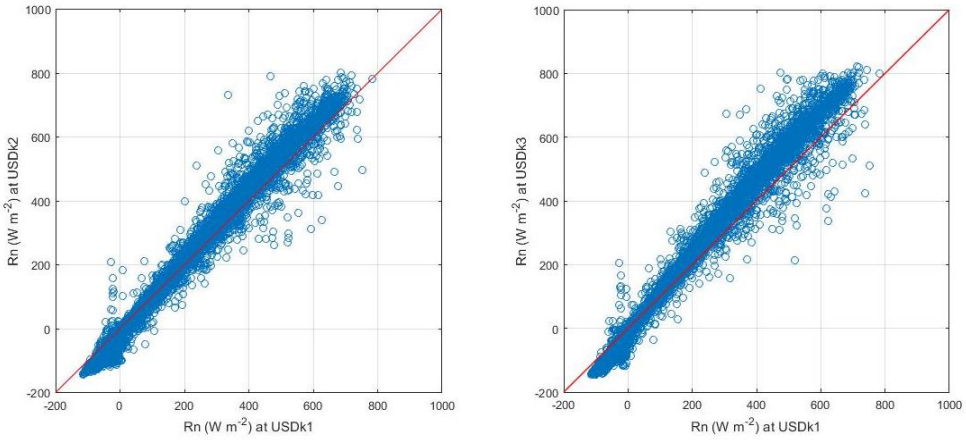

Figure 4.46 Rn at USDK1, USDK2, and USDK3 in 2005

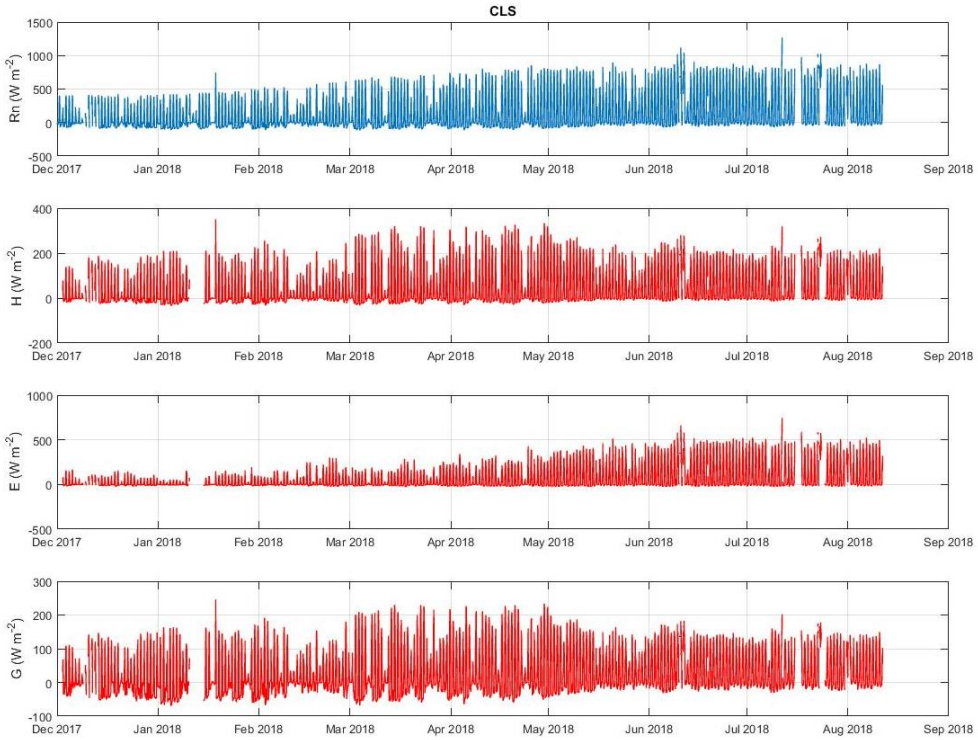

Figure 4.47 MEP modeled heat fluxes at CLS

4.5.3.3 Gap-Fillings of EC CO_2 Fluxes using the HOD model

The HOD model is used to fill the gaps in observations of CO_2 fluxes at ACS and DFS. The HOD model requires net radiation, air temperature, humidity, and CO_2 concentration to estimate CO_2 fluxes. The filled data at ACS and DFS are shown in Figure 4.48. The statistics of the filled CO_2 fluxes are summarized in Table 4.14. Upto 1500 data gaps of the CO_2 fluxes data at ACS and DFS are filled using the HOD model.

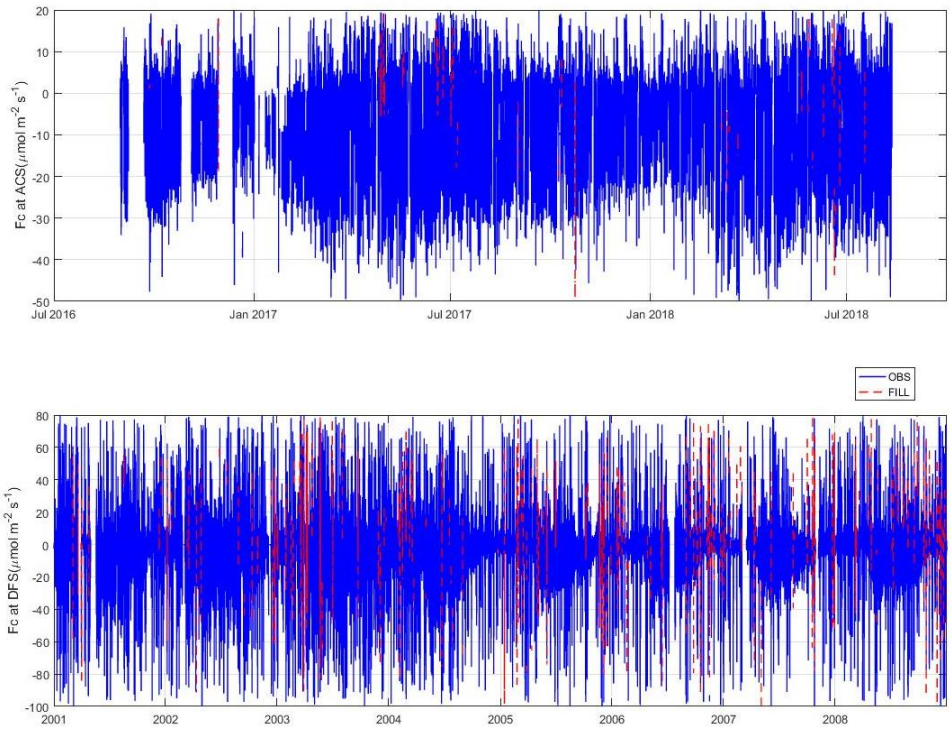

Figure 4.48 Gap-filling of CO_2 fluxes at ACS and DFS

4.5.4 Conclusion

The MEP and HOD models are used to fill the gaps of the observed turbulent fluxes at ACS, BCS, and DFS. Comparing to the classic method, the MEP and HOD models are based on strong physical concepts rather than merely experience and statistics. Up to 7000 data gaps of the EC observed heat fluxes are filled using the MEP model. Up to 1500 data gaps of the EC observed CO_2 fluxes are filled using the HOD model. The MEP model is used to estimate surface heat fluxes at CLS in terms of net radiation at ACS, and air temperature and humidity at CLS. The gap-filled data are used to investigate the evolution of the energy, water, and carbon cycle due to land-use change at Calhoun critical zone.

4.6 Summary

This chapter introduces three models of land surface turbulent fluxes, tests them using field observations at many field sites including the CCZ sites with different climate and vegetation conditions, and applies them to fill the data gaps of EC fluxes at CCZ.

Section 4.2 introduces the MEP model of land surface heat fluxes. Before testing the MEP model, the energy balance of the observed heat fluxes is tested at ACS, BCS, and DFS using the bulk energy balance equation and the linear regressions. Results of the energy balance analysis indicate a good energy balance closure at ACS, a lack of energy balance closure at BCS, and a reasonable energy balance closure at DFS. The MEP model is tested using half-hourly field observations of 17months, 7 months, 7.6 years at ACS, BCS, and DFS, respectively. The MEP model estimates the heat fluxes at all sites accurately with NRMSEs no greater than 9 %, justifying the applicability of the MEP model in gap-fillings of the EC heat fluxes at CCZ sites.

Section 4.3 introduces a novel model to estimate land surface water and carbon fluxes with single-level concentration measurement. The HOD model of surface turbulent gas fluxes is derived based on fractional calculus that transforms the spatial gradient to an integral of a historic record. The eddy-diffusivity used in the HOD model is calculated from friction velocity that is calculated using the extreme solution of MOST. The HOD model is tested to estimate water vapor and CO_2 fluxes using field observations at six sites with contrasting climates and vegetation types at diurnal and seasonal scales. The case studies suggest that the HOD model is able to capture the diurnal and seasonal variations of gas fluxes using single-level concentration measurement. As CO_2 concentration is more accurately

measured than CO_2 fluxes, the HOD model is useful to fill the data gaps of EC CO_2 fluxes at CCZ sites.

Section 4.4 introduces a method to estimate friction velocity from surface heat flux. The new model is derived from an extreme solution of the Monin-Obukhov similarity equations that directly relating friction velocity with the sensible heat flux using, which can be estimated using the MEP model. The model is tested using half-hourly observations at field sites with diverse climate, geography, and vegetation types at sub-daily and seasonal scales. The good results of the model demonstrate the possibility for estimating friction velocity and surface wind speed using remote sensing observations. The model also provides a new way to estimate the turbulent eddy-diffusivity that is used in the HOD model. The uncertainty test of the three models are in Appendix J.

Section 4.5 applies the MEP and HOD models in gap-fillings and estimations of EC heat and CO_2 fluxes at CCZ field sites. Comparing to the classic method in gap-fillings, the MEP and HOD models are bases on stronger physical concepts rather than experience and statistics. The MEP model fills up to 7000 data gaps of the EC heat fluxes, and the HOD model fills up to 1500 data gaps of the EC CO2 fluxes at CCZ field sites. The MEP model is also used to estimate surface heat fluxes at CCZ cropland site from December 2017 to August 2018. The gap-filled data and modeling results of surface heat and CO_2 fluxes are used in Chapter 5 to investigate the evolution of the energy, water, and carbon cycle due to land-use change at CCZ.

CHAPTER 5. EVOLUTION OF ENERGY, WATER, AND CARBON CYCLE DUE TO LAND-USE CHANGE AT CALHOUN CRITICAL ZONE

This chapter describes the evolution of the energy, water, and carbon cycle due to land-use change at CCZ using field observations and modeling results presented in Chapter 3 and 4. Section 5.1 states the motivation. Section 5.2 describes the methodology. Section 5.3 reports the investigation of the evolution of temperature. Section 5.4 reports the investigation of the evolution of the energy cycle. Section 5.5 reports the investigation of the evolution of the water cycle. Section 5.6 reports investigation of the evolution of the carbon cycle. Section 5.7 discusses the results. Section 5.8 summarizes the findings of this chapter.

5.1 Motivation

The terrestrial ecological system plays an important role in the global energy, water, and carbon cycle. Human activities change the energy, water, and carbon cycle in the ecological systems predominantly through fossil fuel consumption and land-use change. The global land-use has changed dramatically since civilization. By 1750, only about 6% of the global land surface were cultivated. Until 2011, the global areas for planting crops, grazing livestock, and building urban landscapes are 11%, 25%, and 5% of the total land area, respectively [*Pielke et al.*, 2011].

In the United States, two third of the eastern land was converted from its natural states by 1920. Since the 1970s, the United States has experienced another dramatic land-use

change—including declines in cropland, increases in forests, and accelerated expansions of urban areas—that departs from conversion of forests to cropland over the previous two centuries. Between 1982 and 2002, total cropland in the United States declined by 27 million acres (6 % of total cropland in 1982) after rising 25 million acres (6 % of total cropland in 1964) over 1964-1982 [*Lubowski et al.*, 2006]. Forest area grew by 11 million acres over 1987-2002 after falling 24 million acres over 1963-1987 [*Smith et al.*, 2004]. The average urbanization rate rose from 1.0 to 1.4 million acres annually from 1960-1990 to 1990-1997 [*Lubowski et al.*, 2008]. Projected land-use change from 2001 to 2051 for the United States results in increases in carbon storage, timber and food production, and more than 10 % decreases in habitat for 25 % of plant species [*Lawler et al.*, 2014].

In the Eastern United States, the average overall amount of land-use change between 1973 and 2000 was 12.5 %, meaning that 207,000 km^2 of the 1.65 million km^2 land area changed at least once. The majority land cover in the ecoregions in 2000 was forest (52.4 % of the region); however, the amount of forest cover has declined since 1973. Meanwhile, the agriculture (21.6 % of the region) has also declined, and the developed land, primarily related to urban growth, has increased (10.6 % of the region) [*Loveland and Acevedo*, 2006].

The land-use change alters the ecosystem, the climate, and the carbon storage. This chapter investigates the evolution of the energy, water, and carbon cycle due to land-use change at CCZ, where land-use has dramatically changed since 18^{th} century, to broaden our knowledge of the impact of land-use change on regional climate in the northeastern United States.

5.2 Methodology

5.2.1 Space-For-Time Substitution Approach

The space-for-time (SFT) substitution approach is one of the most commonly encountered techniques in ecology. The SFT approach, also known as the static approach to vegetation dynamics [*Van der Maarel and Werger*, 1978], is an extrapolation of a temporal trend from a series of different-aged samples. This technique assumes that spatial and temporal variations are equivalent, thus the differences in space can be considered as an alternative of the differences in time [*Molnár and Botta-Dukát*, 1998].

Since the inception of ecology as a discipline, the SFT technique has been used in a variety of ecosystems including forests, metropolises, and water bodies [*Cowles*, 1899]. The SFT method is successfully applied to study the hill soil in New Zealand to retrieve the history in decades [*Sparling et al.*, 2003], the long-term decline in genotypic diversity of a widespread salt marsh plant over a span of 1500 years [*Travis and Hester*, 2005], the historical phonological changes in urban environment [*Buyantuyev et al.*, 2012], and the variability in lake and wetland [*Liu and Schwartz*, 2012]. the SFT has also been used to study the soil organic carbon at CCZO for decades [*Daniel deB. Richter et al.*, 2014]. In this study, the SFT approach is applied to a set of current ecosystems, with which the historic ecosystems through CCZ's land-use history are reproduced.

The SFT method requires different ecosystems in the same time frame representing the ecosystems in a chronological order. In this study, Duke Forest site (DFS) is regarded as the pre-agricultural ecosystem before cultivation in the 1800s at Calhoun Forest. Duke Forest is located in Durham, North Carolina (NC), and the long-term mean annual

temperature and precipitation (PREC) at Duke Forest are 15.5 °C and 1145 mm, respectively [*C. et al.*, 2006]. According to the GPS location, Duke Forest is also very close to Chapel Hill, NC. Calhoun Forest is location in Union, South Carolina (SC), and the long-term mean annual temperature and PREC at Calhoun Forest is 16 °C and 1180 mm, respectively [*Coughlan et al.*, 2017]. The climate conditions at Duke Forest and Calhoun Forest are similar.

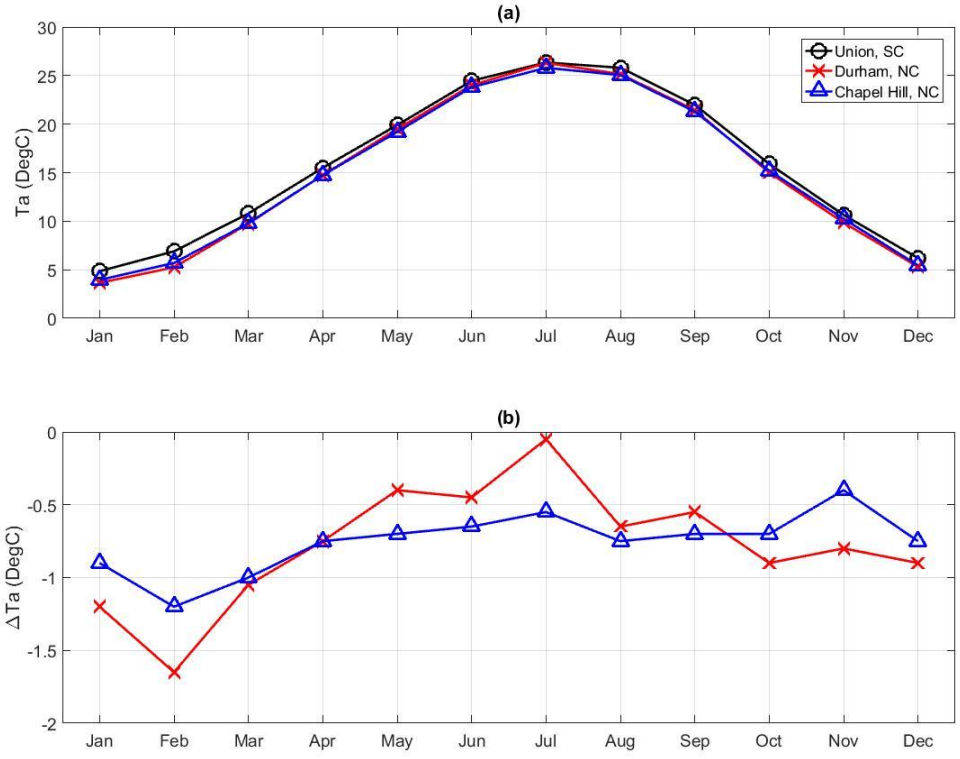

Figure 5.1 (a) Historic monthly mean and (b) absolute changes of Ta at Union, SC Durham, NC, and Chapel Hill, NC

The long-term monthly mean climate conditions at Union, Durham, and Chapel Hill are also investigated. Figures 5.1 and 5.2 show the historic monthly mean and absolute change of air temperature (Ta) and PREC at Union, Durham, and Chapel Hill. The monthly mean

values at Union, SC and Chapel Hill, NC are calculated using data from 1981 to 2010, and those at Durham, NC are calculated using data from 1961 to 1990 (www.usclimatedata.com). The monthly mean Ta and PREC at these three locations are comparable; the differences of Ta and PREC are no greater than 2 °C and 50 mm. The average Ta and PREC at Union, Durham, and Chapel Hill are 15.75 °C and 1181 mm, 15 °C and 1211 mm, and 15 °C and 1203 mm, respectively. The climates at Duke Forest and Calhoun Forest are almost identical, and the SFT method has been proved reliable using similar yet distant (> 2000 km) ecosystems [*Lester et al.*, 2014], and thus Duke Forest site could be a substitute of the pre-agricultural ecosystem before cultivation in the 1800s at Calhoun Forest.

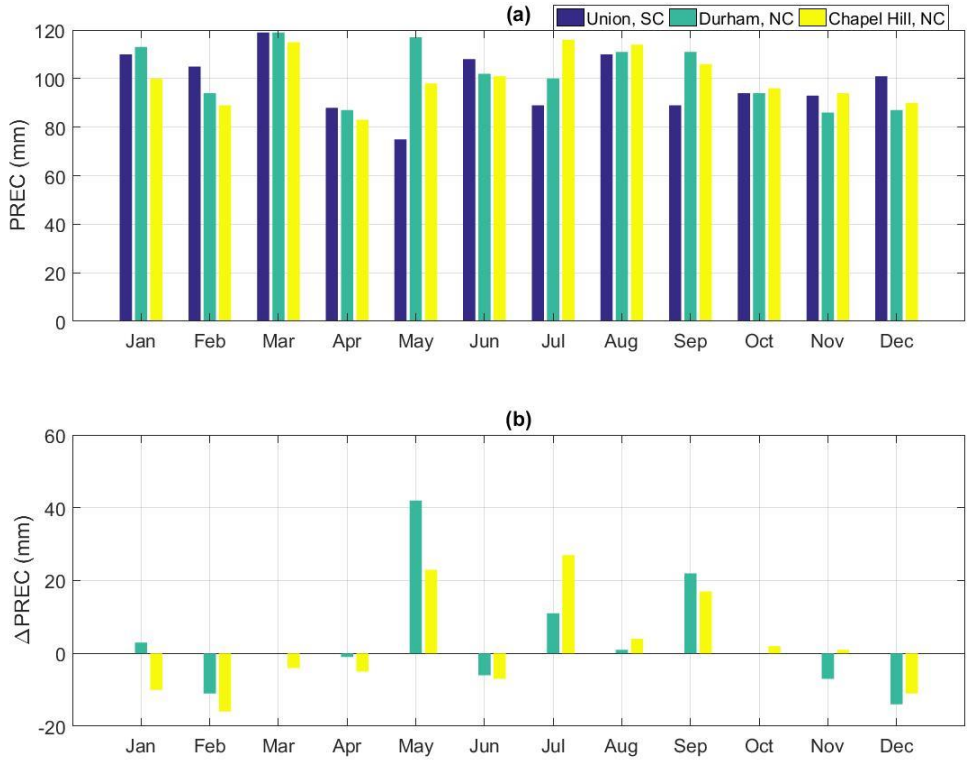

Figure 5.2 (a) Historic monthly mean and (b) absolute changes of PREC at Union, SC Durham, NC, and Chapel Hill, NC

Cropland site (CLS) at CCZ is regarded as the agricultural ecosystem from the 1800s to the early 1900s. Above-canopy flux tower site (ACS) in the young pine forest at CCZ is regarded as the post-agricultural ecosystem. By comparing the field observations and the modeling results of the eco-hydro-meteorological variables at the pre-agricultural ecosystem (DFS), agricultural ecosystem (CLS), and the post-agricultural ecosystem (ACS), the evolution of the energy, water, and carbon cycle due to land-use change at CCZ is investigated.

5.2.2 Methods to Quantify the Evolution

The eco-hydro-meteorological variables used to study the evolution are categorized into four groups:

- Group 1: air and soil temperature to study the evolution of temperature.
- Group 2: net radiation, sensible and soil heat fluxes to study the evolution of the energy cycle.
- Group 3: humidity, soil moisture, and evapotranspiration to study the evolution of the water cycle.
- Group 4: CO_2 concentration, CO_2 flux, and water use efficiency to study the evolution of the carbon cycle.

Long-term mean, monthly mean, and mean diurnal cycles (MDC) of these variables among different ecosystems are used to investigate the evolution at long-term, seasonal, and sub-daily scales, respectively. The long-term mean of a variable includes the growing seasonal

(GS) and annual mean (AM) values. The growing season for corn at CCZ is from March to August (spring and summer, six months) [*USDA*, 2010], and the dormant season is from September to February (fall and winter, six month). As there are gaps in the data due to power outage, rain events, sensor damage and malfunction among other reasons, the long-term mean is calculated from the long-term MDCs assuming the data-gaps are filled with long-term mean values at sub-daily scale.

The impact of land-use change on microclimate at seasonal scale is investigated from two perspectives: firstly, if land-use change alters the seasonal cycle of a climate condition; secondly, if land-use change alters the climate condition differently in different seasons. The seasonal cycle including the phase and the amplitude is evaluated using the monthly mean, which is calculated from the monthly MDC. The amplitude, the maximum minus minimum monthly mean, is used to estimate the strength of a seasonal cycle.

The impact of land-use change on microclimate at sub-daily scale is investigated also from two perspectives: firstly, if land-use change alters the diurnal cycle of a climate condition; secondly, if land-use change alters the climate condition differently at sub-daily scale. A diurnal cycle is any pattern that recurs every 24 hours as a result of one full rotation of the Earth around its own axis. In climatology, the diurnal cycle is one of the most basic forms of climate patterns. As an essential characteristic of a diurnal cycle, the amplitude is calculated as the maximum minus the minimum at sub-daily scale.

The absolute and relative changes of a variable due to land-use change are calculated according to the chronological order of the ecosystems such as the pre-agricultural ecosystem, agricultural ecosystem, and the post-agricultural ecosystem as in Eq. 5.1

$$\begin{cases} \Delta V(\boldsymbol{Unit}) = \boldsymbol{V_B - V_A} \\ \Delta V(\%) = \frac{\Delta V(\boldsymbol{Unit})}{\boldsymbol{V_A}} \end{cases} \quad \textbf{5.1}$$

where V_A and V_B are any variables at ecosystems A and B, respectively. According to the chronological order, B is a more recent ecosystem than A. *Unit* is the same unit of the variable V. With the methods in this section, the eco-hydro-meteorological variables at the pre-agricultural (DFS), the agricultural (CLS), and the post-agricultural (ACS) ecosystems are quantified and plotted in black, red, and blue, respectively.

5.3 Evolution of Temperature

Temperature is the most commonly measured weather parameter. In this section, the evolution of air and soil temperatures due to land-use change at CCZ is investigated using field observations at DFS, CLS, and ACS.

Table 5.1 Long-term mean air and soil temperatures

Period	Variables	Unit	DFS	CLS	ACS
GS	Ta	℃	19.43	21.57	20.77
	Ts	℃	19.38	23.06	20.21
	Ts@30cm	℃	NA	22.15	19.55
AM	Ta	℃	15.30	NA	16.87
	Ts	℃	15.52	20.71	16.35
	Ts@30cm	℃	NA	19.74	16.51

5.3.1 Air Temperature

Air temperature (Ta) affects the growth and reproduction of plants and animals, with warmer temperatures promoting biological growth. Ta also affects nearly all weather parameters such as relative humidity and evapotranspiration. The long-term trend, diurnal and seasonal variations of Ta at different ecosystems are analysed using the long-term

mean, monthly mean, and MDCs of Ta observed at DFS, CLS, and ACS. Figure 5.3 shows the long-term mean Ta. The annual mean Ta at CLS is not available as Ta at CLS is measured less than one year. The long-term mean Ta are also summarized in Table 5.1. Figure 5.4 shows the monthly mean Ta at DFS, CLS, and ACS. Figure 5.6 shows the long-term MDCs of Ta at DFS, CLS, and ACS. The absolute and relative changes in Figures 5.3, 5.4, and 5.6 are calculated respect to DFS.

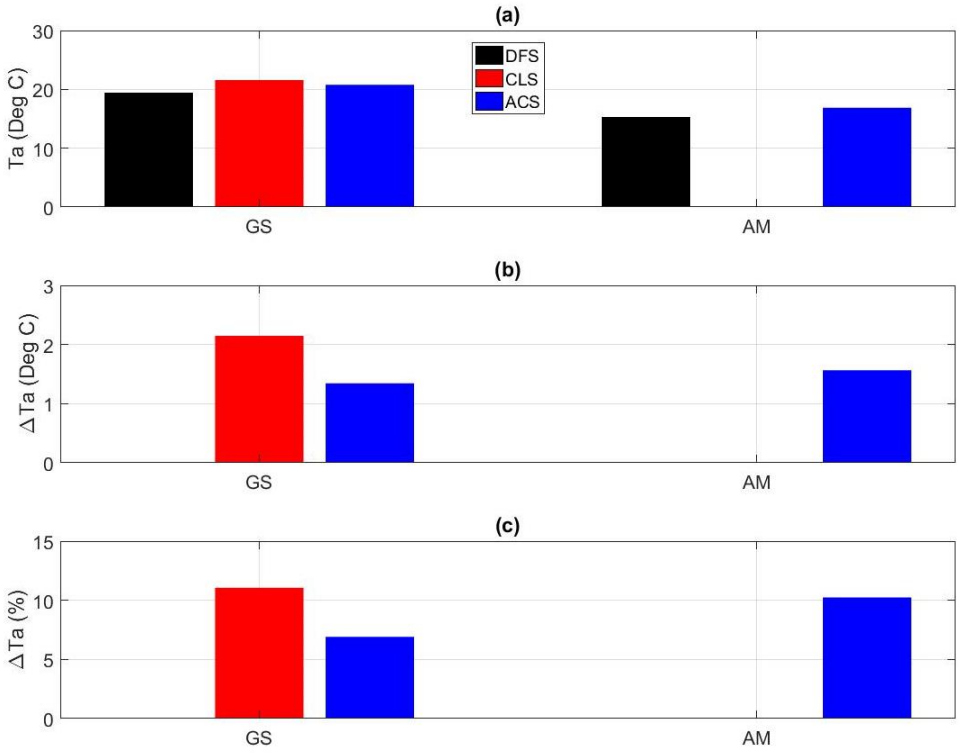

Figure 5.3 (a) Growing seasonal and annual mean, (b) absolute and (c) relative changes of Ta at DFS, CLS, and ACS

Figure 5.3 (a) shows the growing seasonal and annual mean of Ta at DFS, CLS, and ACS. During the growing season, the mean Ta at DFS, CLS, and ACS are 19.43 °C, 21.57 °C, and 20.77 °C, respectively. Ta at CLS is 2.14 °C (11 %) higher than that at DFS. Ta at ACS is 0.8 °C (4 %) lower than that at CLS, and 1.34 °C (7 %) higher than that at DFS.

Deforestation increases Ta by 2.14 °C and reforestation decreases Ta by 0.8 °C. The impact of deforestation on Ta is 1.7 times stronger than that of reforestation. The annual mean Ta at DFS and ACS are 15.30 °C and 16.87 °C, and the annual mean Ta at ACS is 1.57 °C (10 %) higher than that at DFS. Although the real differences of Ta between DFS and the other two sites might be overestimated given Ta at Calhoun Forest is generally 0.5 to 1 °C higher than Ta at Duke Forest, the 2.14 °C and 1.57 °C differences can not be neglected. The probable explanation of these differences is that deforestation increases Ta. Results also indicate that Ta at the post-agricultural ecosystem is higher than that at the pre-agricultural ecosystem.

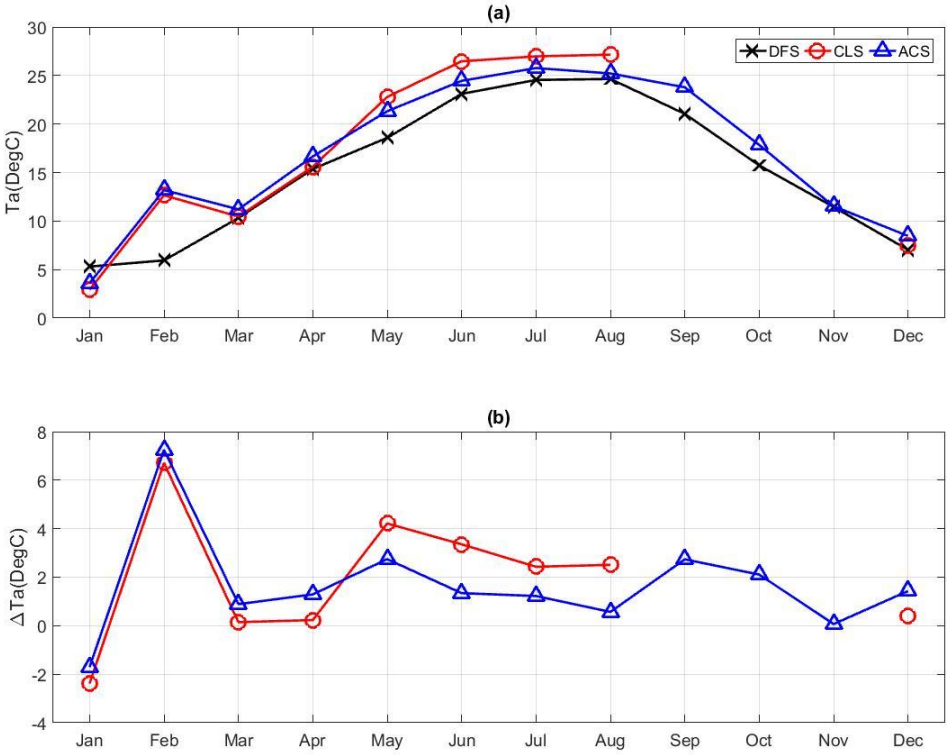

Figure 5.4 (a) Monthly mean and (b) absolute changes of Ta at DFS, CLS, and ACS

Figure 5.4 (a) shows the monthly mean Ta at DFS, CLS, and ACS. The maximum (minimum) monthly mean Ta at DFS, CLS, and ACS are in August (January), August (January), and July (January), respectively. The phases of the seasonal cycles of Ta are almost the same. The maxima (minima) of monthly mean Ta at DFS, CLS, and ACS are 24.64 (5.3) °C, 27.15 (2.92) °C, and 25.77 (3.6) °C, respectively. The seasonal amplitudes of Ta at DFS, CLS, and ACS are 19.34 °C, 24.23 °C, and 22.17 °C, respectively. Deforestation increases the seasonal variation of Ta and reforestation decreases it.

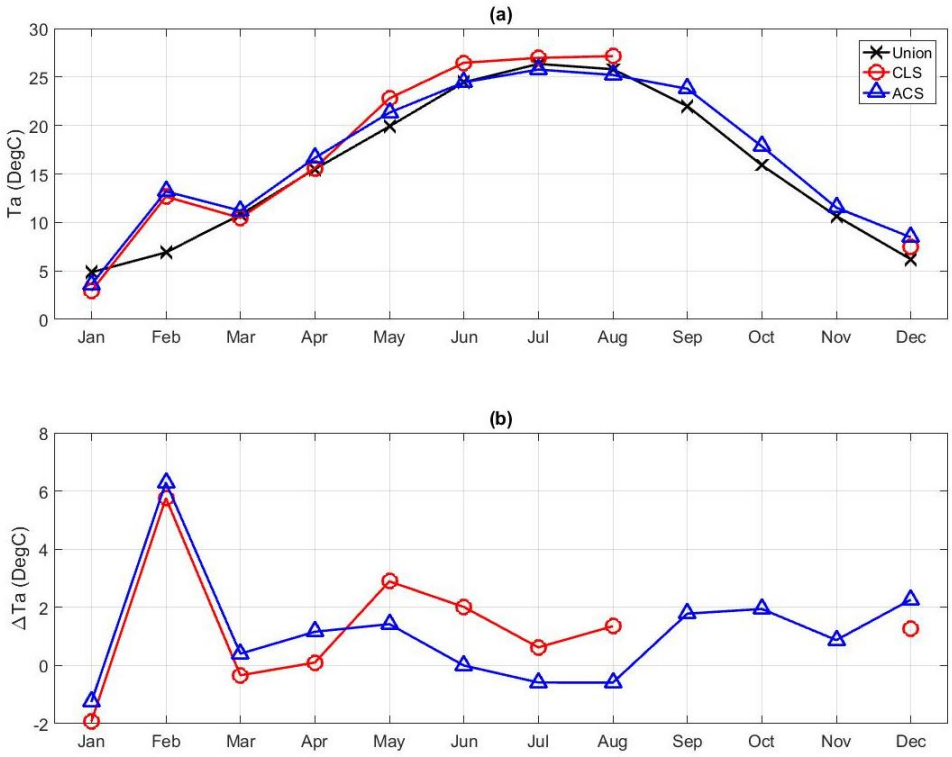

Figure 5.5 (a) Monthly mean, and (b) absolute change of Ta at Union, CLS, and ACS

Figure 5.4 (b) shows the absolute changes of Ta at CLS and ACS respect to DFS. ΔTa at CLS is negative in January and positive in other months, implying deforestation decreases the minimum monthly Ta and increases the maximum one. ΔTa at CLS is greater in

summer than in winter, implying that land-use change alters Ta more in summer than in winter. ΔTa at ACS is greater in winter and smaller in summer than that at CLS, implying that reforestation increases the minimum monthly Ta and decreases the maximum one. Therefore, at seasonal scale, deforestation increases the maximum and diurnal variation of monthly mean Ta, and decreases the minimum one; reforestation alters monthly mean Ta oppositely.

The monthly mean Ta in February at CLS and ACS are much greater than that in DFS. Figure 5.5 shows the monthly mean Ta at CLS and ACS comparing with the historic monthly mean Ta at Union, SC. The monthly mean Ta in February measured at CLS and ACS in 2018 are much higher than the historic average Ta in February at Calhoun, SC. Therefore, the large difference of Ta in February is not caused by land-use change, but by abnormal weather event with high air temperature in February 2018.

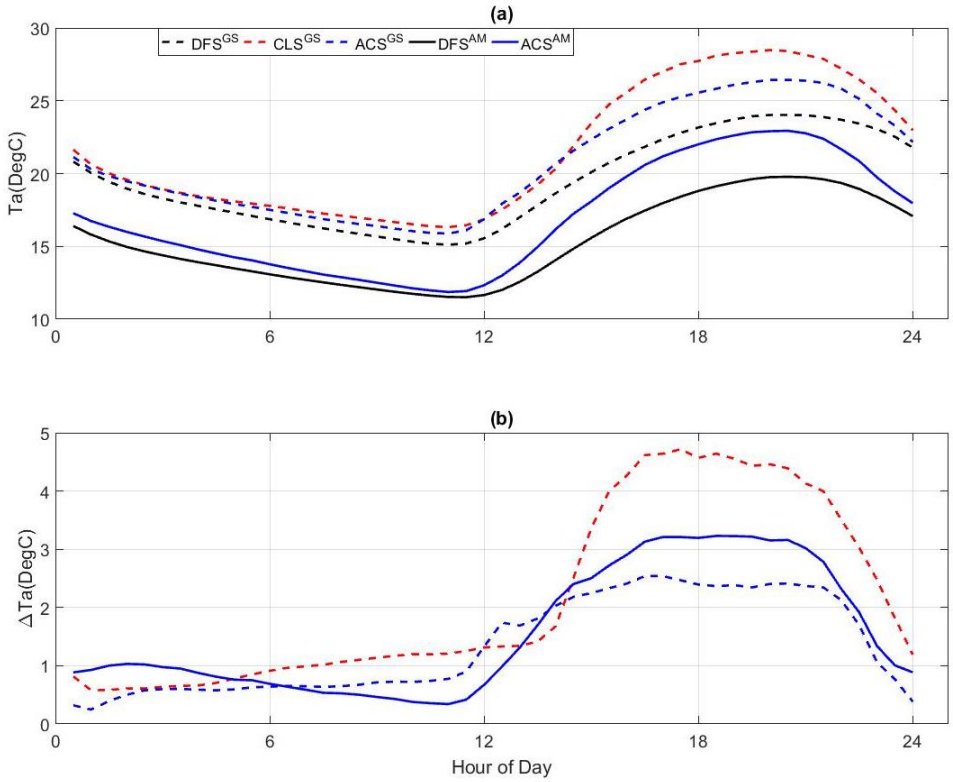

Figure 5.6 (a) Growing seasonal and annual MDCs, and (b) absolute changes of Ta at DFS, CLS, and ACS

Figure 5.6 (a) shows the growing seasonal and annual mean MDCs of Ta at DFS, CLS, and ACS. Ta is lowest in the early mornings and highest in the afternoon. The phases of the diurnal cycles of Ta at DFS, CLS, and ACS are almost identical. During the growing season, the maxima (minima) of Ta at DFS, CLS, and ACS are 24.02 (15.11) ℃, 28.48 (16.32) ℃, and 26.43 (15.88) ℃, respectively. The diurnal amplitudes of Ta at DFS, CLS, and ACS are 8.91 ℃, 12.16 ℃, and 10.55 ℃, respectively. Deforestation increases the diurnal variation of Ta and reforestation decreases it.

Figure 5.6 (b) shows the growing seasonal and annual MDCs of ΔTa. ΔTa at CLS is always greater than zero, implying that deforestation generally increases Ta at sub-daily scale

including the maximum and minimum Ta. ΔTa at CLS during the daytime is much greater than that during the nighttime, implying that deforestation alters daytime Ta more than nighttime Ta. ΔTa at ACS is almost always smaller than that at CLS, implying that reforestation generally decreases Ta at sub-daily scale including the maximum and minimum Ta. The difference of ΔTa between CLS and ACS is greater during the daytime than during the nighttime, implying that reforestation also alters daytime Ta more than nighttime Ta. Therefore, at sub-daily scale, deforestation increases the maximum, minimum and diurnal variation of Ta, and reforestation decreases them.

The analysis of Ta among different ecosystems results in the following findings:

(1) At long-term, deforestation increases Ta and reforestation decreases it. The change of Ta due to deforestation is 1.7 times greater than that due to reforestation. Ta in the post-agricultural ecosystem is greater than that at the pre-agricultural ecosystem.

(2) At seasonal scale, deforestation increases the maximum monthly mean and the seasonal variation of Ta, and decreases the minimum monthly mean Ta. Reforestation influences Ta oppositely. Land-use change alters Ta more significantly during summer than during winter.

(3) At sub-daily scale, deforestation increases daily maximum and minimum, and the diurnal variation of Ta, and reforestation decreases them. Land-use change alters daytime Ta more significantly than nighttime Ta.

5.3.2 Soil Temperature

Soil temperature is an important factor that drives germination, blooming, composting, soil respiration, and a variety of other processes. Soil temperature measured at surface and 30 cm depth are used in this subsection. Surface soil temperature (Ts) is measured at about 5 cm in depth at DFS, CLS, and ACS. Figure 5.7 shows the long-term mean and changes of Ts at DFS, CLS, and ACS. The long-term mean Ts are summarized in Table 5.1. Figure 5.8 shows the monthly mean Ts at DFS, CLS, and ACS. Figure 5.9 shows the growing seasonal and annual MDCs of Ts at DFS, CLS, and ACS.

Figure 5.7 (a) shows the growing seasonal and annual mean Ts at DFS, CLS, and ACS. During the growing season, the mean Ts at DFS, CLS, and ACS are 19.38 ℃, 23.06 ℃, and 20.21 ℃, respectively. Ts at CLS is 3.69 ℃ (19 %) higher than that at DFS. Ts at ACS is 2.86 ℃ (12 %) lower than that at CLS, and 0.83 ℃ (4 %) higher than that at DFS. The annual mean Ts at DFS, CLS, and ACS are 15.52 ℃, 20.71 ℃, and 16.35 ℃, respectively. The annual mean Ts at CLS is 5.19 ℃ (33 %) higher than that at DFS. The annual mean Ts at ACS is 4.37 ℃ (21 %) lower than that at CLS, and 0.83 ℃ (5 %) higher than that at DFS. Deforestation increases long-term mean Ts by 5.19 ℃ and reforestation decreases it by 4.37 ℃. The impact of deforestation on Ts is 1.19 times as large as that of reforestation. The long-term mean Ts at DFS and ACS are comparable, implying that both deforestation and reforestation alters Ts rapidly. The differences of the growing seasonal mean Ts among different ecosystems are smaller than those of the annual ones, implying that land-use change alters Ts more in the dormant season than in the growing season. ΔTs between DFS and CLS, and CLS and ACS are greater than ΔTa, indicating land-use change alters Ts more than Ta.

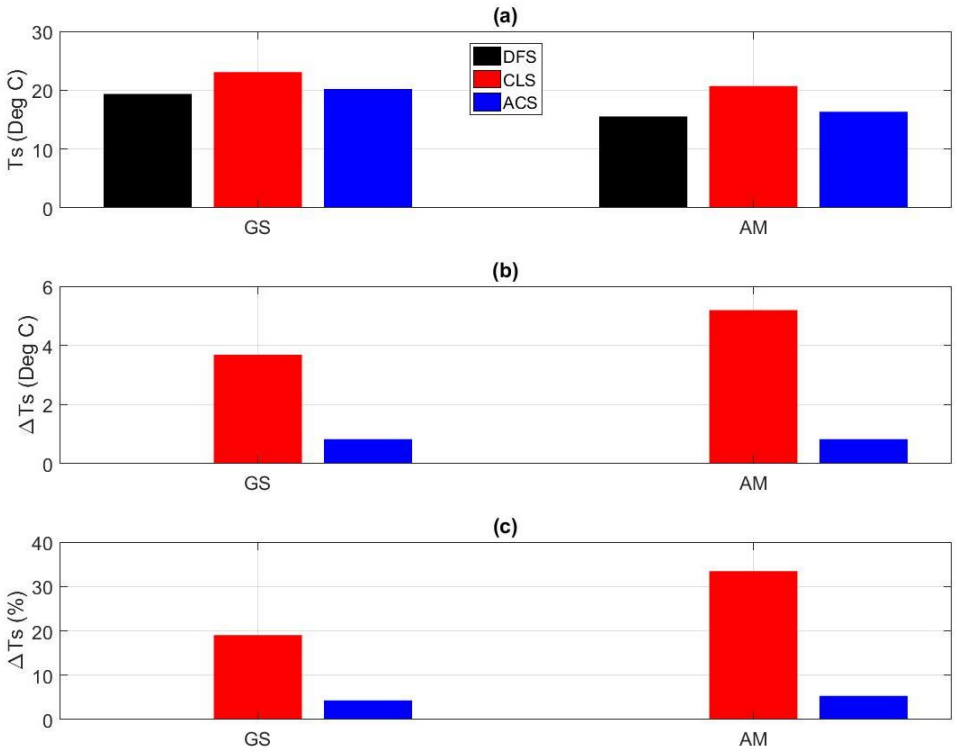

Figure 5.7 (a) Growing seasonal and annual mean, (b) absolute and (c) relative changes of Ts at DFS, CLS, and ACS

Figure 5.8 (a) shows the monthly mean Ts at DFS, CLS, and ACS. Ts at DFS, CLS, and ACS reach to maxima (minima) in July (January), June (January), and July (January), respectively, implying that there is no obvious phase shift in the seasonal cycles. The maxima (minima) of monthly mean Ts at DFS, CLS, and ACS are 24.74 (6.23) °C, 28.15 (5.52) °C, and 25.25 (6.43) °C, respectively. The seasonal amplitudes of monthly mean Ts at DFS, CLS, and ACS are 18.51 °C, 22.63 °C, and 18.85 °C, respectively. Deforestation increases the seasonal variation of Ts and reforestation decreases it.

Figure 5.8 (b) shows the absolute changes of Ts at DFS, CLS, and ACS. ΔTs between CLS and the other two ecosystems are greater during the summer than during the winter. Land-use change alters Ts more significantly during the summer than during the winter. ΔTs

between DFS and ACS is mostly within 2 °C, implying that Ts at pre- and post-agricultural are comparable. The large ΔTs in February is due to the abnormal weather in February 2018.

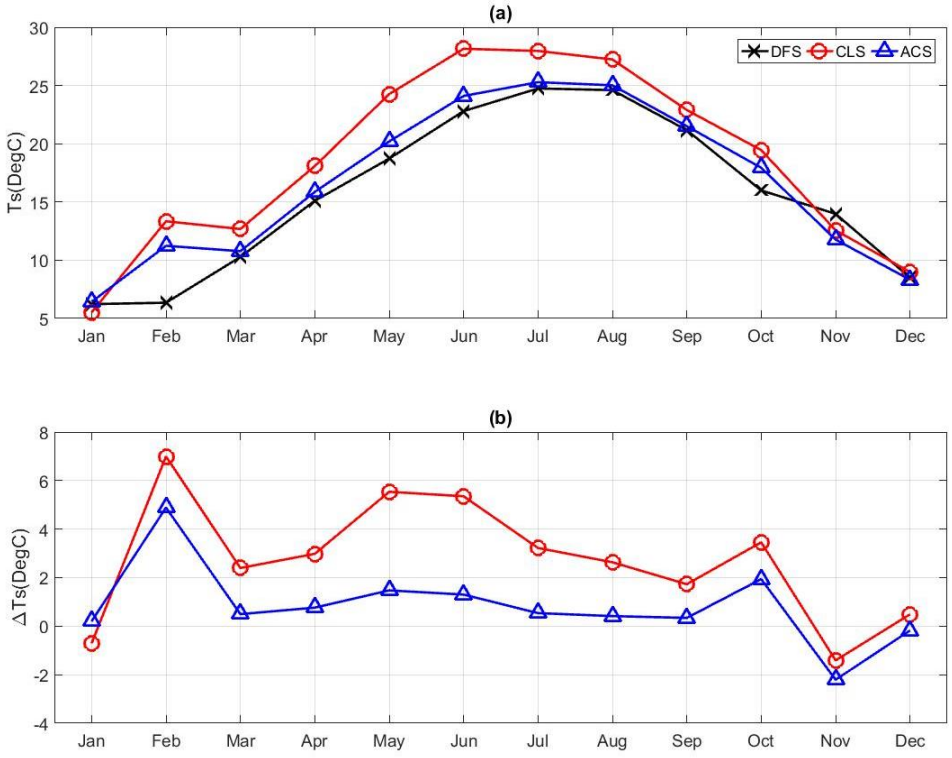

Figure 5.8 (a) Monthly mean, and (b) absolute changes of Ts at DFS, CLS, and ACS

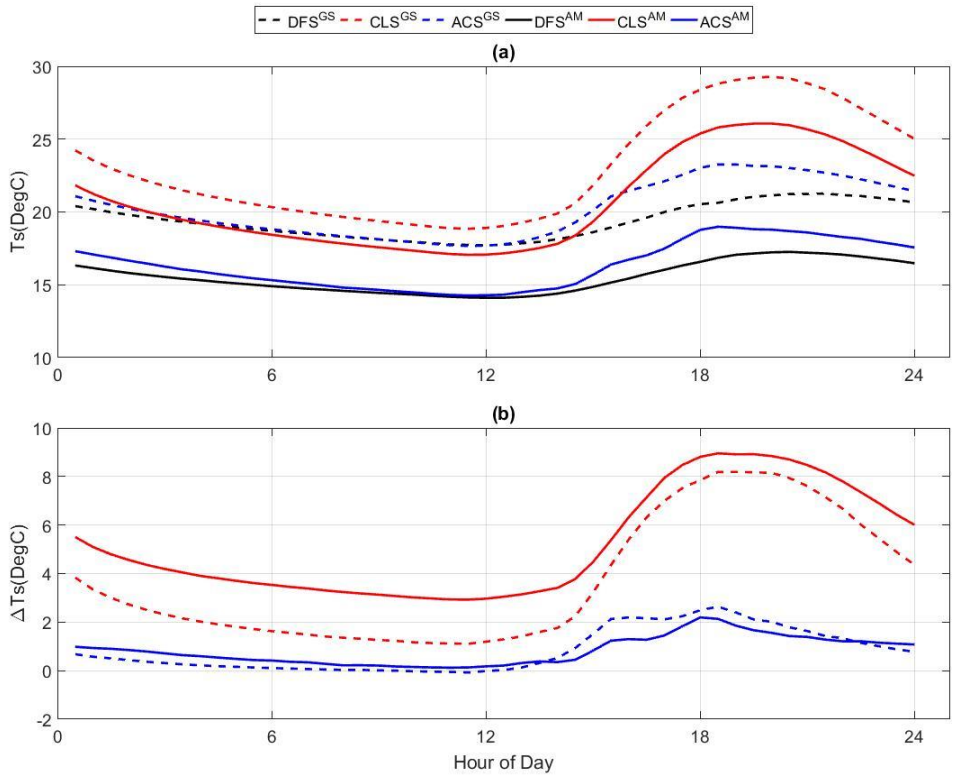

Figure 5.9 (a) Growing seasonal and annual MDCs, and (b) absolute changes of Ts at DFS, CLS, and ACS

Figure 5.9 (a) shows the growing seasonal and annual MDCs of Ts at DFS, CLS, and ACS. The dash lines are the growing seasonal MDCs and the solid lines are the annual mean MDCs. The diurnal variation of Ts is weakest at DFS and strongest at CLS. During the growing season, the maxima (minima) of sub-daily Ts at DFS, CLS, and ACS are 21.26 (17.7) °C, 29.28 (18.85) °C, and 23.26 (17.66) °C, respectively. The diurnal amplitudes of Ts at DFS, CLS, and ACS are 3.56 °C, 10.43 °C, and 5.60 °C, respectively. Deforestation significantly increases the diurnal variation of Ts and reforestation decreases it rapidly. At annual scale, the maxima (minima) of sub-daily Ts at DFS, CLS, and ACS are 17.26 (14.11) °C, 26.07 (17.06) °C, and 18.98 (14.26) °C, respectively. The daily amplitudes of

sub-daily Ts at DFS, CLS, and ACS are 3.15 ℃, 9.01 ℃, and 4.72 ℃, respectively. The differences of the diurnal variations of Ts during growing season is greater than those throughout the year, indicating that the land-use change alters the diurnal variation more during the growing season than during the dormant season.

Figure 5.9 (b) shows ΔTs at sub-daily scale at DFS, CLS, and ACS. ΔTs between CLS and DFS is always positive and that between ACS and CLS is always negative. Deforestation increases both maximum and minimum Ts, and reforestation decreases them. ΔTs are much greater during the daytime than during the nighttime, implying that land-use change alters daytime Ts much more than nighttime Ts.

Soil temperature at 30 cm (Ts@30cm) at CLS and ACS are compared to investigate the soil depth that land-use change could influence. Figure 5.10 shows the long term mean Ts@30cm at CLS and ACS. The long-term mean Ts@30cm are summarized in Table 5.1. Figure 5.11 shows the monthly mean Ts@30cm at CLS and ACS. Figure 5.12 shows the growing seasonal and annual MDCs of Ts@30cm at CLS and ACS. The absolute changes are calculated respect to Ts@30cm at CLS.

Figure 5.10 (a) shows the growing seasonal and annual mean Ts@30cm at CLS and ACS. During the growing season, the mean Ts@30cm at CLS and ACS are 22.15 ℃ and 19.55 ℃, respectively. The mean Ts@30cm at ACS is 2.6 ℃ (12%) smaller than that at CLS. The difference of Ts between CLS and ACS at surface is 0.2 ℃ greater than that at 30 cm. The annual mean Ts@30cm at CLS and ACS are 19.74 ℃ and 16.51 ℃, respectively. The annual mean Ts@30cm at ACS is 3.23 ℃ (16%) smaller than that at CLS. The difference of the annual mean Ts between CLS and ACS at surface is 1.14 ℃ greater than that at 30

cm. Reforestation decreases Ts@30cm, and the influence is stronger during the dormant season than the growing season. The impact of land-use change on soil temperature decreases more rapidly through depth during the dormant season than during the growing season.

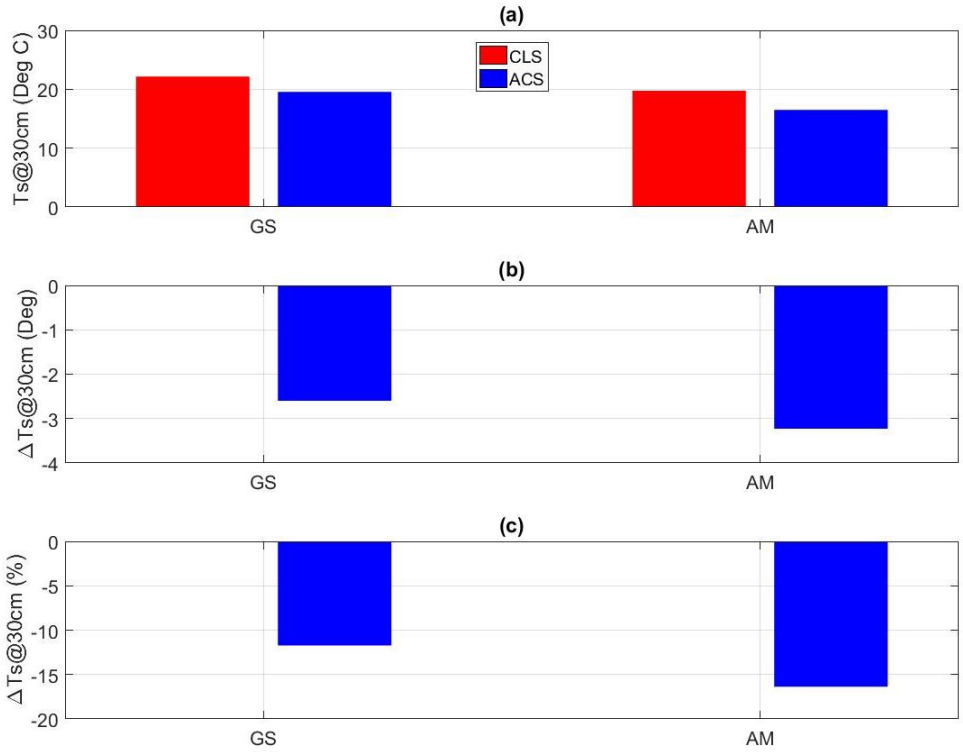

Figure 5.10 (a) Growing seasonal and annual mean, (b) absolute and (c) relative changes of Ts@30cm at CLS, and ACS

Figure 5.11 (a) shows the monthly mean Ts@30cm at CLS and ACS. Monthly mean Ts@30cm at both CLS and ACS reach to maximum (minimum) in July (January). The phases of the seasonal cycles of Ts@30cm at CLS and ACS are identical. Monthly mean Ts@30cm at CLS and ACS from November to January are almost identical, while Ts@30cm at ACS is smaller than that at CLS for other months, implying that reforestation alters Ts@30cm more severely during the summer than during the winter. The maximum

(minimum) Ts@30cm at CLS and ACS are 26.8 (7.71) °C and 24.45 (7.43) °C, respectively. The seasonal amplitudes of Ts@30cm at CLS and ACS are 19.09 °C and 17.01 °C, respectively, indicating that reforestation decreases the seasonal variation of Ts@30cm. ΔTs@30cm is much greater during the summer than during the winter (Figure 5.11 (b)), further implying that the reforestation alters Ts@30cm more in summer than in winter.

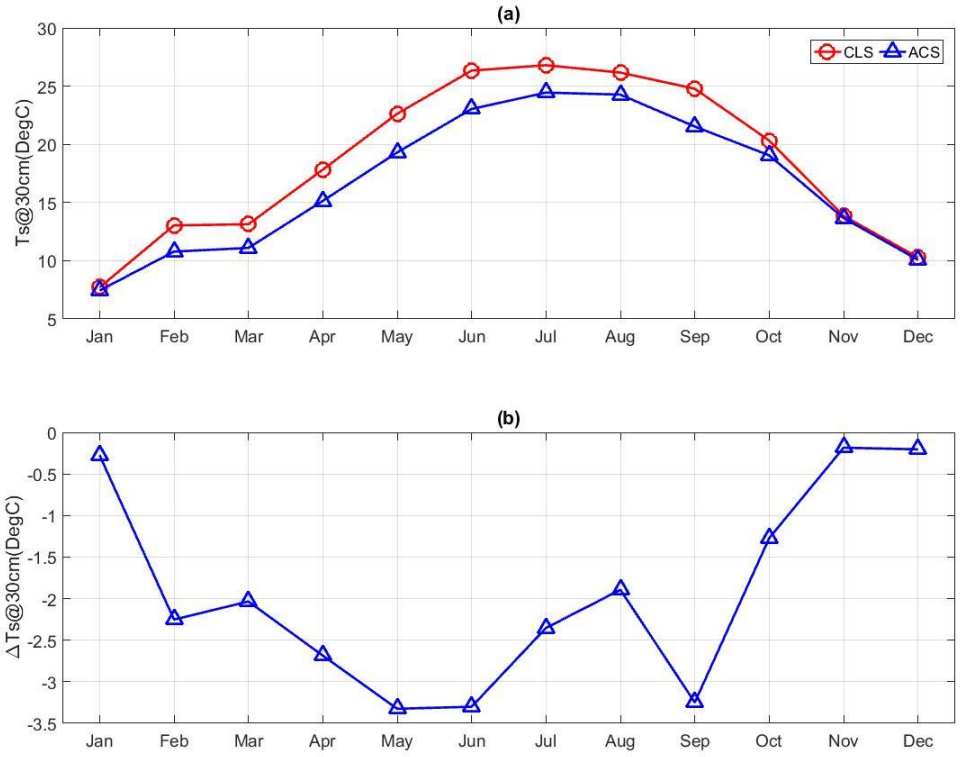

Figure 5.11 (a) Monthly mean, and (b) absolute changes of Ts@30cm at CLS and ACS

Figure 5.12 (a) shows the growing seasonal and annual MDCs of Ts@30cm at CLS and ACS. During the growing season, the maxima (minima) of Ts@30cm at CLS and ACS are 22.94 (21.37) °C and 19.93 (19.10) °C, respectively. The diurnal amplitudes of Ts@30cm

at CLS and ACS are 1.57 °C and 0.83 °C, respectively, implying that reforestation decreases the diurnal variation of Ts@30cm. At annual scale, the maxima (minima) of sub-daily Ta@30cm at CLS and ACS are 20.36 (19.09) °C and 17.07 (15.87) °C, respectively. The mean diurnal amplitudes of Ta@30cm at CLS and ACS are 1.28 °C and 1.2 °C, respectively. Although Ts@30cm at ACS is smaller than that at CLS, the annual mean diurnal variations of Ts@30cm at CLS and ACS are almost identical, implying that at annual scale although reforestation decreases Ts@30cm, it does not alter the diurnal variation of Ts@30cm.

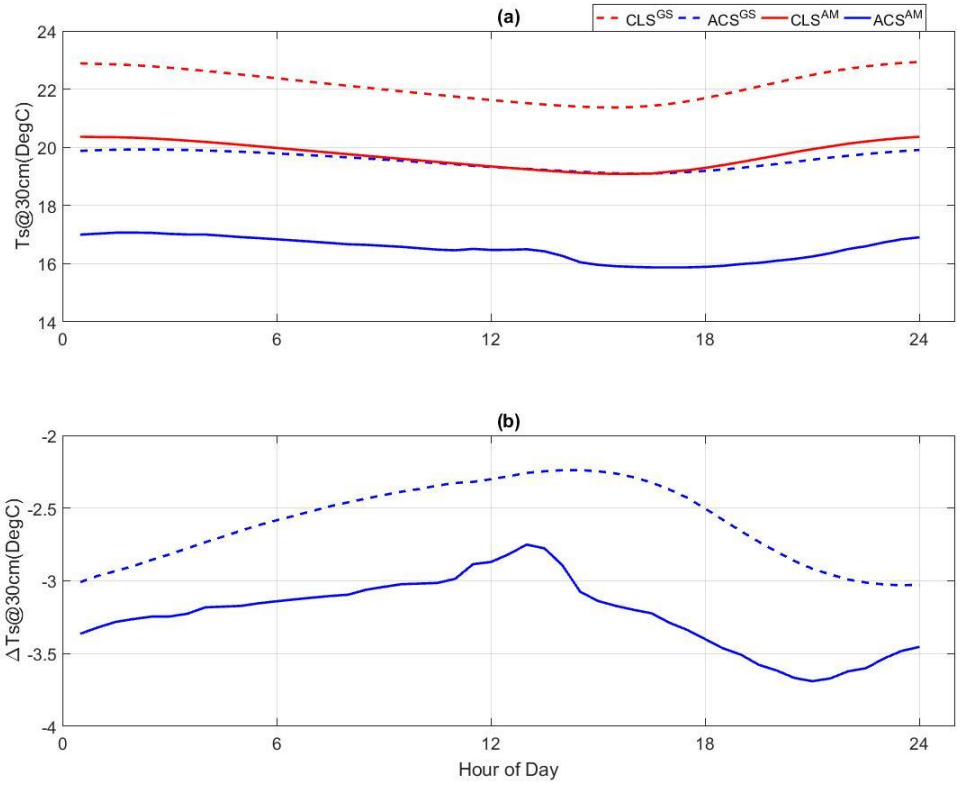

Figure 5.12 (a) Growing seasonal and annual MDCs, and (b) absolute changes of Ts@30cm at CLS and ACS

Figure 5.12 (b) shows the absolute changes of growing seasonal and annual MDCs of Ts@30cm at CLS and ACS. ΔTs@30cm is always negative, implying that reforestation decreases Ts@30cm at sub-daily scale. The magnitude ΔTs@30cm is small around noontime and large in the afternoon, implying that land-use change alters Ts@30cm more significantly in the afternoon than in the noontime and there is a phase shift of diurnal cycles of Ts at surface and at 30 cm. The magnitude of ΔTs@30cm of the annual MDCs is always greater than that of the growing seasonal MDCs, implying that land-use change alters Ts@30cm more significantly during the dormant season than during the growing season.

Analysis of Ts and Ts@30cm demonstrates the following key findings:

(1) At long-time scale, deforestation increases Ts significantly, and reforestation restores it effectively. The impact of land-use change on soil temperature penetrates to at least 30 cm depth.

(2) At seasonal scale, deforestation increases the maximum and the seasonal variation of monthly mean Ts, and decreases the minimum monthly Ts; and reforestation alters them oppositely. Land-use change alters Ts more significantly in summer than in winter.

(3) At sub-daily scale, deforestation increases both maximum, minimum, and the diurnal variations of Ts, and reforestation decreases them. Land-use change alters daytime Ts more than nighttime Ts. Reforestation does not change the diurnal variation of Ts@30cm at annual scale.

5.3.3 Conclusion

This section investigates the evolution of air and soil temperatures due to land-use change at CCZ using field observations at DFS, CLS, and ACS. The key findings are:

(1) At long-time scale, deforestation increases both Ta and Ts, and reforestation decreases them. Land-use change alters Ts more significantly than Ta. During the growing season, deforestation increases Ta and Ts by 2.14 °C and 3.69 °C, respectively; and reforestation decreases Ta and Ts by 0.8 °C and 2.86 °C, respectively.

(2) At seasonal scale, deforestation increases the monthly mean maxima and seasonal variations of Ta and Ts, and decreases the monthly mean minimum Ta and Ts; reforestation alters them oppositely. Land-use change alters Ta and Ts more significantly in summer than in winter.

(3) At sub-daily scale, deforestation increases diurnal maxima, minima, and variations of Ta and Ts; and reforestation decreases them. Land-use change alters daytime Ts and Ta more than nighttime ones.

5.4 Evolution of Energy Cycle

There are four types of energy fluxes at land surface, namely, the net radiation to or from the surface, the sensible and latent heat fluxes to or from the surface, and the soil heat fluxes into or out of the soil. This section discusses the evolution of net radiation, sensible and soil heat fluxes due to land-use change at CCZ. As an essential part in the water cycle, the latent heat flux is discussed in the next section.

Table 5.2 Mean values of variables related to the energy cycle

Period	Variables	Unit	DFS	CLS	ACS
GS	Rn	W m^{-2}	135.18	NA	170.79
	H	W m^{-2}	32.03	52.08	50.27
	G	W m^{-2}	1.98	32.71	4.87
AM	Rn	W m^{-2}	96.05	NA	123.78
	H	W m^{-2}	25.59	NA	40.47
	G	W m^{-2}	-0.61	NA	-0.11

5.4.1 Net Radiation

The net radiation (Rn) is a result of the radiation balance at the surface. During the daytime, Rn is usually dominated by the solar radiation and almost always directed toward the surface, while at night Rn is much weaker and directed away from the surface. As a result, the surface warms up during the daytime, while it cools during the nighttime, especially under clear sky and undisturbed weather conditions. Rn is measured at 40 m and 9 m above the ground at DFS and ACS, respectively. The net radiation is not measured at CLS due to safety concerns. Figure 5.13 shows the long-term mean Rn at DFS and ACS. The long-term mean Rn are summarized in Table 5.2. Figure 5.14 shows the monthly mean Rn at DFS and ACS. Figure 5.15 shows the growing seasonal and annual MDCs of Rn at DFS and ACS.

Figure 5.13 (a) shows the growing seasonal and annual mean Rn at DFS and ACS. During the growing season, the mean Rn at DFS and ACS are 135.18 W m^{-2} and 170.79 W m^{-2}, respectively. The mean Rn at ACS is 35.61 W m^{-2} (26 %) more than that at DFS. The annual mean Rn at DFS and ACS are 96.05 W m^{-2} and 123.78 W m^{-2}, respectively. The annual mean Rn at ACS is 27.73 W m^{-2} (29 %) more than that at DFS. The annual mean

ΔRn is smaller than the growing seasonal mean ΔRn, implying that land-use change alters Rn more significantly during the growing season than during the dormant season.

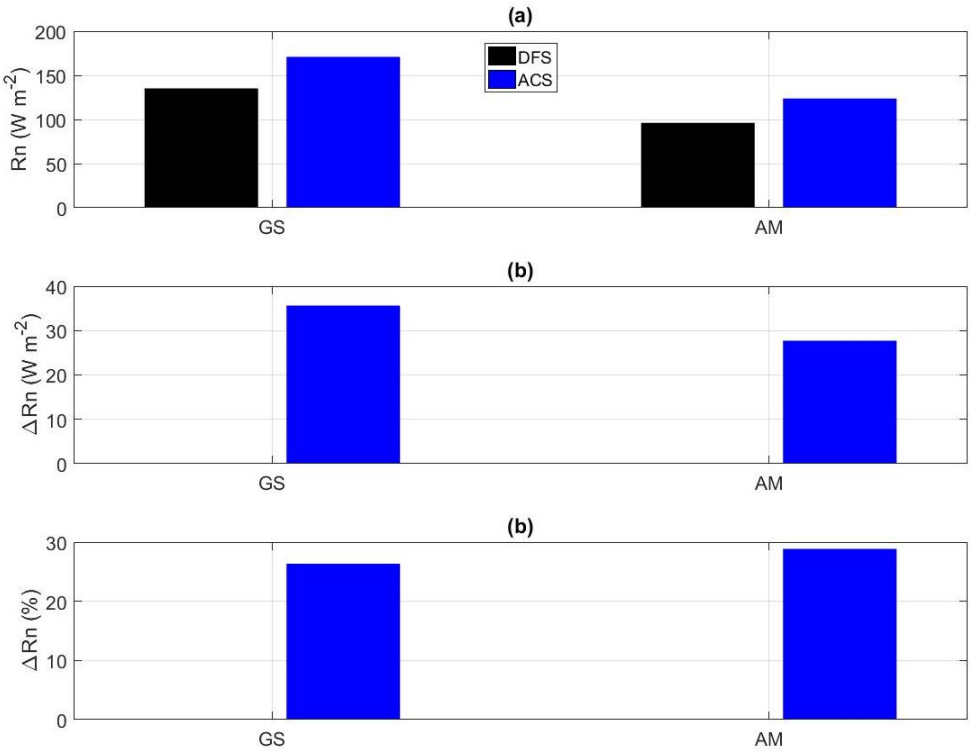

Figure 5.13 (a) Growing seasonal and annual mean, (b) absolute and (c) relative changes of Rn at DFS and ACS

Figure 5.14 (a) shows the monthly mean Rn at DFS and ACS. Rn reach to maxima (minima) at DFS and ACS in July (December) and (June), respectively. The phases of the seasonal cycles are almost identical. The maxima (minima) of Rn at DFS and ACS are 159.38 (27.09) W m^{-2} and 211.63 (22.16) W m^{-2}, respectively. The seasonal variations of Rn at DFS and ACS are 132.29 W m^{-2} and 189.47 W m^{-2}, respectively. Land-use change alters the seasonal variation of Rn. Figure 5.14 (b) shows the ΔRn of the monthly mean values at DFS and ACS. ΔRn is positive for all months except for January. Land-use change from boardleaf forest to needleleaf forest increases the maximum monthly mean Rn and

decreases the minimum one at the seasonal scale. The magnitude of ΔRn is greater during the summer than during the winter, implying that the impact of land-use change to Rn is greater during the summer than during the winter.

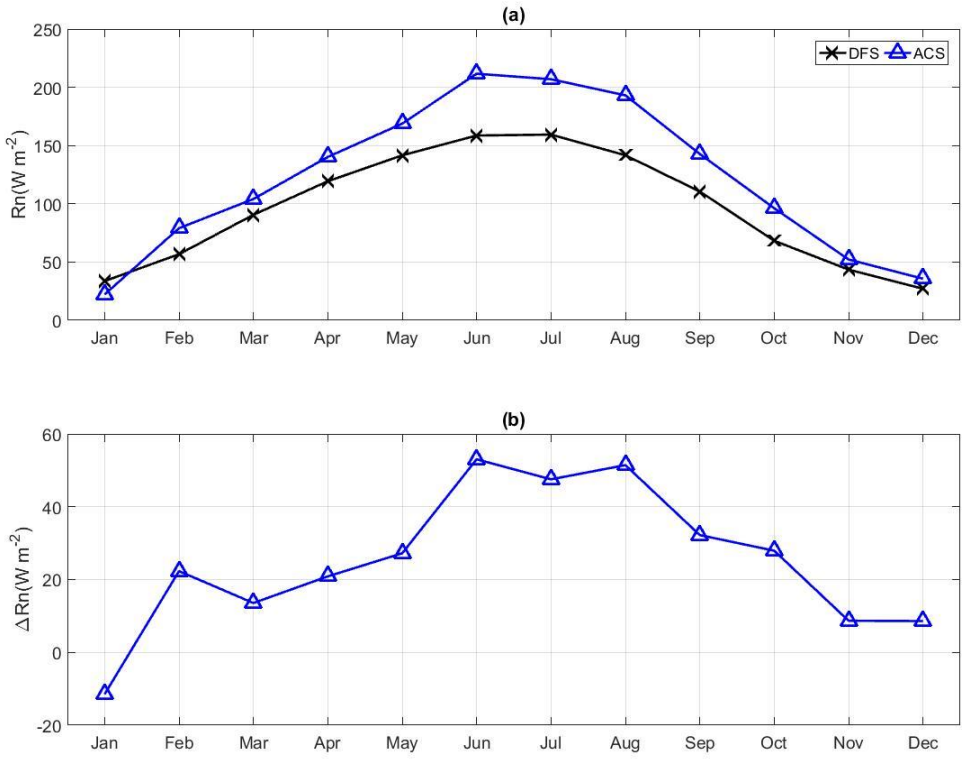

Figure 5.14 (a) Monthly mean, and (b) absolute changes of Rn at DFS and ACS

Figure 5.15 (a) shows the growing seasonal and annual MDCs of Rn at DFS and ACS. The phases of the diurnal cycles are the same. During the growing season, the maxima (minima) of sub-daily Rn at DFS and ACS are 530.8 (-53.85) W m^{-2} and 609.22 (-41.18) W m^{-2}, respectively. The diurnal variations of Rn at DFS and ACS are 584.65 W m^{-2} and 650.39, respectively W m^{-2}. The annual mean maxima (minima) of sub-daily Rn at DFS and ACS are 441.63 (-53.51) W m^{-2} and 513.98 (-47.01) W m^{-2}, respectively. The diurnal variations

of Rn at DFS and ACS are 495.15 W m^{-2} and 560.99, respectively W m^{-2}. Land-use change from pre-agricultural ecosystem to post-agricultural ecosystem increases the maximum, minimum, and diurnal variation of Rn. The growing seasonal mean ΔRn is slightly greater than the annual mean ΔRn, implying that the change of Rn is greater during the growing season than during the dormant season.

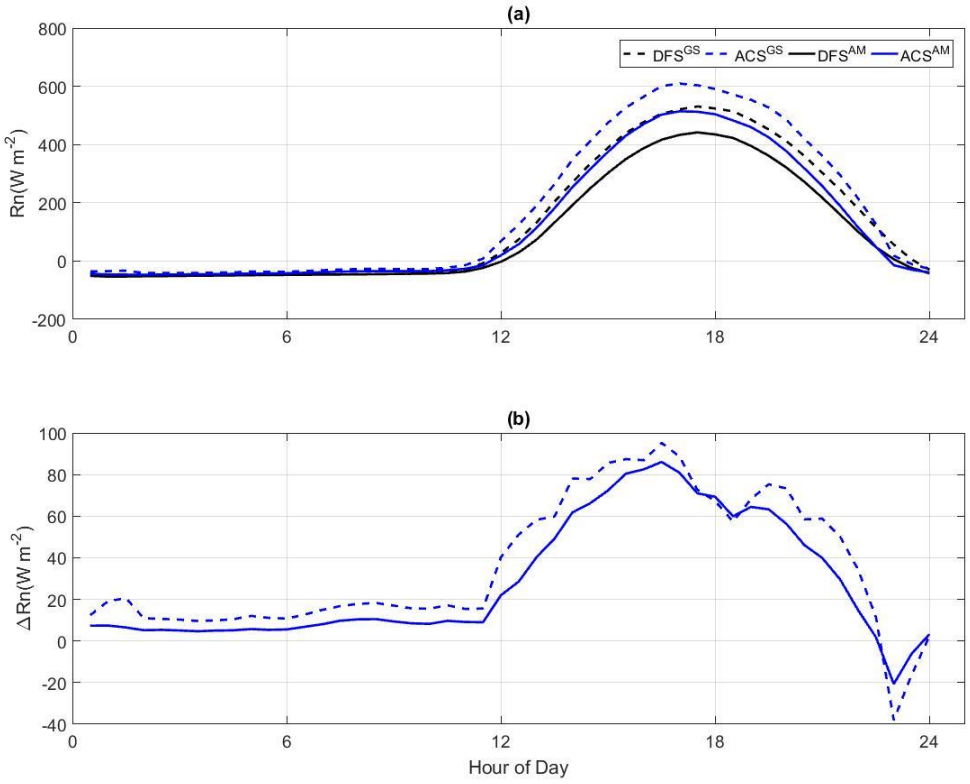

Figure 5.15 (a) Growing seasonal and annual MDCs, and (b) absolute changes of Rn at DFS and ACS

Rn at ACS is constantly greater than that at DFS. As DFS and ACS are about 200 miles apart. A theoretical analysis is conducted to check if the difference of Rn at the two locations is caused by difference in latitude. Locations of DFS and ACS are (36.0 °N, 79.1

°W) and (34.6 °N, 81.7 °W), respectively. The total solar energy reaching Earth surface for idealized case

$$I_0 = I_{sc} cos\theta_z \qquad 5.2$$

$$cos\theta_z = sin\delta sin\phi + cos\delta cos\phi cos\omega \qquad 5.3$$

where δ is the declination, meaning the hit-on latitude of the sun light depending on the day of year; ϕ is the latitude, ω is the hour angle, $\omega = 0$ at noon. δ can be calculated approximately from:

$$\delta = 2\pi \frac{23.45}{360} \cos\left[2\pi \frac{172 - D}{365}\right] \qquad 5.4$$

where D is the Julian day, and 172 is the summer solstice.

$$\phi = 2\pi \frac{latitude}{360} \qquad 5.5$$

The ratios of $cos\theta_z$ at ACS to that at DFS on summer solstice and on the first day of year are 1.0051 and 1.0052, respectively, and thus the annual mean ratio of $cos\theta_z$ at ACS to that at DFS is approximately 1.005, implying only a 0.5 % difference of Rn between DFS and ACS is due to the difference of locations. The theoretical analysis demonstrates that the 29 % difference of Rn between DFS and ACS is not due to the difference of locations.

The difference of Rn between DFS and ACS is likely caused by the difference of the albedo over different canopy types as the albedo of evergreen needle-leaf forests (Calhoun young pine forest) is smaller than that of mature deciduous broadleaf forests (Duke Forests) [*Leonardi et al.*, 2015]. It is evident that the difference of Rn at DFS and ACS is large during the day and small during the night as there is solar radiation during the day. Another

evidence is that the difference of Rn at DFS and ACS is large during the summer (when Duke Forest is full of leaves) and small during winter (when Duke Forest is without leaves).

Analysis of Rn at DFS and ACS results in the following findings:

(1) At annual scale, land-use change from the pre-agricultural ecosystem to the post-agricultural ecosystem increases Rn by 29 %.

(2) At seasonal scale, land-use change increases the maximum and the seasonal variation of Rn and decreases the minimum Rn. Land-use change alters Rn more in summer than in winter.

(3) At sub-daily scale, land-use change increase the maximum, minimum, and diurnal variation of Rn. Land-use change alters Rn more in daytime than in nighttime.

5.4.2 Sensible Heat Flux

Sensible heat flux (H) at the land surface arises as a result of the difference in the temperatures of the surface and the air above. H is usually directed away from the surface during the daytime when the surface is warmer than the air above, and vice versa during the nighttime. Therefore, H is opposite in direction with the average temperature gradient. H at DFS and ACS are mainly from EC measurements. Some of the data gaps are filled using the MEP model as described in Chapter 4. H at CLS is estimated using the MEP model with Rn at ACS, Ta and humidity at CLS. H at CLS is available during December to August as Ta and humidity at CLS were not measured until December 2017, and thus the annual mean H is not available. Figure 5.16 shows the long term mean H at DFS, CLS, and ACS. The long-term mean H are summarized in Table 5.2. Figure 5.17 shows the

monthly mean H at DFS, CLS, and ACS. Figure 5.18 shows the growing seasonal and annual MDCs of H at DFS, CLS, and ACS.

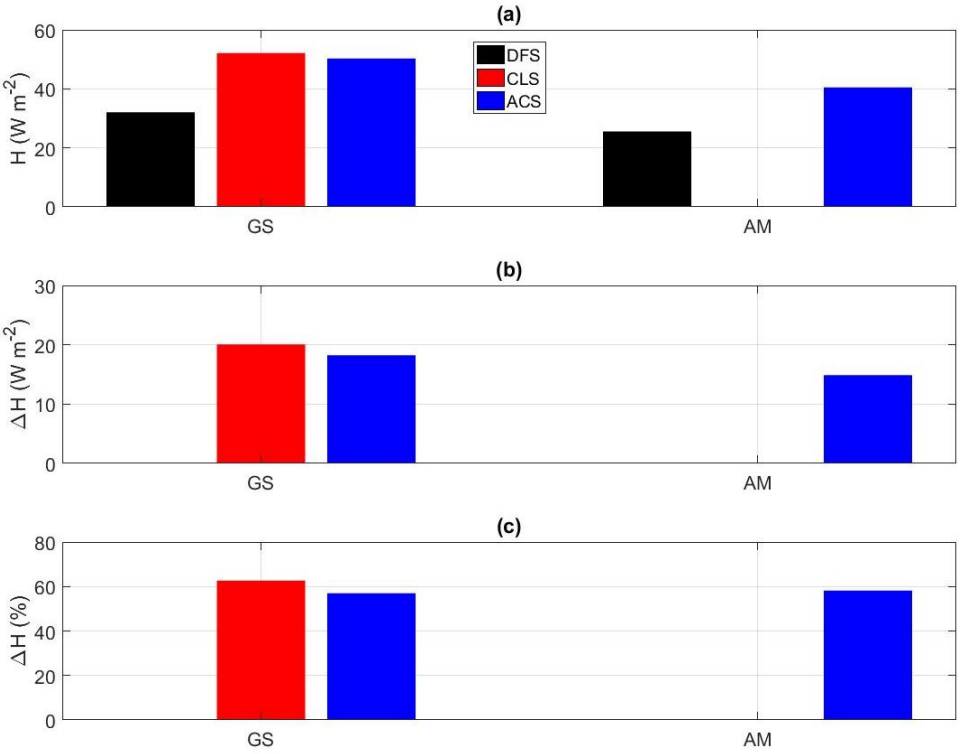

Figure 5.16 (a) Growing seasonal and annual mean, (b) absolute and (c) relative changes of H at DFS, CLS, and ACS

Figure 5.16 (a) shows the growing seasonal and annual mean H at DFS, CLS, and ACS. During growing season, the mean H at DFS, CLS, and ACS are 32.03 W m^{-2}, 52.08 W m^{-2}, and 50.27 W m^{-2}, respectively. The mean H at CLS is 20.05 W m^{-2} (63 %) more than that at DFS. The mean H at ACS is only 1.81 W m^{-2} (3 %) less than that at CLS, and 18.24 W m^{-2} (57 %) more than that at DFS. The annual mean H at DFS and ACS are 25.59 W m^{-2} and 40.47 W m^{-2}, respectively. The annual mean H at ACS is 14.88 W m^{-2} (58 %) more than that at DFS. H is greatest at CLS and smallest at DFS. Deforestation increases H dramatically by 63 %, while reforestation decreases H slightly by 3 %.

Figure 5.17 (a) shows the monthly mean H at DFS, CLS, and ACS. The seasonal cycles of H at all sites are clearly observed. H reaches maximum (minimum) at DFS, CLS, and ACS in March (August), June (December), and August (December), respectively. The phases of the seasonal cycles of H at CLS and ACS are almost the same, while the phase of the seasonal cycle of H at DFS is quite different. The phases of H at CLS and ACS are consistent with that of Rn, while the phase of H at DFS is influenced by both Rn and leaves. With the increase of Rn and yet without leaves, H at DFS increases from December to March, while with the growth of leaves, H at DFS starts to decreases until H reaches to minimum in August, when leaves are thickest.

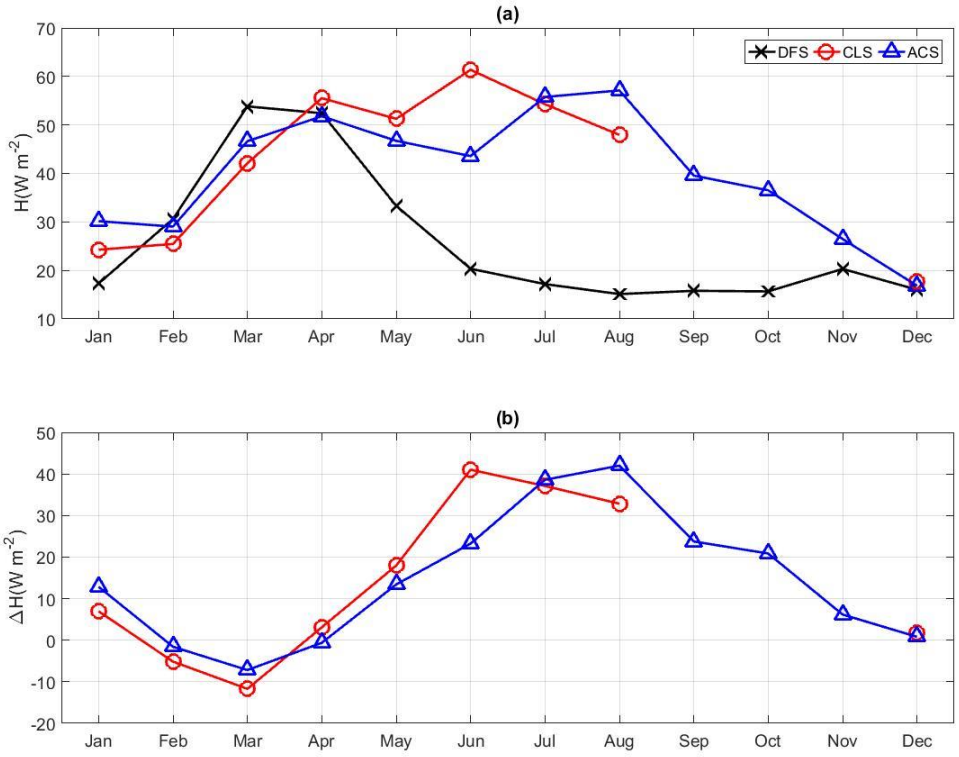

Figure 5.17 (a) Monthly mean, and (b) absolute changes of H at DFS, CLS, and ACS

The maxima (minima) of the monthly mean H at DFS, CLS, and ACS are 53.82 (15.12) W m^{-2}, 61.37 (17.76) W m^{-2}, and 57.11 (16.85) W m^{-2}, respectively. The seasonal amplitudes of monthly mean H at DFS, CLS, and ACS are 38.71 W m^{-2}, 43.60 W m^{-2}, and 40.27 W m^{-2}, respectively. Deforestation increases the seasonal variation and reforestation decreases it. Figure 5.17 (b) shows the absolute changes of H at DFS, CLS, and ACS. Deforestation increases both maximum and minimum monthly mean H, and reforestation does the opposite. The magnitude of ΔH is greater during the summer than during the winter, implying that land-use change alters H more significantly during the summer than during the winter.

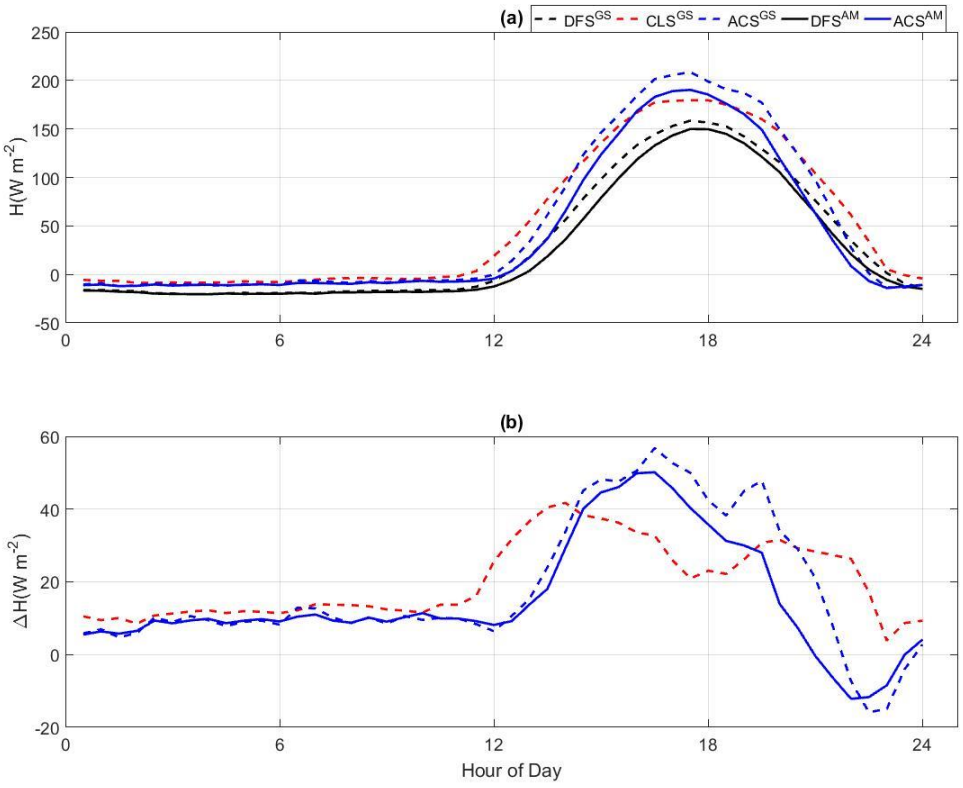

Figure 5.18 Growing seasonal and annual MDCs, and (b) absolute changes of H at DFS, CLS, and ACS

Figure 5.18 (a) shows the growing seasonal and annual MDCs of H at DFS, CLS, and ACS. The phase of the diurnal cycles at DFS, CLS, and ACS are almost the same. The daytime H is smallest at DFS and greatest at ACS. The nighttime H at DFS is slightly smaller than those at CLS and ACS, which are almost identical. During the growing season, the maxima (minima) of sub-daily H at DFS, CLS, and ACS are 158.53 (-20.56) W m^{-2}, 179.56 (-8.77) W m^{-2}, and 208.51 (-13.49) W m^{-2}, respectively. The diurnal amplitudes of H at DFS, CLS, and ACS are 179.09 W m^{-2}, 188.33 W m^{-2}, and 222.00 W m^{-2}, respectively. Deforestation and reforestation both increase the diurnal variation of H. The maxima (minima) of the annual MDCS of H at DFS and ACS are 149.96 (-20.49) W m^{-2} and 190.29 (-14.07) W m^{-2}, respectively. The annual diurnal amplitudes of sub-daily H at DFS and ACS are 170.45 W m^{-2} and 204.36 W m^{-2}, respectively. The difference (40.33 W m^{-2}) of the annual mean diurnal variations of H at DFS and ACS is slightly (2.58 W m^{-2}) smaller than that (42.91 W m^{-2}) of the growing seasonal one, implying that land-use change alters the diurnal variation of H slightly more in the growing season than in the dormant season.

Figure 5.18 (b) shows the absolute change of MDCs of H at DFS, CLS, and ACS. ΔH at CLS is always positive, indicating that deforestation increases the average H at sub-daily scale. Daytime ΔH at ACS is greater than that at CLS, and nighttime ΔH at ACS is smaller than that at CLS, implying that reforestation increases the maximum H and decreases the minimum H at sub-daily scale. The magnitude of ΔH is much greater during the daytime than during the nighttime, implying that land-use change alters H more significantly during the daytime than during the nighttime. The growing seasonal ΔH during the daytime is greater than the annual mean ΔH, implying that land-use change alters H more significantly during the growing season than the dormant season.

Analysis of H at DFS, CLS, and ACS results in the following key findings:

(1) At the long time scale, deforestation increases H and reforestation decreases it. Deforestation increases H dramatically by 63 %, while reforestation decreases H slightly by 3 %. H in the post-agricultural ecosystem is greater than that in the pre-agricultural ecosystem.

(2) At seasonal scale, the phases of the seasonal cycles of H at the agricultural and post-agricultural ecosystems are consistent with that of Rn, while that at the pre-agricultural ecosystem is influenced by both Rn and leaves. Deforestation increases seasonal maximum, minimum, and variation of H, and reforestation does the opposite. Land-use change alters H more significantly during the summer than during the winter.

(3) At sub-daily scale, both deforestation and reforestation increase the maximum and diurnal variation of H. Deforestation increases minimum H, and reforestation decrease it. Land-use change alters H more significantly during the daytime than during the nighttime.

5.4.3 Soil Heat Flux

Soil heat flux (G) is primarily due to conduction through the soil. The depth of the soil that responds to and is affected by changes in the energy fluxes at the surface on a diurnal basis is typically less than a meter for land surfaces. The measurement depths of surface G at DFS and ACS are approximately 5 cm. G at CLS is estimated using the MEP model. G at CLS is available from December to August and the annual mean G at CLS is not available. Figure 5.19 shows the long-term mean G at DFS, CLS, and ACS. The long-term mean G

are summarized in Table 5.2. Figure 5.20 shows the monthly mean G at DFS, CLS, and ACS. Figure 5.21 shows the growing seasonal and annual MDCs of G at DFS, CLS, and ACS.

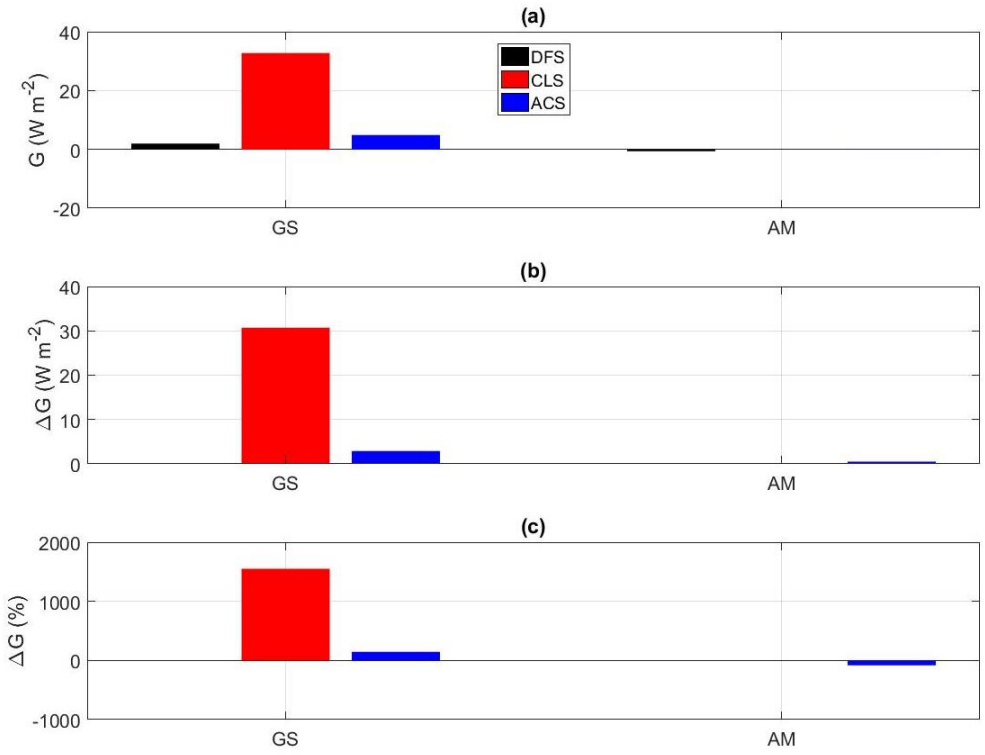

Figure 5.19 (a) Growing seasonal and annual mean, (b) absolute and (c) relative changes of G at DFS, CLS, and ACS

Figure 5.19 (a) shows the growing seasonal and annual mean G at DFS, CLS, and ACS. During the growing season, the mean G at DFS, CLS, and ACS are 1.98 W m^{-2}, 32.71 W m^{-2}, and 4.87 W m^{-2}, respectively. G at ACS is 30.73 W m^{-2} (15 times) more than that at DFS. G at ACS is 27.84 W m^{-2} (85 %) less than that at ACS and 2.89 W m^{-2} (146%) more than that at DFS. Deforestation increases G and reforestation decreases it. The annual mean G at DFS and ACS are -0.61 W m^{-2} and -0.11 W m^{-2}, respectively. Annual mean G over

forestation are approximately zero. At annual scale, soil over forest does not receive net heat flux.

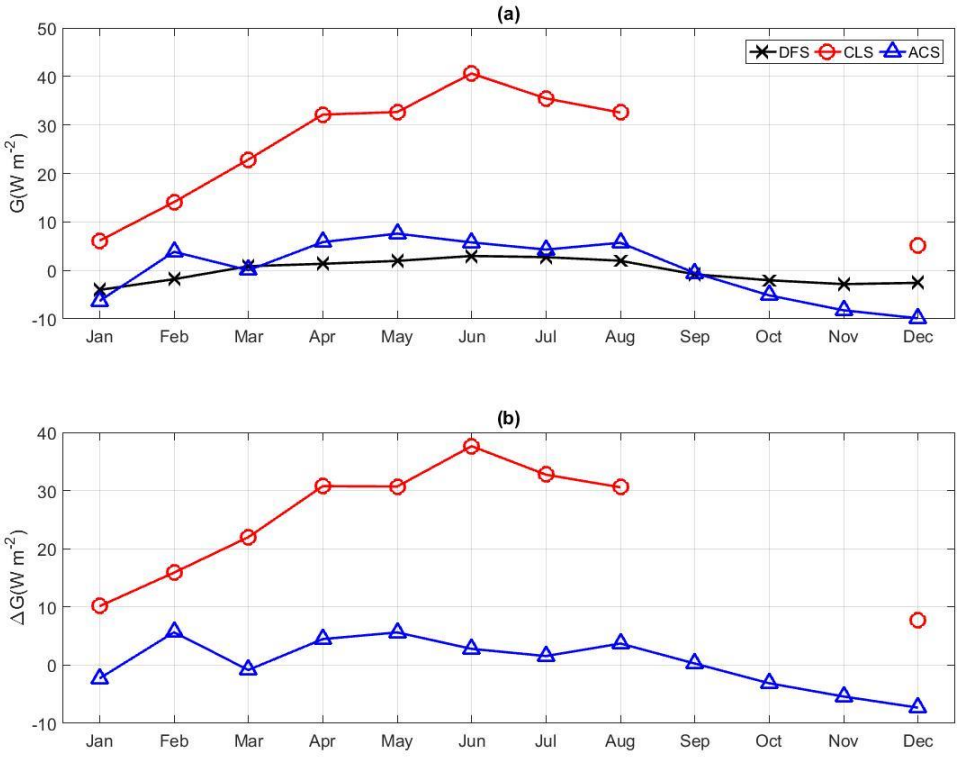

Figure 5.20 (a) Monthly mean, and (b) absolute changes of G at DFS, CLS, and ACS

Figure 5.20 (a) shows the monthly mean G at DFS, CLS, and ACS. G over ACS is constantly greater than those at DFS and ACS. Monthly mean G at DFS, CLS, and ACS reaches to maximum (minimum) in June (January), June (December), and May (December), respectively. The phases of the seasonal cycles of G at all sites are almost the same. The maximum (minimum) of monthly mean G at DFS, CLS, and ACS are 2.97 (-4.02) W m^{-2}, 40.61 (5.18) W m^{-2}, and 7.58 (-9.87) W m^{-2}, respectively. The seasonal amplitudes of monthly mean G at DFS, CLS, and ACS are 6.99 W m^{-2}, 35.43 W m^{-2}, and

17.46 W m^{-2}, respectively. Deforestation increases the seasonal variation and reforestation decreases it. G at CLS is always positive, implying that soil over cropland is always absorbing heat flux. G at DFS and ACS is negative during the winter and positive during the summer, implying that soil over forest is absorbing heat during the summer and releasing heat during the winter.

Figure 5.20 (b) shows the absolute changes of G at CLS and ACS respect to DFS. ΔG at CLS is always positive, implying that deforestation increases both the maximum and minimum G. ΔG at ACS is always smaller than ΔG at CLS, implying that deforestation decreases both the maximum and minimum G. The magnitude of ΔG at CLS is larger during the summer than during the winter, indicating that land-use change alters G more significantly during the summer than during the winter.

Figure 5.21 (a) shows the growing seasonal and annual MDCs of G at DFS, CLS, and ACS. The daytime G is greatest at CLS and smallest at DFS. The nighttime G at CLS and ACS are almost identical and smaller than that at DFS. G at DFS does not have an obvious diurnal variation. The decrease of G at noontime at ACS is due to periodic shadings in the young pine forest. During the growing season, the maxima (minima) of sub-daily G at DFS, CLS, and ACS are 10.67 (-3.34) W m^{-2}, 127.99 (-20.45) W m^{-2}, and 74.26 (-19.73) W m^{-2}, respectively. The amplitudes of the sub-daily G at DFS, CLS, and ACS are 14.01 W m^{-2}, 148.44 W m^{-2}, and 94.00 W m^{-2}, respectively. Deforestation increases the diurnal variation of G and reforestation decreases it.

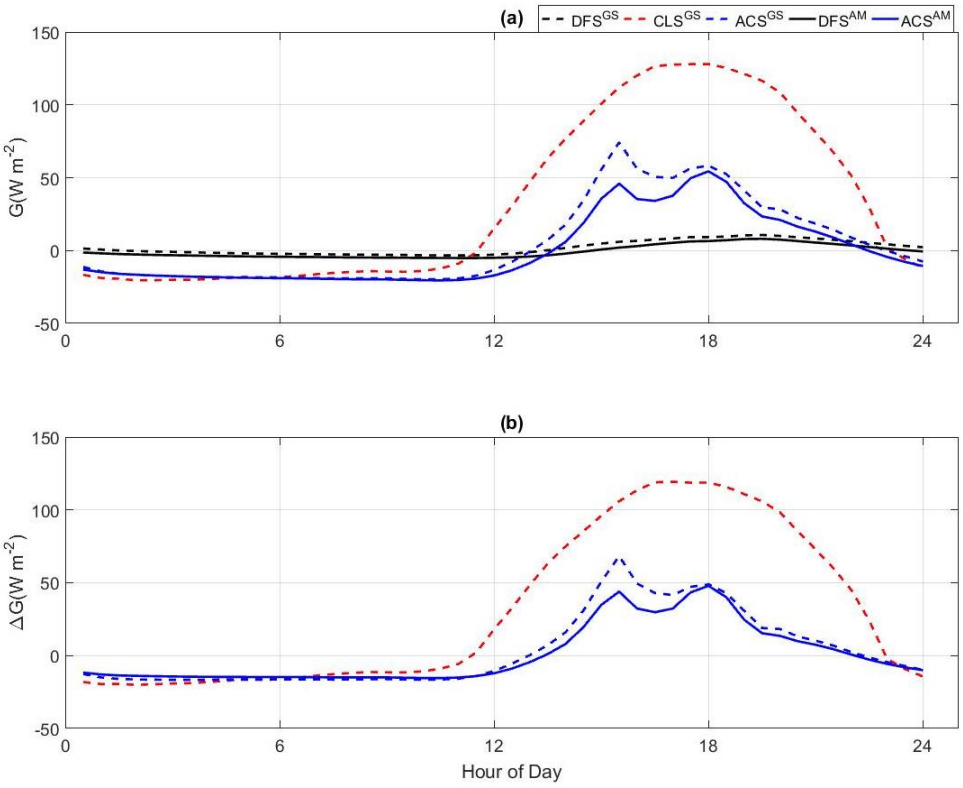

Figure 5.21 (a) Growing seasonal and annual MDCs, and (b) absolute changes of G at DFS, CLS, and ACS

Figure 5.21 (b) shows the absolute change of the growing seasonal and annual MDCs. ΔG at CLS are positive during the day and negative during the night, indicating that deforestation increases the maximum G and decreases the minimum G. ΔG at ACS is smaller during the daytime and smaller during the nighttime than ΔG at CLS, indicating that reforestation decreases the maximum G and increases the minimum G. ΔG is larger during the daytime than during the nighttime, implying that land-use change alters G more significantly during the daytime than during the nighttime.

Analysis of G at DFS, CLS, and ACS results in the following key findings:

(1) At long time scale, land-use change significantly alters, G. Deforestation increases G and reforestation decreases it. The annual mean G over forest are approximately zero.

(2) At seasonal scale, deforestation increases both the maximum, the minimum, and the seasonal variation of G. Reforestation influences them oppositely. Land-use change alters G more significantly during the summer than during the winter.

(3) At sub-daily scale, deforestation increases the maximum G, decreases the minimum G, and significantly increases the diurnal variation of G. Reforestation alters G oppositely. Land-use change alters G more significantly during the daytime than during the nighttime.

5.4.4 Conclusion

This section investigates the evolution of the energy cycle due to land-use change at CCZ by comparing Rn, H, and G at DFS, CLS, and ACS at long-term, seasonal, and sub-daily scales. The key findings are:

(1) At long time scale, deforestation increases H and G, and reforestation decreases them. Land-use change alters G much more significantly than H, and alters H and G greater than Ta and Ts. During the growing season, deforestation increases H, G, Ta, and Ts by 63 %, 1500 %, 11 %, and 19 % respectively, and reforestation decreases them by 3%, 85 %, 4 %, and 12 %, respectively. R, H, and G at the post-agricultural ecosystem is 27.73 W m^{-2}

(29 %), 14.88 W m^{-2} (58 %) and 0.5 W m^{-2} (82 %) greater than those at the pre-agricultural ecosystem.

(2) At seasonal scale, deforestation increases the maxima, the minima, and the seasonal variations of H and G, and reforestation alters them oppositely. Land-use change alters Rn, H, and G more significantly during the summer than during the winter. The phases of the seasonal cycle of H at DFS is dominant by the seasonality of Rn and vegetation.

(3) At sub-daily scale, deforestation increases the minimum H, and the maxima and the diurnal variations of H and G; and decrease the minimum G. Reforestation increases the minimum H and G, and the maximum and the diurnal variation of H; and decreases the maximum and the diurnal variation of G. Land-use change alters Rn, H, and G more significantly during the daytime than during the nighttime.

5.5 Evolution of Water Cycle

The water cycle describes the continuous movement of water on, above, and below the surface of the Earth. This section investigates the evolution of the water cycle due to land-use change by comparing field observations and modeling results at different ecosystems including the humidity (the water vapor in the air), the soil moisture (the water in the soil), and the evapotranspiration (the water transport from the soil to the air).

Table 5.3 Mean values of variables related to the water cycle

Period	Variables	Unit	DFS	CLS	ACS
GS	RH	%	69.33	75.73	74.37
	AH	g m^{-3}	12.48	15.68	14.45
	θ	m^3 m^{-3}	0.32	0.14	0.13
	θ@30cm	m^3 m^{-3}	NA	0.13	0.15
	E	W m^{-2}	77.78	90.13	110.47
AM	RH	%	68.12	NA	72.49
	AH	g m^{-3}	10.17	NA	11.62
	θ	m^3 m^{-3}	0.32	0.13	0.12
	θ@30cm	m^3 m^{-3}	NA	0.12	0.14
	E	W m^{-2}	55.44	NA	80.72

5.5.1 Humidity

Humidity is used to describe the amount of water vapor in the air, and indicate the likelihood for precipitation, dew, and fog. This subsection of humidity investigates the relative humidity and water vapour density at different ecosystems. Relative humidity (RH) is a percentage that indicates the ratio of absolute humidity relative to a maximum humidity given the same temperature. The unit of RH is %. Water vapour density (Cv) describes the water content of air. The unit of Cv is usually g m^{-3}.

RH is directly measured using the CS215 temperature and relative humidity probe. The measurement heights at DFS, CLS, and ACS are 40 m, 9 m, and 0.5 m, respectively. Figure 5.22 shows the long-term mean RH at DFS, CLS, and ACS. The annual mean of RH at CLS is not available as RH is measured since December 2017. The long-term mean RH are also summarized in Table 5.3. Figure 5.23 shows the monthly mean RH at DFS, CLS, and ACS. Figure 5.24 shows the growing seasonal and annual MDCs of RH at DFS, CLS, and ACS.

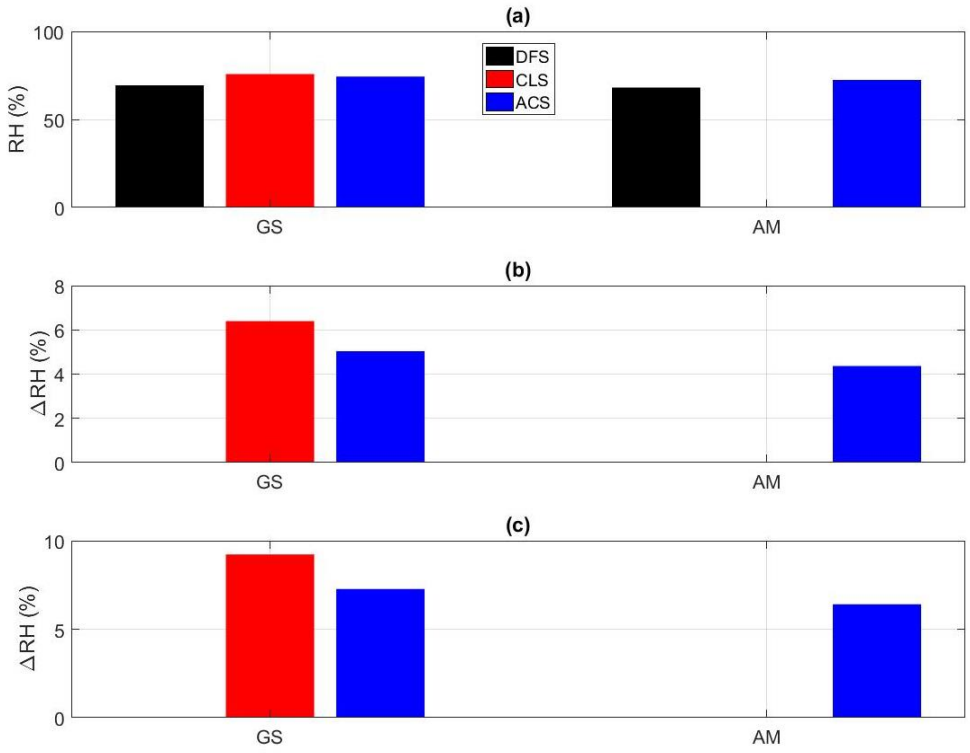

Figure 5.22 (a) Growing seasonal and annual mean, (b) absolute and (c) relative changes of RH at DFS, CLS, and ACS

Figure 5.22 (a) shows the growing seasonal and annual mean RH at DFS, CLS, and ACS. The growing seasonal mean RH at DFS, CLS, and ACS are 69.33 %, 75.73 %, and 74.37 %, respectively. RH is greatest at CLS and smallest at DFS, implying that deforestation increases RH and reforestation decreases it. The annual mean RH at DFS and ACS are 68.12 % and 72.49 %, respectively. The annual mean RH at the post-agricultural ecosystem is higher than that at the pre-agricultural ecosystem.

Figure 5.23 (a) shows the monthly mean RH at DFS, CLS, and ACS. RH at DFS, CLS, and ACS reach to maxima (minima) in September (February), July (January), and July (January), respectively. The phases of the seasonal cycles of RH at CLS and ACS are one to two months ahead of that at DFS. The maxima (minima) of RH at DFS, CLS, and ACS

are 78 (58) %, 81 (64) %, and 80 (61) %, respectively. The seasonal amplitudes of RH are 21 %, 17 %, and 19 %, respectively. Deforestation increases both the maximum and minimum H and reforestation decreases them. Deforestation decreases the seasonal variation of RH and reforestation increases it.

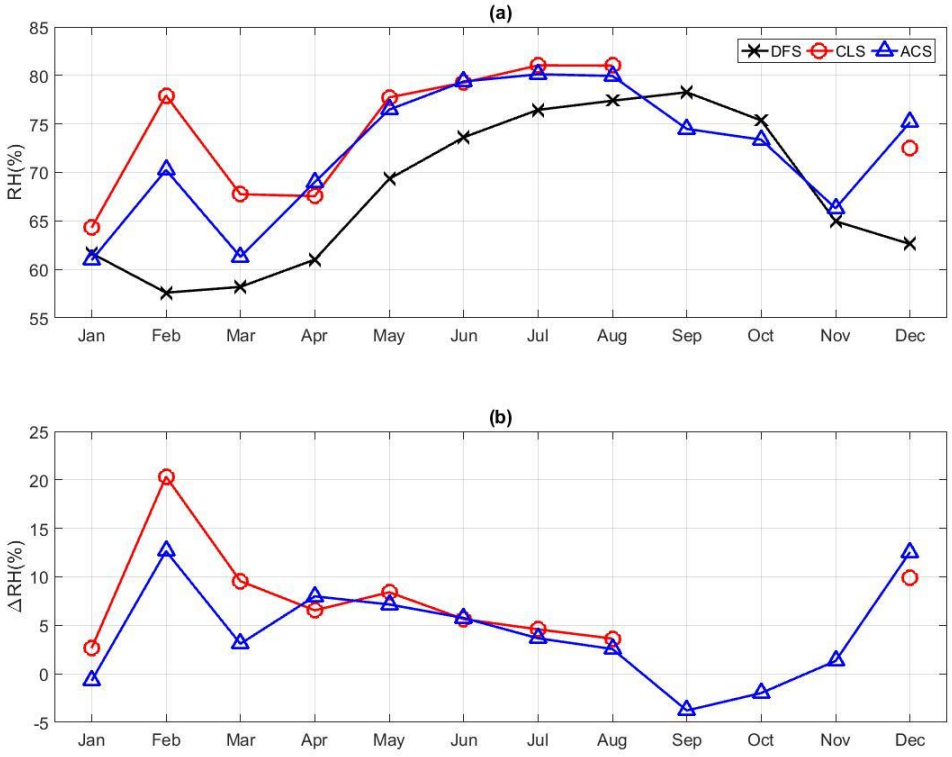

Figure 5.23 (a) Monthly mean, and (b) absolute changes of RH at DFS, CLS, and ACS

Figure 5.24 (a) shows the growing seasonal and annual MDCs of RH at DFS, CLS, and ACS. During the growing season, RH at CLS and ACS are constantly higher than that at DFS. The phases of the diurnal cycles at DFS, CLS, and ACS are almost the same, with the maximum RH in the early mornings and the minimum RH in the late afternoon. The maxima (minima) of sub-daily RH at DFS, CLS, and ACS are 85.55 (51.07) %, 89.47

(56.14) %, and 90.59 (54.74) %, respectively. Deforestation increases both maximum and minimum RH, and reforestation increases maximum RH and decreases minimum RH. The diurnal amplitudes of RH at DFS, CLS, and ACS are 34.47 %, 33.33 %, and 35.85 %, respectively. Deforestation slightly decreases the diurnal variation of RH and reforestation increases it. As the accuracy of the RH measurements by the CS215 probe is $\pm$ 2 % over 10 to 90 %, the differences of RH among the three sites are not obvious. Compared to RH, Cv is a better indicator of the air humidity as Cv is the exact water content in the air.

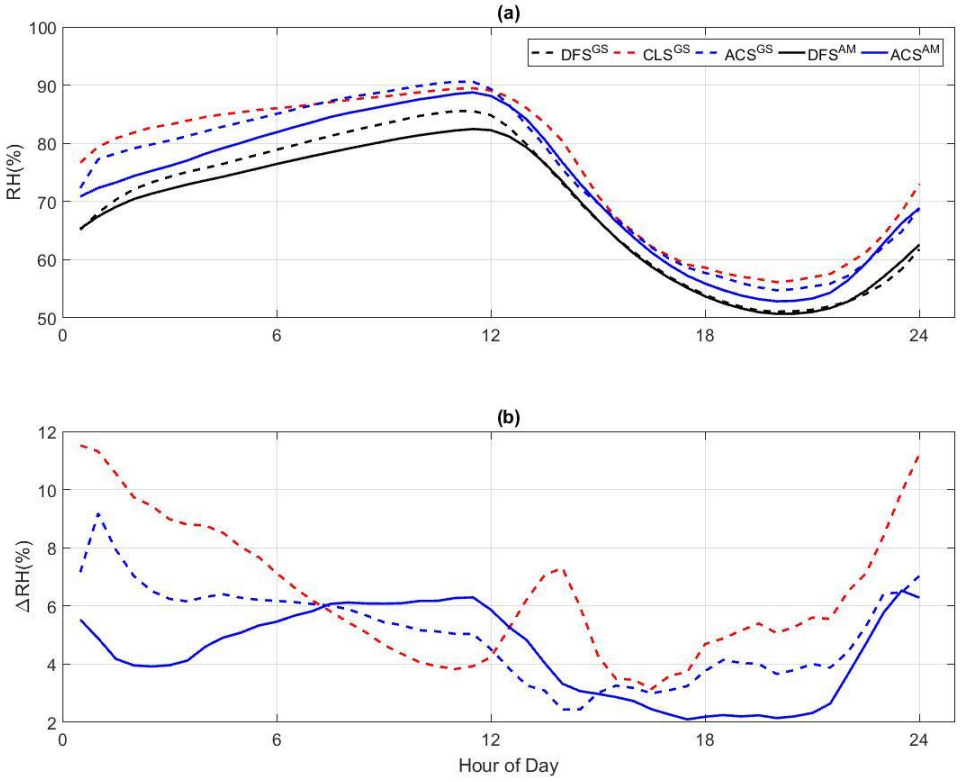

Figure 5.24 (a) Growing seasonal and annual MDCs, and (b) absolute changes of RH at DFS, CLS, ACS

Cv is calculated using Ta and RH measurements using the Clausius-Clapeyron equation (Appendix G). Figure 5.25 shows the long-term mean AH at DFS, CLS, and ACS. The

long-term mean AH are summarized in Table 5.3. Figure 5.26 shows the monthly mean Cv at DFS, CLS, and ACS. Figure 5.26 shows the long term MDCs of Cv at DFS, CLS, and ACS.

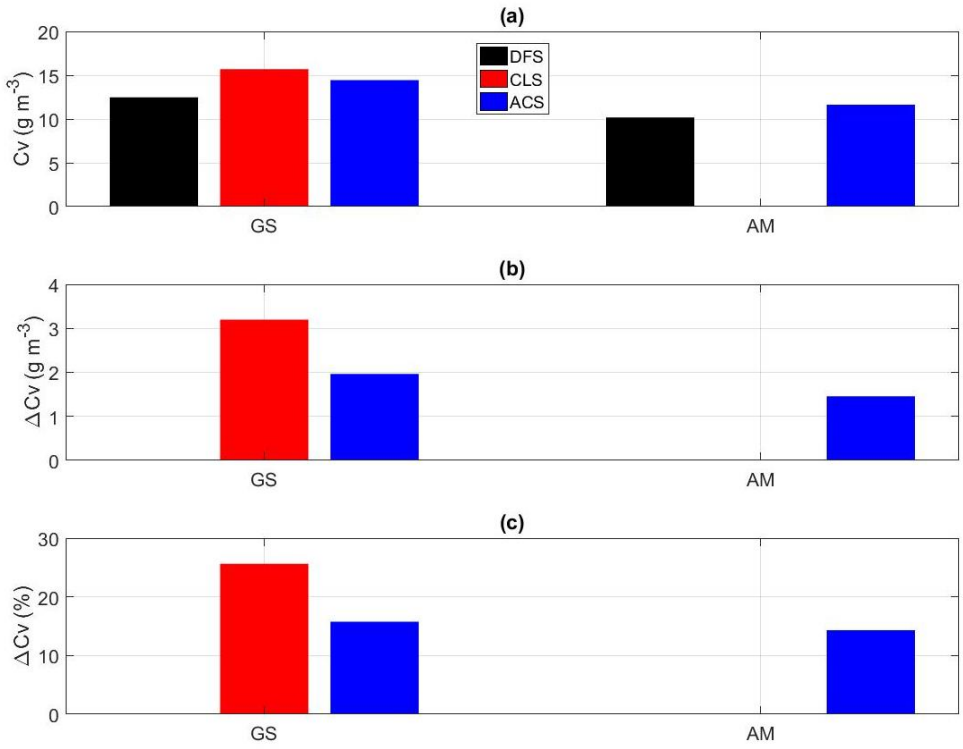

Figure 5.25 (a) Growing seasonal and annual mean, and (b) absolute and (c) relative changes of Cv at DFS, CLS, and ACS

Figure 5.25 (a) shows the growing seasonal and annual mean Cv at DFS, CLS, and ACS. During growing season, the mean Cv at DFS, CLS, and ACS are 12.48 g m^{-3}, 15.68 g m^{-3}, and 14.45 g m^{-3}, respectively. Cv at CLS is 3.2 g m^{-3} (26 %) more than that at DFS. AH at ACS is 1.23 g m^{-3} (8 %) less than that at CLS, and 1.97 g m^{-3} (16 %) more than that at DFS. Cv is largest at CLS and smallest at DFS. Deforestation increases Cv and reforestation decreases it. The change of Cv due to deforestation is greater than that due to reforestation. Throughout the year, the mean Cv at DFS and ACS are 10.17 g m^{-3} and 11.62

g m^{-3}, respectively. The mean Cv at ACS is 1.46 g m^{-3} (14 %) more than that at DFS. Air is more humid in the post-agricultural ecosystem than in the pre-agricultural ecosystem. ΔCv between DFS and ACS is greater during the growing season than throughout the year, implying that land-use change alters Cv more significantly during the growing season than the dormant season.

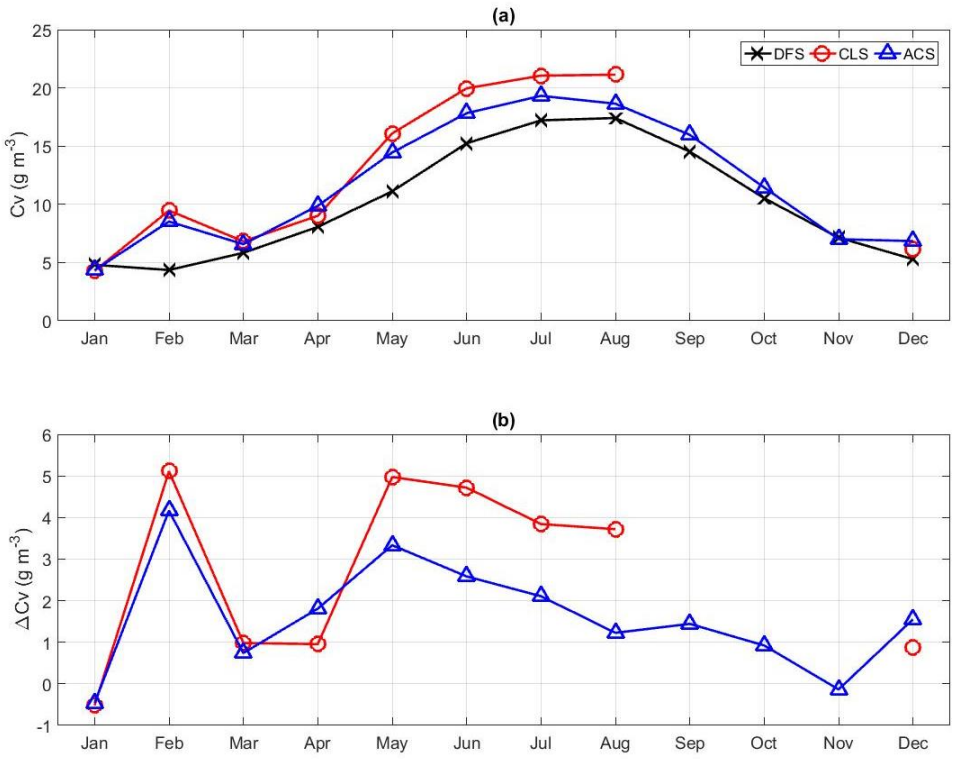

Figure 5.26 (a) Monthly mean, and (b) absolute changes of Cv at DFS, CLS, and ACS

Figure 5.26 (a) shows the monthly mean of Cv at DFS, CLS, and ACS. It is evident that AH at all sites have a strong seasonal cycle. Monthly mean Cv at DFS, CLS, and ACS reach to maxima (minima) in August (February), August (January), and July (January), respectively. Cv is large during the summer and small during the winter. The phases of the seasonal cycles of AH at all sites are almost identical. The large Cv at CLS and ACS in

February are due to the abnormal high air temperature in February 2018 at Calhoun. The maxima (minima) of monthly mean Cv at DFS, CLS, and ACS are 17.41 (4.36) g m^{-3}, 21.13 (4.29) g m^{-3}, and 19.32 (4.34) g m^{-3}, respectively. Deforestation increases the maximum Cv and decreases the minimum Cv, and reforestation influences them oppositely. The seasonal amplitudes of AH at DFS, CLS, and ACS are 13.06 g m^{-3}, 16.84 g m^{-3}, and 14.98 g m^{-3}, respectively. The seasonal variation of AH is greatest at CLS and smallest at DFS, indicating that deforestation increases the seasonal variation of AH and reforestation decreases it. Figure 5.26 (b) shows the absolute changes of Cv at DFS, CLS, and ACS. Except for February, ΔCv is much greater during the summer than during the winter, implying that land-use change alters Cv more significantly during the summer than during the winter.

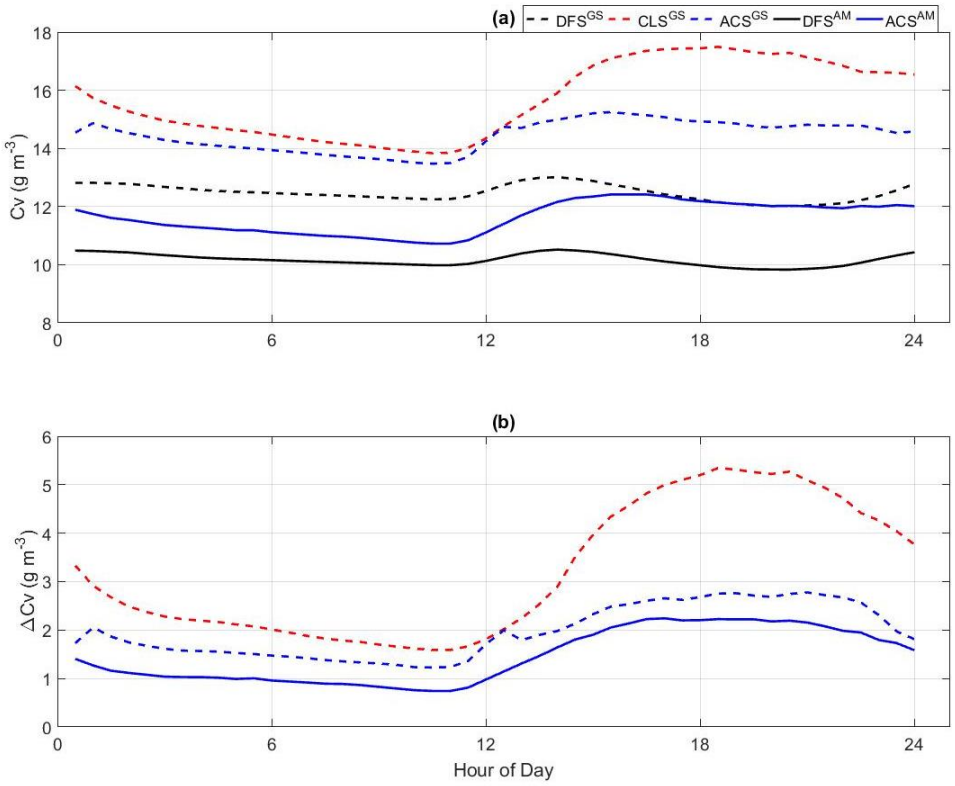

Figure 5.27 (a) Growing seasonal and annual MDCs, and (b) absolute changes of Cv at DFS, CLS, and ACS

Figure 5.27 (a) shows the growing seasonal and annual MDCs of Cv at DFS, CLS, and ACS. Cv at all sites reach to minima in the early mornings due to low air temperature, reach to maxima around noon due to air temperature increase, and stay high through the afternoon until Cv decreases in the evening due to condensation. During the growing season, the maxima (minima) of sub-daily Cv at DFS, CLS, and ACS are 13.01 (12.02) g m^{-3}, 17.49 (13.84) g m^{-3}, and 15.25 (13.48) g m^{-3}, respectively. Deforestation increases both minimum and maximum Cv, and reforestation decreases them. The diurnal amplitudes of Cv at DFS, CLS, and ACS are 0.99 g m^{-3}, 3.66 g m^{-3}, and 1.77 g m^{-3}, respectively. ΔCv are greater during the daytime than during the nighttime (Figure 5.27 (b)), implying that land-use change influences Cv more significantly during the daytime than during the nighttime.

Analysis of humidity at DFS, CLS, and ACS results in the following key findings:

(1) At long time scale, deforestation increases Cv and reforestation decreases it. The change of Cv due to deforestation is greater than that due to reforestation. Air is more humid in the post-agricultural ecosystem than in the pre-agricultural ecosystem.

(2) At seasonal scale, deforestation increases the maximum and the seasonal variation of Cv, and decreases the minimum Cv; and reforestation influences them oppositely. Land-use change alters Cv more significantly during the summer than during the winter.

(3) At sub-daily scale, deforestation increase the maximum, the minimum, and the diurnal variation of Cv, and reforestation decreases them. Land-use change alters Cv more significantly during the daytime than during the nighttime.

(4) The trend of the evolution of humidity due to land-use change at CCZ is consistent with that of Ta, implying that Cv is dominant by Ta according to the Clausius Clapeyron equation as the Southeast of United States is very humid.

5.5.2 Soil Moisture

Soil moisture is water held in the spaces between soil particles. Soil moisture is important to many hydrological, biological, and biogeochemical processes. It is a key variable in controlling the exchange of energy and water between the land surface and the atmosphere through evapotranspiration. Surface soil moisture (θ) and soil moisture at 30 cm deep ($\theta@30cm$) are used to investigate the evolution of soil moisture due to land-use change. θ is measured at about 5 cm below surface soil. The long-term mean, MDCs, and monthly mean of θ are computed using observations at DFS, CLS, and ACS. Figure 5.28 shows the long-term mean θ at DFS, CLS, and ACS. The long-term mean θ at all sites are also summarized in Table 5.3. Figure 5.29 shows the monthly mean θ at DFS, CLS, and ACS. Figure 5.30 shows the growing seasonal and annual MDCs of θ at DFS, CLS, and ACS.

Figure 5.28 (a) shows the growing seasonal and annual mean θ at DFS, CLS, and ACS. θ is greatest at DFS and smallest at ACS. During the growing season, the mean θ at DFS, CLS, and ACS are 0.32 m^3 m^{-3}, 0.14 m^3 m^{-3}, and 0.13 m^3 m^{-3}, respectively. θ at CLS is

0.18 m^3 m^{-3} (56 %) smaller than that at DFS. θ at ACS is 0.01 m^3 m^{-3} (5 %) smaller than that at CLS, and 0.19 m^3 m^{-3} (58 %) smaller than that at DFS. Throughout the year, the mean θ at DFS, CLS, and ACS are 0.32 m^3 m^{-3}, 0.13 m^3 m^{-3}, and 0.12 m^3 m^{-3}, respectively. θ at CLS is 0.19 m^3 m^{-3} (59 %) smaller than that at DFS. θ at ACS is 0.01 m^3 m^{-3} (10 %) smaller than that at CLS, and 0.2 m^3 m^{-3} (63 %) smaller than that at DFS. Both deforestation and reforestation decreases θ, and the impact of deforestation on θ is much greater than that of reforestation.

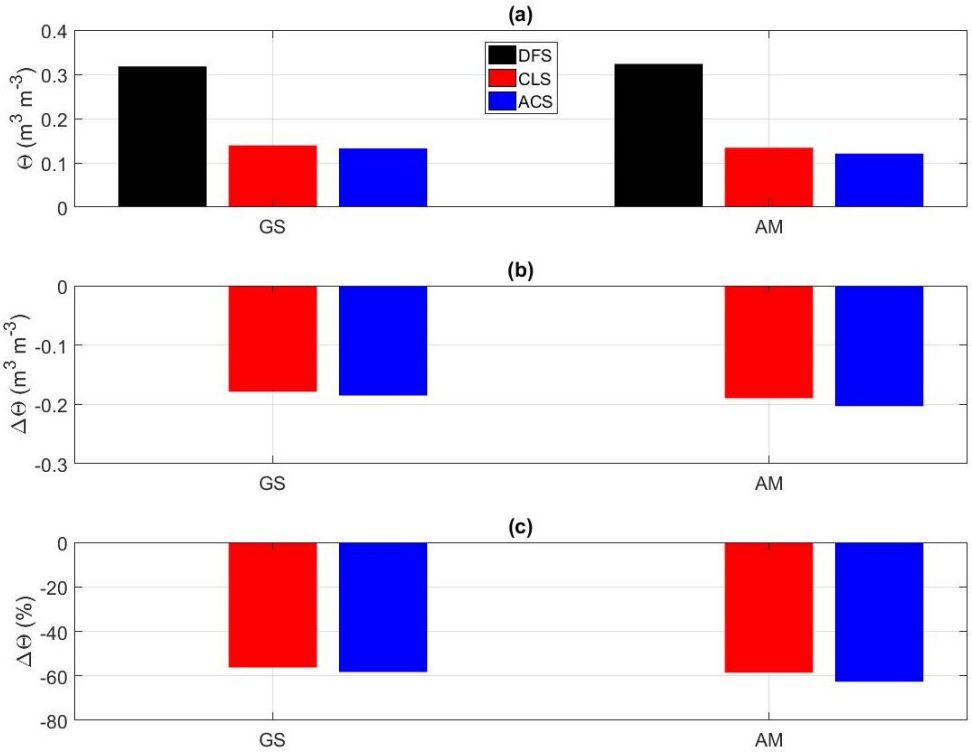

Figure 5.28 (a) Growing seasonal and annual mean, (b) absolute and (c) relative changes of θ at DFS, CLS, and ACS

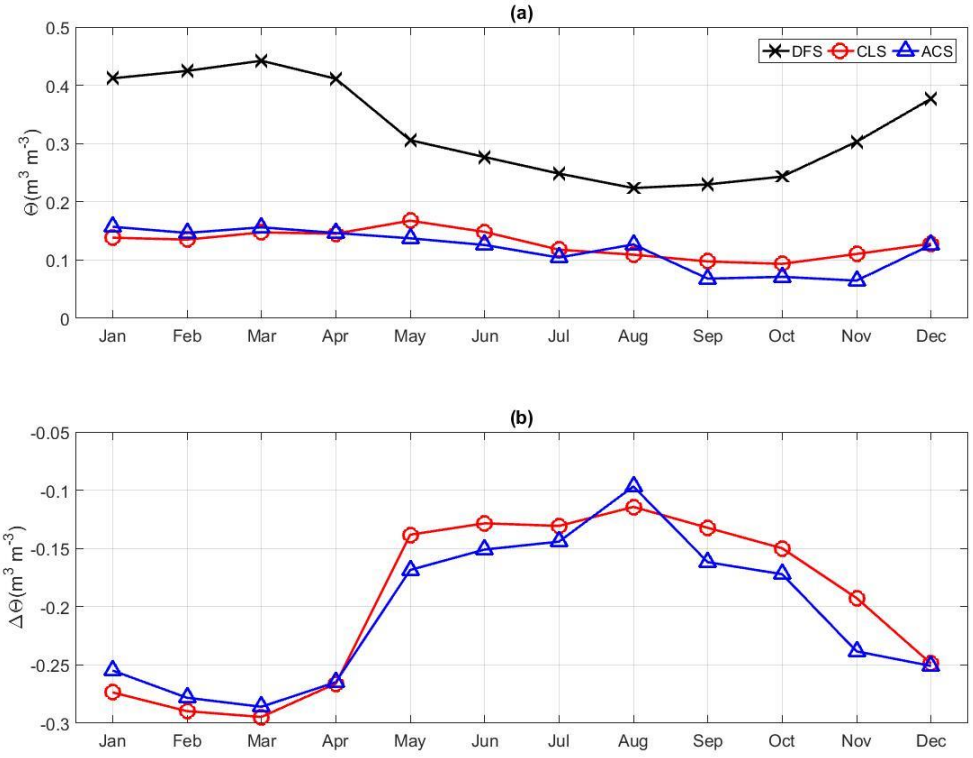

Figure 5.29 (a) Monthly mean, and (b) absolute changes of θ at DFS, CLS, and ACS

Figure 5.29 (a) shows the monthly mean θ at DFS, CLS, and ACS. θ at DFS is constantly greater than those at CLS and ACS. θ at DFS, CLS, and ACS reach to maxima (minima) in March (August), May (October), and January (November), respectively. The seasonal cycles of θ at CLS and ACS are not obvious. θ at DFS is lower during the summer and higher during the winter, oppositely correlated with the trend of evapotranspiration that is discussed in 5.5.3. Deforestation alters both the phase and the amplitude of the seasonal cycle of θ. Figure 5.30 shows the growing seasonal and annual MDCs of θ at DFS, CLS, and ACS. θ at DFS is constantly greater than that at CLS and ACS. No clear diurnal cycle is observed except for θ during the growing season at ACS.

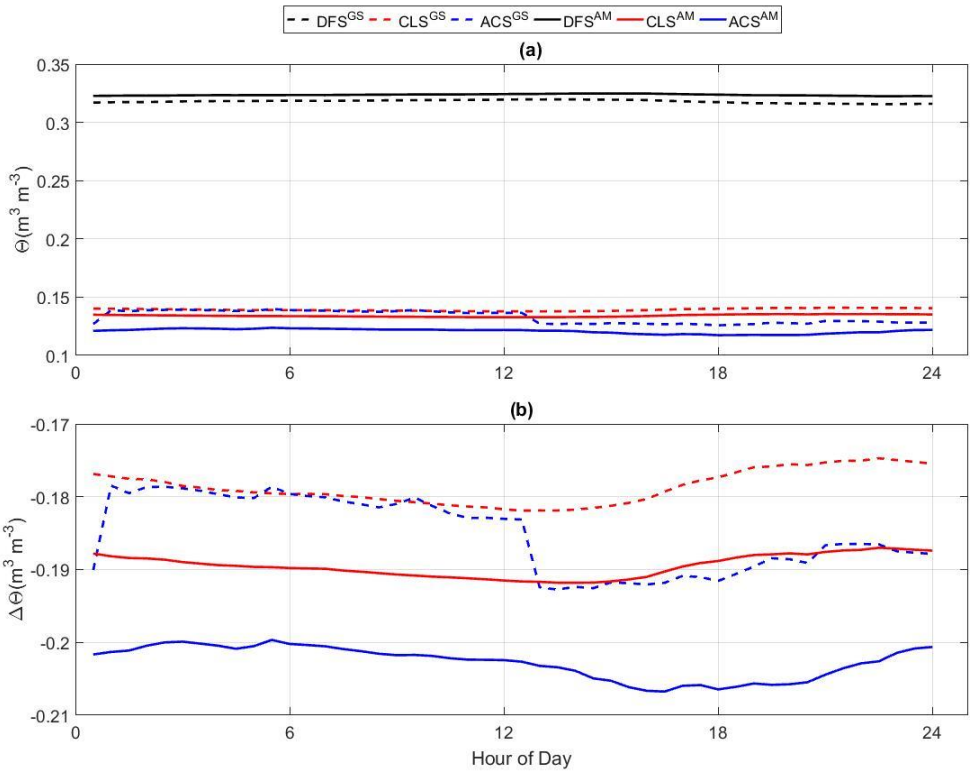

Figure 5.30 (a) Growing seasonal and annual MDCs, and (b) absolute changes of θ at DFS, CLS, and ACS

$\theta@30cm$ is available at CLS and ACS. Figure 5.31 shows the long-term mean $\theta@30cm$ at CLS and ACS. The long-term mean $\theta@30cm$ are also summarized in Table 5.3. Figure 5.32 shows the monthly mean $\theta@30cm$ at CLS and ACS. Figure 5.32 shows the long-term MDCs of $\theta@30cm$ at CLS and ACS. The absolute and relative changes are calculated with respect to $\theta@30cm$ at CLS.

Figure 5.31 (a) shows the growing seasonal and annual mean $\theta@30cm$ at CLS and ACS. The long-term mean $\theta@30cm$ at ACS is slightly greater than that at CLS. During the growing season, the mean $\theta@30cm$ at CLS and ACS are 0.13 m^3 m^{-3} and 0.15 m^3 m^{-3}, respectively. $\theta@30cm$ at ACS is 0.02 m^3 m^{-3} (17 %) more than that at CLS. Annual mean

$\theta@30cm$ at CLS and ACS are 0.12 m^3 m^{-3}, and 0.14 m^3 m^{-3}, respectively. Annual mean $\theta@30cm$ at ACS is 0.02 m^3 m^{-3} (15 %) more than that at CLS. Reforestation increases $\theta@30cm$.

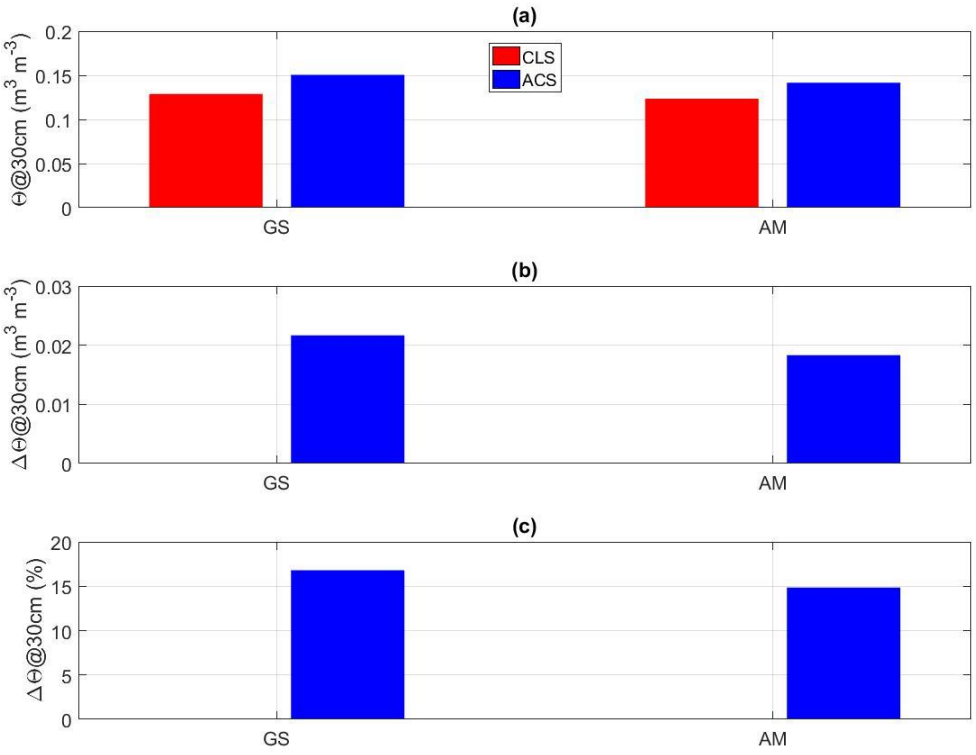

Figure 5.31 (a) Growing seasonal and annual mean, (b) absolute and (c) relative changes of $\theta@30cm$ at CLS and ACS

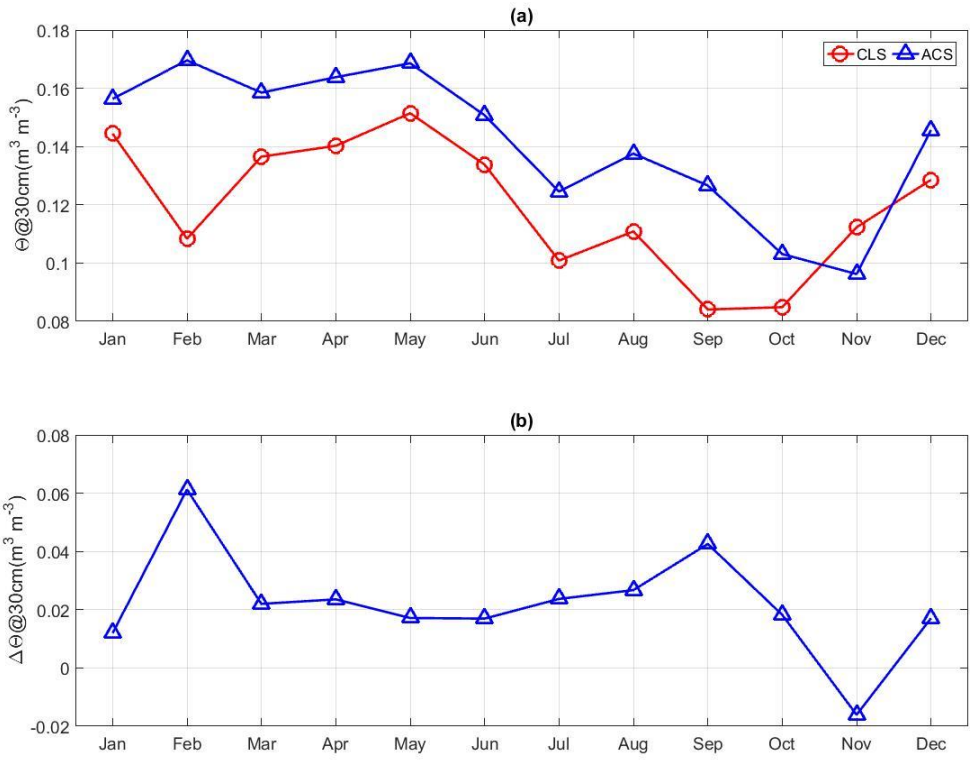

Figure 5.32 (a) Monthly mean, and (b) absolute changes of $\theta@30cm$ at CLS and ACS

Figure 5.32 shows the monthly mean and absolute changes of $\theta@30cm$ at CLS and ACS. $\theta@30cm$ at ACS is greater than that at CLS for all months except for November. $\Delta\theta@30cm$ is around 0.02 m^3 m^{-3} for most of the months. Figure 5.33 shows the long-term MDCs of $\Delta\theta@30cm$ at CLS and ACS. $\theta@30cm$ at ACS is constantly higher than that at CLS. The diurnal variation of $\theta@30cm$ at CLS is stronger than that at ACS. Reforestation increases $\theta@30cm$ at sub-daily scale, and decreases the diurnal variation of $\theta@30cm$. The mean $\theta@30cm$ during the growing season at both sites are greater than the annual mean $\theta@30cm$, indicating that $\theta@30cm$ during the growing season is greater than that during the dormant season.

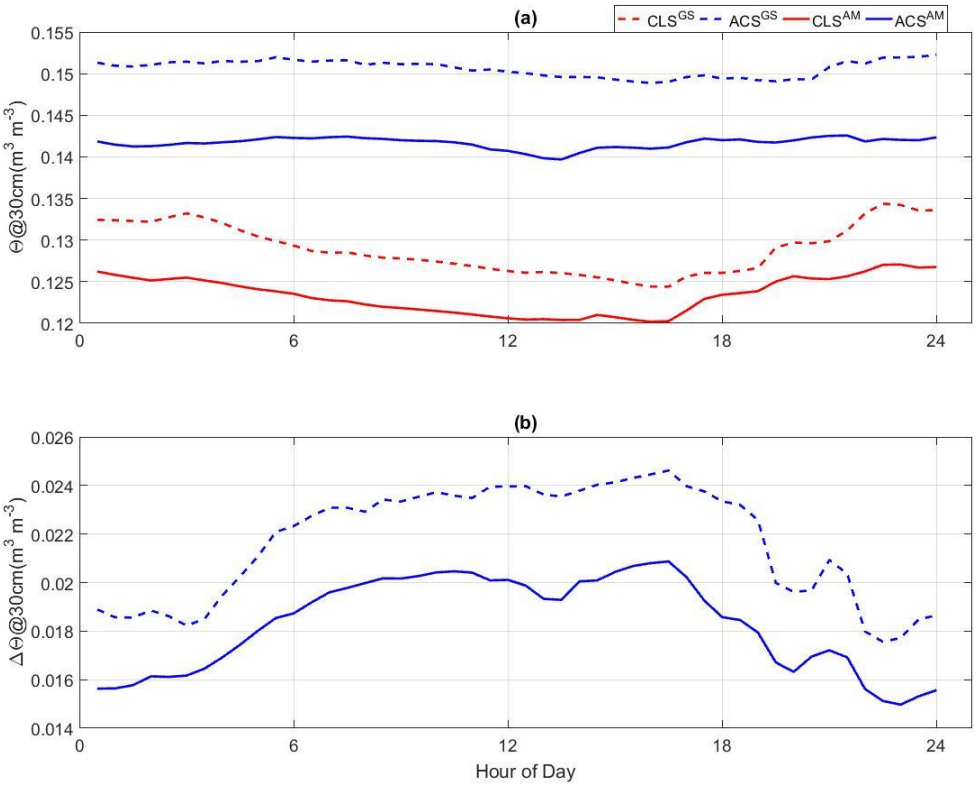

Figure 5.33 (a) Growing seasonal and annual MDCs, and (b) absolute changes of $\boldsymbol{\theta@30cm}$ at CLS and ACS

Analysis of soil moisture at DFS, CLS, and ACS results in the following key findings:

(1) At surface, both deforestation and reforestation decreases soil moisture. The impact of deforestation on soil moisture is much greater than that of reforestation. Deforestation decreases the seasonal variation of soil moisture.

(2) At 30 cm, reforestation increases soil moisture by about 15 %. Soil moisture at both ecosystems is higher during the growing season than during the dormant season.

5.5.3 Evapotranspiration

Evapotranspiration is the sum of soil evaporation and plant transpiration from the Earth's surface to the atmosphere. Evaporation accounts for the movement of water to the air from sources such as the soil and waterbodies. Transpiration accounts for the movement of water within a plant and the subsequent loss of water as vapor through stomata. Evapotranspiration is an important part of the water cycle. As both the EC system and the MEP model estimate the total evapotranspiration from the ecosystem, soil evaporation and plant transpiration are discussed together as evapotranspiration in this subsection.

Evapotranspiration (E) is measured using the EC system at DFS and ACS. The data gaps are partly filled using the MEP model of land surface heat fluxes. As the EC system is not installed at CLS, E is calculated using the MEP model in terms of net radiation, air temperature, and humidity from December 2017 to August 2018, and thus the annual mean E at CLS is not available. The long-term mean, MDCs, and monthly mean of E are computed. Figure 5.34 shows the long-term mean and changes of E at DFS, CLS, and ACS. The long-term mean E are also summarized in Table 5.3. Figure 5.35 shows the monthly mean and absolute changes of E at DFS, CLS, and ACS. Figure 5.36 shows the growing seasonal and annual MDCs, and absolute changes of E at DFS, CLS, and ACS.

Figure 5.34 (a) shows the growing seasonal and annual mean E at DFS, CLS, and ACS. E is smallest at DFS and greatest at ACS. During the growing season, the mean E at DFS, CLS, and ACS are 77.78 W m^{-2}, 90.13 W m^{-2}, and 110.47 W m^{-2}, respectively. E at CLS is 12.34 W m^{-2} (16 %) greater than that at DFS. E at ACS is 20.35 W m^{-2} (23 %) greater than that at CLS, and 32.69 W m^{-2} (42 %) greater than that at DFS. Both deforestation and

reforestation increase E. As the CCZ is very humid throughout the year, deforestation increases soil evaporation and thus increases the total E. In the early stage of reforestation, E includes both soil evaporation and plant transpiration, and thus reforestation also increases the total E. The impact of reforestation on E is greater than that of deforestation. The annual mean E at DFS and ACS are 55.44 W m^{-2} and 80.72 W m^{-2}, respectively. The annual mean E at ACS is 25.28 W m^{-2} (46 %) greater than that at DFS. E at the post-agricultural ecosystem is greater than that at the pre-agricultural ecosystem.

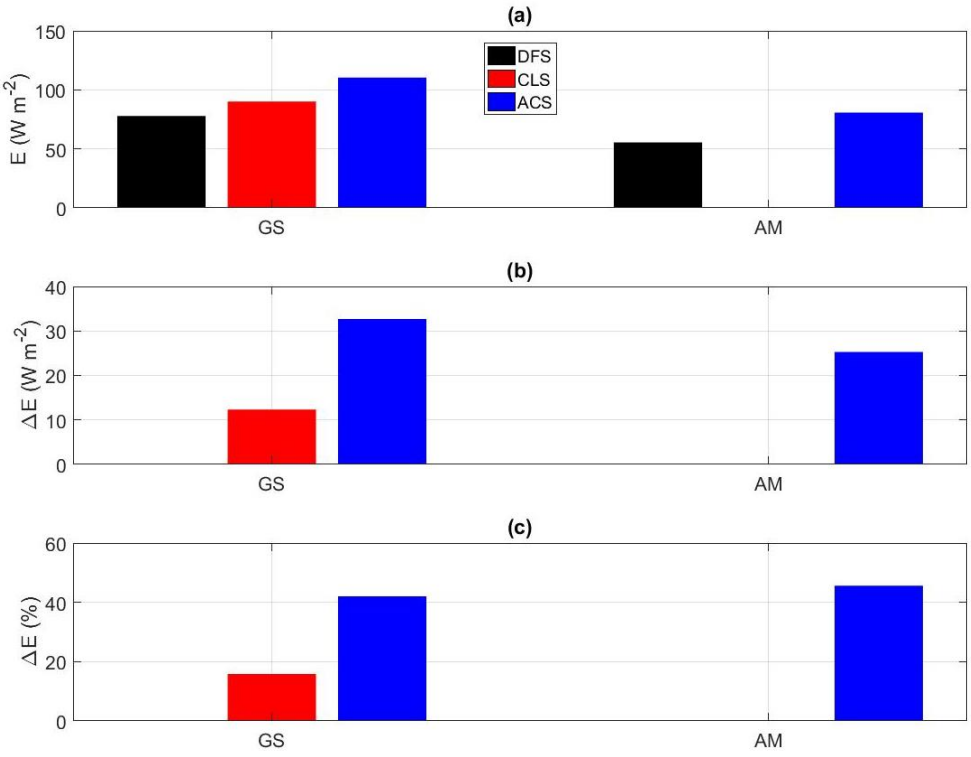

Figure 5.34 (a) Growing seasonal and annual mean, (b) absolute and (c) relative changes of E at DFS, CLS, and ACS

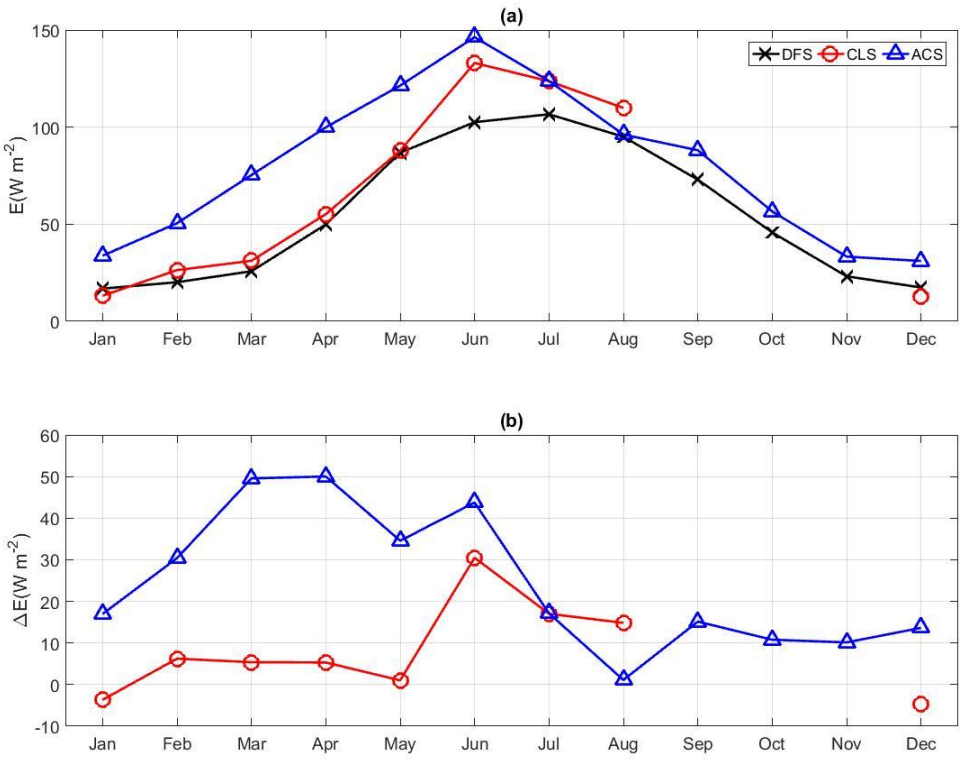

Figure 5.35 (a) Monthly mean, and (b) absolute changes of E at DFS, CLS, and ACS

Figure 5.35 (a) shows the monthly mean E at DFS, CLS, and ACS. The seasonal cycles of E are obvious. E at DFS, CLS, and ACS reaches to maxima (minima) in July (January), June (December), and June (December), respectively. The phases of the seasonal cycles at three sites are almost the same. The maxima (minima) of monthly mean E at DFS, CLS, and ACS are 106.63 (16.82) W m^{-2}, 133.04 (12.77) W m^{-2}, and 146.31 (31.07) W m^{-2}, respectively. Deforestation increases the maximum E and decreases the minimum E. Reforestation increases both the maximum and minimum E. The seasonal amplitudes of monthly mean E at DFS, CLS, and ACS are 89.81 W m^{-2}, 120.27 W m^{-2}, and 115.25 W m^{-2}, respectively. Deforestation increases the seasonal variation and reforestation decreases it.

Table 5.4 Accumulative E (mm)

Month	DFS	CLS	ACS
Jan	18	14	36
Feb	19	26	49
Mar	28	33	81
Apr	52	57	104
May	93	94	130
Jun	106	138	152
Jul	114	132	133
Aug	102	118	103
Sep	76	NA	91
Oct	49	NA	61
Nov	24	NA	35
Dec	19	14	33
GS	495	626	702
Annual	700	NA	1006

Figure 5.35 (b) shows the absolute changes of E at CLS and ACS with respect to DFS. E at CLS is much greater than E at DFS in June, July and August, and yet for the other months, ΔE at CLS is within 10 W m^{-2}. Deforestation alters E more significantly during the summer than during the winter. E at ACS is greater than E at DFS throughout the year. ΔE between CLS and ACS is greater from March to May than from June to August, implying that reforestation alters E more significantly during the spring than during the summer. Deforestation and reforestation alter E differently in seasons due to different canopy types of the ecosystems. Deciduous broadleaf forest (the pre-agricultural ecosystem) and crops (the agricultural ecosystem) both have strong seasonal cycles of E, strong during the summer and weak during the winter. The young pine forest (the post-agricultural ecosystem) is consuming more water for the fast growth throughout the year. Therefore, deforestation alters E more during the summer, while reforestation alters E more during the spring.

Monthly and annual accumulative E are essential to understand the water cycle. The monthly and annual accumulative E at DFS, CLS, and ACS are summarized in Table 5.4. During the growing season, the accumulative E at DFS, CLS, and ACS are 495 mm, 626 mm, and 702 mm, respectively. The annual accumulative E at DFS and ACS are 700 mm and 1006 mm, respectively. The percentages of growing seasonal E to annual E at DFS and ACS are 71 % and 70 %, respectively. For both DFS and ACS, about 70 % of the total E is from the growing season.

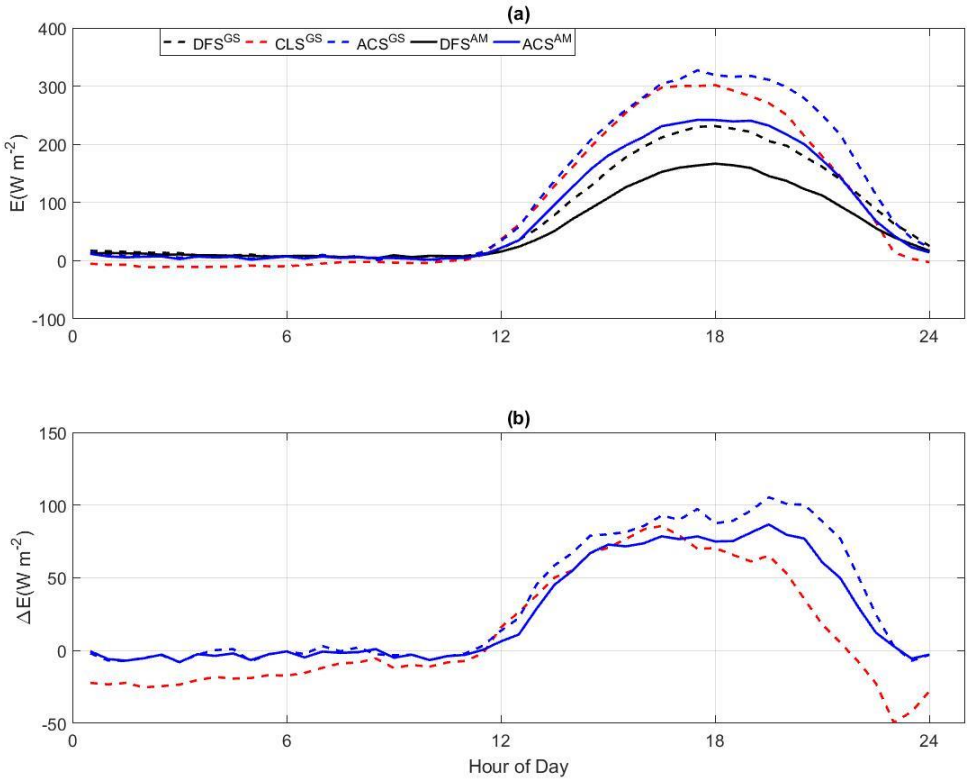

Figure 5.36 (a) Growing seasonal and annual MDCs, and (b) absolute changes of E at DFS, CLS, and ACS

Figure 5.36 (a) shows the growing seasonal and annual MDCs of E at DFS, CLS, and ACS. The phases of the diurnal cycles at all sites are almost identical. The maxima (minima) of

sub-daily E at DFS, CLS, and ACS are 231.36 (3.43) W m^{-2}, 301.77 (-11.24) W m^{-2}, and 327.37 (0.87) W m^{-2}, respectively. Deforestation increases maximum E and decreases minimum E. Reforestation increases both maximum and minimum E. The diurnal amplitudes of E at DFS, CLS, and ACS are 227.93 W m^{-2}, 313.01 W m^{-2}, and 326. 50 W m^{-2}, respectively. Both deforestation and reforestation increases the diurnal variation of E.

Figure 5.36 (b) shows the absolute changes of long-term MDCs of E at CLS and ACS with respect to DFS. ΔE at CLS and ACS are much greater during the daytime than during the nighttime, implying that land-use change alters E more significantly during the daytime than during the nighttime. The growing seasonal mean ΔE is greater than the annual mean ΔE, implying that land-use change alters E more significantly during the growing season than the dormant season.

Analysis of E at DFS, CLS, and ACS results in the following key findings:

(1) At long time scale, both deforestation and reforestation increase E. Reforestation influences E more significantly than deforestation does. E at the post-agricultural ecosystem is greater than E at the pre-agricultural ecosystem.

(2) At seasonal scale, deforestation increases the maximum and the seasonal variation of E, and decreases the minimum E. Reforestation increases both the maximum and minimum E, and decreases the seasonal variation of E. Deforestation alters E more significantly during the summer than during the winter. Reforestation alters E more significantly during the spring than

during the summer. For both pre- and post-agricultural ecosystems, about 70 % of the total E is from the growing season.

(3) At sub-daily scale, deforestation increases the maximum and the diurnal variation of E, and decreases the minimum E. Reforestation increases the maximum, the minimum, and the diurnal variation of E. Land-use change alters E more significantly during the daytime than during the nighttime.

5.5.4 Conclusion

This section investigates the evolution of the water cycle due to land-use change at CCZ using field observations and modeling results of humidity, soil moisture, and evapotranspiration. The key findings are:

(1) At long time scale, deforestation increases Cv and E, and decreases θ. Reforestation increases E, and decreases Cv and θ. Deforestation influences Cv and θ more and influences E less significantly than reforestation does. The post-agricultural ecosystem has larger Cv and E, and smaller θ than the pre-agricultural ecosystem.

(2) At seasonal scale, deforestation increases the maximum and the seasonal variations of Cv and E; and decreases the minimum Cv and E, and the seasonal variation of θ. Reforestation increases the minimum Cv and E, and the maximum E; and decreases the maximum Cv and the seasonal variations of Cv and E. Land-use change alters Cv more significantly during the summer than during the winter. Deforestation alters E more significantly during the summer than during the winter, and reforestation alters E more

significantly during the spring than during the summer due to the seasonality of the vegetation. For both pre- and post-agricultural ecosystems, about 70 % of the total E is from the growing season.

(3) At sub-daily scale, deforestation increases the minimum Cv, and the maximum and the diurnal variations of Cv and E, and decreases the minimum E. Reforestation increases the maximum, the minimum and the diurnal variation of E, and decreases the maximum, the minimum, and the diurnal variation of Cv. Land-use change alters Cv and E more significantly during the daytime than during the nighttime.

(4) Land-use change alters E more significantly than Cv. At annual scale, Cv and E at the post-agricultural ecosystem are 14 % and 45 % more than those at the pre-agricultural ecosystem, respectively.

5.6 Evolution of Carbon Cycle

The movement of carbon between the atmosphere, biosphere, and geosphere is described by the carbon cycle, which can be divided into geological and biological components. The geological carbon cycle operates on a time scale of millions of years, whereas the biological carbon cycle operates on a timescale of days to thousands of years. This section investigates the evolution of the biological carbon cycle due to land-use change at CCZ using field observations and modeling results of CO_2 concentration, CO_2 flux (Fc), and water use efficiency (WUE). As the EC system is not available at CLS, only data at the pre- and post-agricultural ecosystems are analyzed.

5.6.1 CO_2 Concentration

As atmospheric carbon dioxide is the most important greenhouse gas on Earth, atmospheric CO_2 concentration is one of the most concerned parameters in climate science. CO_2 concentration (CO_2) is measured at DFS and ACS for more than two years. Figure 5.37 shows long-term mean CO_2 at DFS and ACS. The long-term mean CO_2 is also summarized in Table 5.5. Figure 5.38 shows the monthly mean CO_2 at DFS and ACS. Figure 5.39 shows the growing seasonal and annual MDCs of CO_2 at DFS and ACS.

Table 5.5 Mean values of variables related to the carbon cycle

Period	Variables	Unit	DFS	ACS
GS	CO_2	ppm	375	367
	Fc	umol m^{-2} s^{-1}	-3.25	-6.42
	Fv	mmol m^{-2} s^{-1}	1.73	2.45
	WUE	umol CO_2 mmol H_2O^{-1}	1.88	2.61
AM	CO_2	ppm	376	376
	Fc	umol m^{-2} s^{-1}	-1.98	-5.48
	Fv	mmol m^{-2} s^{-1}	1.23	1.79
	WUE	umol CO_2 mmol H_2O^{-1}	1.61	3.06

Figure 5.37 (a) shows the growing seasonal and annual mean CO_2 at DFS and ACS. During the growing season, the mean CO_2 at DFS and ACS are 375 ppm and 367 ppm, respectively. The CO_2 at ACS is 8 ppm (2 %) smaller than that at DFS. The annual mean CO_2 at DFS and ACS are both 376 ppm. The growing seasonal CO_2 at the post-agricultural ecosystem is slightly lower than that at the pre-agricultural ecosystem, while the annual mean CO_2 at the two ecosystems are identical. Land-use change does not alter the long-term CO_2.

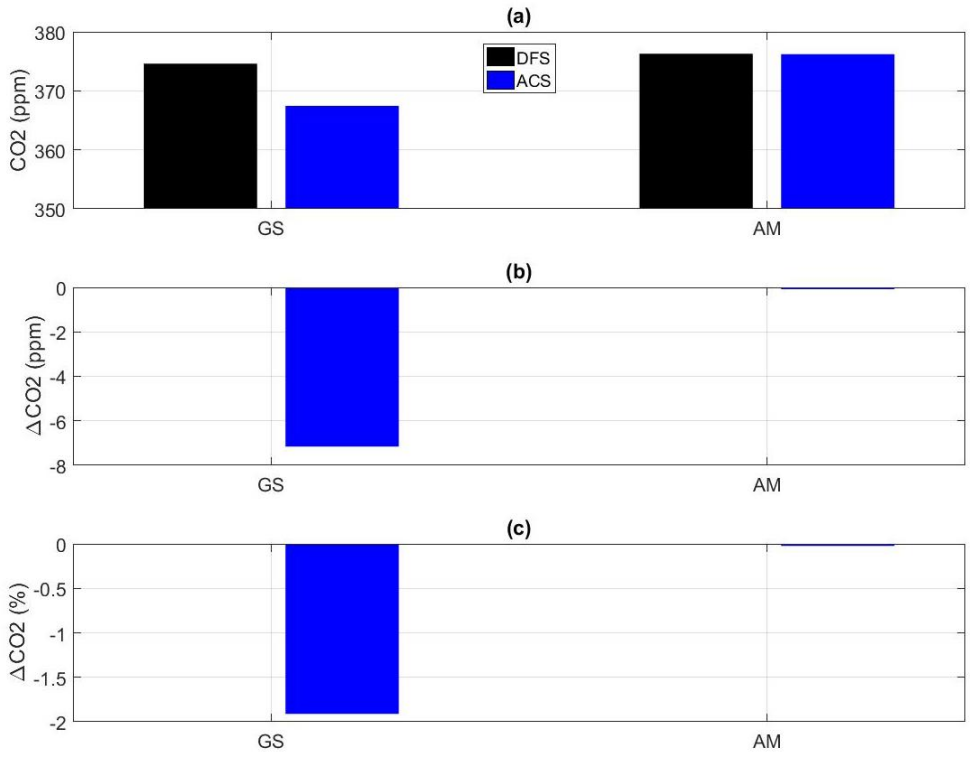

Figure 5.37 (a) Growing seasonal and annual mean, (b) absolute and (c) relative changes of CO_2 at DFS and ACS

Figure 5.38 (a) shows the monthly mean CO_2 at DFS and ACS. CO_2 at ACS is higher (lower) than that at DFS in winter (summer). CO_2 at ACS has a stronger seasonal cycle than that at DFS. CO_2 at DFS and ACS reach to maxima (minima) in February (June) and January (August), respectively. The phases of the seasonal cycles of CO_2 at pre- and post-agricultural ecosystems are comparable. The maximum (minimum) CO_2 at DFS and ACS are 381 (372) ppm and 406 (356) ppm, respectively. The seasonal amplitudes of CO_2 at DFS and ACS are 10 ppm and 50 ppm, respectively. Land-use change alters the seasonal variation of CO_2. Figure 5.38 (b) shows the absolute change of monthly CO_2 at ACS with respect to DFS. ΔCO_2 at ACS is positive from October to March, and negative from April to September. Land-use change alters the seasonal maximum and minimum CO_2. The

magnitude of ΔCO_2 is larger during the winter than during the summer, implying that land-use change alters CO_2 more significantly in winter than in summer.

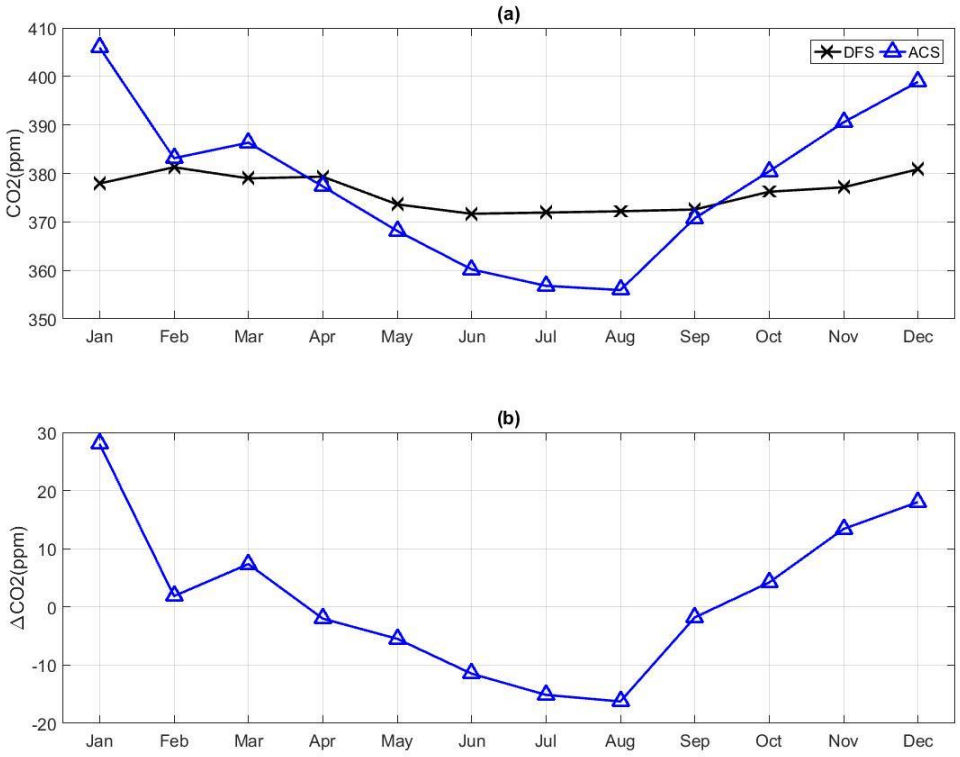

Figure 5.38 (a) Monthly mean, and (b) absolute changes of CO_2 at DFS and ACS

Figure 5.39 (a) shows the growing seasonal and annual MDCs of CO_2 at DFS and ACS. CO_2 reaches to a maximum in the early morning and a minimum in the late afternoon. The phases of the diurnal cycles are almost identical. During the growing season, the maxima (minima) of sub-daily CO_2 at DFS and ACS are 393 (362) ppm and 405 (336) ppm, respectively. Land-use change from the pre-agricultural ecosystem to the post-agricultural ecosystem increases the maximum CO_2 and decreases the minimum CO_2. Land-use change alters both the maximum and minimum CO_2 at sub-daily scale. The amplitudes of sub-

daily CO_2 at DFS and ACS are 31 ppm and 70 ppm, respectively. The diurnal variation of CO_2 at the post-agricultural ecosystem is 39 ppm (122%) more than that at the pre-agricultural ecosystem. Land-use change alters the diurnal variation of CO_2.

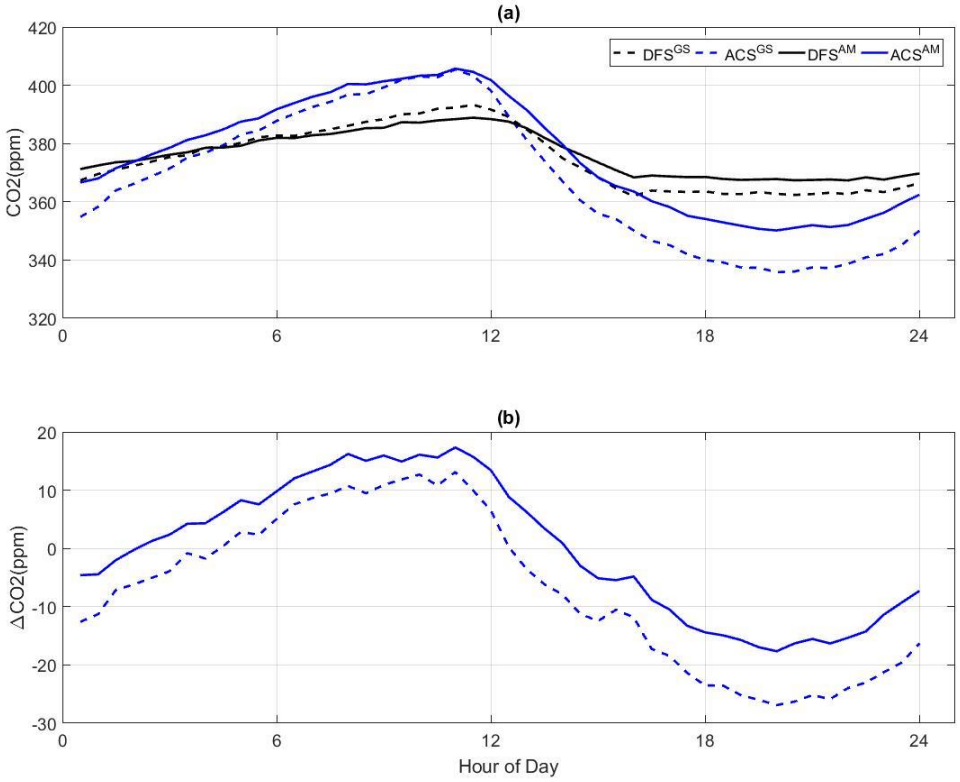

Figure 5.39 (a) Growing seasonal and annual MDCs, and (b) absolute changes of CO_2 at DFS and ACS

Figure 5.39 (b) shows the absolute changes of long-term MDCs of CO_2 at ACS with respect to DFS. During the growing season, the magnitude of ΔCO_2 during the daytime is higher than that during the nighttime, implying that land-use change alters CO2 more significantly during the daytime than during the nighttime. Throughout the year, the magnitude of ΔCO_2 during the daytime and during the nighttime are comparable, implying that at annual scale, land use change alters CO_2 equally strong during the daytime and the nighttime.

Analysis of CO_2 at DFS and ACS results in the following key findings:

(1) At long time scale, although the growing seasonal mean CO_2 at the post-agricultural ecosystem is slightly lower than that at the pre-agricultural ecosystem, the annual mean CO_2 at the two ecosystems are identical. Land-use change at CCZ does not alter the long-term CO_2.

(2) At seasonal scale, the post-agricultural ecosystem has a larger maximum CO_2 and a smaller minimum CO_2, and thus a larger seasonal variation of CO_2 than the pre-agricultural ecosystem. Land-use change at CCZ alters the maximum, minimum and seasonal variation of CO_2. The magnitude of ΔCO_2 between two ecosystems is larger during the winter than during the summer. Land-use change alters CO_2 more significantly in winter than in summer.

(3) At sub-daily scale, the post-agricultural ecosystem has a larger maximum CO_2 and a smaller minimum CO_2, and thus a larger diurnal variation of CO_2 than the pre-agricultural ecosystem does. Land-use change at CCZ alters the maximum, the minimum and the diurnal variation of CO_2. During the growing season, land-use change alters daytime CO_2 more than nighttime CO_2; while throughout the year, land-use change alters daytime and nighttime CO_2 equally strong.

The difference of CO_2 at pre- and post-agricultural ecosystem is due to the difference of the canopy types of the pre- and post-agricultural ecosystem. The pre-agricultural ecosystem is deciduous broadleaf forest that has a strong seasonal cycle of photosynthesis. The post-agricultural ecosystem is fast-growing evergreen needleleaf forest that has strong

photosynthesis and respiration throughout the year. Therefore, CO_2 at the post-agricultural ecosystem has stronger diurnal variation and seasonal variation than the pre-agricultural ecosystem.

5.6.2 CO_2 Flux

Carbon exchange between the terrestrial ecosystem and the atmosphere is one of the most important processes in the global carbon cycle. Understanding carbon exchange fluxes is essential for accurately predicting and evaluating the carbon budget. CO_2 flux (Fc) between the ecosystem and the atmosphere is measured using the EC systems at DFS and ACS. Many gaps of the EC measured Fc are filled using the HOD model described in Chapter 4. The long-term mean, MDCs, and monthly mean Fc at DFS and ACS are computed. Figure 5.40 shows the long-term mean and changes of Fc at DFS and ACS. The long-term mean Fc are also summarized in Table 5.5. Figure 5.41 shows the monthly mean Fc at DFS and ACS. Figure 5.42 shows the growing seasonal and annual MDCs of Fc at DFS and ACS.

Figure 5.40 (a) shows the growing seasonal and annual mean Fc at DFS and ACS. Fc at both DFS and ACS are negative, implying that both the pre- and post-agricultural ecosystems are a carbon sink during the growing season and throughout the year. Both the growing seasonal and annual mean Fc at ACS are greater than those at DFS. During the growing season, the mean Fc at DFS and ACS are -3.25 umol m^{-2} s^{-1} and -6.42 umol m^{-2} s^{-1}, respectively. Fc at ACS is 3.17 umol m^{-2} s^{-1} (98 %) more than that at DFS. Throughout the year, the annual mean Fc at DFS and ACS are -1.98 and -5.48, respectively. Annual mean Fc at ACS is 3.5 umol m^{-2} s^{-1} (177 %) more than that at DFS. The carbon intake at the post-agricultural ecosystem is greater than that at the pre-agricultural ecosystem. Land-

use change at CCZ alters annual mean Fc. The difference of the annual mean Fc between the two ecosystems is greater than that of the growing seasonal mean Fc, implying that land-use change alters Fc more in the dormant season than in the growing season.

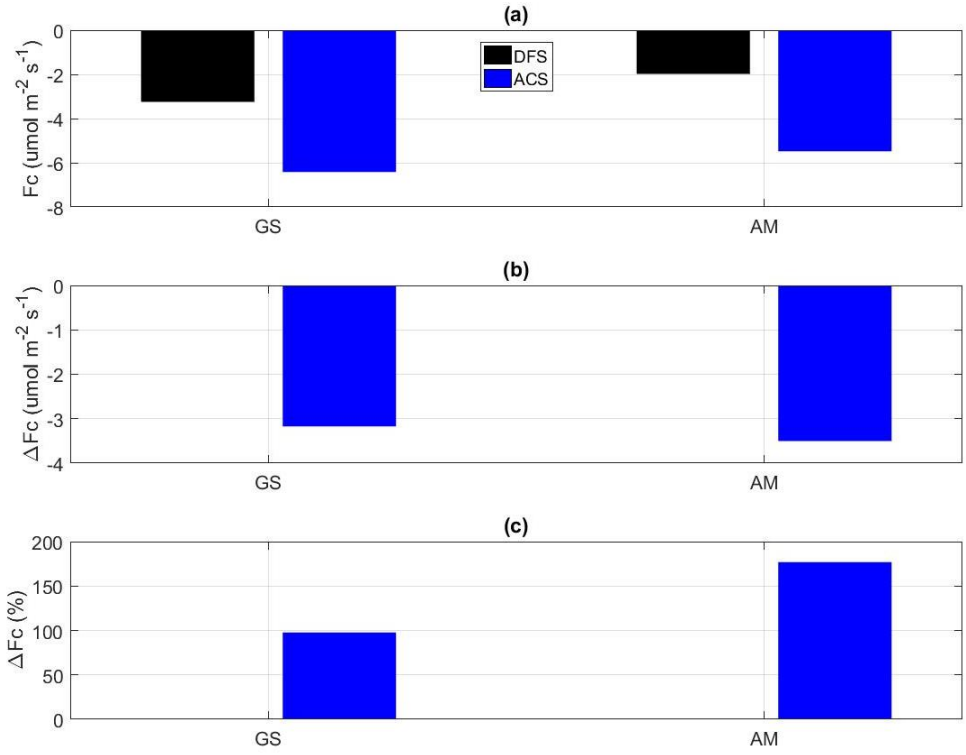

Figure 5.40 (a) Growing seasonal and annual mean, (b) absolute and (c) relative changes of Fc at DFS and ACS

Figure 5.41 (a) shows the monthly mean Fc at DFS and ACS. The seasonal cycles of Fc at DFS and ACS are obvious. Monthly mean Fc at ACS is always negative, implying that the post-agricultural ecosystem is always a carbon sink throughout the year. Monthly mean Fc at DFS is negative in all months except for March and November, when the pre-agricultural ecosystem is a carbon source. Fc at ACS is constantly smaller than that at DFS, implying the post-agricultural ecosystem is a stronger carbon sink than the pre-agricultural ecosystem for every month. Fc at DFS and ACS reach to maxima (minima) in March (May)

and December (May), respectively. The phases of the seasonal cycles at two ecosystems are slightly different. The phase of the seasonal cycle of Fc at DFS is influenced by the seasonality of both solar radiation and deciduous trees, and thus Fc increases from January to March as the trees are without leaves. The phase of the seasonal cycle of Fc at ACS is dominated by the seasonality of solar radiation. The land-use change at CCZ alters the phase of the seasonal cycle of Fc.

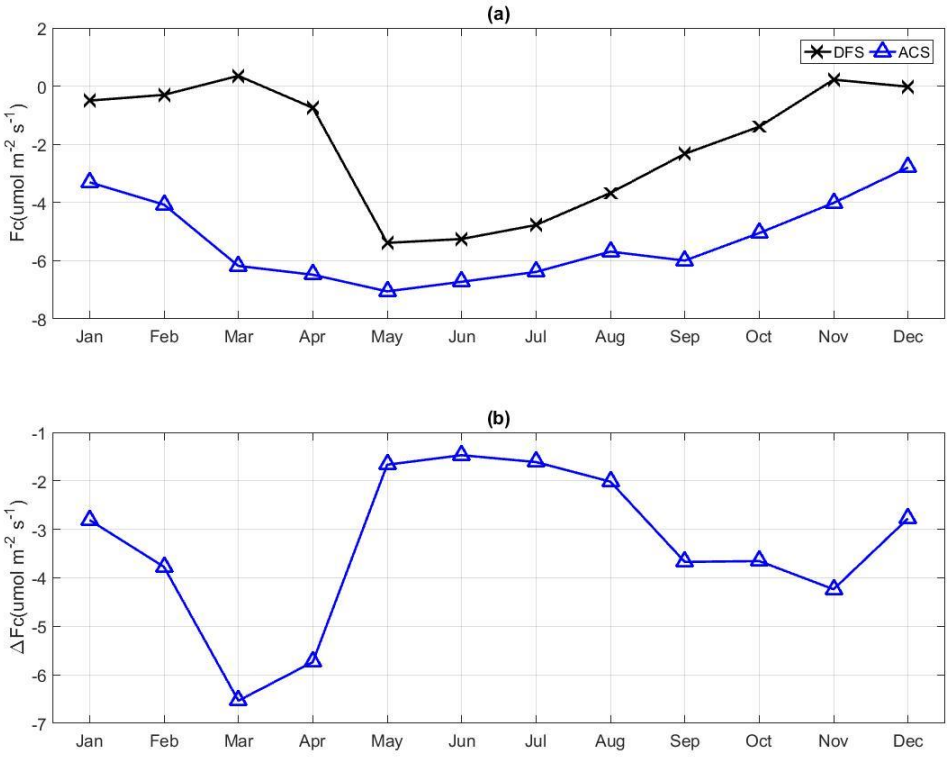

Figure 5.41 (a) Monthly mean, and (b) absolute changes of Fc at DFS and ACS

The maxima (minima) of monthly mean Fc at DFS and ACS are 0.35 (-5.39) umol m^{-2} s^{-1} and -2.79 (-7.05) umol m^{-2} s^{-1}, respectively. Land-use change at CCZ decreases both the maximum and minimum Fc at seasonal scale. The seasonal amplitudes of Fc at DFS and

ACS are 5.74 umol m^{-2} s^{-1} and 4.26 umol m^{-2} s^{-1}, respectively. Land-use change at CCZ decreases the seasonal variation of Fc. Figure 5.41 (b) shows the absolute change of Fc at ACS with respect to DFS. The magnitude of ΔFc is greatest in spring and smallest in summer, implying that the land-use change alters Fc more significantly in spring than in summer.

Table 5.6 Accumulative Fc (gC m^{-2})

Month	DFS	ACS
Jan	-16	-106
Feb	-9	-118
Mar	11	-199
Apr	-23	-202
May	-173	-227
Jun	-163	-209
July	-153	-205
Aug	-118	-183
Sep	-72	-187
Oct	-45	-162
Nov	7	-125
Dec	-1	-90
GS	-620	-1224
Annual	-755	-2012

As important parameters to understand the carbon cycle, the monthly and annual accumulative Fc at DFS and ACS are computed and summarized in Table 5.6. The growing seasonal accumulative Fc at DFS and ACS are -620 gC m^{-2} and -1224 gC m^{-2}, respectively. The annual accumulative Fc at DFS and ACS are -755 gC m^{-2} and -2012 gC m^{-2}, respectively. The percentages of the growing seasonal accumulative Fc to the annual accumulative Fc at DFS and ACS are 82 % and 61 %, respectively. 82 % and 61 % of carbon at pre- and post-agricultural ecosystems is stored during the growing season,

respectively. During the dormant season, the post-agricultural ecosystem is more effective in storing carbon than the pre-agricultural ecosystem.

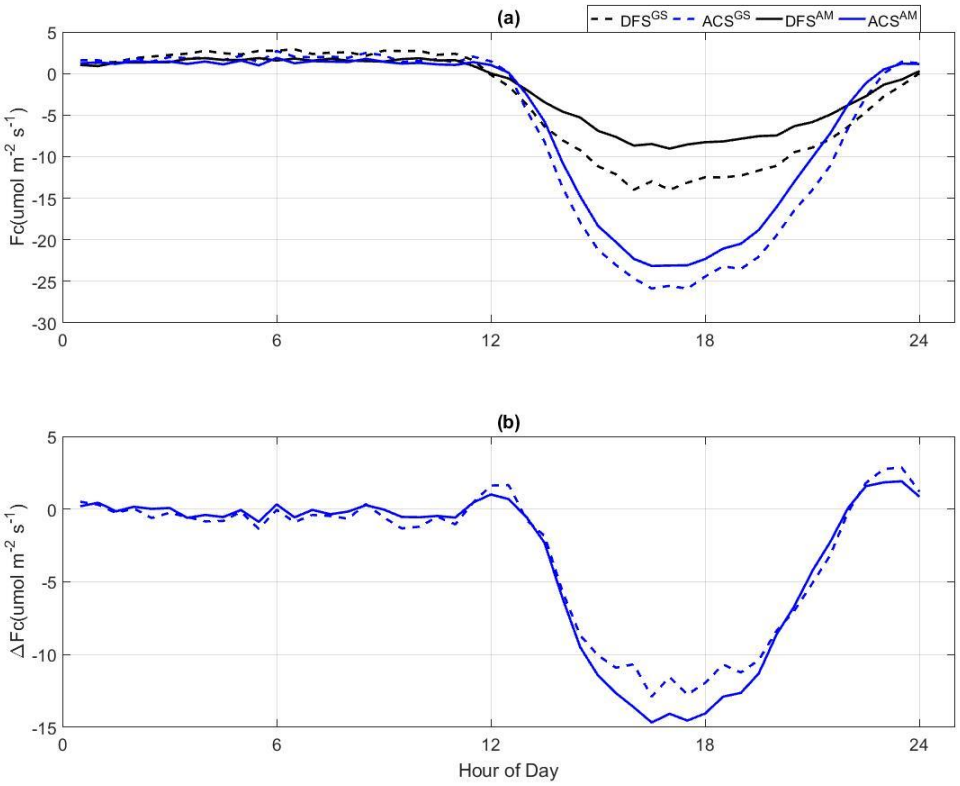

Figure 5.42 (a) Growing seasonal and annual MDCs, and (b) absolute changes of Fc at DFS and ACS

Figure 5.42 (a) shows the growing seasonal and annual mean MDCs of Fc at DFS and ACS. The phases of the diurnal cycles are almost identical. The nighttime Fc at DFS and ACS are both almost zero. The daytime Fc at ACS is much greater in magnitude than that at DFS. During the growing season, the maxima (minima) of sub-daily Fc at DFS and ACS are -14.0 (2.92) umol m^{-2} s^{-1} and -25.88 (2.70) umol m^{-2} s^{-1}, respectively. Both the maximum and minimum Fc at ACS are smaller than that at DFS. Land-use change at CCZ decreases both the maximum and minimum Fc at sub-daily scale. The diurnal amplitudes

of sub-daily Fc at DFS and ACS are 16.92 umol m^{-2} s^{-1} and 28.58 umol m^{-2} s^{-1}, respectively. The diurnal variation of Fc at the post-agricultural ecosystem is 11.66 umol m^{-2} s^{-1} (69 %) greater than that at the pre-agricultural ecosystem. The land-use change at CCZ increases the diurnal variation of Fc.

Figure 5.42 (b) shows the absolute changes of the long-term MDCs of Fc at ACS with respect to DFS. ΔFc are much greater during the daytime than during the nighttime, implying that land-use change alters the daytime Fc more significantly. The growing seasonal ΔFc is slightly smaller than the annual mean ΔFc during the daytime, implying that land-use change alters Fc more significantly during the dormant season than the growing season.

The analysis of Fc at DFS and ACS results in the following key findings:

(1) At annual scale, the annual carbon intake at the post-agricultural ecosystem is 2.8 times of that at the pre-agricultural ecosystem. Land-use change at CCZ increases the annual Fc.

(2) At seasonal scale, the post-agricultural ecosystem is always a carbon sink for every month, while the pre-agricultural ecosystem is a carbon source in March and November. Land-use change at CCZ decreases the maximum, the minimum, and the seasonal variation of Fc. Land-use change alters Fc more significantly in spring than in winter.

(3) At sub-daily scale, the maximum daytime carbon intake at the post-agricultural ecosystem is 1.6 times more than that at the pre-agricultural ecosystem. Land-use change decreases the maximum and minimum of Fc,

and increases the diurnal variation of Fc. Land-use change alters daytime Fc more significantly than nighttime Fc.

The difference of Fc at the pre- and post-agricultural ecosystems at CCZ is due to the differences of the ecosystems in canopy types and maturity. The pre-agricultural ecosystem is mature deciduous broadleaf forest that has a strong seasonal cycle of photosynthesis and a strong respiration. The pre-agricultural ecosystem is mostly a carbon sink. However, during the winter, it could become a carbon source due to the weak photosynthesis and strong respiration. The post-agricultural ecosystem is fast-growing evergreen needleleaf forest that has strong photosynthesis and respiration throughout the year. Therefore, the post-agricultural ecosystem is a stronger carbon sink with a weaker seasonal variation than the pre-agricultural ecosystem.

5.6.3 Water Use Efficiency

Water use efficiency (WUE) refers to the ratio of water used in plant metabolism to water lost by plant through transpiration. WUE is an important indicator of the plant tolerance of drought. Increasing WUE could increase yield production and decrease transpirational water loss [*Jones*, 2004]. In this study, WUE is defined as the flux ratio: CO_2 fluxes divided by water vapour flux [*E.A. et al.*, 2007] (the negative sign is added for convenience)

$$\boldsymbol{WUE = -\frac{F_c}{F_v}} \qquad \textbf{5.6}$$

where Fc is the long-term mean CO_2 flux (umol m^{-2} s^{-1}), Fv is the long-term mean H_2O flux (mmol m^{-2} s^{-1}), and the unit of WUE is umolCO_2 mmolH_2O^{-1}. A greater WUE indicates the ecosystem stores more carbon with the same amount of evapotranspiration. WUE is

calculated using the growing seasonal and annual mean Fc and Fv at DFS and ACS. The long-term mean values of WUE are summarized in Table 5.5. Figure 5.43 shows the long-term mean and changes of WUE at DFS and ACS.

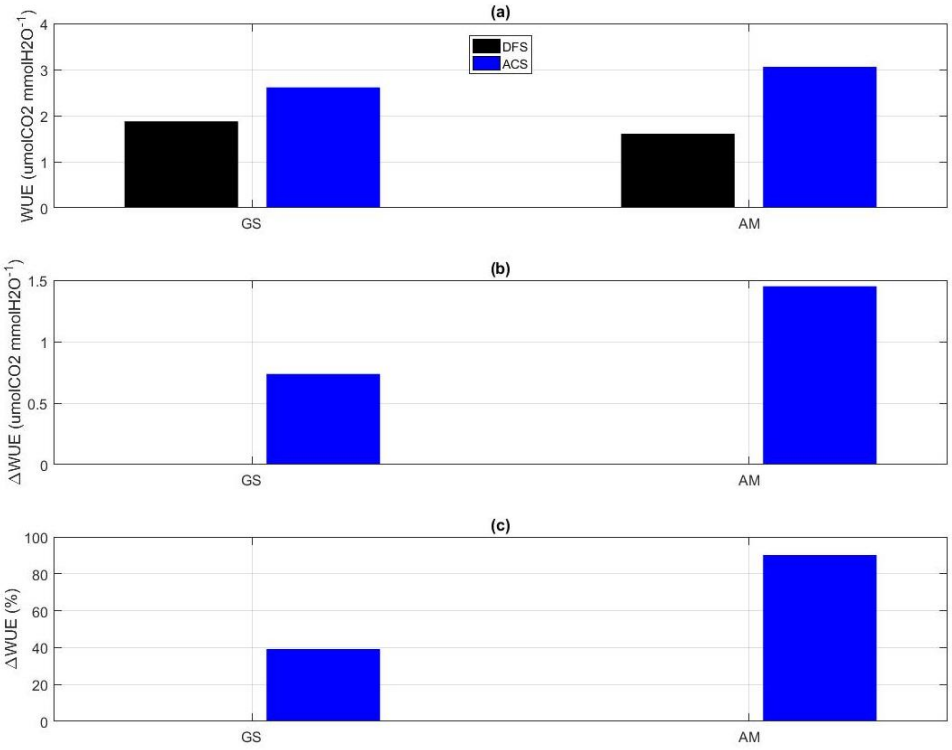

Figure 5.43 (a) Growing seasonal and annual mean, (b) absolute and (c) relative changes of WUE at DFS and ACS

Figure 5.43 (a) shows the growing seasonal and annual mean WUE at DFS and ACS. The growing seasonal and annual mean WUE at ACS are higher than that at DFS. The growing seasonal (annual) mean WUE at DFS and ACS are 1.88 (1.61) umolCO_2 mmolH_2O^{-1} and 2.61 (3.06) umolCO_2 mmolH_2O^{-1}, respectively. At DFS, the growing seasonal mean WUE is greater than the annual mean, implying that the WUE during growing season is greater than that during the dormant season. The pre-agricultural ecosystem is more efficient in storing carbon during the growing season than the dormant season. At ACS, the growing

seasonal mean WUE is smaller than the annual mean, implying that the WUE during growing season is smaller than that during the dormant season. The post-agricultural ecosystem is more efficient in storing carbon during the dormant season than the growing season.

The growing seasonal and annual mean WUE at ACS are 0.73 umolCO_2 mmolH_2O^{-1} (39 %) and 1.45 umolCO_2 mmolH_2O^{-1} (90 %) more than those at DFS, respectively. The annual ΔWUE at DFS and ACS is greater than that of the growing seasonal ones, implying that the difference of WUE at DFS and ACS during the dormant season is much greater than that during the growing season. The post-agricultural ecosystem uses water more efficiently than the pre-agricultural ecosystem throughout the year and especially during the dormant season. Land-use change at CCZ increases the water use efficiency throughout the year and especially during the dormant season.

5.6.4 Conclusion

This section investigates the evolution of the carbon cycle due to land-use change at CCZ using field observations and modeling results of CO_2, Fc, and WUE at DFS and ACS. The key findings are

(1) At annual scale, the annual mean CO_2 at pre- and post-agricultural ecosystems are identical, while the annual mean Fc and WUE at the post-agricultural ecosystem are 177 % and 90 % more than those at the pre-agricultural ecosystem, respectively. The managed regrew pine forest absorbs more carbon and uses water more efficiently than the primary forest.

(2) At seasonal scale, the post-agricultural ecosystem has higher maximum monthly CO_2 and carbon intake, lower minimum monthly CO_2, a greater seasonal variation of CO_2, and a smaller seasonal variation of Fc than the pre-agricultural ecosystem. The post-agricultural ecosystem is a carbon sink for all months, while the pre-agricultural ecosystem is a carbon source in March and November. The pre-agricultural ecosystem uses water more efficiently during the growing season than during the dormant season, while the post-agricultural ecosystem uses water more efficiently during the dormant season. Land-use change alters CO_2 and Fc more significantly during the winter and the spring than during other seasons, respectively.

(3) At sub-daily scale, the post-agricultural ecosystem has higher maximum CO_2 and carbon intake, lower minimum CO_2, and larger diurnal variations of CO_2 and Fc than the pre-agricultural ecosystem. During the growing season, land-use change alters daytime CO_2 more than nighttime CO_2; while throughout the year, land-use change alters daytime and nighttime CO_2 equally strong. Land-use change alters Fc more significantly during the daytime than during the nighttime.

The differences of CO_2, Fc, and WUE at the pre- and post-agricultural ecosystems are mainly due to the differences of the two ecosystems in land covers and maturity. The pre-agricultural ecosystem is mature deciduous broadleaf forest that has a strong seasonal cycle of photosynthesis and a strong respiration. The post-agricultural ecosystem is managed fast-growing evergreen needleleaf forest that has strong photosynthesis and respiration

throughout the year. Therefore, the post-agricultural ecosystem has larger diurnal and seasonal variations of CO_2, annual carbon intake and WUE.

5.7 Discussions

5.7.1 Interannual Variability of State and Flux Variables

The eco-hydro-meteorological variables used to study the interannual variability of pre- and post-agricultural ecosystems are characterized by the state and flux variables:

- State variables: air temperature (Ta), soil temperature (Ts), water vapor density (Cv), and CO_2 concentration (CO_2).
- Flux variables: sensible (H), soil (G), and latent heat fluxes (E), CO_2 flux (Fc) and water use efficiency (WUE).

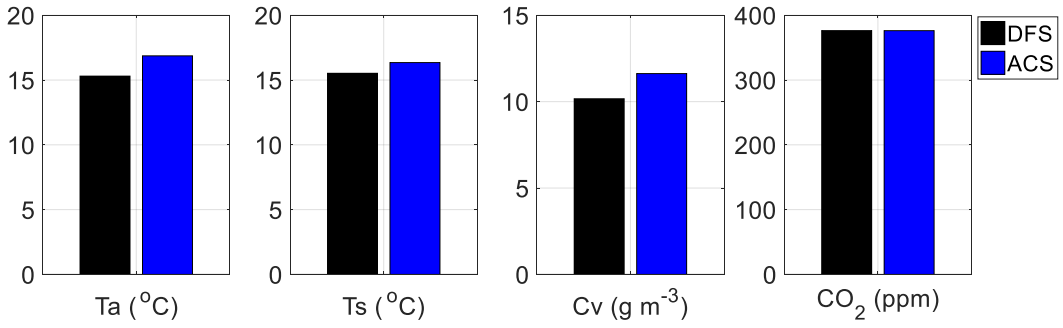

Figure 5.44 Interannual variability of state variables at DFS and ACS

The interannual variabilities of the state variables at pre- (DFS) and post (ACS)-agricultural ecosystems are shown in Figure 5.44. The annual mean Ta, Ts, and Cv at ACS are slightly greater than those at DFS. The annual mean CO_2 at DFS and ACS are identical. Figure 5.45 shows the interannual variability of the flux variables at DFS and ACS. The

annual mean G at DFS and ACS are both almost zero, indicating that G over forest is negligible. The annual H, E, Fc, and WUE at ACS are significantly greater in magnitude than those at DFS. Figure 5.46 shows the relative changes of the state and flux variables through the Calhoun's land-use history. Relative changes of the flux variables are significantly higher than those of the state variables. Quantitatively, the averaged relative change of the flux variables is seven times greater than that of the state variables.

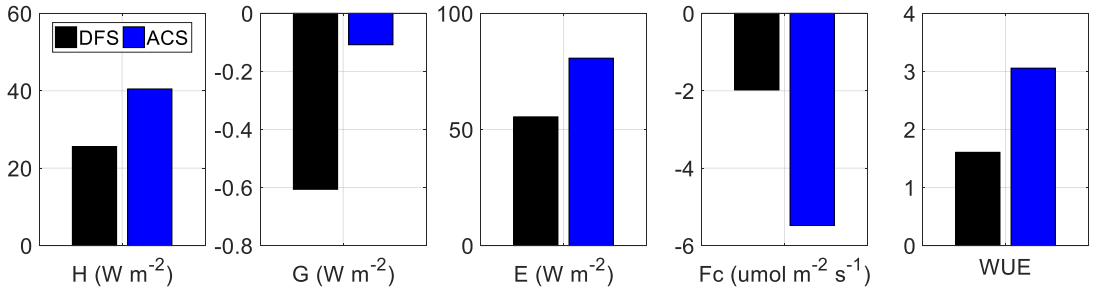

Figure 5.45 Interannual variability of flux variables at DFS and ACS

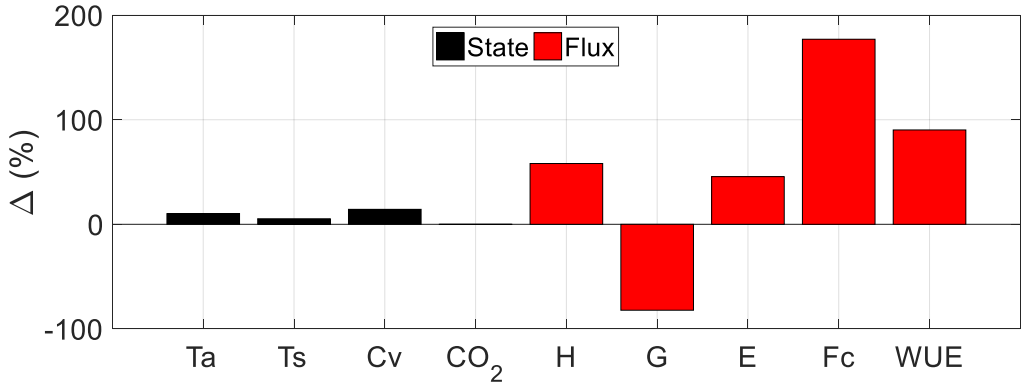

Figure 5.46 Relative changes of state and flux variables from DFS to ACS

5.7.2 Calhoun's Land-Use Change and Global Climate Change

One of the advantages of the space-for-time approach is that it separates the impacts of the global climate change and the local land-use change on the local climate. However, in reality, the global climate change and the local land-use change influence the local climate simultaneously. Figure 5.47 shows the historic records of total solar irradiation (TSI) on the Earth since 1700, and air temperature (Ta) and precipitation (Rain) in the southeast US since 1895. The TSI records are calculated using the solar irradiance variability models [*Coddington et al.*, 2016]. The Ta and Rain records are field measurements since 1895 obtained from National Oceanic and Atmospheric Administration (NOAA).

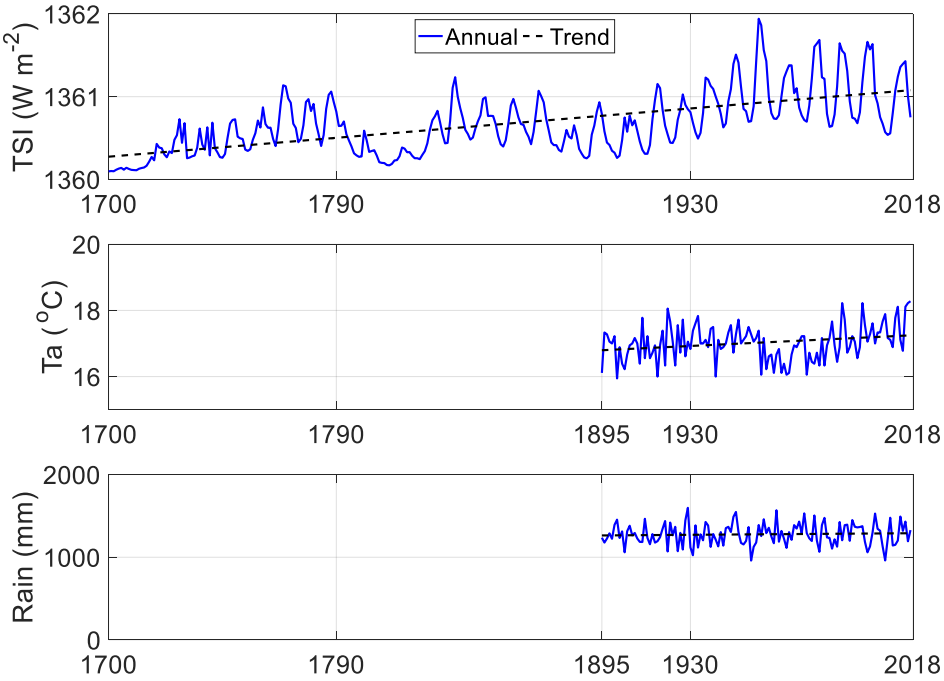

Figure 5.47 Global TSI since 1700, and Ta and Rain in Southeast US since 1895

The trend of the global TSI is only 0.25 W m^{-2} per century. Given that the mean TSI is about 1361 W m^{-2}, the relative change of TSI from 1700 to 2018 is less than 0.1 %. The trends of Ta and Rain in the southeast US are 0.37 °C per century, and 22 mm per century,

respectively. The relative changes of the southeastern Ta and Rain are less than 2 % per century, much smaller than the relative changes (more than 10 %) of the variables related to the energy and water cycle at Calhoun. Therefore, Calhoun's local climate change since 1700s is mainly due to its land-use change rather than the global climate change.

5.7.3 Carbon Fertilization Effect

Although the global TSI, and the southeastern Ta and Rain only increased slightly since 1700, the Earth's atmospheric CO_2 concentration has increased dramatically. Figure 5.48 shows the annual atmospheric CO_2 concentration (CO_2) of the North Hemisphere since 1700 and of the Mauna Loa Observatory (MLO) since 1959. The CO_2 data for the North Hemisphere are compiled by the Institute for Atmospheric and Climate Science at ETH Zurich, Switzerland and downloaded from www.CO2.earth. MLO is well known for the continuous monitoring of atmospheric CO_2 concentration since March 1958. Data at MLO can be obtained from the Earth System Research Laboratory of NOAA.

Through the Calhoun's land-use history, the CO_2 concentration of the North Hemisphere has increased 130 ppm. The free-air CO_2 enrichment (FACE) experiment in the Duke Forest found that the net primary productivity (NPP) or the net CO_2 flux increases about 27 % given CO_2 increased by 200 ppm [*Schlesinger et al.*, 2006], which might be an overestimation according to recent studies [*Wieder et al.*, 2015]. Assuming NPP of Calhoun Forest increases 18 % given CO_2 increased by 130 ppm since 1700 according to the FACE experiment, NPP at the primary forest in the 1700s would be smaller than that at the current primary forest. Therefore, the actual difference of NPPs at pre- and post-agricultural ecosystems is greater than the estimated difference according to this study,

which strengthens this study's argument that the Calhoun's land-use change alters the CO_2 flux more than the atmospheric CO_2 concentration.

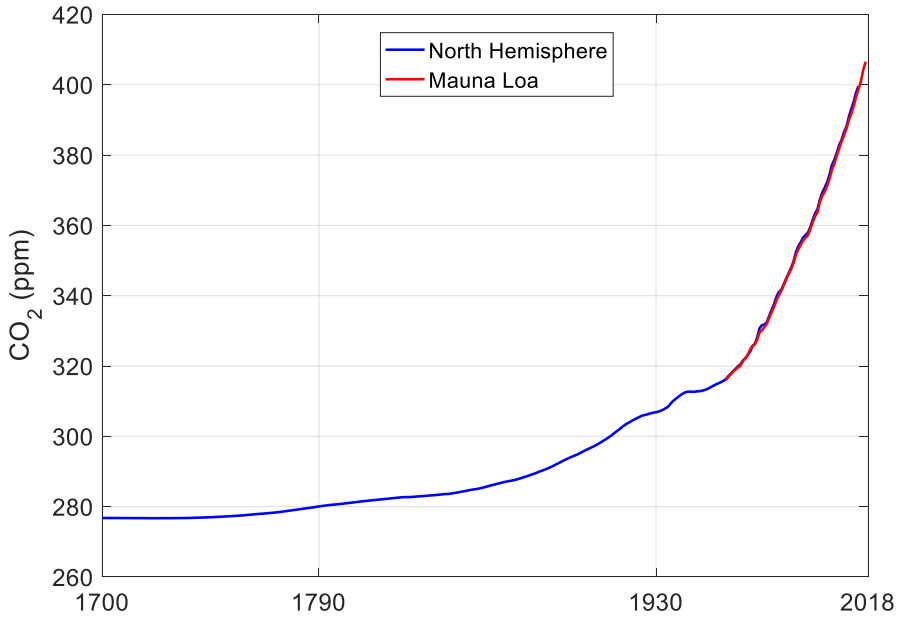

Figure 5.48 CO_2 concentration in North Hemisphere and Mauna Loa since 1700

5.8 Summary

This chapter investigates the evolution of the energy, water, and carbon cycle due to land-use change at CCZ by comparing the eco-hydro-meteorological variables at different ecosystems assumed in a chronological order according to the Space-For-Time substitution approach. The variables are categorized into four groups to study the evolution of temperature, the energy cycle, the water cycle, and the carbon cycle, respectively. The detailed findings are

(1) At long time scale, deforestation increases Ta, Ts, H, G, Cv, and E, and decreases θ. Reforestation increases E and decreases Ta, Ts, H, G, Cv, and

θ. Note that both deforestation and reforestation increase E and decrease θ. The post-agricultural ecosystem has greater Ta, Ts, Rn, H, Cv, E, carbon intake, and WUE, and smaller G and θ than the pre-agricultural ecosystem. The influence of deforestation on microclimate change is generally greater than that of reforestation. Variables such as Ta, Ts, H, G, Cv, and θ changes more due to deforestation than due to reforestation. However, E increases more due to reforestation than due to deforestation.

(2) At seasonal scale, deforestation increases seasonal variations of Ta, Ts, H, G, Cv, and E, and decreases seasonal variations of θ. Reforestation decreases seasonal variations of Ta, Ts, Ts@30cm, H, G, Cv, and E. Deforestation increases the maxima of Ta, Ts, H, G, Cv, and E. Reforestation decreases the maxima of Ta, Ts, H, G, Cv, and increases the maximum E. Deforestation increases the minima of H, and G, and decreases the minima of Ta, Ts, Cv, and E. Reforestation increases the minima of Ta, Ts, Cv, and E, and decreases the minima of H and G. Land-use change alters Ta, Ts, H, G, and Cv more significantly during the summer than during other seasons. Deforestation alters E more significantly during the summer, and reforestation alters E more significantly during the spring. Land-use change at CCZ alters CO_2 more significantly in winter and Fc more significantly in spring. The post-agricultural ecosystem has greater seasonal variations of Ta, Ts, Rn, H, G, Cv, E, and CO_2, and smaller seasonal variations of θ and Fc than the pre-agricultural ecosystem.

(3) At sub-daily scale, deforestation increases diurnal variations of Ta, Ts, H, G, Cv, and E. Reforestation decreases diurnal variations of Ta, Ts, Ts@30cm, and Cv, and increases diurnal variations of H and E. Note that both deforestation and reforestation increase the diurnal variations of H and E. Deforestation increases the maxima of Ta, Ts, H, G, Cv, and E. Reforestation increases the maxima of H and E, and decreases the maxima of Ta, Ts, G, and Cv. Deforestation increases the minima of Ta, Ts, H, Cv, and decreases the minima of G and E. Reforestation increases the minima of H, G, and E, and decreases the minima of Ta, Ts, and Cv. The post-agricultural ecosystem has greater diurnal variations of Ta, Ts, Rn, H, G, AH, E, CO_2 and Fc than the pre-agricultural ecosystem. Land-use change alters almost all variables more significantly during the daytime than during the nighttime. However, throughout the year, land-use change alters daytime and nighttime CO_2 equally strong.

(4) The differences of the pre- and post-agricultural ecosystems in vegetation types and maturity are the major reason for the differences of the two ecosystems in seasonal cycles of H, CO_2, Fc and WUE.

Three conclusions are drawn from these findings. Firstly, the averaged relative change of the flux variables due to land-use change is seven times greater than that of the state variables. Although the state variables including Ta, Ts, Cv, and CO_2 at pre- and post-agricultural ecosystems are almost identical, the flux variables including H, E, Fc and WUE at the post-agricultural ecosystem are almost twice of those at the pre-agricultural ecosystem. Secondly, deforestation alters land surface variables including the state and flux

variables six times more than reforestation does. Thirdly, land-use change alters soil conditions such as Ts, G, and θ three times more than the corresponding air conditions such as Ta, H, and Cv. Therefore, microclimate change would be significantly underestimated using the most concerned and commonly measured variables such as air temperature, relative humidity, and atmospheric CO_2 concentration.

CHAPTER 6. CONCLUSIONS AND FUTURE RESEARCH

6.1 Research Contributions and Findings

This thesis studies the evolution of the energy, water, and carbon cycle due to land-use change at Calhoun critical zone (CCZ) using field observations and modeling results at different ecosystems assumed in a chronological order according to the CCZ's land-use history. Land-use change such as deforestation, cultivation, and reforestation alters the energy, water, and carbon cycle by changing temperature, heat fluxes, evapotranspiration, and carbon intake. CCZ is an ideal platform for investigating this issue as Calhoun has experienced a huge land-use change including severe deforestation in the 18^{th} century, intensive cultivation in the 19^{th} century, and tremendous reforestation in the 20^{th} century. This study selects current CCZ's ecosystems such as mature forest, cropland, and young pine forest as CCZ's historic ecosystems in a chronological order, and designs a thorough instrumentation to measure energy, water, and carbon fluxes among other eco-hydro-meteorological variables. By comparing field observations and modeling results of the eco-hydro-meteorological variables at different ecosystems, the evolution of the energy, water, and carbon cycle due to land-use change is quantitatively investigated.

Chapter 3 describes the eco-hydro-meteorological observations at CCZ. Three field observational sites were constructed at CCZ. The above-canopy flux tower site (ACS) was constructed at the CCZ young pine forest in August 2016. The below-canopy flux tower site (BCS) was constructed at the same young pine forest in May 2017. The cropland site (CLS) was constructed at the CCZ hunting field in February 2017. The observational system at CCZ measures more than 300 eco-hydro-meteorological variables from 7 m

below ground to 9 m above ground and records more than 500 GB raw data. Variables essential to the energy, water, and carbon cycle are converted to a half-hourly time resolution. Data samples during a typical sunny ten-day period are plotted to exhibit the ordinary diurnal cycles of the variables of interest. All available data are plotted to exhibit the long-term seasonal cycles of essential variables and the total observational time span. The observations are valuable to test and improve the existing models of land surface processes, and to understand the evolution of the energy, water, and carbon cycle due to land-use change at CCZ.

Chapter 4 introduces three new models of land surface turbulent fluxes; tests them using field observations at ACS, BCS, and Duke Forest site (DFS); and applies them in gap-fillings and estimations of turbulent fluxes. The key findings of Chapter 4 are:

(1) Bases on the energy balance analysis, the observed heat fluxes at ACS have a good energy balance closure, those at BCS have a lack of energy balance closure, and those at DFS have a reasonable energy balance closure.

(2) The maximum entropy production (MEP) model of land surface heat fluxes estimates heat fluxes at all sites accurately with relative errors no greater than 9 %, justifying the application of the MEP model in gap-fillings and estimations of the turbulent heat fluxes at CCZ field sites.

(3) A proof-of-concept study of the half-order derivative (HOD) model implies the feasibility of surface gas fluxes derived from single-level near surface gas concentration data. The case studies suggest that the HOD model is able to capture the diurnal and seasonal variations of gas fluxes using fewer input

variables and model parameters than the conventional models such as the Bulk-Transfer model.

(4) Another proof-of-concept study of the extreme solution model demonstrates the application of estimating friction velocity from sensible heat flux without using wind speed data. Case studies using data from five field sites with diverse climate and vegetation types validate the model at sub-daily, daily, and seasonal scales. The good results of the model indicate the possibility for estimating land surface friction velocity and wind speed using remote sensing only observations as sensible heat flux in the model is estimated using the MEP model in terms of net radiation.

(5) The proposed models are reliable in gap-fillings of eddy-covariance heat and CO_2 fluxes as they are bases on strong physical concepts rather than experience and statistics. The MEP model fills 8000 data gaps of heat fluxes at BCS, and the combination of the three models fills 2000 data gaps of CO_2 fluxes at DFS.

With the field observations in Chapter 3, and the gap-filled data and modeling results in Chapter 4, Chapter 5 describes the evolution of the energy, water, and carbon cycle due to land-use change at CCZ by comparing the eco-hydro-meteorological variables at different ecosystems assumed in a chronological order according to the Space-For-Time substitution approach. The key findings of Chapter 5 are:

- At long time scale, deforestation increases air temperature (Ta), soil temperature (Ts), sensible heat flux (H), soil heat flux (G), water vapour density (Cv), and evapotranspiration (E), and decreases surface soil

moisture (θ). Reforestation decreases Ta, Ts, H, G, Cv, and θ, and increases E. Note that both deforestation and reforestation increase E and decrease θ. The post-agricultural ecosystem has greater Ta, Ts, Rn, H, Cv, E, carbon intake, and water use efficiency (WUE), and smaller G and θ than the pre-agricultural ecosystem. The influence of deforestation on microclimate change is generally greater than that of reforestation. Variables such as Ta, Ts, H, G, Cv, and θ changes more due to deforestation than due to reforestation. However, E increases more due to reforestation than due to deforestation.

- At seasonal scale, deforestation increases seasonal variations of Ta, Ts, H, G, Cv, and E, and decreases seasonal variations of θ. Reforestation decreases seasonal variations of Ta, Ts, soil temperature at 30 cm depth (Ts@30cm), H, G, Cv, and E. Land-use change alters Ta, Ts, H, G, and Cv more significantly during the summer than during other seasons. Deforestation alters E more significantly during the summer, and reforestation alters E more significantly during the spring. Land-use change at CCZ alters CO_2 more significantly in winter and CO_2 flux (Fc) more significantly in spring. The post-agricultural ecosystem has greater seasonal variations of Ta, Ts, Rn, H, G, Cv, E, and CO_2, and smaller seasonal variations of θ and Fc than the pre-agricultural ecosystem.
- At sub-daily scale, deforestation increases diurnal variations of Ta, Ts, H, G, Cv, and E. Reforestation decreases diurnal variations of Ta, Ts, Ts@30cm, and Cv, and increases diurnal variations of H and E. Note that

both deforestation and reforestation increase the diurnal variations of H and E. Land-use change alters almost all variables more significantly during the daytime than during the nighttime. However, throughout the year, land-use change alters daytime and nighttime CO_2 equally strong. The post-agricultural ecosystem has greater diurnal variations of Ta, Ts, Rn, H, G, Cv, E, CO_2 and Fc than the pre-agricultural ecosystem.

- The differences of the pre- and post-agricultural ecosystems in vegetation types and maturity are the major reason for the differences of the two ecosystems in seasonal cycles of H, CO_2, Fc and WUE.

Three conclusions are drawn from the findings of Chapter 5. Firstly, the flux variables such as H, G, E, and Fc are seven times more significantly influenced by land-use change than the corresponding meteorological state variables such as Ta, Ts, Cv, and CO_2. Although the state variables including Ta, Ts, Cv, and CO_2 at pre- and post-agricultural ecosystems are almost identical, the flux variables including H, E, Fc and WUE at the post-agricultural ecosystem are almost twice of those at the pre-agricultural ecosystem. Secondly, deforestation alters land surface variables including state and flux variables six times more than reforestation does. Thirdly, land-use change alters soil conditions such as Ts, G, and θ three times more than the corresponding air conditions such as Ta, H, and Cv. Therefore, microclimate change would be significantly underestimated using the most concerned and commonly measured variables such as air temperature, relative humidity, and atmospheric CO_2 concentration.

6.2 Recommendations for Future Work

Based on the findings described above, several topics deserve further investigation:

(1) Field observations at Calhoun critical zone

- Integrate existing measurements by all teams. For example, the Duke University team has measured tree biomass, soil CO_2 concentration, and soil organic carbon. It is essential to investigate the connection between the soil carbon cycle represented by the soil carbon measurements and the atmospheric carbon cycle represented by the atmospheric CO_2 concentration and flux measurements.
- Add flux towers at the mature forest, cropland and grassland to observe the eco-hydro-meteorological conditions among different ecosystems.
- Add sap flow sensors at the young pine forest to measure the plant transpiration, and investigate the ratio of the plant transpiration to the total evapotranspiration.
- Add methane sensors at the young pine forest to observe the atmospheric methane concentration and fluxes, and investigate the impacts of methane on the carbon cycle.

(2) Land surface modeling studies

- Validation: Test the extreme solution model (ESM) of friction velocity and the half-order derivative model (HOD) of gas fluxes over various surface types, climate, and weather conditions using long-term data to investigate the applicability and limitations of the model.

- Application: Estimate surface wind speed using the modeled friction velocity based on the wind shear derived from the Monin-Obukhov similarity equations or the classic logarithmic equation. Estimate the long-term greenhouse gas emission using the historical gas concentration observations using the HOD model. For example, estimate the CO_2 flux using the long-term atmospheric CO_2 concentration data at Moana Loa Observatory since March 1958.
- Expansion: Test the ESM and HOD to estimate surface friction velocity, wind speed and gas fluxes at regional and global scales using remote sensing data; and implement the scheme in land surface models.
- Development: Develop MEP models of coupled energy, water, and carbon cycle.

(3) Data Analysis

- With the above- and below-canopy measurements of EC fluxes at the young pine forest, investigate the ratio of soil evaporation to total evapotranspiration, and the ratio of soil respiration to net primary productivity.
- With measurements of air temperature and humidity profiles at the young pine forest, investigate the usefulness of the Monin-Obukhov similarity theory for modeling under-canopy turbulence.

- With EC systems at the mature forest, regrow pre-mature forest, grassland, and cropland, study the responses of different ecosystems to extreme events such as floods, storms, and droughts.

APPENDIX A. A LOCAL NETWORK OF DATA LOGGERS

It is possible to set up a small local network of CR1000s using the RS-232 serial port on one CR1000 and some 3-conductor cables. The distance between any two CR1000's must be less than 25 feet (7.6 m).

Figure A.1 illustrates the network configuration and wiring. COM1 TX and RX are digital I/O ports 1 and 2; COM2 TX and RX are digital I/O ports 3 and 4. The TX from one CR1000 is connected to the RX at the other end and vise versa.

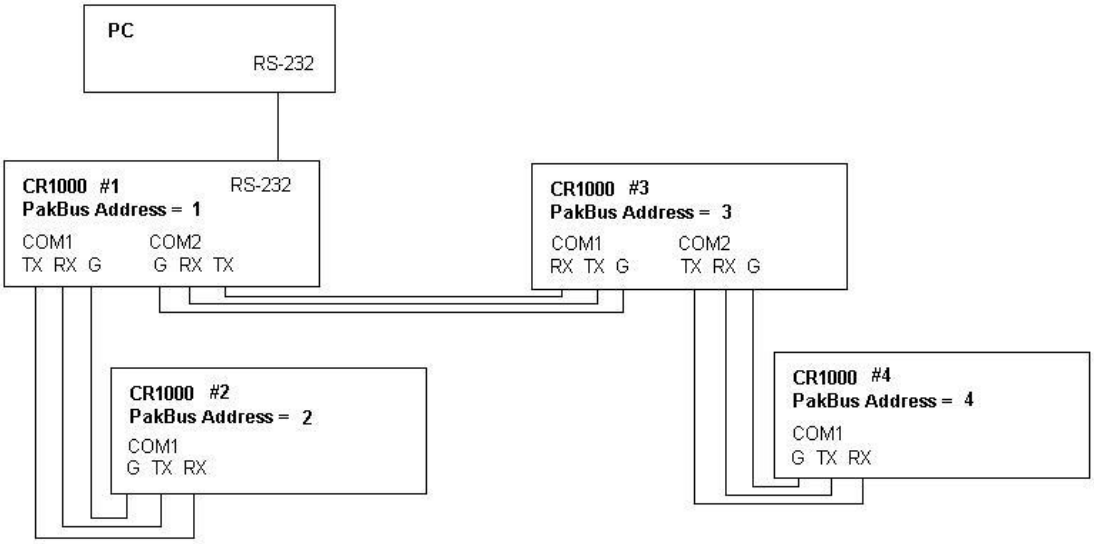

Figure A1 Configuration and Wiring of Local Network of CR1000's Setup

Before placing them in the network, the CR1000's are connected directly to the PC and configured with unique PakBus addresses. Use Campbell Scientific's Device Configuration Utility to set the PakBus addresses.

1. Connect the RS-232 port on the CR1000 to a serial port on your computer with a serial cable. Apply 12 VDC to the CR1000's Power In connector.
2. Open Device Configuration Utility by clicking on the shortcut or navigating to C:\Program Files\Campbellsci\DevConfig\DevConfig.exe. Be sure that other programs that require access to the computer's serial port are closed (LoggerNet, PC400, PC200W, HotSync, etc.)
3. Choose device type CR1000 from the list on the left side and click on the Connect button at the lower left. Under the Datalogger tab, give the CR1000 a unique Pakbus address.

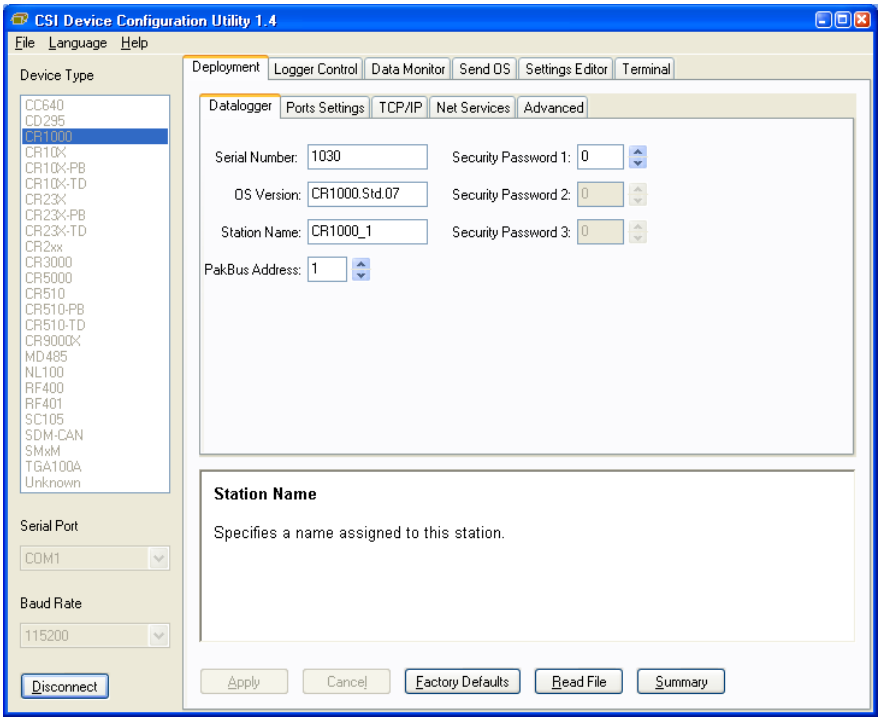

4. In the Ports Settings tab, select the RS-232 port and assign a beacon interval. This is the interval at which you want the CR1000 to broadcast PakBus messages to search for new PakBus neighboring nodes.

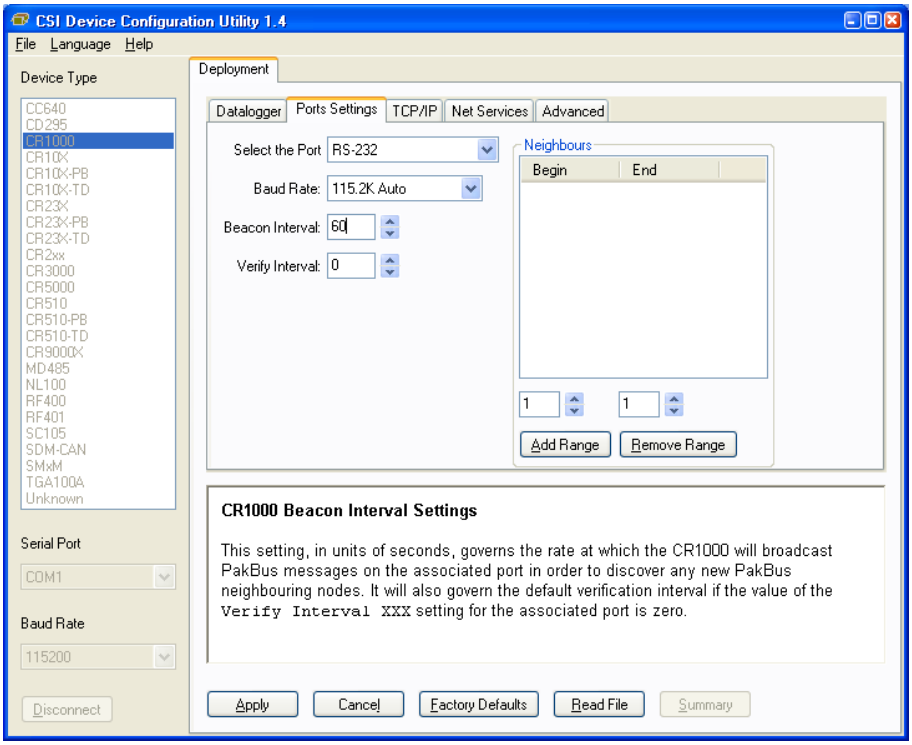

5. On the Advanced tab, change the Is Router setting to Yes if the CR1000 is connected to the computer, or if it is to be connected to more than one CR1000 through its COM pairs. In the example system above, CR1000 #1 and #3 are routers.

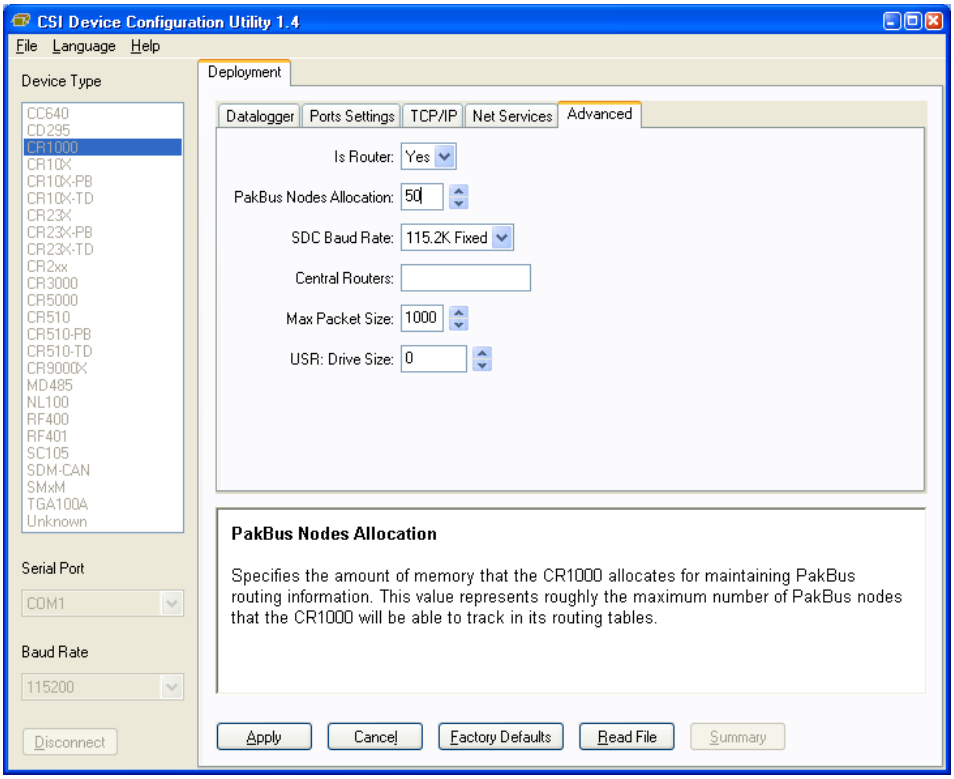

6. Save the changes by clicking on the Apply button at the bottom of the screen. A window with a summary of the CR1000's configuration will open. You can print this or save it to file.

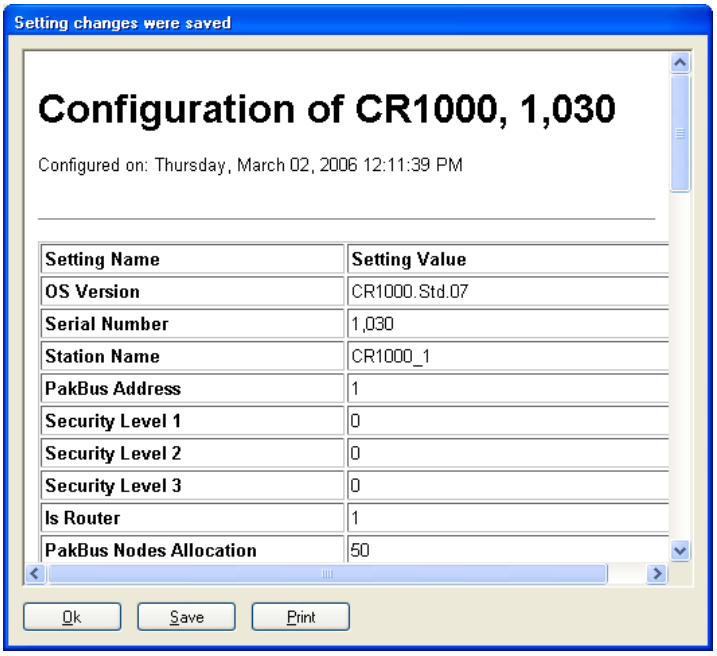

7. Repeat steps 1 to 6 for each of the CR1000s in the network.
8. Connect the CR1000s to each other with 3-conductor cable as shown in the example network above.

The PC running LoggerNet can now use the RS-232 port of the first CR1000 to communicate with any of the other CR1000s in the network to send programs, monitor measurements or collect data.

You can use DevConfig to assign known neighbors to the list. This seems to work better than beaconing.

APPENDIX B. WIRING INSTRUCTIONS AND PROGRAMS OF DATA LOGGERS

B.1 CR1000 SN12211 at cropland site

```
'CCZO CR1000 SN 12211 data logger program

'Dec 1, 2017 for CCZO CR1000 at Cropland

'contributer: Yao Tang, tangyao1208@gatech.edu

'The following sensors are measured

'Sensor          count       description

'CS616           4                water content reflectometer

'107L             6                soil temperature'

'CS215            1                Air temperature and RH

'TB4              1             Precipitation

'

'****Station Constants.

Const Scan_interval = 1  'scan interval 1 s

Const Output_interval = 1 'output interval 1 min
```

```
Dim ii As Long                          'Slow sequence scan index variable.

'*** Wiring Instructions***

'*** CS616 wiring ***

Const CS616_ANALOG_INPUT = 1       'Unique single-ended analog input channel.

Const CS616_POWER_CTRL = 1         'Unique control port.

Const NMBR_CS616 = 5               'Unique number of CS616 to measure.

'*** Beginning of CS616 wiring ***

'SE1(1H)      Signal #1 (green)

'SE2(1L)      Signal #2 (green)

'SE3(2H)      Signal #3 (green)

'SE4(2L)      Signal #4 (green)

'SE5(3H)      Signal #5 (green) (Not Installed)

'SE6(3L)      Signal #6 (green) (Not installed)

'C1      Power control #1 (orange)

'C2      Power control #2 (orange)

'C3      Power control #3 (orange)

'C4      Power control #4 (orange)
```

'C5 Power control #5 (orange)

'C6 Power control #6 (orange)

'G Shield #1 (clear)

' Shield #2 (clear)

' Shield #3 (clear)

'G Shield #4 (clear)

' Shield #5 (clear)

' Shield #6 (clear)

'12V Power #1 (red)

' Power #2 (red)

' Power #3 (red)

'12V Power #4 (red)

' Power #5 (red)

' Power #6 (red)

'G Signal reference #1 (black)

' Signal reference #2 (black)

' Signal reference #3 (black)

```
'G       Signal reference #4 (black)

'        Signal reference #5 (black)

'        Signal reference #6 (black)

'*** End of CS616 wiring ***



'****107 L temperature probe ***

Const S107L_ExINPUT = Ex1

'Ex1 for 1 and 2

'Ex2 for 3 and 4

'Ex3 for 5 and 6

Const S107L_SEINPUT = 9 '5H

Const NMBR_S107L = 6

'1st 107 L

' Wire

' Color          Function                        CR1000

' -----          --------                        ------

' Black          Voltage-excitation input        EX1
```

```
' Red          Analog-voltage output              SE9 (5H)

' Purple       Bridge-resistor ground             AG*9

' Clear        Shield                             G*

'*AG = Analog Ground (represented by ground symbol on CR1000 wiring panel

'2nd 107 L

' Wire

' Color        Function                           CR1000

' -----        --------                           ------

' Black        Voltage-excitation input           EX1

' Red          Analog-voltage output              SE10 (5L)

' Purple       Bridge-resistor ground             AG*10

' Clear        Shield                             G*

'*AG = Analog Ground (represented by ground symbol on CR1000 wiring panel

'3rd 107 L

' Wire

' Color        Function                           CR1000

' -----        --------                           ------
```

```
' Black         Voltage-excitation input              EX2

' Red           Analog-voltage output                 SE11 (6H)

' Purple        Bridge-resistor ground                AG*11

' Clear         Shield                          G*

'*AG = Analog Ground (represented by ground symbol on CR1000 wiring panel

'4th 107 L

' Wire

' Color         Function                        CR1000

' -----         --------                        ------

' Black         Voltage-excitation input              EX2

' Red           Analog-voltage output                 SE12 (6L)

' Purple        Bridge-resistor ground                AG*12

' Clear         Shield                          G*

'*AG = Analog Ground (represented by ground symbol on CR1000 wiring panel

'5th 107 L

' Wire

' Color         Function                        CR1000
```

```
' -----          --------                    ------

' Black          Voltage-excitation input          EX3

' Red            Analog-voltage output             SE13 (7H)

' Purple         Bridge-resistor ground            AG*13

' Clear          Shield                      G*

'*AG = Analog Ground (represented by ground symbol on CR1000 wiring panel

'6th 107 L

' Wire

' Color          Function                    CR1000

' -----          --------                    ------

' Black          Voltage-excitation input          EX3

' Red            Analog-voltage output             SE14 (7L)

' Purple         Bridge-resistor ground            AG*14

' Clear          Shield                      G*

'*AG = Analog Ground (represented by ground symbol on CR1000 wiring panel

'*** End of 107L wiring ***
```

```
'**** CS215***

Const CS215_C_INPUT = 7         'Unique differential analog input channel.

'*** Beginning of CS215 (1)wiring ***

' Color   Function          CR3000

' -----   --------          -------

' Red     Power (12V)       12V

' Green   SDI-12 signal     C7

' Black   Power ground      G

' White   Power ground      G

' Clear   Shield           Signal Ground (C1 Ground)



'****SENSOR_TB4***



Const TB4_INPUT = 1         'P1

'*** Beginning of TB4 wiring ***

' Color   Function                Pulse Channel CR1000

' -----   --------                -------
```

```
' Black   Rain signal                  P1

' White  Rain signal reference          AG

' Clear  Shield                       AG

'*** End of TB4 wiring ***



'*** Constants ***

'*** Beginning of CS616 constants and variables ***

Public cs616_wcr(NMBR_CS616)          'Water content reflectometer period.

Public soil_water(NMBR_CS616)         'Volumetric soil water content with temperature
correction.

Units cs616_wcr = uSeconds

Units soil_water = frac_v_wtr

'CS616 Default Calibration Constants

const a0= -0.0663

const a1= -0.0063

const a2= 0.0007

'*** End of CS616 constants and variables ***
```

```
'*** Beginning of 107 constants and variables ***

Public T107_C(NMBR_S107L)

'*** End of 107 constants and variables ***



'*** Beginning of CS215 constants and variables ***

Public CS215_TRHData(2)

Alias CS215_TRHData(1) = AirTC

Alias CS215_TRHData(2) = RH

Units AirTC = Deg C

Units RH = %



'*** End of CS215 constants and variables ***



'*** Beginning of TB4 constants and variables ***

Public Rain_mm

Units Rain_mm = mm
```

```
'*** End of TB4 constants and variables ***




'****''''''''''''''''''''Tables''''''''''''''''''''''''''''****

'*** Output data tables ***

'CS616

DataTable (SN12211,TRUE,-1)

'CardOut(0,-1)

  DataInterval (0,OUTPUT_INTERVAL,Min,0)

  TableFile ("CRD:DoveField1Min",8,1000,0,7,Day,0,0)

  '107Loutput'

  Average(NMBR_S107L,T107_C(1),IEEE4,0)

  '107Loutput

  '*** Beginning of CS616 output data ***

  Average (NMBR_CS616,soil_water(1),IEEE4,0)

  Average (NMBR_CS616,cs616_wcr(1),IEEE4,0)
```

```
  '*** End of CS616 output data ***

'air T and RH

Average(1,AirTC,FP2,False)

Sample(1,RH,FP2)

' raingauge

Totalize(1,Rain_mm,IEEE4,0)



EndTable



'*** Program ***

BeginProg



 Scan (1,Sec,3,0)



    '*** Beginning of CS616 measurements ***

    CS616

(cs616_wcr,NMBR_CS616,CS616_ANALOG_INPUT,CS616_POWER_CTRL,1,1,0)
```

```
'Apply temperature correction to CS616 period and find volumetric water content.
For ii = 1 To NMBR_CS616 'NMBR_TCAV must equal NMBR_CS616
   soil_water(ii) = -0.0663+cs616_wcr(ii)*(-0.0063+cs616_wcr(ii)*0.0007)
Next ii


'  CallTable CS616_12211
'*** End of CS616 measurements ****


'*** Beginning of 107L measurements ***
'Const S107L_VxINPUT = Ex3
'Const S107L_SEINPUT = 39
Therm107(T107_C(1),1,9,Ex1,0,_60Hz,1.0,0.0)
Therm107(T107_C(2),1,10,Ex1,0,_60Hz,1.0,0.0)
Therm107(T107_C(3),1,11,Ex2,0,_60Hz,1.0,0.0)
Therm107(T107_C(4),1,12,Ex2,0,_60Hz,1.0,0.0)
Therm107(T107_C(5),1,13,Ex3,0,_60Hz,1.0,0.0)
Therm107(T107_C(6),1,14,Ex3,0,_60Hz,1.0,0.0)
```

```
        'CallTable(SN12211_backup)
    '*** End of 107L measurements ***


'*** Beginning of CS215 measurements ***
    SDI12Recorder(CS215_TRHData(),CS215_C_INPUT,"0","M!",1,0)
'*** End of CS215 measurements ***



 '*** Beginning of TB4 measurements ***
    PulseCount(Rain_mm,1,TB4_INPUT,2,0,0.254,0)
    '*** End of TB4 measurements ***
    CallTable(SN12211)
 NextScan
EndProg
```

B.2 CR1000 SN2588 at CCZO young pine forest

```
'CCZO CR1000 SN 2588 data logger program

'Nov. 3 for CCZO CR1000

'contributer: Yao Tang, tangyao1208@gatech.edu

'The following sensors are measured

'Sensor          count       description

'HFP01           1         soil heat flux

'CS616           3                 water content reflectometer

'107L             3                 soil temperature'

'

'****Station Constants.

Const Scan_interval = 1  'scan interval 1 s

Const Output_interval = 1 'output interval 1 min

Dim ii As Long                              'Slow sequence scan index variable.

'*** Wiring Instructions***

'****HFP01SC Wiring instructions***

Const SHF_ANALOG_INPUT = 1         'Unique differential analog input channel.

Const NMBR_SHF = 1                 'Unique number of HFP01 to measure.
```

'Soil heat plate 4

'Cable 1, heat flux sensor signal

'1H HFP01 #1 signal (white)

'1L HFP01 #1 signal reference (green)

'gnd HFP01 #1 shield (clear)

'Cable 2, heater connection

'SE7 (4H) (yellow)

'SE7 Ground (purple)

'SE7 Ground (clear)

'SW12-1 (red)

'SW12 Ground (black)

'Soil heat plate 5

'Cable 1, heat flux sensor signal

'2H HFP01 #1 signal (white)

'2L HFP01 #1 signal reference (green)

'gnd HFP01 #1 shield (clear)

'Cable 2, heater connection

'SE8 (4L) (yellow)

'SE8 Ground (purple)

'SE8 Ground (clear)

'SW12-1 (red)

'SW12 Ground (black)

'Soil heat plate 6

'Cable 1, heat flux sensor signal

'3H HFP01 #1 signal (white)

'3L HFP01 #1 signal reference (green)

'gnd HFP01 #1 shield (clear)

'Cable 2, heater connection

'SE9 (5H) (yellow)

'SE9 Ground (purple)

'SE9 Ground (clear)

```
'SW12-1 (red)

'SW12 Ground (black)



'*** End of HFP01SC wiring ***



'*** CS616 wiring ***

Const CS616_ANALOG_INPUT = 11       'Unique single-ended analog input channel.

Const CS616_POWER_CTRL = 1          'Unique control port.

Const NMBR_CS616 = 3                'Unique number of CS616 to measure.

'*** Beginning of CS616 wiring ***

'SE11 (6H)      Signal #1 (green)

'SE12(6L)      Signal #2 (green)

'SE13(7H)      Signal #3 (green)

'C1      Power control #1 (orange)

'C2      Power control #2 (orange)

'C3      Power control #3 (orange)

'G       Shield #1 (clear)
```

```
'       Shield #2 (clear)

'           Shield #3 (clear)

'12V     Power #1 (red)

'       Power #2 (red)

'           Power #3 (red)

'G       Signal reference #1 (black)

'       Signal reference #2 (black)

'       Signal reference #3 (black)

'*** End of CS616 wiring ***



'****107 L temperature probe ***

Const S107L_VxINPUT = Vx1

Const S107L_SEINPUT = 14 '7L

Const NMBR_S107L = 3

'1st 107 L

' Wire

' Color          Function                    CR1000
```

```
' -----          --------                    ------

' Black          Voltage-excitation input          EX1

' Red            Analog-voltage output             SE14 (7L)

' Purple         Bridge-resistor ground            AG*14

' Clear          Shield                      G*

'*AG = Analog Ground (represented by ground symbol on CR1000 wiring panel

'2nd 107 L

' Wire

' Color          Function                    CR1000

' -----          --------                    ------

' Black          Voltage-excitation input          EX2

' Red            Analog-voltage output             SE15 (8H)

' Purple         Bridge-resistor ground            AG*15

' Clear          Shield                      G*

'*AG = Analog Ground (represented by ground symbol on CR1000 wiring panel

'3rd 107 L

' Wire
```

```
' Color          Function                        CR1000

' -----          --------                        ------

' Black          Voltage-excitation input        EX3

' Red            Analog-voltage output           SE16 (8L)

' Purple         Bridge-resistor ground          AG*16

' Clear          Shield                          G*

'*AG = Analog Ground (represented by ground symbol on CR1000 wiring panel

'*** End of 107L wiring ***



'*** Constants ***

'*** Beginning of CS616 constants and variables ***

Public cs616_wcr(NMBR_CS616)          'Water content reflectometer period.

Public soil_water(NMBR_CS616)         'Volumetric soil water content

'Dim cs616_T(NMBR_CS616)              'Water content reflectometer period

Units cs616_wcr = uSeconds

Units soil_water = frac_v_wtr
```

```
'CS616 Default Calibration Constants

const a0= -0.0663

const a1= -0.0063

const a2= 0.0007

'*** End of CS616 constants and variables ***



'*** Beginning of HFP01 constants and variables ***

Const CAL_INTERVAL = 1440 'HFP01SC insitu calibration interval (minutes).

Const END_CAL = 10 'End HFP01SC insitu calibration one minute before the next Output.

Const HFP01SC_CAL_1 = 1000/62.4 'Unique multiplier for HFP01SC #1 (1000/sensitivity).

'Const HFP01SC_CAL_2 = 1000/59.7 'Unique multiplier for HFP01SC #2 (1000/sensitivity).

'Const HFP01SC_CAL_3 = 1000/59.7 'Unique multiplier for HFP01SC #3 (1000/sensitivity).

'*** Variables ***

Public shf(1)
```

```
Public shf_cal(1)

Units shf = W/m^2

Units shf_cal = W/(m^2 mV)

'HFP01SC calibration variables.

Dim shf_mV(1)

Dim shf_mV_0(1)

Dim shf_mV_180(1)

Dim shf_mV_end(1)

Dim V_Rf(1)

Dim V_Rf_180(1)

Dim shf_cal_on_f As Boolean

Dim sw12_1_state As Boolean 'State of the switched 12Vdc port 1.

'*** End of HFP01SC constants and variables ***



'*** Beginning of 107 constants and variables ***

Public T107_C(NMBR_S107L)

'*** End of 107 constants and variables ***
```

```
'****''''''''''''''''''Tables''''''''''''''''''''''''****

'*** Output data tables ***

'CS616

DataTable (SN2588,TRUE,-1)

'CardOut(0,-1)

  DataInterval (0,OUTPUT_INTERVAL,Min,0)

  TableFile ("CRD:SN2588",8,1000,0,7,Day,0,0)

' soil temperature output

Average(NMBR_S107L,T107_C(1),IEEE4,0)

'soil temperature output

'*** Beginning of CS616 output data ***

  Average (NMBR_CS616,soil_water(1),IEEE4,0)

  Average (NMBR_CS616,cs616_wcr(1),IEEE4,0)

  '*** End of CS616 output data ***

'soil heat flux output'

Average (1,shf(1),IEEE4,shf_cal_on_f)
```

```
Sample (1,shf_cal(1),IEEE4)

EndTable



'*** Program ***

BeginProg



'HFP01SC factory calibration in W/(m^2 mV) = 1000/sensitivity.

 shf_cal(1) = HFP01SC_CAL_1

' shf_cal(2) = HFP01SC_CAL_2

' shf_cal(3) = HFP01SC_CAL_3



 Scan (1,Sec,3,0)



    '*** Beginning of CS616 measurements ***

    CS616
(cs616_wcr,NMBR_CS616,CS616_ANALOG_INPUT,CS616_POWER_CTRL,1,1,0)

    'Apply temperature correction to CS616 period and find volumetric water content.
```

```
    For ii = 1 To NMBR_CS616 'NMBR_TCAV must equal NMBR_CS616
      soil_water(ii) = -0.0663+cs616_wcr(ii)*(-0.0063+cs616_wcr(ii)*0.0007)
    Next ii
'   CallTable CS616_2588

    '*** Beginning of HFP01SC measurements ***
    'Measure the HFP01SC soil heat flux plates.
VoltDiff
(shf_mV(1),NMBR_SHF,AutoRange,SHF_ANALOG_INPUT,TRUE,0,_60Hz,1,0)
'Apply calibration to HFP01SC soil heat flux plates.

shf(1) = shf_mV(1)*shf_cal(1)

'Power the HFP01SC heaters.
PortSet (9,sw12_1_state)
'Measure voltage across the heater (Rf_V).
VoltSe (V_Rf(1),NMBR_SHF,mV5000,7,TRUE,0,_60Hz,0.001,0)
```

```
'CallTable (Soil_Heat_2588)

'Begin HFP01SC calibration on a fixed interval.

If ( IfTime (1,1440,Min) ) Then

shf_cal_on_f = TRUE

Move (shf_mV_0(1),1,shf_mV(1),1)

sw12_1_state = TRUE

EndIf

If ( IfTime (4,1440,Min) ) Then

Move (shf_mV_180(1),1,shf_mV(1),1)

Move (V_Rf_180(1),1,V_Rf(1),1)

sw12_1_state = FALSE

EndIf

If ( IfTime (60,1440,Min) ) Then

Move (shf_mV_end(1),1,shf_mV(1),1)

'Compute new HFP01SC calibration factors.
```

```
shf_cal(1)                    =                    V_Rf_180(1)*V_Rf_180(1)*128.7/ABS
(((shf_mV_0(1)+shf_mV_end(1))/2)-shf_mV_180(1))


shf_cal_on_f = FALSE
EndIf
   '*** End of HFP01SC measurements ***


   '*** Beginning of 107L measurements ***
   Therm107(T107_C(1),1,14,Ex1,0,_60Hz,1.0,0.0)
   Therm107(T107_C(2),1,15,Ex2,0,_60Hz,1.0,0.0)
   Therm107(T107_C(3),1,16,Ex3,0,_60Hz,1.0,0.0)
   CallTable(SN2588)
        'CallTable(SN2588_backup)
   '*** End of 107L measurements ***


 NextScan
EndProg
```

B.3 CR1000 SN2589 at CCZO young pine forest

```
'CCZO CR1000 SN 2589 data logger program

'Sep. 20 for CCZO CR1000

'contributer: Yao Tang, tangyao1208@gatech.edu

'The following sensors are measured

'Sensor          count        description

'HFP01           3         soil heat flux

'CS616           3                 water content reflectometer

'107L             3                soil temperature'

'

'****Station Constants.

Const Scan_interval = 1  'scan interval 1 s

Const Output_interval = 1 'output interval 1 min

Dim ii As Long                          'Slow sequence scan index variable.

'*** Wiring Instructions***

'****HFP01 Wiring instructions***

Const SHF_ANALOG_INPUT = 1        'Unique differential analog input channel.
```

```
Const NMBR_SHF = 3              'Unique number of HFP01 to measure.

'at 2cm depth

'1H HFP01 #1 signal (white)

'1L HFP01 #1 signal reference (green)

'gnd HFP01 #1 shield (clear)



'at 15cm depth

'2H HFP01 #2 signal (white)

'2L HFP01 #2 signal reference (green)

'gnd HFP01 #2 shield (clear)



'at 40cm depth

'3H HFP01 #3 signal (white)

'3L HFP01 #3 signal reference (green)

'gnd HFP01 #3 shield (clear)



'*** End of HFP01 wiring ***
```

```
'*** CS616 wiring ***

Const CS616_ANALOG_INPUT = 9       'Unique single-ended analog input channel.

Const CS616_POWER_CTRL = 1         'Unique control port.

Const NMBR_CS616 = 3               'Unique number of CS616 to measure.

'*** Beginning of CS616 wiring ***

'SE9 (5H)      Signal #1 (green)   2cm

'SE10(5L)      Signal #2 (green)   15cm

'SE11(6H)      Signal #3 (green)   40cm

'C2      Power control #1 (orange)

'C4      Power control #2 (orange)

'C6      Power control #3 (orange)

'G       Shield #1 (clear)

'        Shield #2 (clear)

'           Shield #3 (clear)

'12V     Power #1 (red)

'        Power #2 (red)
```

```
'           Power #3 (red)

'G      Signal reference #1 (black)

'       Signal reference #2 (black)

'       Signal reference #3 (black)

'*** End of CS616 wiring ***



'****107 L temperature probe ***

Const S107L_VxINPUT = Vx1

Const S107L_SEINPUT = 14 '7L

Const NMBR_S107L = 3

'1st 107 L 2cm

' Wire

' Color          Function                        CR1000

' -----          --------                        ------

' Black          Voltage-excitation input        EX1

' Red            Analog-voltage output           SE14 (7L)

' Purple         Bridge-resistor ground          AG*14
```

```
' Clear          Shield                          G*

'*AG = Analog Ground (represented by ground symbol on CR1000 wiring panel

'2nd 107 L 15cm

' Wire

' Color          Function                        CR1000

' -----          --------                        ------

' Black          Voltage-excitation input        EX2

' Red            Analog-voltage output           SE15 (8H)

' Purple         Bridge-resistor ground          AG*15

' Clear          Shield                          G*

'*AG = Analog Ground (represented by ground symbol on CR1000 wiring panel

'3rd 107 L 40cm

' Wire

' Color          Function                        CR1000

' -----          --------                        ------

' Black          Voltage-excitation input        EX3

' Red            Analog-voltage output           SE16 (8L)
```

```
' Purple         Bridge-resistor ground                AG*16

' Clear          Shield                                G*

'*AG = Analog Ground (represented by ground symbol on CR1000 wiring panel

'*** End of 107L wiring ***



'Wiring Diagram

'==============

'CS215

' Wire

' Color Function CR1000

' ----- -------- -------

' Red Power (12V) 12V

' Green SDI-12 signal C1 C3 C5 (High to Low, C5 install two, change C7 wire to C5)

' Black Power ground G

' White Power ground G

' Clear Shield Signal Ground
```

```
'*** Constants ***

'*** Beginning of CS616 constants and variables ***

Public cs616_wcr(NMBR_CS616)          'Water content reflectometer period.

Public soil_water(NMBR_CS616)         'Volumetric soil water content with temperature
correction.

'Dim cs616_T(NMBR_CS616)                    'Water content reflectometer period with
temperature correction.

Units cs616_wcr = uSeconds

Units soil_water = frac_v_wtr

'CS616 Default Calibration Constants

const a0= -0.0663

const a1= -0.0063

const a2= 0.0007

'*** End of CS616 constants and variables ***



'*** Beginning of HFP01 constants and variables ***

Public shf(NMBR_SHF)                  'HFP01 soil heat flux plates.
```

```
Dim shf_cal(NMBR_SHF)

Units shf = W/m^2

Const HFP01_CAL_1 = 1000/59.68 'Unique multiplier for HFP01 #1. 1000/sensitivity (1000/67.1)

Const HFP01_CAL_2 = 1000/61.89 'Unique multiplier for HFP01 #2. 1000/sensitivity (1000/67.0)

Const HFP01_CAL_3 = 1000/59.6 'Unique multiplier for HFP01 #1. 1000/sensitivity (1000/67.1)

'Const HFP01_CAL_2 = 14.92 'Unique multiplier for HFP01 #2. 1000/sensitivity (1000/67.0)

'*** End of HFP01 constants and variables ***



'*** Beginning of 107 constants and variables ***

Public T107_C(NMBR_S107L)

'*** End of 107 constants and variables ***

'Declare the variable array for the measurement

Public TRH1(2)

Alias TRH1(1)=AirTC1
```

```
Alias TRH1(2)=RH1

Units AirTC1=Deg C

Units RH1=%



'Declare the variable array for the measurement

Public TRH3(2)

Alias TRH3(1)=AirTC3

Alias TRH3(2)=RH3

Units AirTC3=Deg C

Units RH3=%



'Declare the variable array for the measurement

Public TRH5(2)

Alias TRH5(1)=AirTC5

Alias TRH5(2)=RH5

Units AirTC5=Deg C
```

```
Units RH5=%



'Declare the variable array for the measurement

Public TRH7(2)

Alias TRH7(1)=AirTC7

Alias TRH7(2)=RH7

Units AirTC7=Deg C

Units RH7=%



'****''''''''''''''''''Tables''''''''''''''''''''''''****

'*** Output data tables ***



DataTable (SN2589,TRUE,-1)

'CardOut(0,-1)

  DataInterval (0,OUTPUT_INTERVAL,Min,0)

  TableFile ("CRD:SN2589",8,1000,0,7,Day,0,0)
```

```
'*** Beginning of CS215 output data ***
 Average(1,AirTC1,FP2,False)
 Sample(1,RH1,FP2)
 Average(1,AirTC3,FP2,False)
 Sample(1,RH3,FP2)
 Average(1,AirTC5,FP2,False)
 Sample(1,RH5,FP2)
 Average(1,AirTC7,FP2,False)
 Sample(1,RH7,FP2)
'*** End of CS215 output data ***


'CS616 and Soil heat flux
'*** Beginning of CS616 output data ***
Average (NMBR_CS616,soil_water(1),IEEE4,0)
Average (NMBR_CS616,cs616_wcr(1),IEEE4,0)
'*** End of CS616 output data ***
```

```
  '*** Beginning of HFP01 output data ***
  Average (NMBR_SHF,shf(1),IEEE4,0)
  '*** End of HFP01 output data ***

  '*** Beginning of S107L output data ***
  Average(NMBR_S107L,T107_C(1),IEEE4,0)
  '*** End of S107L output data ***

EndTable
'*** End of data tables ***

'*** Program ***
BeginProg

'Load the HFP01 factory calibration.
 shf_cal(1) = HFP01_CAL_1
```

```
shf_cal(2) = HFP01_CAL_2

shf_cal(3) = HFP01_CAL_3



Scan (5,Sec,3,0)



  '*** Beginning of CS616 measurements ***

  CS616 (cs616_wcr(1),1,9,2,1,1,0)

  CS616 (cs616_wcr(2),1,10,4,1,1,0)

  CS616 (cs616_wcr(3),1,11,6,1,1,0)

  'Apply temperature correction to CS616 period and find volumetric water content.

  For ii = 1 To NMBR_CS616 'NMBR_TCAV must equal NMBR_CS616

    soil_water(ii) = -0.0663+cs616_wcr(ii)*(-0.0063+cs616_wcr(ii)*0.0007)

  Next ii



  '*** Beginning of HFP01 measurements ***

  VoltDiff
(shf(1),NMBR_SHF,AutoRange,SHF_ANALOG_INPUT,TRUE,200,250,shf_cal(),0)
```

```
'*** End of HFP01 measurements ***

'*** End of CS616 and HFP01 measurements ****



'*** Beginning of 107L measurements ***

'Const S107L_VxINPUT = Vx3

'Const S107L_SEINPUT = 39

Therm107(T107_C(1),1,14,Ex1,0,_60Hz,1.0,0.0)

Therm107(T107_C(2),1,15,Ex2,0,_60Hz,1.0,0.0)

Therm107(T107_C(3),1,16,Ex3,0,_60Hz,1.0,0.0)

'*** End of 107L measurements ***

    'CS215 Temperature & Relative Humidity Sensor measurements 'AirTC' and 'RH'

    SDI12Recorder(TRH1(),1,"0","M!",1,0)

     SDI12Recorder(TRH3(),3,"0","M!",1,0)

    SDI12Recorder(TRH5(),5,"1","M!",1,0)

    SDI12Recorder(TRH7(),5,"0","M!",1,0)

    'SDI12Recorder(Dest,SDIPort,SDIAddress,"SDICommand",Multiplier,Offset)

    'Call Data Tables and Store Data
```

```
        CallTable(SN2589)

        'CallTable(SN2589_backup)

 NextScan

EndProg
```

B.4 CR3000 on the 3 m flux tower

```
'CR3000 Program

'For use at CCZO below canopy flux tower site

'program author: Yao Tang Date: 05/18/2017

'rainfall also record every minutes.

'Using TableFile() with Option 64 with memory card instead of cardout.



'Settings before wiring

'

'****RM Young 3-D sonic anemometer-thermometer*****

'Serial Number: 4890

' Baud Rate 38400

'Output Rate 10hz
```

'Voltage Output Format 1) U V W Temp

'Scale -25 to 25 m/s

'Range 5000 mv

'

'The following sensors are measured:

'RM Young 3-D sonic anemometer-thermometer Model 81000

'Licor 7500 Gas Analyzer

'CNR4 net radiometer

'CS215 temperature and relative humidity sensor

'SI111 Precision Infrared Radiometer

'107L Probe soil temperature probe

'CS616 water content reflectometers (volumetric soil moisture)

'HFP01 soil heat flux plates

'TB4 Rain Gauge

'Wiring:

'*******RM Young 3-D sonic anemometer-thermometer*****

```
Const RMY_Input = 1

'ANALOG PORTS:

'1H/L                  RM Young V1 (1H: Red, 1L:Oringe)

'2H/L                  RM Young V2 (2H: Green, 2L: Brown)

'3H/L                  RM Young V3 (3H: Blue, 3L: White)

'4H/L                  RM Young V4 (4H: Yellow, 4L:Black)



'EXTERNAL POWER SUPPLY

'12V      RM Young power + (Blue)

'G        RM Young power - (Brown)

'Power Ground   RM Young Earth Ground(clear)

'*******RM Young 3-D sonic anemometer-thermometer*****



'*******Licor 7500 Gas Analyzer**********************

'SDM-C1  SDM Data (gray)

'SDM-C2  SDM Clock (blue)

'SDM-C3  Enable (brown)
```

```
'G       SDM reference (black)

'G        SDM shield (white)



'EXTERNAL POWER SUPPLY

'+12V    Red (Do not from Data logger, Use switcher)

'G       Green (Do not from Data logger)

'*******Licor 7500 Gas Analyzer************************



'***CNR 4 Wiring Instructions*****

Const CNR4_NRInput = 5

Const CNR4_EC = Ix1

Const CNR4_TInput = 9

'

'ANALOG CHANNELS

'5H CNR4 Pyranometer Upper signal (red)

'5L CNR4 Pyranometer Upper signal reference (blue)

'gnd jumper to 5L (Wire 5L and 5 Ground)
```

'

'6H CNR4 Pyranometer Lower signal (white)

'6L CNR4 Pyranometer Lower signal reference (thin black)

'gnd jumnper to 6L

'

'7H CNR4 Pyrgeometer Upper signal (grey)

'7L CNR4 Pyrgeometer Upper signal reference (yellow)

'gnd jumper to 7L

'

'8H CNR4 Pyrgeometer Lower signal (brown)

'8L CNR4 Pyrgeometer Lower signal reference (green)

'gnd jumper to 8L

' CNR4 shield (clear)

'

'

'9H CNR4 PRT (Pt-100) signal (green)

'9L CNR4 PRT (Pt-100) signal reference (yellow)

```
'gnd CNR4 PRT (Pt-100) shield (clear)

'

'CURRENT EXCITATION

'IX1 CNR4 PRT (Pt-100) current excitation (grey)

'

'IXR CNR4 PRT (Pt-100) current excitation return (brown)

'

'CNR4 sensor

'*** End of CNR 4 wiring ***



'**** CS215***

Const CS215_C_INPUT = 1         'Unique differential analog input channel.

'*** Beginning of CS215 (1)wiring ***

' Color   Function           CR3000

' -----   --------          -------

' Red     Power (12V)        12V

' Green   SDI-12 signal      C1
```

```
' Black   Power ground        G

' White   Power ground        G

' Clear   Shield         Signal Ground (C1 Ground)



'*** Beginning of CS215 (2)wiring ***

' Color   Function          CR3000

' -----   --------          -------

' Red     Power (12V)       12V

' Green   SDI-12 signal      C3

' Black   Power ground        G

' White   Power ground        G

' Clear   Shield         Signal Ground (C1 Ground)

'*** End of CS215 wiring ***



'SENSOR_SI111

Const SI111_DIFFINPUT = 10        'Unique differential analog input channel.

Const SI111_SEINPUT = 21          'Unique SE input channel
```

```
Const SI111_VEINPUT = Vx1                    'Unique Vx input channel

'*** Beginning of SI111 wiring ***

' Color   Function              Pulse Channel CR5000

'       SI-111 Thermopile            -------

' Red      Diff.High                  10H

' Black    Diff.Low                   10L

' Clear    Analog Ground              AG

'      SI-111 Thermistor             -------

' Green      Singled-ended            SE21 (Or 11H)

' Blue       Analog Ground            AG

' White      Exicitation              VX1

'*** End of SI111 wiring ***



'*** CS616 wiring ***

'Only install one CS616

Const CS616_ANALOG_INPUT = 22       'Unique single-ended analog input channel.

Const CS616_POWER_CTRL = 2          'Unique control port.
```

```
Const NMBR_CS616 = 1              'Unique number of CS616 to measure.

'*** Beginning of CS616 wiring ***

'11L      Signal #1 (green)

'C1       Power control #1 (orange)

'G        Shield #1 (clear)

'12V      Power #1 (red)

'G        Signal reference #1 (black)

'*** End of CS616 wiring ***



'****HFP01 Wiring instructions***

Const SHF_ANALOG_INPUT = 12       'Unique differential analog input channel.

Const NMBR_SHF = 1                'Unique number of HFP01 to measure.



'*** Beginning of HFP01 wiring ***

'12H HFP01 #1 signal (white)

'12L HFP01 #1 signal reference (green)

'gnd HFP01 #1 shield (clear)
```

```
'*** End of HFP01SC wiring ***



'****107 L temperature probe ***

Const S107L_VxINPUT = Vx2

Const S107L_SEINPUT = 26 '7L

Const NMBR_S107L = 1

'1st 107 L

' Wire

' Color          Function                        CR3000

' -----          --------                        ------

' Black          Voltage-excitation input        VX2

' Red            Analog-voltage output           SE26 (13L)

' Purple         Bridge-resistor ground          AG*26

' Clear          Shield                          G*

'*AG = Analog Ground (represented by ground symbol on CR3000 wiring panel)

'****107 L temperature probe ***
```

```
'****SENSOR_TB4***



Const TB4_INPUT = 1         'P1

'*** Beginning of TB4 wiring ***

' Color   Function                Pulse Channel CR3000

' -----   --------                -------

' Black   Rain signal                  P1

' White  Rain signal reference          AG

' Clear  Shield                        AG

'*** End of TB4 wiring ***



'Constants:

'*** Station constants.

Const LF_SCAN_INTERVAL = 5  'Low Frenquency Scan Interval, 5 second

Const LF_OUTPUT_INTERVAL = 1 'Low Frequency Output Interval, 1min

'Dim i As Long                          'Main scan index variable.

Dim ii As Long                         'Slow sequence scan index variable.
```

```
'**************BM Young 81000 and Licor 75000

Const EC_SCAN_INTERVAL = 100      '100 (mSec) ==>CR3000 Measurement Rate 10
hz

Const EC_SCAN_BUFFER_SIZE = 240*INT (1000/EC_SCAN_INTERVAL)
          'Compute a 60 second scan buffer.

Const Vel_Scale = -25.0        'Scale in m s^-1 for RM Young sonic velocity, it is also the
offset

Const Vel_Multiplier = 0.01   'Multiplier for velocity = 2 x 25 / 5000

Const Temp_Multiplier = 0.02  'Multiplier for RMY sonic temperature

Const Temp_offset = 220    'Offset for RMY sonic temperature, including conversion from
degK

'BM Young 81000

'Public Variables

'Public Batt_Volt 'output batt voltage and ptemp at low frenquency

'Public PTemp

Public rmy(4)      'RM Young Analogue signals in mV

Public Ux          'RM Young sonic U velocity in m s^-1
```

```
Public Uy          'RM Young sonic V velocity in m s^-1

Public Uz          'RM Young sonic W velocity in m s^-1

Public Ts          'RM Young sonic temperature in degC

Public CO2_mg_m3

Public H2O_g_m3

Public irga(4)

Alias irga(1) = CO2

Alias irga(2) = H2O

Alias irga(3) = press

Alias irga(4) = irga_diag




Units rmy = mV

Units Ux = m s^-1

Units Uy = m s^-1

Units Uz = m s^-1

Units Ts = degC
```

```
Units CO2 = mmol/m^3 '(Original is mmol/m^3, save original when install)

Units H2O = mmol/m^3  '(Original is mmol/m^3)

Units press = kPa

Units irga_diag = arb

Units CO2_mg_m3 = mg/m^3

Units H2O_g_m3 = g_m3

'*** Beginning of CNR 4 constants and variables ***

Public logger_temp, batt_volt

Public cnr4(4)

Alias cnr4(1) = short_up

Alias cnr4(2) = short_dn

Alias cnr4(3) = long_up

Alias cnr4(4) = long_dn

Public cnr4_T_C 'CNR4 thermistor temperature in Celcius

Public cnr4_T_K 'CNR4 thermistor temperature in Kelvin

Public long_up_corr 'Downwelling long-wave radiation with temperature correction
```

Public long_dn_corr 'Upwelling long-wave radiation with temperature correction

Public Rs_net 'short-wave net radiation

Public Rl_net 'long-wave net radiation

Public albedo 'Albedo

Public Rn 'total net radiation

Units logger_temp = degC

Units batt_volt = volts

Units short_up = W/m^2

Units short_dn = W/m^2

Units long_up = W/m^2

Units long_dn = W/m^2

Units cnr4_T_C = deg_C

Units cnr4_T_K = K

Units long_up_corr = W/m^2

Units long_dn_corr = W/m^2

Units Rs_net = W/m^2

Units Rl_net = W/m^2

Units albedo = W/m^2

Units Rn = W/m^2

Dim cnr4_prt_R, Rs_R0

'CNR4 sensitivities: refer to the Certificate of Calibration from Kipp & Zonen for sensitivity values

'for each probes, and enter them below.

'**********ATTENTION, Change for every sensor!!!!!!!!!!

'SN: 150540

Const pyranometer_up_sensitivity = 10.47 'unique sensitivity for upper pyranometer '(microV/W/m^2)

Const pyranometer_dn_sensitivity = 10.33 'unique sensitivity for lower pyranometer '(microV/W/m^2)

Const pyrgeometer_up_sensitivity = 10.42 'unique sensitivity for upper pyrgeometer '(microV/W/m^2)

Const pyrgeometer_dn_sensitivity = 10.27 'unique sensitivity for lower pyrgeometer '(microV/W/m^2)

'**********ATTENTION, Change for every sensor!!!!!!!!!!

'CNR4 multipliers

```
Public cnr4_mult(4)

Const pyranometer_up_mult = 1000/pyranometer_up_sensitivity '(W/m^2/mV)

Const pyranometer_dn_mult = 1000/pyranometer_dn_sensitivity '(W/m^2/mV)

Const pyrgeometer_up_mult = 1000/pyrgeometer_up_sensitivity '(W/m^2/mV)

Const pyrgeometer_dn_mult = 1000/pyrgeometer_dn_sensitivity '(W/m^2/mV)

'*** End of CNR 4 constants and variables ***



'*** Beginning of CS616 constants and variables ***

Public cs616_wcr(NMBR_CS616)          'Water content reflectometer period.

Public soil_water(NMBR_CS616)        'Volumetric soil water content

Dim cs616_T(NMBR_CS616)               'Water content reflectometer period.

Units cs616_wcr = uSeconds

Units soil_water = frac_v_wtr

'*** End of CS616 constants and variables ***



'*** Beginning of HFP01 constants and variables ***

'**********ATTENTION!!!!!!!!!!!!!!!!!!!
```

```
Const HFP01_CAL_1 = 1000/60.79 'Unique multiplier for HFP01 #1. 1000/sensitivity (1000/67.1)

'*** Variables ***

Public shf(1)

Dim shf_cal(1)

Units shf = W/m^2

'*** End of HFP01SC constants and variables ***



'*** Beginning of CS215 constants and variables ***

Public CS215_TRHData(2)

Alias CS215_TRHData(1) = AirTC

Alias CS215_TRHData(2) = RH

Units AirTC = Deg C

Units RH = %



'Declare the variable array for the measurement

Public TRH3(2)
```

```
Alias TRH3(1)=AirTC3

Alias TRH3(2)=RH3

Units AirTC3=Deg C

Units RH3=%

'*** End of CS215 constants and variables ***



'*** Beginning of TB4 constants and variables ***

Public Rain_mm

Units Rain_mm = mm

'*** End of TB4 constants and variables ***



'*** Beginning of SI111 constants and variables ***

Public PanelT, SBTempC, SBTempK, TargmV, m, b, TargTempK, TargTempC

'**********ATTENTION!!!!!!!!!!!!!!!!!!!

'SN:SI-111_5784

'Declare constants (replace the listed values with coefficients received with sensor)

Const mC2 = 95990.1
```

```
Const mC1 = 8396720

Const mC0 = 1494500000

Const bC2 = 4442.66

Const bC1 = 162370

Const bC0 = -6764470

'*** End of SI111 constants and variables ***

'*** Beginning of 107 constants and variables ***

Public T107_C

'*** End of 107 constants and variables ***



'**********Output Data Tables:******

'**********1. EC data table**********

DataTable (ECData,True,-1)

  DataInterval (0,EC_SCAN_INTERVAL,mSec,0)

'  CardOut(0,-1)

  TableFile("CRD:"&Status.SerialNumber(1,1)&"EC_data",64,-1,0,10,Day,0,0)
```

```
' Change details
  Sample (4,rmy,IEEE4)
  Sample (1,Ux,IEEE4)
  Sample (1,Uy,IEEE4)
  Sample (1,Uz,IEEE4)
  Sample (1,Ts,IEEE4)
  Sample (4,CO2,IEEE4)
  Sample (1,CO2_mg_m3,IEEE4)
  Sample (1,H2O_g_m3,IEEE4)
EndTable

'***************2. Low Frenquency data table*******
DataTable (Data_1min,True,-1)
'CardOut(0,-1)
DataInterval (0,LF_OUTPUT_INTERVAL,Min,0)
TableFile("CRD:"&Status.SerialNumber(1,1)&"1_min",64,-1,0,10,Day,0,0)
' Change details
```

Minimum (1,batt_volt,FP2,0,False)

Sample (1,logger_temp,FP2)

'cnr4 data

Average (4,cnr4(1),IEEE4,False)

Average (1,cnr4_T_C,IEEE4,False)

Average (1,cnr4_T_K,IEEE4,False)

Average (1,long_up_corr,IEEE4,False)

Average (1,long_dn_corr,IEEE4,False)

Average (1,Rs_net,IEEE4,False)

Average (1,Rl_net,IEEE4,False)

Average (1,albedo,IEEE4,False)

Average (1,Rn,IEEE4,False)

'air T and RH

Average(1,AirTC,FP2,False)

Sample(1,RH,FP2)

Average(1,AirTC3,FP2,False)

Sample(1,RH3,FP2)

```
'infrared temp
  Sample (1,PanelT,FP2)
  Average (1,TargmV,FP2,False)
  Average (1,SBTempC,FP2,False)
  Average (1,TargTempC,FP2,False)
'soil moisture
Average (NMBR_CS616,soil_water(1),IEEE4,0)
Average (NMBR_CS616,cs616_wcr(1),IEEE4,0)
'soil temperature
Average(1,T107_C,IEEE4,0)
'soil heat flux
Average (1,shf(1),IEEE4,False)
'rainfall
Totalize(1,Rain_mm,IEEE4,0)
EndTable
'End of data_1min Data Tables
```

```
'***END of Define Table***'



'**********Main Program

BeginProg

    cnr4_mult(1) = pyranometer_up_mult

    cnr4_mult(2) = pyranometer_dn_mult

    cnr4_mult(3) = pyrgeometer_up_mult

    cnr4_mult(4) = pyrgeometer_dn_mult

    shf_cal(1) = HFP01_CAL_1

'*****EC data*********

  Scan(EC_SCAN_INTERVAL,mSec,EC_SCAN_BUFFER_SIZE,0)



    'Battery Voltage

    'Battery(Batt_Volt)



    'Panel Temperature
```

```
'PanelTemp (PTemp,250)



'RMY 81000 3-D sonic

VoltDiff (rmy(1),4,mV5000,1,TRUE,200,250,1,0)

Ux = ( rmy(1) * Vel_Multiplier + Vel_Scale )

Uy = ( rmy(2) * Vel_Multiplier + Vel_Scale )

Uz = ( rmy(3) * Vel_Multiplier + Vel_Scale )

Ts = ( rmy(4) * Temp_Multiplier + Temp_offset )



CS7500 (CO2,1,7,6)

                '44 (g/mol) - molecular weight of carbon dioxide

                '0.018 (g/mmol) - molecular weight of water vapor

  CO2_mg_m3 = CO2*44 'Comment these when using

  H2O_g_m3 = H2O*0.018 'Comment these when using

 CallTable ECdata

'*** Beginning of TB4 measurements ***

PulseCount(Rain_mm,1,TB4_INPUT,2,0,0.254,0)
```

```
    '*** End of TB4 measurements ***

          CallTable Data_1min

  NextScan

'*****EC data*********

'*****Low Frenquency data*********

  SlowSequence



  Scan (LF_SCAN_INTERVAL,Sec,3,0)

    'Measure battery voltage.

    Battery (batt_volt)



    '*** Beginning of CNR 4 measurements ***

    PanelTemp (logger_temp,250)

    'CNR4 radiation measurements

    VoltDiff (cnr4(),4,mV20C,CNR4_NRInput,True ,0,_60Hz,cnr4_mult(),0)

   'PRT (Pt-100) temperature measurement
```

```
  Resistance
(cnr4_prt_R,1,mV200,CNR4_TInput,CNR4_EC,1,1500,True,True,0,_60Hz,1,0)
  Rs_R0 = cnr4_prt_R/100
  PRT (cnr4_T_C,1,Rs_R0,1,0)
  'Convert CNR4 temperature to Kelvin
  cnr4_T_K = cnr4_T_C+273.15
  'Correct the long-wave radiation values from pyrgeometers
  long_up_corr = long_up+5.67e-8*cnr4_T_K^4
  long_dn_corr = long_dn+5.67e-8*cnr4_T_K^4
  'Compute short-wave net radiation
  Rs_net = short_up - short_dn
 'Compute long-wave net radiation
  Rl_net = long_up - long_dn
 'Compute albedo
  albedo = short_dn/short_up
 'Compute net radiation
  Rn = Rs_net + Rl_net
```

'*** End of CNR 4 measurements ***

'*** Beginning of SI111 measurements ***

'Const SI111_DIFFINPUT = 10 'Unique differential analog input channel.

'Const SI111_SEINPUT = 21 'Unique SE input channel

'Const SI111_VEINPUT = Vx1 'Unique Vx input channel

Therm109 (SBTempC,1,SI111_SEINPUT,SI111_VEINPUT,0,_60Hz,1.0,0)

'Instruction to measure mV output of thermopile detector (red wire to 2H, black wire to 2L,

'clear wire to ground)

VoltDiff (TargmV,1,mV20,SI111_DIFFINPUT,True ,0,_60Hz,1.0,0)

'Calculation of m (slope) and b (intercept) coefficients for target temperature calculation

m = mC2 * SBTempC^2 + mC1 * SBTempC + mC0

b = bC2 * SBTempC^2 + bC1 * SBTempC + bC0

'Calculation of target temperature

```
    SBTempK = SBTempC + 273.15

    TargTempK = ((SBTempK^4) + m * TargmV + b)^0.25

    TargTempC = TargTempK - 273.15

    'Call output tables

  '*** End of SI111 measurements ***


  '*** Beginning of CS616 measurements ***

  CS616
(cs616_wcr(1),NMBR_CS616,CS616_ANALOG_INPUT,CS616_POWER_CTRL,NMB
R_CS616,1,0)


  For ii = 1 To NMBR_CS616

    cs616_T(ii) = cs616_wcr(ii)

    soil_water(ii) = -0.0663+cs616_T(ii)*(-0.0063+cs616_T(ii)*0.0007)

  Next ii


 '*** End of CS616 measurements ****
```

'*** Beginning of HFP01 measurements ***

VoltDiff

(shf(1),NMBR_SHF,mV50C,SHF_ANALOG_INPUT,TRUE,200,250,shf_cal(),0)

'*** End of HFP01SC measurements ***

'*** Beginning of 107L measurements ***

Therm107(T107_C,1,S107L_SEINPUT,S107L_VxINPUT,0,_60Hz,1.0,0.0)

'*** End of 107L measurements ***

'*** Beginning of CS215 measurements ***

SDI12Recorder(CS215_TRHData(),CS215_C_INPUT,"0","M!",1,0)

SDI12Recorder(TRH3(),3,"0","M!",1,0)

'*** End of CS215 measurements ***

'*** Beginning of TB4 measurements ***

'PulseCount(Rain_mm,1,TB4_INPUT,2,0,0.254,0)

'*** End of TB4 measurements ***

```
    '*****output of 1 min table'


        CallTable Data_1min

    NextScan

EndProg
```

B.5 CR5000 on the 9 m flux tower

```
'================================================================
=

'

' Data Sampling Program for the Campbell Scientific CR5000 logger

'03 Nov 2016

'version 7 for CCZO only with installed sensors

'Contributer: Yao Tang, tangyao1208@gatech.edu

'delete HFP01 and 107L

'Combine 1min output to one table
```

```
'Combine 30min output to one table

'Check cnr4_data and cnr4_Ts

'Rainfall also outputs every minute.



'Start of Constants Customization Section

'The following sensors are measured:

'

'Const SENSOR_CNR_4       = TRUE  'CNR 4                  net radiometer

'Const SENSOR_CS616       = TRUE  'CS616                  water content reflectometers
(volumetric soil moisture)

'Const SENSOR_CS215       = TRUE  'CS215                  temperature and relative humidity
sensor

'Const SENSOR_TB4         = TRUE  'TB4                    TB4 and TB4mm Rain Gages

'Const SENSOR_SI111        = TRUE   'SI111                  SI-111 Precision Infrared
Radiometer



'Const FIND_DIAG_BITS     = TRUE   'Set to TRUE to find individual diagnostic bits.
```

```
'End of Constants Customization Section


' The sign convention for the fluxes is positive away from the surface and
'negative towards the surface.
'
' Before computing online fluxes, the datalogger will introduce lags into the
'eddy covariance data to account for the fixed instrument delays. The lags are
'dependent on the instrument setting and/or the scan interval. Search for "Fixed
'inherent lag" and set the delay to the appropriate value. The raw data is not
'lagged.
'
' The site attendant must load in several constants and calibration values.
'Search for the text string "unique" to find the locations where unique
'constants and calibration values are entered.


'*** Unit Definitions ***
```

'Symbol Units

'C Celsius

'degrees degrees (angle)

'g grams

'J Joules

'kg kilograms

'kPa kilopascals

'm meters

'mg milligrams

'mmol millimoles

'mol moles

's seconds

'umol micromols

'uSeconds microseconds

'V volts

'W Watts

```
'*** Station constants.

Const SCAN_INTERVAL = 1  'Unique value 1s, measurement rate 100 ms (10 Hz) or 50 ms (20 Hz).

Const OUTPUT_INTERVAL = 1 'Unique value, online flux data output interval in minutes.

Dim i As Long                    'Main scan index variable.

Dim ii As Long                   'Slow sequence scan index variable.



'*** Wiring Instructions********

'***CNR 4 Wiring Instructions*****

Const CNR4_NRInput = 1

Const CNR4_EC = Ix1

Const CNR4_TInput = 5

'

'ANALOG CHANNELS
```

'1H CNR4 Pyranometer Upper signal (red)

'1L CNR4 Pyranometer Upper signal reference (blue)

'gnd jumper to 1L

'

'2H CNR4 Pyranometer Lower signal (white)

'2L CNR4 Pyranometer Lower signal reference (thin black)

'gnd jumnper to 2L

'

'3H CNR4 Pyrgeometer Upper signal (grey)

'3L CNR4 Pyrgeometer Upper signal reference (yellow)

'gnd jumper to 3L

'

'4H CNR4 Pyrgeometer Lower signal (brown)

'4L CNR4 Pyrgeometer Lower signal reference (green)

'gnd jumper to 4L

' CNR4 shield (clear)

'

'

'5H CNR4 PRT (Pt-100) signal (green)

'5L CNR4 PRT (Pt-100) signal reference (yellow)

'gnd CNR4 PRT (Pt-100) shield (clear)

'

'CURRENT EXCITATION

'IX1 CNR4 PRT (Pt-100) current excitation (grey)

'

'IXR CNR4 PRT (Pt-100) current excitation return (brown)

'

'CNR4 sensor

'*** End of CNR 4 wiring ***

'*** CS616 wiring ***

'Only install one CS616

Const CS616_ANALOG_INPUT = 27 'Unique single-ended analog input channel.

Const CS616_POWER_CTRL = 4 'Unique control port.

```
Const NMBR_CS616 = 1              'Unique number of CS616 to measure.

'*** Beginning of CS616 wiring ***

'14H      Signal #1 (green)

'14L      Signal #2 (green) (neglecting Signal #2) if only install 1 sensor

'C4       Power control #1 (orange)

'         Power control #2 (orange)

'G        Shield #1 (clear)

'         Shield #2 (clear)



'12V      Power #1 (red)

'         Power #2 (red)

'G        Signal reference #1 (black)

'         Signal reference #2 (black)

'*** End of CS616 wiring ***



'**** CS215***

Const CS215_ANALOG_INPUT = 1      'Unique differential analog input channel.
```

```
'*** Beginning of CS215 wiring ***
' Color   Function          CR5000
' -----   --------          -------
' Red     Power (12V)       12V
' Green   SDI-12 signal     C1
' Black   Power ground      G
' White   Power ground      G
' Clear   Shield          Signal Ground (C1 Ground)
'*** End of CS215 wiring ***


'****SENSOR_TB4***


Const TB4_INPUT = 1       'Unique differential analog input channel.
'*** Beginning of TB4 wiring ***
' Color   Function               Pulse Channel CR5000
' -----   --------               -------
' Black   Rain signal            P,P_SW, or U (pulse channel)
```

```
' White  Rain signal reference         AG or downward (Analog ground)

' Clear  Shield                        AG or downward

'*** End of TB4 wiring ***



'SENSOR_SI111

Const SI111_DIFFINPUT = 11         'Unique differential analog input channel.

Const SI111_SEINPUT = 40           'Unique SE input channel

Const SI111_VEINPUT = Vx2                  'Unique Vx input channel

'*** Beginning of SI111 wiring ***

' Color   Function               Pulse Channel CR5000

'       SI-111 Thermopile             -------

' Red      Diff.High                  11H

' Black    Diff.Low                   11L

' Clear    Analog Ground              AG

'      SI-111 Thermistor             -------

' Green      Singled-ended            SE40

' Blue       Analog Ground            AG
```

```
' White      Exicitation              VX2

'*** End of SI111 wiring ***



'POWER IN

'12V     datalogger (red)

'G       datalogger (black)



'EXTERNAL POWER SUPPLY

'+12V    datalogger (red)

'G       datalogger (black)



'*** Beginning of CNR 4 constants and variables ***

Public logger_temp, batt_volt

Public cnr4(4)

Alias cnr4(1) = short_up

Alias cnr4(2) = short_dn
```

Alias cnr4(3) = long_up

Alias cnr4(4) = long_dn

Public cnr4_T_C 'CNR4 thermistor temperature in Celcius

Public cnr4_T_K 'CNR4 thermistor temperature in Kelvin

Public long_up_corr 'Downwelling long-wave radiation with temperature correction

Public long_dn_corr 'Upwelling long-wave radiation with temperature correction

Public Rs_net 'short-wave net radiation

Public Rl_net 'long-wave net radiation

Public albedo 'Albedo

Public Rn 'total net radiation

Units logger_temp = degC

Units batt_volt = volts

Units short_up = W/m^2

Units short_dn = W/m^2

Units long_up = W/m^2

Units long_dn = W/m^2

Units cnr4_T_C = deg_C

```
Units cnr4_T_K = K

Units long_up_corr = W/m^2

Units long_dn_corr = W/m^2

Units Rs_net = W/m^2

Units Rl_net = W/m^2

Units albedo = W/m^2

Units Rn = W/m^2

Dim cnr4_prt_R, Rs_R0

'CNR4 sensitivities: refer to the Certificate of Calibration from Kipp & Zonen for sensitivity values

'for each probes, and enter them below.

Const pyranometer_up_sensitivity = 10.30 'unique sensitivity for upper pyranometer '(microV/W/m^2)

Const pyranometer_dn_sensitivity = 10.30 'unique sensitivity for lower pyranometer '(microV/W/m^2)

Const pyrgeometer_up_sensitivity = 12.09 'unique sensitivity for upper pyrgeometer '(microV/W/m^2)
```

```
Const pyrgeometer_dn_sensitivity = 12.09 'unique sensitivity for lower pyrgeometer '(microV/W/m^2)

'CNR4 multipliers

Public cnr4_mult(4)

Const pyranometer_up_mult = 1000/pyranometer_up_sensitivity '(W/m^2/mV)

Const pyranometer_dn_mult = 1000/pyranometer_dn_sensitivity '(W/m^2/mV)

Const pyrgeometer_up_mult = 1000/pyrgeometer_up_sensitivity '(W/m^2/mV)

Const pyrgeometer_dn_mult = 1000/pyrgeometer_dn_sensitivity '(W/m^2/mV)

'*** End of CNR 4 constants and variables ***



'*** Beginning of CS616 constants and variables ***

Public cs616_wcr(NMBR_CS616)          'Water content reflectometer period.

Public soil_water(NMBR_CS616)        'Volumetric soil water content

Dim cs616_T(NMBR_CS616)               'Water content reflectometer period.

Units cs616_wcr = uSeconds

Units soil_water = frac_v_wtr
```

'*** End of CS616 constants and variables ***

'*** Beginning of CS215 constants and variables ***

Public CS215_TRHData(2)

Alias CS215_TRHData(1) = AirTC

Alias CS215_TRHData(2) = RH

Units AirTC = Deg C

Units RH = %

'*** End of CS215 constants and variables ***

'*** Beginning of TB4 constants and variables ***

Public Rain_mm

Units Rain_mm = mm

'*** End of TB4 constants and variables ***

'*** Beginning of SI111 constants and variables ***

Public PanelT, BattV, SBTempC, SBTempK, TargmV, m, b, TargTempK, TargTempC

```
'***************ATTENTION

'SN:SI-111-5783

'Declare constants (replace the listed values with coefficients received with sensor)

Const mC2 = 96630.5

Const mC1 = 8303050

Const mC0 = 1438870000

Const bC2 = 3302.07

Const bC1 = 192496

Const bC0 = -3518730

'*** End of SI111 constants and variables ***



'****''''''''''''''''''''Tables''''''''''''''''''''''''''''****

'*** Output data tables ***



'Define 1min_data Data Tables

DataTable (data_1min,True,-1)

CardOut(0,-1)
```

DataInterval (0,OUTPUT_INTERVAL,Min,0)

Minimum (1,batt_volt,FP2,0,False)

Sample (1,logger_temp,FP2)

'cnr4 data

Average (4,cnr4(1),IEEE4,False)

Average (1,cnr4_T_C,IEEE4,False)

Average (1,cnr4_T_K,IEEE4,False)

Average (1,long_up_corr,IEEE4,False)

Average (1,long_dn_corr,IEEE4,False)

Average (1,Rs_net,IEEE4,False)

Average (1,Rl_net,IEEE4,False)

Average (1,albedo,IEEE4,False)

Average (1,Rn,IEEE4,False)

'air T and RH

Average(1,AirTC,FP2,False)

Sample(1,RH,FP2)

'infrared temp

```
  Sample (1,PanelT,FP2)
  Average (1,TargmV,FP2,False)
  Average (1,SBTempC,FP2,False)
  Average (1,TargTempC,FP2,False)
'soil moisture
Average (NMBR_CS616,soil_water(1),IEEE4,0)
Average (NMBR_CS616,cs616_wcr(1),IEEE4,0)
' Rainfall
Totalize(1,Rain_mm,IEEE4,0)
EndTable
'End of data_1min Data Tables


'***END of Define Table***'


'*** Program ***


BeginProg
```

```
  cnr4_mult(1) = pyranometer_up_mult

  cnr4_mult(2) = pyranometer_dn_mult

  cnr4_mult(3) = pyrgeometer_up_mult

  cnr4_mult(4) = pyrgeometer_dn_mult



Scan (1,Sec,3,0)

  'Measure battery voltage.

  Battery (batt_volt)



  '*** Beginning of CNR 4 measurements ***

  PanelTemp (logger_temp,250)

  'CNR4 radiation measurements

  VoltDiff (cnr4(),4,mV20C,CNR4_NRInput,True ,0,_60Hz,cnr4_mult(),0)

 'PRT (Pt-100) temperature measurement

  Resistance
(cnr4_prt_R,1,mV200,CNR4_TInput,CNR4_EC,1,1500,True,True,0,_60Hz,1,0)
```

```
Rs_R0 = cnr4_prt_R/100

PRT (cnr4_T_C,1,Rs_R0,1,0)

'Convert CNR4 temperature to Kelvin

cnr4_T_K = cnr4_T_C+273.15

'Correct the long-wave radiation values from pyrgeometers

long_up_corr = long_up+5.67e-8*cnr4_T_K^4

long_dn_corr = long_dn+5.67e-8*cnr4_T_K^4

'Compute short-wave net radiation

Rs_net = short_up - short_dn

'Compute long-wave net radiation

Rl_net = long_up - long_dn

'Compute albedo

albedo = short_dn/short_up

'Compute net radiation

Rn = Rs_net + Rl_net

'*** End of CNR 4 measurements ***
```

```
  '*** Beginning of CS616 measurements ***
  CS616
(cs616_wcr(1),NMBR_CS616,CS616_ANALOG_INPUT,CS616_POWER_CTRL,NMB
R_CS616,1,0)

  For ii = 1 To NMBR_CS616
    cs616_T(ii) = cs616_wcr(ii)
    soil_water(ii) = -0.0663+cs616_T(ii)*(-0.0063+cs616_T(ii)*0.0007)
  Next ii

'*** End of CS616 and HFP01 measurements ****

  '*** Beginning of CS215 measurements ***
  SDI12Recorder(CS215_TRHData(),CS215_ANALOG_INPUT,"0","M!",1,0)
  '*** End of CS215 measurements ***

  '*** Beginning of SI111 measurements ***
```

```
'Const SI111_DIFFINPUT = 11        'Unique differential analog input channel.

'Const SI111_SEINPUT = 40          'Unique SE input channel

'Const SI111_VEINPUT = Vx2                'Unique Vx input channel

 'Instruction to measure sensor body temperature (green wire to SE40, white wire to VX2,

'blue wire to ground)

Therm109 (SBTempC,1,SI111_SEINPUT,SI111_VEINPUT,0,_60Hz,1.0,0)

'Instruction to measure mV output of thermopile detector (red wire to 2H, black wire to 2L,

'clear wire to ground)

VoltDiff (TargmV,1,mV20,SI111_DIFFINPUT,True ,0,_60Hz,1.0,0)

'Calculation of m (slope) and b (intercept) coefficients for target temperature calculation

m = mC2 * SBTempC^2 + mC1 * SBTempC + mC0

b = bC2 * SBTempC^2 + bC1 * SBTempC + bC0

'Calculation of target temperature

SBTempK = SBTempC + 273.15
```

```
    TargTempK = ((SBTempK^4) + m * TargmV + b)^0.25
    TargTempC = TargTempK - 273.15
    'Call output tables
  '*** End of SI111 measurements ***
  '*** Beginning of TB4 measurements ***
  PulseCount(Rain_mm,1,TB4_INPUT,2,0,0.254,0)
  '*** End of TB4 measurements ***
  '*****output of 1 min table'
        CallTable data_1min

  '*** Beginning of TB4 measurements ***
  'PulseCount(Rain_mm,1,TB4_INPUT,2,0,0.254,0)
  'CallTable(TB4_mm)
  '*** End of TB4 measurements ***

  NextScan
EndProg
```

APPENDIX C. PROGRAMS TO PLOT DATA

Instructions to plot data in the field:

(1) Collect data from data loggers using LoggerNet or memory card;

(2) Input data to a excel file without headers;

(3) Run the following programs to plot data.

Note: For data from CR3000 data logger, use CardConvert from LoggerNet software to convert data from TOA format to ASCII format.

C.1 Plot data from CR1000 12211 at cropland site

```
clear

clc



filename = 'DoveField.xlsx';

Table = readtable(filename);

T1 = datetime(Table{:,1},'InputFormat','M/d/yyyy h:mm:ss a');

T = table2array(Table(:,2:end));
```

```
Ts_2cm_CL = T(:,2);

Ts_30cm_CL = T(:,3);

Ts_50cm_CL = T(:,4);

Ts_1m_CL = T(:,5);

Ts_2m_CL = T(:,6);

Ts_7m_CL = T(:,7);

Theta_2cm_CL =  T(:,8);

Theta_30cm_CL =  T(:,9);

Theta_130cm_CL =  T(:,10);

Theta_2m_CL =  T(:,11);

Ta_CL = T(:,18);

RH_CL = T(:,19);

Rain_CL = T(:,20);



figure(1);

subplot(2,1,1);

plot(T1,Ts_2cm_CL,T1,Ts_30cm_CL,T1...
```

```
    ,Ts_50cm_CL,T1,Ts_1m_CL,T1,Ts_2m_CL...
    ,T1,Ts_7m_CL,'-b','LineWidth',1);
legend('0cm','30cm','50cm','100cm','200cm','700cm');
ylabel('Ts (Crop) (DegreeC)');


subplot(2,1,2);
plot(T1,Theta_2cm_CL,T1,Theta_30cm_CL,...
    T1,Theta_130cm_CL,T1,Theta_2m_CL,'LineWidth',2);
legend('0cm','30cm','130cm','200cm');
ylabel('\Theta (Crop) (Volumatric Water Content)');


figure(2);
subplot(3,1,1);
plot(T1,Ta_CL);
ylabel('Ta');
subplot(3,1,2);
plot(T1,RH_CL);
```

```
ylabel('RH');

subplot(3,1,3);

plot(T1,Rain_CL);

ylabel('Rain');
```

C.2 Plot data from CR1000 SN2588 data logger

```
clear

clc

filename = 'SN2588.xlsx';

Table = readtable(filename);

T1 = datetime(Table{:,1},'InputFormat','M/d/yyyy h:mm:ss a');

T = table2array(Table(:,2:end));

T(T==-9999) = NaN;

Ts_30cm_YP = T(:,2);

Ts_60cm_YP = T(:,3);

Ts_80cm_YP = T(:,4);

Theta_30cm_YP = T(:,5);

Theta_60cm_YP = T(:,6);
```

```
Theta_80cm_YP = T(:,7);

G_80cm = T(:,11);

figure(2);

subplot(3,1,1);

plot(T1,Ts_30cm_YP,T1,Ts_60cm_YP,T1,Ts_80cm_YP);

legend('30cm','60cm','80cm');

ylabel('Tsoil(C)');



subplot(3,1,2);

plot(T1,Theta_30cm_YP,T1,Theta_60cm_YP,T1,Theta_80cm_YP);

legend('30cm','60cm','80cm');

ylabel('\Theta');



subplot(3,1,3);

plot(T1,G_80cm);

ylabel('G (Wm^-2)');
```

C.3 Plot data from CR1000 SN2589 data logger

```
clear

clc

filename = 'SN2589.xlsx';

Table = readtable(filename);

T1 = datetime(Table{:,1},'InputFormat','M/d/yyyy h:mm:ss a');

T = table2array(Table(:,2:end));

T(T==-9999) = NaN;

Ta_5m = T(:,2);

RH_5m = T(:,3);

Ta_3m = T(:,4);

RH_3m = T(:,5);

Ta_1m = T(:,6);

RH_1m = T(:,7);

Ta_20cm = T(:,8);

RH_20cm = T(:,9);

Theta_2cm_YP = T(:,10);
```

```
Theta_15cm_YP = T(:,11);

Theta_40cm_YP = T(:,12);

G_2cm = T(:,16);

G_15cm = T(:,17);

G_40cm = T(:,18);

Ts_2cm_YP = T(:,19);

Ts_15cm_YP = T(:,20);

Ts_40cm_YP = T(:,21);



figure(1); %Above Canopy

subplot(2,1,1);

plot(T1,Ta_20cm,T1,Ta_1m,T1,Ta_3m,T1,Ta_5m);

legend('20cm','1m','3m','5m');

ylabel('Ta (DegreeC)');

subplot(2,1,2);

plot(T1,RH_20cm,T1,RH_1m,T1,RH_3m,T1,RH_5m);

legend('20cm','1m','3m','5m');
```

```
ylabel('RH (%)');



figure(2);

subplot(3,1,1);

plot(T1,Ts_2cm_YP,T1,Ts_15cm_YP,T1,Ts_40cm_YP);

legend('2cm','15cm','40cm');

ylabel('Tsoil(C)');



subplot(3,1,2);

plot(T1,Theta_2cm_YP,T1,Theta_15cm_YP,T1,Theta_40cm_YP);

legend('2cm','15cm','40cm');

ylabel('\Theta');



subplot(3,1,3);

plot(T1,G_2cm,T1,G_15cm,T1,G_40cm);

legend('2cm','15cm','40cm');

ylabel('G (Wm^-2)');
```

C.4 Plot data from CR5000 data logger

```
clear

clc



filename = 'CR5000.xlsx';

Table = readtable(filename);

T1 = datetime(Table{:,1},'InputFormat','M/d/yyyy h:mm:ss a');

T = table2array(Table(:,2:end));



T(T==-9999) = NaN;



Voltage = T(:,2);

Shortwave_AC_DW = T(:,4);

Shortwave_AC_UW = T(:,5);

Longwave_AC_DW = T(:,10);

Longwave_AC_UW = T(:,11);

T_CNR4 = T(:,8);
```

```
RnS_AC = T(:,12);

RnL_AC = T(:,13);

Albedo_AC = T(:,14);

Rn_AC = T(:,15);

Ta_9m = T(:,16);

RH_9m = T(:,17);

T_SB = T(:,20);

SkinT_AC = T(:,21);

Theta_AC = T(:,22);

Rain_AC = T(:,24);



figure(1);

subplot(4,1,1);

plot(T1,Shortwave_AC_DW);

ylabel('Shortwave DW');
```

```
subplot(4,1,2);

plot(T1,Shortwave_AC_UW);

ylabel('Shortwave UW');



subplot(4,1,3);

plot(T1,Albedo_AC);

ylabel('Albedo');



subplot(4,1,4);

plot(T1,RnS_AC);

ylabel('RnS');



figure(2);

subplot(3,1,1);

plot(T1,Longwave_AC_DW);

ylabel('Longwave DW');
```

```
subplot(3,1,2);

plot(T1,Longwave_AC_UW);

ylabel('Longwave UW');



subplot(3,1,3);

plot(T1,RnL_AC);

ylabel('RnL');



figure(3);

subplot(3,1,1);

plot(T1,RnS_AC);

ylabel('RnS');



subplot(3,1,2);

plot(T1,RnL_AC);

ylabel('RnL');
```

```
subplot(3,1,3);

plot(T1,Rn_AC);

ylabel('Rn');



figure(4);

subplot(3,1,1);

plot(T1,T_CNR4,T1,Ta_9m,T1,T_SB,T1,SkinT_AC);

legend('CNR4','CS215','T_SB','SkinT');

ylabel('T(C)');



subplot(3,1,2);

plot(T1,RH_9m);

ylabel('RH');



subplot(3,1,3);

plot(T1,Theta_AC);

ylabel('Theta');
```

```
figure(5);

plot(T1,Voltage);

ylabel('Voltage');



figure(6);

plot(T1,Rain_AC);

ylabel('Rain(mm/min)');
```

C.5 Plot data from CR3000 data logger

```
clear

clc



filename = 'CR3000.xlsx';

Table = readtable(filename);

T1 = datetime(Table{:,1},'InputFormat','M/d/yyyy h:mm:ss a');

T = table2array(Table(:,2:end));
```

```
T(T==-9999) = NaN;



Voltage_BC = T(:,2);

Shortwave_BC_DW = T(:,4);

Shortwave_BC_UW = T(:,5);

T_CNR4 = T(:,8);

Longwave_BC_DW = T(:,10);

Longwave_BC_UW = T(:,11);

RnS_BC = T(:,12);

RnL_BC = T(:,13);

Albedo_BC = T(:,14);

Rn_BC = T(:,15);

Ta_2m_BC = T(:,16);

RH_2m_BC = T(:,17);

Ta_20cm_BC = T(:,18);

RH_20cm_BC = T(:,19);

T_SB = T(:,22);
```

```
SkinT_BC = T(:,23);

Theta_BC = T(:,24);

Ts_BC = T(:,26);

G_BC = T(:,27);

Rain_BC = T(:,28);




figure(1);

subplot(4,1,1);

plot(T1,Shortwave_BC_DW);

ylabel('Shortwave DW');



subplot(4,1,2);

plot(T1,Shortwave_BC_UW);

ylabel('Shortwave UW');



subplot(4,1,3);
```

```
plot(T1,Albedo_BC);

ylabel('Albedo');



subplot(4,1,4);

plot(T1,RnS_BC);

ylabel('RnS');



figure(2);

subplot(3,1,1);

plot(T1,Longwave_BC_DW);

ylabel('Longwave DW');



subplot(3,1,2);

plot(T1,Longwave_BC_UW);

ylabel('Longwave UW');



subplot(3,1,3);
```

```
plot(T1,RnL_BC);

ylabel('RnL');



figure(3);

subplot(3,1,1);

plot(T1,RnS_BC);

ylabel('RnS');



subplot(3,1,2);

plot(T1,RnL_BC);

ylabel('RnL');



subplot(3,1,3);

plot(T1,Rn_BC);

ylabel('Rn');



figure(4);
```

```
subplot(4,1,1);

plot(T1,T_CNR4,T1,Ta_2m_BC,T1,Ta_20cm_BC,T1,T_SB,T1,SkinT_BC,T1,Ts_BC);

legend('CNR4','2m','20cm','T_SB','SkinT','Tsoil');

ylabel('T(C)');



subplot(4,1,2);

plot(T1,RH_2m_BC,T1,RH_20cm_BC);

legend('2m','20cm');

ylabel('RH');



subplot(4,1,3);

plot(T1,Theta_BC);

ylabel('Theta');

subplot(4,1,4);

plot(T1,G_BC);

ylabel('G');
```

```
figure(5);

plot(T1,Voltage_BC);

ylabel('Voltage');



figure(6);

plot(T1,Rain_BC);

ylabel('Rain(mm/min)');
```

APPENDIX D. EC FLUX DATA QUALITY ANALYSIS

Quality control analysis must be applied to EC measurements because practical instrumentation cannot fully meet the requirements of the underlying micrometeorological theory. Quality control analysis includes the raw data processing, spectral corrections, and fulfillment of theoretical requirement tests, and a final flag system indicating data quality. An overall quality flag system is applied following an overview paper by Foken et al.[2005].

The processing of raw data includes these procedures:

(1) excluding unrealistic spikes

(2) the crosswind correction. In a three-dimensional sonic anemometer, the sonic temperature is estimated on each of the three measurement paths. The three estimates are then averaged into a single value of sonic temperature. The crosswind correction accounts for the effect of a wind component normal to the measurement path on each estimation of the sonic temperature. The crosswind correction is often applied in the firmware of some anemometers. In these cases, applying the correction of the raw data will result in double accounting.

(3) the angle of attack correction. The angle of attack error arises due to the imperfect sine and cosine response of an anemometer. When the wind approaches the anemometer with a considerable angle of attack, the frame of a post-mounted sonic distorts the flow, resulting

in inaccurate measurements. Furthermore, the transducer poles create a self-sheltering effect that also affects the measurement.

(4) Wind tilt correction. Tilt correction algorithms have been developed to correct wind statistics for any misalignment of the sonic anemometer with respect to the local wind streamlines. In particular, this implies that stresses and fluxes evaluated perpendicular to the local streamlines are affected by spurious contributions from the variance of along-streamlines components.

(5) Time lags correction. The last step of raw data processing regards the compensation of possible time lags between anemometric variables and variables measured by any other sensor, notably the gas analyzer. A time lag arises for different reasons in closed path and in open path systems. The presence of the intake tube in closed path systems implies that gas concentrations are always measured with a certain delay with respect to the moment air is sampled. In addition, the residence time of sticky gasses, such as H2O, in the sampling line is a strong function of air relative humidity and temperature. Conversely, sonic anemometers measure wind speed and sonic temperature without detectable delays. In open path systems, the delay is due to the physical distance between the two instruments, which are usually placed several decimeters or less apart to avoid mutual disturbances. The wind field takes some time to travel from one to the other, resulting in a certain delay between the moments the same air parcel is sampled by the two instruments.

(6) Detrending turbulent fluctuations. Detrending refers to the operation of establishing and removing a trend in raw time series before calculating turbulent fluctuations.

After the processing of raw data, spectral corrections must be conducted to obtain accurate fluxes. Spectral corrections compensate flux underestimations due to two distinct effects:

(1) Fluxes are calculated on a finite averaging time, implying that longer-term turbulent contributions are under-sampled to some extent, or completely. The correction for these flux losses is referred to as high-pass filtering correction.

(2) Instrument and setup limitations that do not allow sampling the full spatiotemporal turbulence fluctuations and necessarily imply some space or time averaging of smaller eddies, as well as actual dampening of the small-scale turbulent fluctuations. The correction for these flux losses is referred to as low-pass filtering correction.

After these corrections, the fulfillment of theoretical requirement of EC measurements is tested. The tests include steady state tests and test on developed turbulent conditions. Steady state conditions mean that all statistical parameters do not vary in time. Typical non-stationarity is driven by the change of meteorological variables with the time of the day, changes of weather patterns, significant mesoscale variability, or changes of the measuring point relative to the measuring events such as the phase of a gravity wave. The latter may occur because of changing footprint areas, changing internal boundary layers, or by gravity waves. Presently there are two main tests used to identify non-steady state conditions. The first is based on the trend of a meteorological parameter over the averaging interval of the time series [*Vickers and Mahrt*, 1997], and the second method indicates non-steady state conditions within the averaging interval [*T. Foken and Wichura*, 1996].

The second quality control test is the test on developed turbulent conditions. Flux-variance similarity is a good measure to test the development of turbulent conditions. This similarity

means that the ratio of the standard deviation of a turbulent parameter and its turbulent flux is nearly constant or a function of stability. These integral turbulence characteristics are basic similarity characteristics of the atmospheric turbulence.

To be useful, the results of data quality checking are made available in the final data archive. Measurements are normally flagged according to their status such as uncontrolled, controlled, corrected, etc. The quality tests given above open the possibility to flag also the quality of a single measurement. The most important part of a flag system is the combination of all flags into a general flag for easy use. We adopt the flag system first proposed by Foken and Wichura [1996]. The flag system is classified by micrometeorological experiences so that classes 1 to 3 can be used for fundamental research, such as the development of parameterizations. The classes 4 to 6 are available for general use like for continuously running systems of the FLUXNET program Classes 7 and 8 are only for orientation. Sometimes it is better to use such data instead of a gap filling procedure, but then these data should not differ significantly from the data before and after these data in the time series. Data of class 9 should be excluded under all circumstances.

Data quality tests are conducted with all available turbulent flux data. Figures D.1 to D.3 show the time series of the corrected and uncorrected fluxes and the quality flags at the CCZO ACS. There is no much difference between the corrected and uncorrected fluxes, indicating the appropriate instrumentation and the high quality of the measurements. The unreasonable spikes of the fluxes must be excluded based on field experiences site by site. In the following analysis, these spikes are excluded. Figures D.4 shows the scatter plots of the corrected and uncorrected fluxes at CCZO ACS. The close agreement of the corrected and uncorrected fluxes demonstrates the high quality of our field measurements at CCZO

ACS. Table D.1 shows the percentages of Class 9 EC fluxes data for all available data. At the CCZO ACS, only 1 % of all fluxes are in Class 9 and excluded in the following analysis.

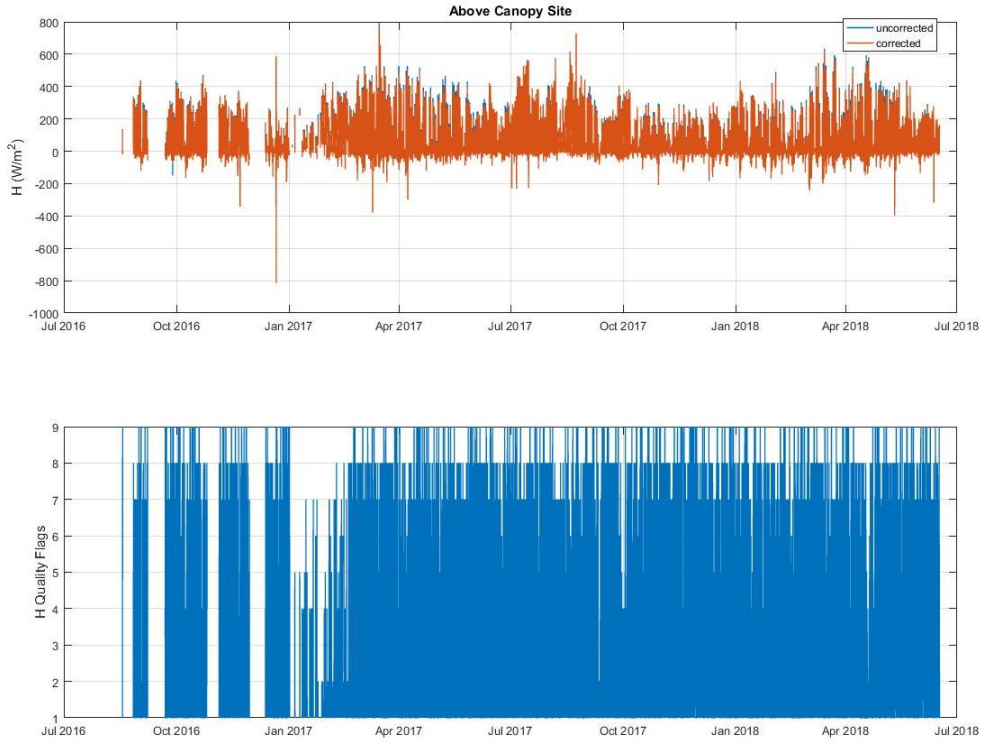

Figure D1 Quality Analysis of H at the CCZO ACS

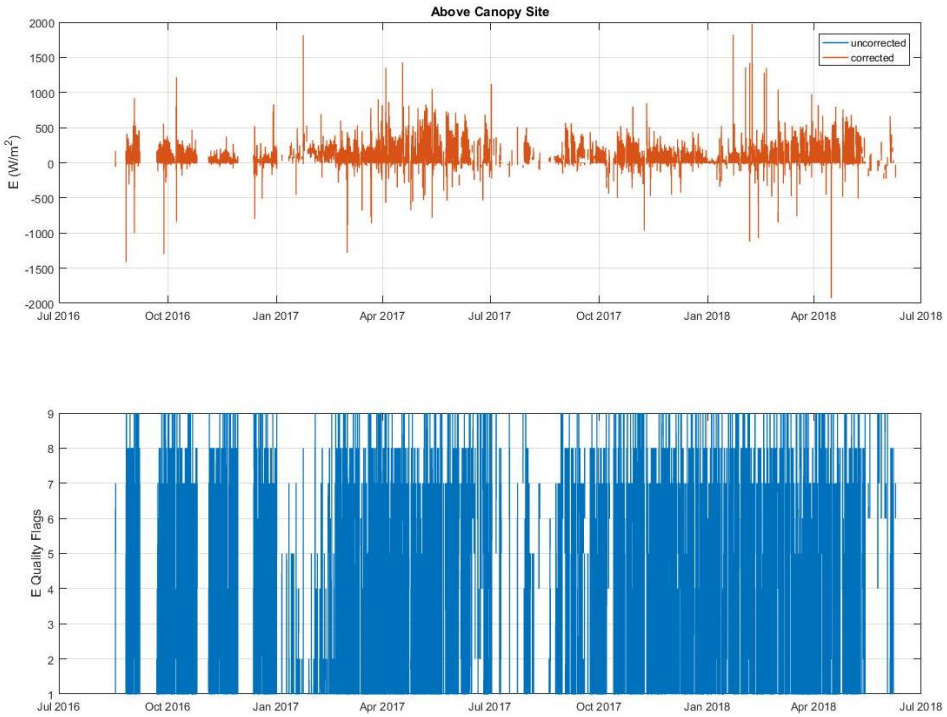

Figure D2 Quality Analysis of E at the CCZO ACS

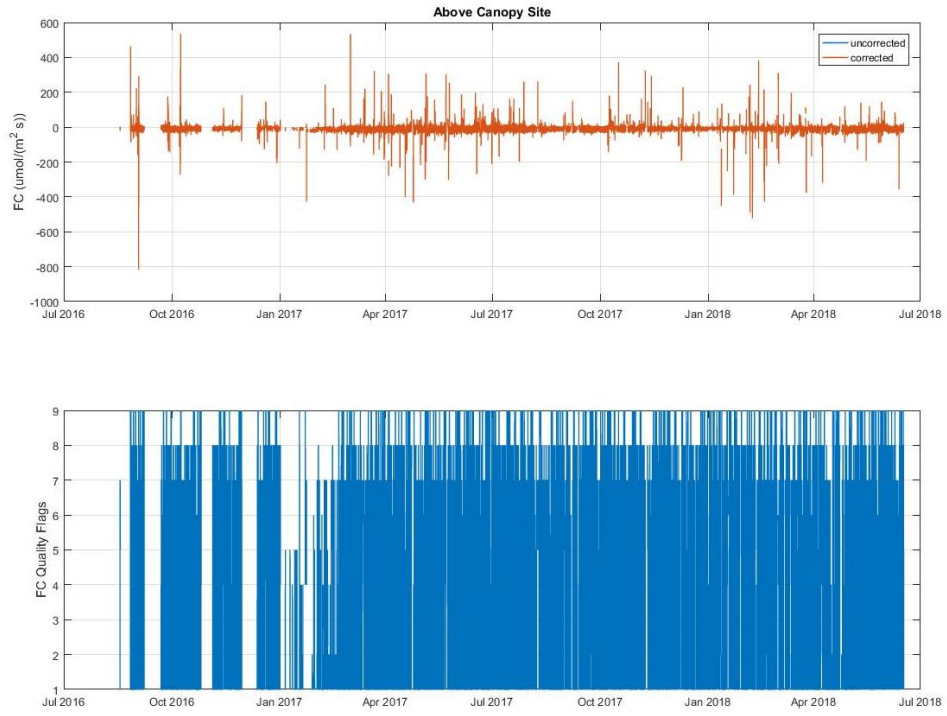

Figure D3 Quality Analysis of FC at the CCZO ACS

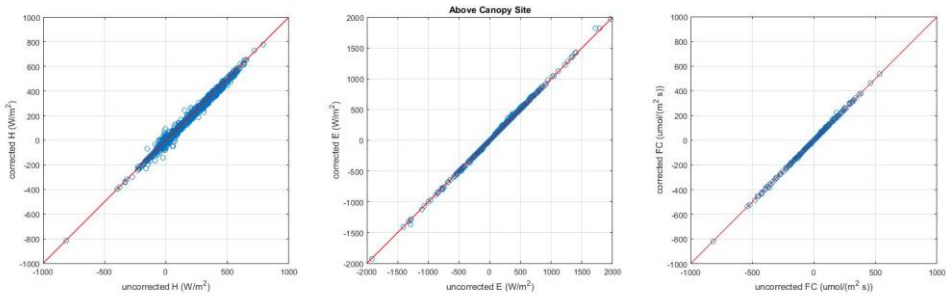

Figure D4 Quality Analysis of EC fluxes at the CCZO ACS

Table D1 Percentages of Class 9 EC Fluxes Data for all available data

Site	n	H	E	Fc
ACS	27682	1	1	1
BCS	6574	1	2	2

Figures D.5 to D.7 show the time series of the corrected and uncorrected fluxes and the quality flags at the CCZO BCS. Figures D.8 shows the scatter plots of the corrected and uncorrected fluxes at CCZO ACS and BCS. The close agreement of the corrected and uncorrected fluxes demonstrates the high quality of our field measurements. The class 9 EC fluxes are no more than 2 % of total available data (Table D.1), demonstrating the high quality of our EC fluxes at CCZO BCS.

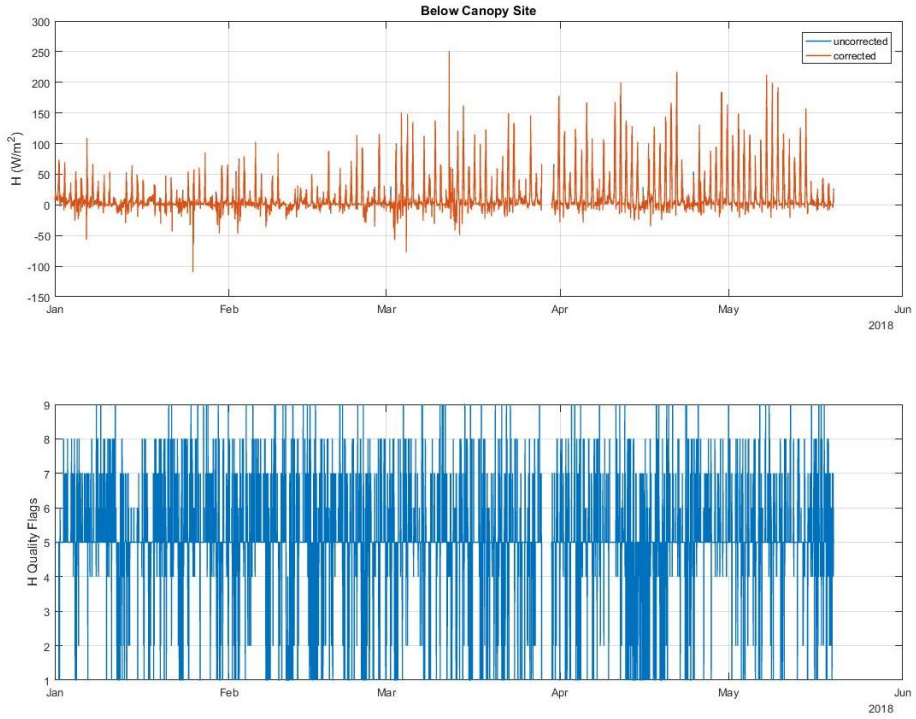

Figure D5 Quality Analysis of H at the CCZO BCS

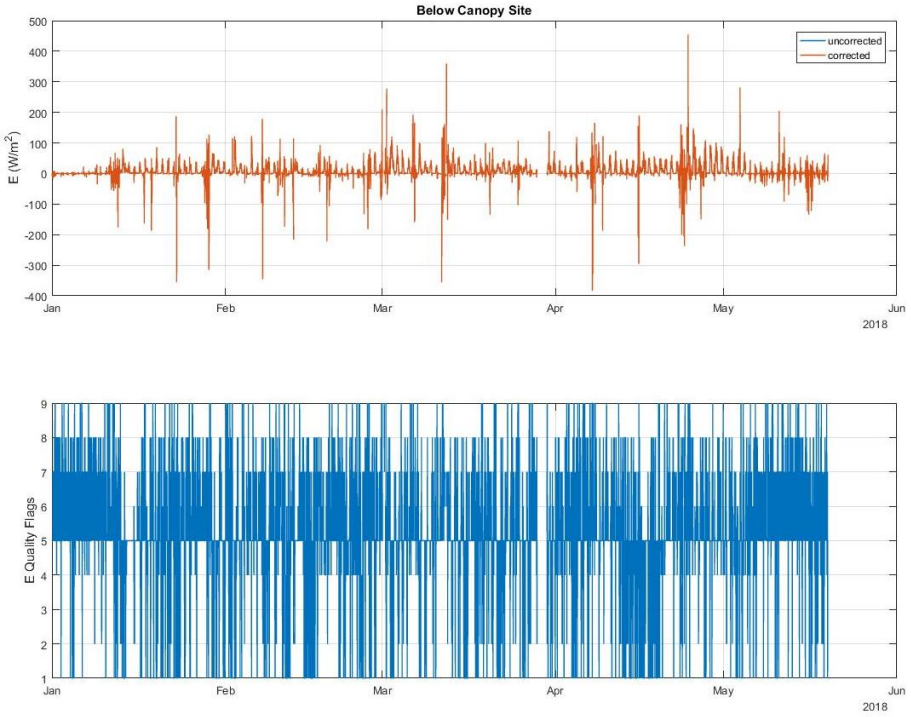

Figure D6 Quality Analysis of E at the CCZO BCS

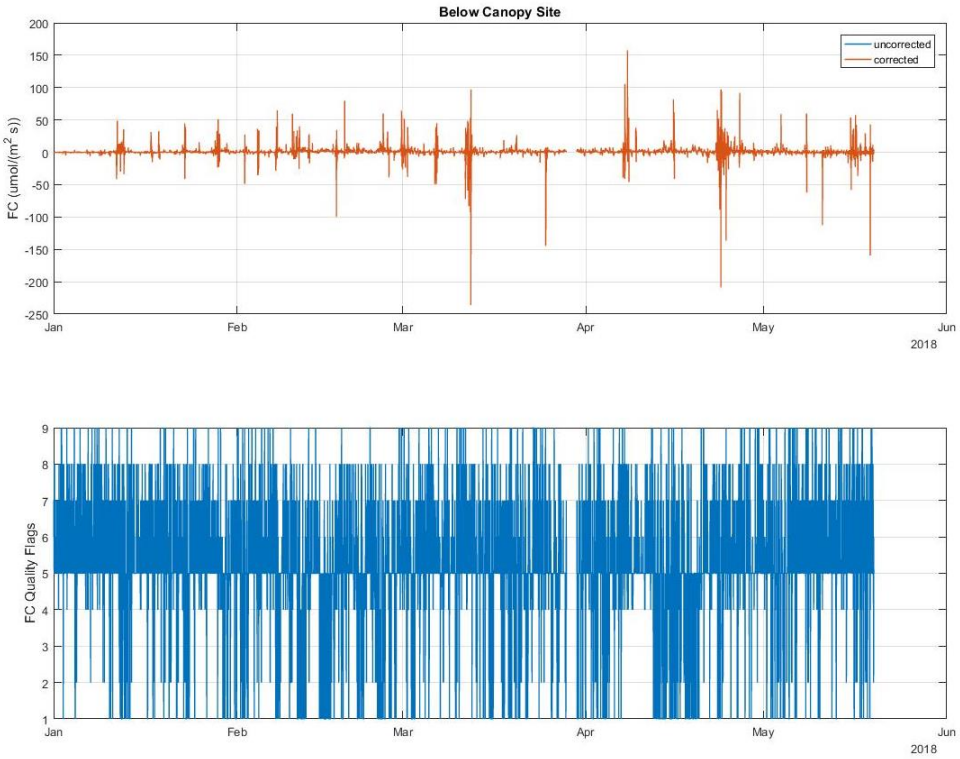

Figure D7 Quality Analysis of FC at the CCZO BCS

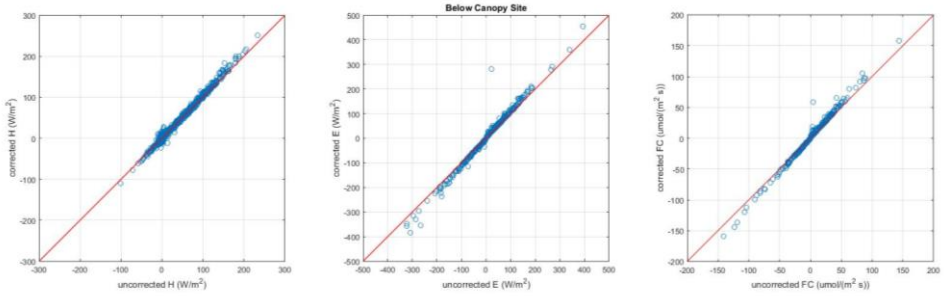

Figure D8 Quality Analysis of EC fluxes at the CCZO BCS

APPENDIX E. DERIVATION OF EQ. 4.17

Eddy-diffusivity D_c in Eq. 4.15 may be parameterized [*Wang and Bras*, 2010] as

$$D_c = C_k \kappa z u_* \tag{E1}$$

where z (m) is the height above the ground or canopy surface, κ (≈ 0.4) the von Karman constant, C_k an empirical constant characterizing the boundary stability in the Monin-Obukhov similarity equations,

$$C_k = \begin{cases} \dfrac{2}{1+2\alpha}, H < 0 \text{ (stable)} \\ \dfrac{\sqrt{3}}{\alpha}, H > 0 \text{ (unsatble)} \end{cases}, \tag{E2}$$

and u_* the friction velocity expressed as a function of sensible heat fluxes H,

$$u_* = \begin{cases} -\left(\dfrac{2\beta\kappa g H z}{\rho c_p T_r} \right)^{\frac{1}{3}}, H < 0 \\ \left(\dfrac{\gamma_2 \kappa g H z}{2\rho c_p T_r} \right)^{\frac{1}{3}}, H > 0 \end{cases}. \tag{E3}$$

where ρ (≈ 1.2 kg m^{-3}) is the representative density of air, T_r (≈ 300 K) the representative environment temperature, g (9.8 m s^{-2}) the gravitational acceleration, the universal empirical coefficients α ~ 0.75 or 1, β ~ 4.7, and γ_2 ~ 9 [*Businger et al.*, 1971]. Then D_0 in Eq. 4.16 is obtained,

$$D_0 = \begin{cases} \dfrac{2(2\beta)^{\frac{1}{3}}}{1+2\alpha}\left(\dfrac{g\kappa^4}{\rho c_p T_r}\right)^{\frac{1}{3}} = 1.25\times10^{-2}, H<0 \\ \dfrac{\sqrt{3}}{\alpha}\left(\dfrac{\gamma_2}{2}\right)^{\frac{1}{3}}\left(\dfrac{g\kappa^4}{\rho c_p T_r}\right)^{\frac{1}{3}} = 2.54\times10^{-2}, H>0 \end{cases} . \quad \text{(E4)}$$

When the air temperature changes from -10 ℃ to 30 ℃ and the air density changes correspondingly, the change of D_0 is less than 1%. Therefore, D_0 is not sensitive to local air temperature and local air density, and can be treated as a constant.

The derivation of Eq. 4.17 below follows Oldham and Spanier [2006]. Assuming H invariant with height (z) within the surface layer, the change of variables $t' = \int_0^t |H(\tau)|^{\frac{1}{3}} d\tau$, $\xi = z^{\frac{1}{3}}$ and $A = \dfrac{D_0}{9}$ allows Eq. 4.15 to be re-written as,

$$\frac{\partial C}{\partial t'} = A\left(\frac{2}{\xi}\frac{\partial C}{\partial \xi} + \frac{\partial^2 C}{\partial \xi^2}\right). \quad \text{(E5)}$$

An analytical solution of Eq. (E5) with the initial and boundary conditions of $C(\xi > 0, t' = 0) = C_0$, and $C(\xi \to \infty, t' > 0) = C_0$, respectively, is given as,

$$\frac{\partial}{\partial \xi} C(\xi, t') = -\frac{1}{\sqrt{A}} \frac{\partial^{\frac{1}{2}}}{\partial t'^{\frac{1}{2}}} \left[C(\xi, t') - C_0\right] - \frac{C(\xi, t') - C_0}{\xi + R}, \quad \text{(E6)}$$

where the half-order derivative of a function $f(t)$ is defined as,

$$\frac{d^{\frac{1}{2}} f(t)}{dt^{\frac{1}{2}}} \equiv \frac{1}{\sqrt{\pi}} \frac{d}{dt} \int_0^t \frac{f(\tau) d\tau}{\sqrt{t-\tau}} . \quad \text{(E7)}$$

For the case of the flat land surface, i.e. $\xi = 0$ and $R \to +\infty$, Eq. (H7) reduces to

$$\frac{\partial}{\partial \xi} C(\xi, t') = -\frac{1}{\sqrt{A}} \frac{\partial^{\frac{1}{2}}}{\partial t'^{\frac{1}{2}}} \left[C(\xi, t') - C_0 \right], \tag{E8}$$

leading to Eq. 4.17,

$$F_c(z,t) \equiv -D_c(z,t) \frac{\partial C}{\partial z} = \frac{D_c(z,t)}{\sqrt{\pi}} \int_0^t \frac{\partial C(z,\tau)}{\partial \tau} \left[\int_\tau^t D_c(z,\zeta) d\zeta \right]^{-\frac{1}{2}} d\tau \,,$$

where Eq. 4.16 is used.

For the case of constant D_c, Eq. 4.17 becomes,

$$F_c(z,t) = \sqrt{\frac{D_c}{\pi}} \int_0^t \frac{\partial C(z,\tau)}{\partial \tau} \frac{d\tau}{\sqrt{t-\tau}} \,. \tag{E9}$$

APPENDIX F. NUMERICAL ALGORITHM FOR COMPUTING F_C USING HOD

Given the time-series data of C measured at discrete times $0 = t_0 < t_1 < t_2 < \ldots < t_N$, F_c at t may be calculated using the following numerical algorithm. To remove the singularity of the integrand, the double integral in Eq. 4.17 is re-written as,

$$\int_0^t \frac{\partial C(z,\tau)}{\partial \tau}\left[\int_\tau^t D_c(z,\zeta)d\zeta\right]^{-\frac{1}{2}} d\tau = -2\int_0^t \frac{\partial C(z,\tau)}{\partial \tau}\frac{1}{D_c(z,\tau)} d\left[\int_\tau^t D_c(z,\zeta)d\zeta\right]^{\frac{1}{2}} \tag{F1}$$

The integral on the right-hand-side of (H1) is the Rienmann-Stieltjes integral $\int_0^t f(\tau)dg(\tau)$

where

$$\begin{aligned} f(\tau) &= \frac{\partial C(z,\tau)}{\partial \tau}\frac{1}{D_c(z,\tau)}, \\ g(\tau) &= \left[\int_\tau^t D_c(z,\zeta)d\zeta\right]^{\frac{1}{2}}. \end{aligned} \tag{F2}$$

The Rienmann-Stieltjes integral may be numerically computed as,

$$\int_0^t f(\tau)dg(\tau) = \sum_{i=1}^{N} f(t_i)[g(t_i) - g(t_{i-1})], \tag{F3}$$

where

$$f(t_i) = \frac{C(z,t_i) - C(z,t_{i-1})}{t_i - t_{i-1}} \frac{1}{D_c(z,t_i)},$$
$$g(t_i) = \left[\sum_{j=i+1}^{N} D_c(z,t_j)(t_j - t_{j-1}) \right]^{\frac{1}{2}}. \quad \text{(F4)}$$

Computation of $D_c(z,t_i)$ ($i=1,\ldots,N$) according to Eq. 4.16 requires the surface sensible heat flux $H(t_i)$, which is parameterized using the MEP model.

APPENDIX G. ESTIMATION OF WATER VAPOR CONCENTRATION

The saturated water vapor pressure can be estimated using Clausius-Clapeyron equation

$$e_s(T_a) = e_0(T_0)\exp\left[\frac{L_v}{R_v}\left(\frac{1}{T_0} - \frac{1}{T_a}\right)\right] \quad \text{(G1)}$$

According the Ideal Gas Law,

$$e_s = R_v \rho_v T_a \quad \text{(G2)}$$

where ρ_v is the saturated water vapor density, which is also the saturated water vapor concentration. Assuming the evaporating surface is saturated, the water vapor concentration (C_v) can be computed using Eq. (G3)

$$C_v = \frac{e_s(T_a)}{R_v T_a} \quad \text{(G3)}$$

The unit of water vapor concentration is converted from kg m^{-3} to mmol mol^{-1}.

APPENDIX H. DERIVATION OF EQ. 4.18

According to Table 1 in [*Wang and Bras*, 2010], friction velocity is expressed in terms of sensible heat flux as,

$$u_* = D_0|zH|^{\frac{1}{3}}, D_0 = \begin{cases} \sqrt[3]{\dfrac{2\beta\kappa g}{\rho c_p T_0}} = 0.037, & H < 0 \\ \sqrt[3]{\dfrac{\gamma_2\kappa g}{2\rho c_p T_0}} = 0.047, & H > 0 \end{cases} \quad \text{(H1)}$$

where ρ ($\approx$ 1.2 kg m^{-3}) is the representative density of air, T_0 ($\approx$ 300 K) the representative environment temperature, c_p (10^3 J kg^{-1} K^{-1}) the specific heat of air at constant pressure, g (9.8 m s^{-2}) the gravitational acceleration, κ ($\approx$ 0.4) the von Karman constant, and α ($\sim$ 0.75 or 1), β ($\sim$ 4.7), and γ_2 ($\sim$ 9) the universal empirical coefficients [*Businger et al.*, 1971].

APPENDIX I. MEASUREMENT ERRORS OF $H^{1/3}$ AND U_*

Table I1 Measurement errors of $H^{1/3}$ and u_*

Site	$\sigma_{H^{\frac{1}{3}}}(W^{\frac{1}{3}}m^{-\frac{2}{3}})$	σ_{u_*}(m s^{-1})
BR-Sa3	0.24	0.09
US-UMB	0.26	0.12
US-Br3	0.21	0.06
US-Dk1	0.22	0.05

APPENDIX J. UNCERTAINTY TESTS OF MODELS

J.1 Uncertainties of MEP surface heat fluxes

The MEP model predicted surface heat fluxes are mathematically expressed as functions of Rn and the dimensionless variable σ. In this study, the MEP model of dense canopy is used. The uncertainty of H estimated using the MEP model may be expressed as

$$\Delta H = \frac{\partial H}{\partial R_n}\Delta R_n + \frac{\partial H}{\partial \sigma}\Delta\sigma \quad \text{(J1)}$$

where

$$\frac{\partial H}{\partial R_n} = \left[1 + B + \frac{5B}{6\sigma}|H|^{-\frac{1}{6}}\right]^{-1}$$

$$\frac{\partial H}{\partial \sigma} = H\left[-\frac{11}{2(B-6)}\right][1+B]^{-1}$$

$$\Delta\sigma = \sigma\left(\frac{\Delta q_s}{q_s} - 2\frac{\Delta T_s}{Ts}\right)$$

As the measurement uncertainties of Rn and Ta are 60 W m^{-2} and 0.4 °C when Rn and Ta are 600 W m^{-2} and 27 °C, respectively. The calculated uncertainties of H and E are 28 W m^{-2} (8.5 %) and 32 W m^{-2} (11.9 %) with H (330 W m^{-2}) and E (270 W m^{-2}), respectively.

J.2 Uncertainty of friction velocity

Friction velocity is estimated using H in the extreme solution model. The uncertainty of friction velocity may be expressed as

$$\Delta u_* = \frac{\partial u_*}{\partial H}\Delta H = \frac{D_0}{3}|H|^{-\frac{2}{3}}\Delta H \quad \text{(J2)}$$

The uncertainty of friction velocity with the condition in J.1 is 0.0072 m s^{-1} (1%) with friction velocity (0.6942 m s^{-1})

J.3 Uncertainty of CO_2 flux

The CO_2 flux is estimated using the HOD model. The uncertainty of CO_2 flux may be expressed as

$$\Delta F_c = \frac{\partial F_c}{\partial D}\Delta D + \frac{\partial F_c}{\partial C}\Delta C \quad \text{(J3)}$$

where

$$\frac{\partial F_c}{\partial D} = \frac{1}{2\sqrt{D\pi}}\int_{-\infty}^{t}\frac{\partial C(z,\tau)}{\partial \tau}d(-2\sqrt{t-\tau}) = \frac{F_c}{2D}$$

If the uncertainty of CO_2 concentration is 4 ppm for all measurements, the uncertainty of CO_2 flux is zero. Therefore, the uncertainty of CO_2 flux is 0.1 umol m^{-2} s^{-1} (0.5 %) with CO_2 flux 20 umol m^{-2} s^{-1}, given the measurement uncertainties of Rn and Ta are 60 W m^{-2} and 0.4 ℃.

REFERENCES

Allen, M. R., and W. J. Ingram (2002), Constraints on future changes in climate and the hydrologic cycle, *Nature*, *419*(6903), 224-232.

Allison, V. J., R. M. Miller, J. D. Jastrow, R. Matamala, and D. R. Zak (2005), Changes in soil microbial community structure in a tallgrass prairie chronosequence, *Soil. Sci. Soc. Am. J.*, *69*(5), 1412-1421, doi:10.2136/sssaj2004.0252.

Anthoni, P. M., B. E. Law, and M. H. Unsworth (1999), Carbon and water vapor exchange of an open-canopied ponderosa pine ecosystem, *Agric. For. Meteorol.*, *95*(3), 151-168, doi:Doi 10.1016/S0168-1923(99)00029-5.

Arya, S. P. (2001), *Introduction to Micrometeorology*, Academic Press.

Aubinet, M. (2008), Eddy covariance CO2 flux measurements in nocturnal conditions: an analysis of the problem, *Ecol Appl*, *18*(6), 1368-1378, doi:10.1890/06-1336.1.

Aubinet, M., et al. (1999), Estimates of the Annual Net Carbon and Water Exchange of Forests: The EUROFLUX Methodology, in *Advances in Ecological Research*, edited by A. H. Fitter and D. G. Raffaelli, pp. 113-175, Academic Press, doi:https://doi.org/10.1016/S0065-2504(08)60018-5.

Aubinet, M., T. Vesala, and D. Papale (2012), *Eddy Covariance: A Practical Guide to Measurement and Data Analysis*, Springer Netherlands.

Baker, W. E., et al. (2014), Lidar-Measured Wind Profiles: The Missing Link in the Global Observing System, *Bulletin of the American Meteorological Society*, *95*(4), 543-564, doi:10.1175/bams-d-12-00164.1.

Baldocchi, D. (2014), Measuring fluxes of trace gases and energy between ecosystems and the atmosphere – the state and future of the eddy covariance method, *Global Change Biol.*, *20*(12), 3600-3609, doi:10.1111/gcb.12649.

Baldocchi, D. D. (2003), Assessing the eddy covariance technique for evaluating carbon dioxide exchange rates of ecosystems: past, present and future, *Global Change Biol.*, *9*(4), 479-492, doi:DOI 10.1046/j.1365-2486.2003.00629.x.

Baldocchi, D. D., C. A. Vogel, and B. Hall (1997), Seasonal variation of energy and water vapor exchange rates above and below a boreal jack pine forest canopy, *J. Geophys. Res. D: Atmos.*, *102*(D24), 28939-28951, doi:doi:10.1029/96JD03325.

Banwart, S. (2011), Save our soils, *Nature*, *474*(7350), 151-152.

Banwart, S., J. Chorover, J. Gaillardet, D. Sparks, T. White, S. Anderson, A. Aufdenkampe, S. Bernasconi, S. Brantley, and O. Chadwick (2013), Sustaining Earth's critical zone basic

science and interdisciplinary solutions for global challenges, *University of Sheffield, Sheffield*, 47.

Barkstrom, B. R., and G. L. Smith (1986), The Earth Radiation Budget Experiment: Science and implementation, *Rev. Geophys.*, *24*(2), 379-390, doi:10.1029/RG024i002p00379.

Barr, A. G., K. M. King, T. J. Gillespie, G. Den Hartog, and H. H. Neumann (1994), A comparison of bowen ratio and eddy correlation sensible and latent heat flux measurements above deciduous forest, *Boundary-Layer Meteorology*, *71*(1), 21-41, doi:10.1007/bf00709218.

Barr, A. G., K. Morgenstern, T. A. Black, J. H. McCaughey, and Z. Nesic (2006), Surface energy balance closure by the eddy-covariance method above three boreal forest stands and implications for the measurement of the CO2 flux, *Agric. For. Meteorol.*, *140*(1-4), 322-337, doi:10.1016/j.agrformet.2006.08.007.

Beven, K. (1979), A sensitivity analysis of the Penman-Monteith actual evapotranspiration estimates, *J. Hydrol.*, *44*(3-4), 169-190, doi:10.1016/0022-1694(79)90130-6.

Billings, S. A., R. W. Buddemeier, D. deB. Richter, K. Van Oost, and G. Bohling (2010), A simple method for estimating the influence of eroding soil profiles on atmospheric CO2, *Global Biogeochemical Cycles*, *24*(2), n/a-n/a, doi:10.1029/2009GB003560.

Binkley, D., D. Valentine, C. Wells, and U. Valentine (1989), An empirical analysis of the factors contributing to 20-year decrease in soil pH in an old-field plantation of loblolly pine, *Biogeochemistry*, *8*(1), 39-54, doi:10.1007/bf02180166.

Blanken, P. D., T. A. Black, H. H. Neumann, G. D. Hartog, P. C. Yang, Z. Nesic, R. Staebler, W. Chen, and M. D. Novak (1998), Turbulent Flux Measurements Above and Below the Overstory of a Boreal Aspen Forest, *Boundary-Layer Meteorology*, *89*(1), 109-140, doi:10.1023/a:1001557022310.

Brienen, R. J., et al. (2015), Long-term decline of the Amazon carbon sink, *Nature*, *519*(7543), 344-348, doi:10.1038/nature14283.

Buford, M. A. (1991), Performance of four yield models for predicting stand dynamics of a 30-year-old loblolly pine (Pinus taeda L.) spacing study, *Forest Ecology and Management*, *46*(1), 23-38, doi:http://dx.doi.org/10.1016/0378-1127(91)90242-N.

Businger, J. A., J. C. Wyngaard, Y. Izumi, and E. F. Bradley (1971), Flux-Profile Relationships in the Atmospheric Surface Layer, *J. Atmos. Sci.*, *28*(2), 181-189, doi:10.1175/1520-0469(1971)028<0181:fprita>2.0.co;2.

Buyantuyev, A., P. Xu, J. Wu, S. Piao, and D. Wang (2012), A Space-For-Time (SFT) Substitution Approach to Studying Historical Phenological Changes in Urban Environment, *PLOS ONE*, *7*(12), e51260, doi:10.1371/journal.pone.0051260.

C., S. P., K. G. G., S. M. B. S., J. JEHN-YIH, N. K. A., M. H. R., C. O. A., U. J. M., K. HYUN-SEOK, and O. RAM (2006), Separating the effects of climate and vegetation on evapotranspiration along a successional chronosequence in the southeastern US, *Global Change Biol.*, *12*(11), 2115-2135, doi:doi:10.1111/j.1365-2486.2006.01244.x.

Chahine, M. T. (1992a), GEWEX: The Global Energy and Water Cycle Experiment, *Eos, Transactions American Geophysical Union*, *73*(2), 9-14, doi:10.1029/91EO00007.

Chahine, M. T. (1992b), The hydrological cycle and its influence on climate, *Nature*, *359*(6394), 373-380.

Chase, T. N., R. A. Pielke Sr., T. G. F. Kittel, R. R. Nemani, and S. W. Running (2000), Simulated impacts of historical land cover changes on global climate in northern winter, *Clim. Dyn.*, *16*(2), 93-105, doi:10.1007/s003820050007.

Cheng, Y., M. B. Parlange, and W. Brutsaert (2005), Pathology of Monin‐Obukhov similarity in the stable boundary layer, *J. Geophys. Res. D: Atmos.*, *110*(D6), doi:doi:10.1029/2004JD004923.

Chorover, J., et al. (2011), How Water, Carbon, and Energy Drive Critical Zone Evolution: The Jemez–Santa Catalina Critical Zone Observatory, *Vadose Zone Journal*, *10*(3), 884-899, doi:10.2136/vzj2010.0132.

Coddington, O., J. L. Lean, P. Pilewskie, M. Snow, and D. Lindholm (2016), A Solar Irradiance Climate Data Record, *Bulletin of the American Meteorological Society*, *97*(7), 1265-1282, doi:10.1175/bams-d-14-00265.1.

Cook, B. D., et al. (2004), Carbon exchange and venting anomalies in an upland deciduous forest in northern Wisconsin, USA, *Agric. For. Meteorol.*, *126*(3), 271-295, doi:https://doi.org/10.1016/j.agrformet.2004.06.008.

Coughlan, M., and R. Avissar (1996), The Global Energy and Water Cycle Experiment (GEWEX) Continental-Scale International Project (GCIP): An overview, *J. Geophys. Res. D: Atmos.*, *101*(D3), 7139-7147, doi:10.1029/96JD00125.

Coughlan, M., D. Nelson, M. Lonneman, and A. Block (2017), Historical Land Use Dynamics in the Highly Degraded Landscape of the Calhoun Critical Zone Observatory, *Land*, *6*(2), 32.

Cowles, H. C. (1899), The Ecological Relations of the Vegetation on the Sand Dunes of Lake Michigan. Part I.-Geographical Relations of the Dune Floras, *Botanical Gazette*, *27*(2), 95-117.

Cox, C., and W. Munk (1954), Measurement of the Roughness of the Sea Surface from Photographs of the Sun's Glitter, *J. Opt. Soc. Am.*, *44*(11), 838, doi:10.1364/josa.44.000838.

da Rocha, H. R., M. L. Goulden, S. D. Miller, M. C. Menton, L. D. V. O. Pinto, H. C. de Freitas, and A. M. e Silva Figueira (2004), Seasonality of Water and Heat Fluxes over a Tropical Forest in Eastern Amazonia, *Ecol. Appl.*, *14*(sp4), 22-32, doi:10.1890/02-6001.

Davies, M. E., and S. Singh (1985), Thorney Island: Its geography and meteorology, *Journal of Hazardous Materials*, *11*, 91-124, doi:https://doi.org/10.1016/0304-3894(85)85034-2.

DeBell, D. S., W. R. Harms, and C. D. Whitesell (1989), Stockability: A major factor in productivity differences between Pinus taeda plantations in Hawaii and the Southeastern United States., *Forest Science*.

DETWILER, R. P., and C. A. S. HALL (1988), Tropical Forests and the Global Carbon Cycle, *Science*, *239*(4835), 42-47, doi:10.1126/science.239.4835.42.

Dialynas, Y. G., S. Bastola, R. L. Bras, S. A. Billings, D. Markewitz, and D. d. Richter (2016a), Topographic variability and the influence of soil erosion on the carbon cycle, *Global Biogeochemical Cycles*, *30*(5), 644-660, doi:10.1002/2015GB005302.

Dialynas, Y. G., S. Bastola, R. L. Bras, E. Marin-Spiotta, W. L. Silver, E. Arnone, and L. V. Noto (2016b), Impact of hydrologically driven hillslope erosion and landslide occurrence on soil organic carbon dynamics in tropical watersheds, *Water Resour. Res.*, *52*(11), 8895-8919, doi:10.1002/2016WR018925.

Dialynas, Y. G., R. L. Bras, and D. deB. Richter (2017), Hydro-geomorphic perturbations on the soil-atmosphere CO2 exchange: How (un)certain are our balances?, *Water Resour. Res.*, *53*(2), 1664-1682, doi:10.1002/2016WR019411.

Dines, W. H. (1917), The heat balance of the atmosphere, *Quarterly Journal of the Royal Meteorological Society*, *43*(182), 151-158, doi:10.1002/qj.49704318203.

Douglass, J. E. (1972), Annotated bibliography of publications on watershed management by the Southeastern Forest Experiment Station, 1928-1970, *Res. Pap. SE-93. Asheville, NC: US Department of Agriculture, Forest Service, Southeastern Forest Experiment Station. 17 p., 93*.

Dyer, A. J., and B. B. Hicks (1970), Flux-gradient relationships in the constant flux layer, *Quarterly Journal of the Royal Meteorological Society*, *96*(410), 715-721, doi:10.1002/qj.49709641012.

E.A., T., B. J., and A. J.L. (2007), Water use efficiency in C3 cereals under Mediterranean conditions: a review of physiological aspects, *Annals of Applied Biology*, *150*(3), 307-321, doi:doi:10.1111/j.1744-7348.2007.00143.x.

Energy, N. R. C. G., and W. C. E. Panel (1998), *GCIP, global energy and water cycle experiment (GEWEX), continental-scale international project: a review of progress and opportunities*, National Academies Press.

Falge, E., et al. (2001), Gap filling strategies for defensible annual sums of net ecosystem exchange, *Agric. For. Meteorol.*, *107*(1), 43-69, doi:Doi 10.1016/S0168-1923(00)00225-2.

Field, J. P., D. D. Breshears, D. J. Law, J. C. Villegas, L. López-Hoffman, P. D. Brooks, J. Chorover, G. A. Barron-Gafford, R. E. Gallery, and M. E. Litvak (2015), Critical Zone services: Expanding context, constraints, and currency beyond ecosystem services, *Vadose Zone Journal*, *14*(1).

Foken, T., M. Göockede, M. Mauder, L. Mahrt, B. Amiro, and W. Munger (2005), Post-Field Data Quality Control, in *Handbook of Micrometeorology: A Guide for Surface Flux Measurement and Analysis*, edited by X. Lee, W. Massman and B. Law, pp. 181-208, Springer Netherlands, Dordrecht, doi:10.1007/1-4020-2265-4_9.

Foken, T., and B. Wichura (1996), Tools for quality assessment of surface-based flux measurements, *Agric. For. Meteorol.*, *78*(1), 83-105, doi:https://doi.org/10.1016/0168-1923(95)02248-1.

Franks, P. J., D. L. Royer, D. J. Beerling, P. K. Van de Water, D. J. Cantrill, M. M. Barbour, and J. A. Berry (2014), New constraints on atmospheric CO2 concentration for the Phanerozoic, *Geophys. Res. Lett.*, *41*(13), 4685-4694, doi:10.1002/2014gl060457.

Galik, C. S., M. L. Mobley, and D. deB. Richter (2009), A virtual "field test" of forest management carbon offset protocols: the influence of accounting, *Mitigation and Adaptation Strategies for Global Change*, *14*(7), 677-690, doi:10.1007/s11027-009-9190-9.

Garrison, J. L., S. J. Katzberg, and M. I. Hill (1998), Effect of sea roughness on bistatically scattered range coded signals from the Global Positioning System, *Geophys. Res. Lett.*, *25*(13), 2257-2260, doi:Doi 10.1029/98gl51615.

Garrison, J. L., A. Komjathy, V. U. Zavorotny, and S. J. Katzberg (2002), Wind speed measurement using forward scattered GPS signals, *IEEE Trans. Geosci. Remote Sens.*, *40*(1), 50-65, doi:Doi 10.1109/36.981349.

Gatti, L. V., et al. (2014), Drought sensitivity of Amazonian carbon balance revealed by atmospheric measurements, *Nature*, *506*(7486), 76-80, doi:10.1038/nature12957.

Goulden, M. L., R. G. Anderson, R. C. Bales, A. E. Kelly, M. Meadows, and G. C. Winston (2012), Evapotranspiration along an elevation gradient in California's Sierra Nevada, *Journal of Geophysical Research: Biogeosciences*, *117*(G3), n/a-n/a, doi:10.1029/2012JG002027.

Goulden, M. L., and R. C. Bales (2014), Mountain runoff vulnerability to increased evapotranspiration with vegetation expansion, *Proceedings of the National Academy of Sciences*, *111*(39), 14071-14075, doi:10.1073/pnas.1319316111.

Goulden, M. L., J. W. Munger, S. M. Fan, B. C. Daube, and S. C. Wofsy (1996), Measurements of carbon sequestration by long-term eddy covariance: Methods and a critical evaluation of accuracy, *Global Change Biol.*, *2*(3), 169-182, doi:DOI 10.1111/j.1365-2486.1996.tb00070.x.

Grell, G. A., J. Dudhia, and D. R. Stauffer (1994), A description of the fifth-generation Penn State/NCAR Mesoscale Model (MM5), *NCAR Tech. Note NCAR TN-398-1-STR*.

Gu, J., E. A. Smith, and E. A. Merritt (1999), Testing energy balance closure with GOES ‐ retrieved net radiation and in situ measured eddy correlation fluxes in BOREAS, *J. Geophys. Res. D: Atmos.*, *104*(D22), 27881-27893, doi:doi:10.1029/1999JD900390.

Gu, L. H., et al. (2005), Objective threshold determination for nighttime eddy flux filtering, *Agric. For. Meteorol.*, *128*(3-4), 179-197, doi:10.1016/j.agrformet.2004.11.006.

Hajji, I., D. F. Nadeau, B. Music, F. Anctil, and J. Wang (2018), Application of the maximum entropy production model of evapotranspiration over partial vegetated water-limited land surfaces, *J. Hydrometeorol., In Revision*.

Hari Prasad, K. B. R. R., C. Venkata Srinivas, C. Venkateswara Naidu, R. Baskaran, and B. Venkatraman (2016), Assessment of surface layer parameterizations in ARW using micro-meteorological observations from a tropical station, *Meteorological Applications*, *23*(2), 191-208, doi:10.1002/met.1545.

Hatala, J. A., M. Detto, O. Sonnentag, S. J. Deverel, J. Verfaillie, and D. D. Baldocchi (2012), Greenhouse gas (CO2, CH4, H2O) fluxes from drained and flooded agricultural peatlands in the Sacramento-San Joaquin Delta, *Agriculture Ecosystems & Environment*, *150*(Supplement C), 1-18, doi:10.1016/j.agee.2012.01.009.

Hegerl, G. C., et al. (2015), Challenges in Quantifying Changes in the Global Water Cycle, *Bulletin of the American Meteorological Society*, *96*(7), 1097-1115, doi:10.1175/bams-d-13-00212.1.

Hollinger, D. Y., and A. D. Richardson (2005), Uncertainty in eddy covariance measurements and its application to physiological models, *Tree Physiol.*, *25*(7), 873-885, doi:10.1093/treephys/25.7.873.

Hong, S.-Y., and H.-L. Pan (1996), Nonlocal Boundary Layer Vertical Diffusion in a Medium-Range Forecast Model, *Monthly Weather Review*, *124*(10), 2322-2339, doi:10.1175/1520-0493(1996)124<2322:nblvdi>2.0.co;2.

Hong, S., and I. Shin (2013), Wind Speed Retrieval Based on Sea Surface Roughness Measurements from Spaceborne Microwave Radiometers, *Journal of Applied Meteorology and Climatology*, *52*(2), 507-516, doi:10.1175/jamc-d-11-0209.1.

Hoover, M. D. (1950), Hydrologic Characteristics of South Carolina Piedmont Forest Soils.

Houghton, R. A. (1995), Land-use change and the carbon cycle, *Global Change Biol.*, *1*(4), 275-287, doi:10.1111/j.1365-2486.1995.tb00026.x.

Houghton, R. A., R. D. Boone, J. M. Melillo, C. A. Palm, G. M. Woodwell, N. Myers, B. Moore, and D. L. Skole (1985), Net flux of carbon dioxide from tropical forests in 1980, *Nature*, *316*(6029), 617-620.

Huang, S.-Y., Y. Deng, and J. Wang (2016), Revisiting the global surface energy budgets with maximum-entropy-production model of surface heat fluxes, *Clim. Dyn.*, *49*(5-6), 1531-1545, doi:10.1007/s00382-016-3395-x.

IPCC (2013), Summary for Policymakers. In: Climate Change 2013: The Physical Science Basis. Contribution of Working Group I to the Fifth Assessment Report of the Intergovernmental Panel on Climate Change, *Cambridge University Press, Cambridge, United Kingdom and New York, NY, USA*.

Jimenez, P., J. Dudhia, J. F. González Rouco, J. Navarro, J. Montávez, and E. Garcia Bustamante (2012), A Revised Scheme for the WRF Surface Layer Formulation, *Monthly Weather Review*, *140*, 898–918, doi:10.1175/MWR-D-11-00056.1.

Jones, H. (2004), What is water use efficiency, *Water use efficiency in plant biology*, 27-41.

Katul, G., R. Leuning, and R. Oren (2003), Relationship between plant hydraulic and biochemical properties derived from a steady‐state coupled water and carbon transport model, *Plant, Cell & Environment*, *26*(3), 339-350, doi:doi:10.1046/j.1365-3040.2003.00965.x.

Kiehl, J. T., and K. E. Trenberth (1997), Earth's Annual Global Mean Energy Budget, *Bulletin of the American Meteorological Society*, *78*(2), 197-208, doi:10.1175/1520-0477(1997)078<0197:eagmeb>2.0.co;2.

Kim, D., R. L. Ray, and M. Choi (2017), Simulations of energy balance components at snow-dominated montane watershed by land surface models, *Environmental Earth Sciences*, *76*(9), 337, doi:10.1007/s12665-017-6655-0.

Kondepudi, D. K. (2008), *Introduction to modern thermodynamics*, Wiley.

Kondo, J., and T. Watanabe (1992), Studies on the Bulk Transfer-Coefficients over a Vegetated Surface with a Multilayer Energy Budget Model, *J. Atmos. Sci.*, *49*(23), 2183-2199, doi:Doi 10.1175/1520-0469(1992)049<2183:Sotbtc>2.0.Co;2.

Kongoli, C., W. P. Kustas, M. C. Anderson, J. M. Norman, J. G. Alfieri, G. N. Flerchinger, and D. Marks (2014), Evaluation of a Two-Source Snow–Vegetation Energy Balance Model for Estimating Surface Energy Fluxes in a Rangeland Ecosystem, *J. Hydrometeorol.*, *15*(1), 143-158, doi:10.1175/jhm-d-12-0153.1.

Kroon, P. S., A. Hensen, H. J. J. Jonker, H. G. Ouwersloot, A. T. Vermeulen, and F. C. Bosveld (2010), Uncertainties in eddy covariance flux measurements assessed from CH4 and N2O observations, *Agric. For. Meteorol.*, *150*(6), 806-816, doi:10.1016/j.agrformet.2009.08.008.

Kwon, H., B. E. Law, C. K. Thomas, and B. G. Johnson (2018), The influence of hydrological variability on inherent water use efficiency in forests of contrasting composition, age, and precipitation regimes in the Pacific Northwest, *Agric. For. Meteorol.*, *249*, 488-500, doi:10.1016/j.agrformet.2017.08.006.

Lai, C.-T., and G. Katul (2000), The dynamic role of root-water uptake in coupling potential to actual transpiration, *Advances in Water Resources*, *23*(4), 427-439, doi:https://doi.org/10.1016/S0309-1708(99)00023-8.

Lawler, J. J., D. J. Lewis, E. Nelson, A. J. Plantinga, S. Polasky, J. C. Withey, D. P. Helmers, S. Martinuzzi, D. Pennington, and V. C. Radeloff (2014), Projected land-use change impacts on ecosystem services in the United States, *Proceedings of the National Academy of Sciences*, *111*(20), 7492-7497, doi:10.1073/pnas.1405557111.

Lee, X. (1998), On micrometeorological observations of surface-air exchange over tall vegetation, *Agric. For. Meteorol.*, *91*(1), 39-49, doi:https://doi.org/10.1016/S0168-1923(98)00071-9.

Leonardi, S., F. Magnani, A. Nolè, T. Van Noije, and M. Borghetti (2015), A global assessment of forest surface albedo and its relationships with climate and atmospheric nitrogen deposition, *Global Change Biol.*, *21*(1), 287-298, doi:doi:10.1111/gcb.12681.

Lester, R. E., P. G. Close, J. L. Barton, A. J. Pope, and S. C. Brown (2014), Predicting the likely response of data-poor ecosystems to climate change using space-for-time substitution across domains, *Global Change Biol.*, *20*(11), 3471-3481, doi:10.1111/gcb.12634.

Lin, H. (2010), Earth's Critical Zone and hydropedology: concepts, characteristics, and advances, *Hydrol. Earth Syst. Sci.*, *14*(1), 25-45, doi:10.5194/hess-14-25-2010.

Lin, H., J. Hopmans, and D. d. Richter (2011), Interdisciplinary Sciences in a Global Network of Critical Zone Observatories *Vadose Zone Journal*, *10*(3), 781-785, doi:10.2136/vzj2011.0084.

Liu, G., and F. W. Schwartz (2012), Climate-driven variability in lake and wetland distribution across the Prairie Pothole Region: From modern observations to long-term reconstructions with space-for-time substitution, *Water Resour. Res.*, *48*(8), n/a-n/a, doi:10.1029/2011WR011539.

Loveland, T. R., and W. Acevedo (2006), Land Cover Change in the Eastern United States.

Lubowski, R. N., A. J. Plantinga, and R. N. Stavins (2008), What Drives Land-Use Change in the United States? A National Analysis of Landowner Decisions, *Land Economics, University of Wisconsin Press, vol. 84(4).*

Lubowski, R. N., M. Vesterby, S. Bucholtz, A. Baez, and M. J. Roberts (2006), Major Uses of Land in the United States, 2002, *Economic Information Bulletin No. 14*.

Markewitz, D., and D. D. Richter (1998), The Bio in Aluminum and Silicon Geochemistry, *Biogeochemistry*, *42*(1), 235-252, doi:10.1023/a:1005901417165.

Mellor, G. L., and T. Yamada (1982), Development of a turbulence closure model for geophysical fluid problems, *Rev. Geophys.*, *20*(4), 851-875, doi:10.1029/RG020i004p00851.

Metz, L. J. (1958), The Calhoun Experimental Forest, *US Forest Service Southeastern Forest Experiment Station*.

Miller, K. S., and B. Ross (1993), An introduction to the fractional calculus and fractional differential equations, *Wiley, New York*.

Mishra, V., K. A. Cherkauer, D. Niyogi, M. Lei, B. C. Pijanowski, D. K. Ray, L. C. Bowling, and G. Yang (2010), A regional scale assessment of land use/land cover and climatic changes on water and energy cycle in the upper Midwest United States, *International Journal of Climatology*, *30*(13), 2025-2044, doi:10.1002/joc.2095.

Mobley, M. L., D. d. Richter, and P. R. Heine (2012), Accumulation and decay of woody detritus in a humid subtropical secondary pine forest, *Canadian Journal of Forest Research*, *43*(2), 109-118, doi:10.1139/cjfr-2012-0222.

Molnár, Z., and Z. Botta-Dukát (1998), Improved space-for-time substitution for hypothesis generation: secondary grasslands with documented site history in SE-Hungary, *Phytocoenologia*, *28*(1), 1-29.

Monin, A., and A. Obukhov (1954), Basic laws of turbulent mixing in the surface layer of the atmosphere, *Contrib. Geophys. Inst. Acad. Sci. USSR*, *151*, 163-187.

Monteith, J., and M. Unsworth (2013), *Principles of Environmental Physics: Plants, Animals, and the Atmosphere*, Elsevier Science.

Moon, S., J. T. Perron, S. J. Martel, W. S. Holbrook, and J. St. Clair (2017), A model of three-dimensional topographic stresses with implications for bedrock fractures, surface processes, and landscape evolution, *Journal of Geophysical Research: Earth Surface*, *122*(4), 823-846, doi:10.1002/2016JF004155.

Morin, T. H., G. Bohrer, K. C. Stefanik, A. C. Rey-Sanchez, A. M. Matheny, and W. J. Mitsch (2017), Combining eddy-covariance and chamber measurements to determine the methane budget from a small, heterogeneous urban floodplain wetland park, *Agric. For. Meteorol.*, *237*, 160-170, doi:10.1016/j.agrformet.2017.01.022.

Nabuurs, G. J., R. Päivinen, R. Sikkema, and G. M. J. Mohren (1997), The role of European forests in the global carbon cycle—A review, *Biomass and Bioenergy*, *13*(6), 345-358, doi:http://dx.doi.org/10.1016/S0961-9534(97)00036-6.

Nave, L. E., et al. (2011), Disturbance and the resilience of coupled carbon and nitrogen cycling in a north temperate forest, *Journal of Geophysical Research: Biogeosciences*, *116*(G4), doi:doi:10.1029/2011JG001758.

Nearing, G. S., M. S. Moran, R. L. Scott, and G. Ponce-Campos (2012), Coupling diffusion and maximum entropy models to estimate thermal inertia, *Remote Sens. Environ.*, *119*, 222-231, doi:10.1016/j.rse.2011.12.012.

Nelson, K., S. A. Kurc, G. John, R. Minor, and G. A. Barron-Gafford (2014), Influence of snow cover duration on soil evaporation and respiration efflux in mixed-conifer ecosystems, *Ecohydrology*, *7*(2), 869-880, doi:10.1002/eco.1425.

Nieuwstadt, F. T. M. (1980), An Analytic Solution of the Time-Dependent, One-Dimensional Diffusion Equation in the Atmospheric Boundary-Layer, *Atmos. Environ.*, *14*(12), 1361-1364, doi:Doi 10.1016/0004-6981(80)90154-7.

Niu, G.-Y., C. Paniconi, P. A. Troch, R. L. Scott, M. Durcik, X. Zeng, T. Huxman, and D. C. Goodrich (2014a), An integrated modelling framework of catchment-scale ecohydrological processes: 1. Model description and tests over an energy-limited watershed, *Ecohydrology*, *7*(2), 427-439, doi:10.1002/eco.1362.

Niu, G.-Y., P. A. Troch, C. Paniconi, R. L. Scott, M. Durcik, X. Zeng, T. Huxman, D. Goodrich, and J. Pelletier (2014b), An integrated modelling framework of catchment-scale ecohydrological processes: 2. The role of water subsidy by overland flow on vegetation dynamics in a semi-arid catchment, *Ecohydrology*, *7*(2), 815-827, doi:10.1002/eco.1405.

Novick, K. A., R. Oren, P. C. Stoy, M. B. S. Siqueira, and G. G. Katul (2009), Nocturnal evapotranspiration in eddy-covariance records from three co-located ecosystems in the Southeastern U.S.: Implications for annual fluxes, *Agric. For. Meteorol.*, *149*(9), 1491-1504, doi:https://doi.org/10.1016/j.agrformet.2009.04.005.

NRC (2001), *Basic Research Opportunities in Earth Science*, 168 pp., The National Academies Press, Washington, DC, doi:doi:10.17226/9981.

NRC (2012), *New Research Opportunities in the Earth Sciences*, 132 pp., The National Academies Press, Washington, DC, doi:doi:10.17226/13236.

Ochsner, T. E., T. J. Sauer, and R. Horton (2007), Soil heat storage measurements in energy balance studies, *Agronomy Journal*, *99*(1), 311-319.

Oldham, K. B., and J. Spanier (2006), *The Fractional Calculus: Theory and Applications of Differentiation and Integration to Arbitrary Order*, Dover Publications.

Olson, D. F. (1954), *Methods of Soil Moisture Determination Under Field Conditions*, U.S. Department of Agriculture, Forest Service, Southeastern Forest Experiment Station.

Oren, R., C. I. Hsieh, P. Stoy, J. Albertson, H. R. Mccarthy, P. Harrell, and G. G. Katul (2006), Estimating the uncertainty in annual net ecosystem carbon exchange: spatial variation in turbulent fluxes and sampling errors in eddy ‐ covariance measurements, *Global Change Biol.*, *12*(5), 883-896, doi:doi:10.1111/j.1365-2486.2006.01131.x.

Papale, D., et al. (2006), Towards a standardized processing of Net Ecosystem Exchange measured with eddy covariance technique: algorithms and uncertainty estimation, *Biogeosciences*, *3*(4), 571-583, doi:10.5194/bg-3-571-2006.

Pasquill, F. (1961), The estimation of the dispersion of windborne material, *Meteorol. Magazine*, *90*, 33-49.

Patric, J. H., J. E. Douglass, and J. D. Hewlett (1965), Soil Water Absorption by Mountain and Piedmont Forests1, *Soil. Sci. Soc. Am. J.*, *29*(3), 303-308, doi:10.2136/sssaj1965.03615995002900030023x.

Phillips, O. L., et al. (2009), Drought sensitivity of the Amazon rainforest, *Science*, *323*(5919), 1344-1347, doi:10.1126/science.1164033.

Pielke, R. A., G. Marland, R. A. Betts, T. N. Chase, J. L. Eastman, J. O. Niles, D. d. S. Niyogi, and S. W. Running (2002), The influence of land-use change and landscape dynamics on the climate system: relevance to climate-change policy beyond the radiative effect of greenhouse gases, *Philosophical Transactions of the Royal Society of London. Series A: Mathematical, Physical and Engineering Sciences*, *360*(1797), 1705-1719, doi:10.1098/rsta.2002.1027.

Pielke, R. A., et al. (2011), Land use/land cover changes and climate: modeling analysis and observational evidence, *Wiley Interdisciplinary Reviews: Climate Change*, *2*(6), 828-850, doi:10.1002/wcc.144.

Post, H., H. J. H. Franssen, A. Graf, M. Schmidt, and H. Vereecken (2015), Uncertainty analysis of eddy covariance CO2 flux measurements for different EC tower distances using an extended two-tower approach, *Biogeosciences*, *12*(4), 1205-1221, doi:10.5194/bg-12-1205-2015.

Pressley, S., B. Lamb, H. Westberg, and C. Vogel (2006), Relationships among canopy scale energy fluxes and isoprene flux derived from long-term, seasonal eddy covariance measurements over a hardwood forest, *Agric. For. Meteorol.*, *136*(3), 188-202, doi:https://doi.org/10.1016/j.agrformet.2004.11.013.

Rasmussen, C. (2012), Thermodynamic constraints on effective energy and mass transfer and catchment function, *Hydrol. Earth Syst. Sci.*, *16*(3), 725-739, doi:10.5194/hess-16-725-2012.

Rasmussen, C., and E. L. Gallo (2013), Technical Note: A comparison of model and empirical measures of catchment-scale effective energy and mass transfer, *Hydrol. Earth Syst. Sci.*, *17*(9), 3389-3395, doi:10.5194/hess-17-3389-2013.

Rasmussen, C., P. A. Troch, J. Chorover, P. Brooks, J. Pelletier, and T. E. Huxman (2011), An open system framework for integrating critical zone structure and function, *Biogeochemistry*, *102*(1-3), 15-29.

Reba, M. L., D. Marks, T. E. Link, J. Pomeroy, and A. Winstral (2014), Sensitivity of model parameterizations for simulated latent heat flux at the snow surface for complex mountain sites, *Hydrol. Processes*, *28*(3), 868-881, doi:10.1002/hyp.9619.

Reed, D. E., J. M. Frank, B. E. Ewers, and A. R. Desai (2018), Time dependency of eddy covariance site energy balance, *Agric. For. Meteorol.*, *249*, 467-478, doi:https://doi.org/10.1016/j.agrformet.2017.08.008.

Richardson, A. D., et al. (2006), Comparing simple respiration models for eddy flux and dynamic chamber data, *Agric. For. Meteorol.*, *141*(2-4), 219-234, doi:10.1016/j.agrformet.2006.10.010.

Richter, D. d., et al. (2015), *Evolution of soil, ecosystem, and critical zone research at the USDA FS Calhoun Experimental Forest*, 405-433 pp.

Richter, D. d., et al. (2014), Evolution of Soil, Ecosystem, and Critical Zone Research at the USDA FS Calhoun Experimental Forest, in *USDA Forest Service Experimental Forests and Ranges: Research for the Long Term*, edited by D. C. Hayes, S. L. Stout, R. H. Crawford and A. P. Hoover, pp. 405-433, Springer New York, New York, NY, doi:10.1007/978-1-4614-1818-4_18.

Richter, D. d., and S. A. Billings (2015), 'One physical system': Tansley's ecosystem as Earth's critical zone, *New Phytologist*, *206*(3), 900-912, doi:10.1111/nph.13338.

Richter, D. D., D. Markewitz, S. E. Trumbore, and C. G. Wells (1999), Rapid accumulation and turnover of soil carbon in a re-establishing forest, *Nature*, *400*(6739), 56-58.

Richter, D. D., D. Markewitz, C. G. Wells, H. L. Allen, R. April, P. R. Heine, and B. Urrego (1994), Soil Chemical Change during Three Decades in an Old-Field Loblolly Pine (Pinus Taeda L.) Ecosystem, *Ecology*, *75*(5), 1463-1473, doi:10.2307/1937469.

Richter, D. d., and M. L. Mobley (2009), Monitoring Earth's critical zone, *Science*, *326*(5956), 1067-1068.

Rocha, H. R. d., M. L. Goulden, S. D. Miller, M. C. Menton, L. D. V. O. Pinto, H. C. d. Freitas, and A. M. e. S. Figueira (2004), Seasonality of water and heat fluxes over a tropical forest in eastern amazonia, *Ecol. Appl.*, *14*(sp4), 22-32, doi:doi:10.1890/02-6001.

Saleska, S. R., et al. (2003), Carbon in Amazon forests: unexpected seasonal fluxes and disturbance-induced losses, *Science*, *302*(5650), 1554-1557, doi:10.1126/science.1091165.

Sauer, T., and R. Horton (2005), *Micrometeorology in agricultural systems*, 131-154 pp.

Sauer, T. J., J. W. Singer, J. H. Prueger, T. M. DeSutter, and J. L. Hatfield (2007), Radiation balance and evaporation partitioning in a narrow-row soybean canopy, *Agric. For. Meteorol.*, *145*(3-4), 206-214, doi:10.1016/j.agrformet.2007.04.015.

Schimel, D., et al. (2000), Contribution of Increasing CO₂ and Climate to Carbon Storage by Ecosystems in the United States, *Science*, *287*(5460), 2004-2006, doi:10.1126/science.287.5460.2004.

Schimel, D. S. (1995a), Terrestrial Ecosystems and the Carbon-Cycle, *Global Change Biol.*, *1*(1), 77-91, doi:DOI 10.1111/j.1365-2486.1995.tb00008.x.

Schimel, D. S. (1995b), Terrestrial ecosystems and the carbon cycle, *Global Change Biol.*, *1*(1), 77-91, doi:10.1111/j.1365-2486.1995.tb00008.x.

Schlesinger, W. H., et al. (2006), The Duke Forest FACE Experiment: CO2 Enrichment of a Loblolly Pine Forest, in *Managed Ecosystems and CO2: Case Studies, Processes, and Perspectives*, edited by J. Nösberger, S. P. Long, R. J. Norby, M. Stitt, G. R. Hendrey and H. Blum, pp. 197-212, Springer Berlin Heidelberg, Berlin, Heidelberg, doi:10.1007/3-540-31237-4_11.

Sellers, P. J., et al. (1997), Modeling the exchanges of energy, water, and carbon between continents and the atmosphere, *Science*, *275*(5299), 502-509, doi:DOI 10.1126/science.275.5299.502.

Shanafield, M., P. G. Cook, H. A. Gutierrez-Jurado, R. Faux, J. Cleverly, and D. Eamus (2015), Field comparison of methods for estimating groundwater discharge by evaporation and evapotranspiration in an arid-zone playa, *J. Hydrol.*, *527*, 1073-1083, doi:10.1016/j.jhydrol.2015.06.003.

Shi, Y., D. C. Baldwin, K. J. Davis, X. Yu, C. J. Duffy, and H. Lin (2015a), Simulating high-resolution soil moisture patterns in the Shale Hills watershed using a land surface hydrologic model, *Hydrol. Processes*, *29*(21), 4624-4637, doi:10.1002/hyp.10593.

Shi, Y., K. J. Davis, F. Zhang, and C. J. Duffy (2014a), Evaluation of the Parameter Sensitivities of a Coupled Land Surface Hydrologic Model at a Critical Zone Observatory, *J. Hydrometeorol.*, *15*(1), 279-299, doi:10.1175/jhm-d-12-0177.1.

Shi, Y., K. J. Davis, F. Zhang, C. J. Duffy, and X. Yu (2014b), Parameter estimation of a physically based land surface hydrologic model using the ensemble Kalman filter: A synthetic experiment, *Water Resour. Res.*, *50*(1), 706-724, doi:10.1002/2013WR014070.

Shi, Y., K. J. Davis, F. Zhang, C. J. Duffy, and X. Yu (2015b), Parameter estimation of a physically-based land surface hydrologic model using an ensemble Kalman filter: A multivariate real-data experiment, *Advances in Water Resources*, *83*, 421-427, doi:https://doi.org/10.1016/j.advwatres.2015.06.009.

Smith, B. W., P. D. Miles, J. S. Vissage, and S. A. Pugh (2004), Forest Resources of the United States, 2002: A Technical Document Supporting the USDA Forest Service 2005 Update of the RPA Assessment., *General Technical Report NC-241*.

South, C., C. Susan, B. Grimmond, and C. P. Wolfe (1998), Evapotranspiration rates from wetlands with different disturbance histories: Indiana Dunes National Lakeshore, *Wetlands*, *18*(2), 216-229, doi:10.1007/bf03161657.

Sparling, G., D. Ross, N. Trustrum, G. Arnold, A. West, T. Speir, and L. Schipper (2003), Recovery of topsoil characteristics after landslip erosion in dry hill country of New Zealand, and a test of the space-for-time hypothesis, *Soil Biology and Biochemistry*, *35*(12), 1575-1586.

Stannard, D. I., J. H. Blanford, W. P. Kustas, W. D. Nichols, S. A. Amer, T. J. Schmugge, and M. A. Weltz (1994), Interpretation of surface flux measurements in heterogeneous terrain during the Monsoon '90 experiment, *Water Resour. Res.*, *30*(5), 1227-1239, doi:doi:10.1029/93WR03037.

Stoffelen, A., et al. (2005), The atmospheric dynamics mission for global wind field measurement, *Bulletin of the American Meteorological Society*, *86*(1), 73-88, doi:10.1175/bams-86-1-73.

Stull, R. B. (1988), *An Introduction to Boundary Layer Meteorology*, Springer Netherlands.

Sutherland, R. A., F. V. Hansen, and W. D. Bach (1986), A quantitative method for estimating Pasquill stability class from windspeed and sensible heat flux density, *Boundary-Layer Meteorology*, *37*(4), 357-369, doi:10.1007/bf00117483.

Tague, C., and H. Peng (2013), The sensitivity of forest water use to the timing of precipitation and snowmelt recharge in the California Sierra: Implications for a warming climate, *Journal of Geophysical Research: Biogeosciences*, *118*(2), 875-887, doi:10.1002/jgrg.20073.

Thomas, C., J. G. Martin, M. Goeckede, M. B. Siqueira, T. Foken, B. E. Law, H. W. Loescher, and G. Katul (2008), Estimating daytime subcanopy respiration from conditional sampling methods applied to multi-scalar high frequency turbulence time series, *Agric. For. Meteorol.*, *148*(8-9), 1210-1229, doi:10.1016/j.agrformet.2008.03.002.

Thomas, C. K., J. G. Martin, B. E. Law, and K. Davis (2013), Toward biologically meaningful net carbon exchange estimates for tall, dense canopies: Multi-level eddy covariance observations and canopy coupling regimes in a mature Douglas-fir forest in Oregon, *Agric. For. Meteorol.*, *173*, 14-27, doi:10.1016/j.agrformet.2013.01.001.

Thomas, F. (2008), THE ENERGY BALANCE CLOSURE PROBLEM: AN OVERVIEW, *Ecol. Appl.*, *18*(6), 1351-1367, doi:doi:10.1890/06-0922.1.

Tian, H. Q., J. M. Melillo, D. W. Kicklighter, A. D. McGuire, J. V. K. Helfrich, B. Moore, and C. J. Vorosmarty (1998), Effect of interannual climate variability on carbon storage in Amazonian ecosystems, *Nature*, *396*(6712), 664-667, doi:Doi 10.1038/25328.

Tombesi, S., A. Nardini, T. Frioni, M. Soccolini, C. Zadra, D. Farinelli, S. Poni, and A. Palliotti (2015), Stomatal closure is induced by hydraulic signals and maintained by ABA in drought-stressed grapevine, *Sci. Rep.*, *5*, 12449, doi:10.1038/srep12449.

Travis, S. E., and M. W. Hester (2005), A space-for-time substitution reveals the long-term decline in genotypic diversity of a widespread salt marsh plant, Spartina alterniflora, over a span of 1500 years, *Journal of Ecology*, *93*(2), 417-430, doi:10.1111/j.0022-0477.2005.00985.x.

Trenberth, K. E., J. M. Caron, and D. P. Stepaniak (2001), The atmospheric energy budget and implications for surface fluxes and ocean heat transports, *Clim. Dyn.*, *17*(4), 259-276, doi:10.1007/pl00007927.

Twine, T. E., C. J. Kucharik, and J. A. Foley (2004), Effects of Land Cover Change on the Energy and Water Balance of the Mississippi River Basin, *J. Hydrometeorol.*, *5*(4), 640-655, doi:10.1175/1525-7541(2004)005<0640:eolcco>2.0.co;2.

Twine, T. E., W. P. Kustas, J. M. Norman, D. R. Cook, P. R. Houser, T. P. Meyers, J. H. Prueger, P. J. Starks, and M. L. Wesely (2000), Correcting eddy-covariance flux underestimates over a grassland, *Agric. For. Meteorol.*, *103*(3), 279-300, doi:https://doi.org/10.1016/S0168-1923(00)00123-4.

USDA (2010), Field Crops Usual Planting and Harvesting Dates.

Van der Maarel, E., and M. Werger (1978), On the treatment of succession data, *Phytocoenosis*, *7*, 257-278.

Van Oost, K., et al. (2007), The Impact of Agricultural Soil Erosion on the Global Carbon Cycle, *Science*, *318*(5850), 626-629, doi:10.1126/science.1145724.

Vickers, D., M. Gockede, and B. E. Law (2010), Uncertainty estimates for 1-h averaged turbulence fluxes of carbon dioxide, latent heat and sensible heat, *Tellus Series B-Chemical and Physical Meteorology*, *62*(2), 87-99, doi:10.1111/j.1600-0889.2009.00449.x.

Vickers, D., and L. Mahrt (1997), Quality Control and Flux Sampling Problems for Tower and Aircraft Data, *Journal of Atmospheric and Oceanic Technology*, *14*(3), 512-526, doi:10.1175/1520-0426(1997)014<0512:qcafsp>2.0.co;2.

Vickers, D., C. Thomas, C. Pettijohn, J. G. Martin, and B. Law (2012), Five years of carbon fluxes and inherent water-use efficiency at two semi-arid pine forests with different disturbance histories, *Tellus B: Chemical and Physical Meteorology*, *64*(1), 17159, doi:10.3402/tellusb.v64i0.17159.

Wang, H. L., D. Tetzlaff, and C. Soulsby (2017), Testing the maximum entropy production approach for estimating evapotranspiration from closed canopy shrubland in a low-energy humid environment, *Hydrol. Processes*, *31*(25), 4613-4621, doi:10.1002/hyp.11363.

Wang, J., and R. L. Bras (1998), A new method for estimation of sensible heat flux from air temperature, *Water Resour. Res.*, *34*(9), 2281-2288, doi:Doi 10.1029/98wr01698.

Wang, J., and R. L. Bras (1999), Ground heat flux estimated from surface soil temperature, *J. Hydrol.*, *216*(3-4), 214-226, doi:Doi 10.1016/S0022-1694(99)00008-6.

Wang, J., and R. L. Bras (2001), Effect of temperature on surface energy balance, *Water Resour. Res.*, *37*(12), 3383-3386, doi:10.1029/2001WR000483.

Wang, J., and R. L. Bras (2009), A model of surface heat fluxes based on the theory of maximum entropy production, *Water Resour. Res.*, *45*(11), W11422, doi:10.1029/2009wr007900.

Wang, J., and R. L. Bras (2010), An Extremum Solution of the Monin–Obukhov Similarity Equations, *J. Atmos. Sci.*, *67*(2), 485-499, doi:10.1175/2009jas3117.1.

Wang, J., and R. L. Bras (2011), A model of evapotranspiration based on the theory of maximum entropy production, *Water Resour. Res.*, *47*(3), n/a-n/a, doi:10.1029/2010wr009392.

Wang, J., R. L. Bras, V. Nieves, and Y. Deng (2014), A model of energy budgets over water, snow, and ice surfaces, *Journal of Geophysical Research-Atmospheres*, *119*(10), 6034-6051, doi:10.1002/2013jd021150.

Wang, K. C., and R. E. Dickinson (2012), A Review of Global Terrestrial Evapotranspiration: Observation, Modeling, Climatology, and Climatic Variability, *Rev. Geophys.*, *50*(2), n/a-n/a, doi:10.1029/2011rg000373.

Wieder, W. R., C. C. Cleveland, W. K. Smith, and K. Todd-Brown (2015), Future productivity and carbon storage limited by terrestrial nutrient availability, *Nature Geoscience*, *8*, 441, doi:10.1038/ngeo2413

https://www.nature.com/articles/ngeo2413#supplementary-information.

Wilson, K., et al. (2002), Energy balance closure at FLUXNET sites, *Agric. For. Meteorol.*, *113*(1), 223-243, doi:https://doi.org/10.1016/S0168-1923(02)00109-0.

Wilson, K. B., P. J. Hanson, P. J. Mulholland, D. D. Baldocchi, and S. D. Wullschleger (2001), A comparison of methods for determining forest evapotranspiration and its components: sap-flow, soil water budget, eddy covariance and catchment water balance, *Agric. For. Meteorol.*, *106*(2), 153-168, doi:Doi 10.1016/S0168-1923(00)00199-4.

Wohlfahrt, G., C. Anfang, M. Bahn, A. Haslwanter, C. Newesely, M. Schmitt, M. Drösler, J. Pfadenhauer, and A. Cernusca (2005), Quantifying nighttime ecosystem respiration of a

meadow using eddy covariance, chambers and modelling, *Agric. For. Meteorol.*, *128*(3), 141-162, doi:https://doi.org/10.1016/j.agrformet.2004.11.003.

Woodwell, G. M., J. E. Hobbie, R. A. Houghton, J. M. Melillo, B. Moore, B. J. Peterson, and G. R. Shaver (1983), Global Deforestation: Contribution to Atmospheric Carbon Dioxide, *Science*, *222*(4628), 1081-1086, doi:10.1126/science.222.4628.1081.

Wutzler, T., A. Lucas-Moffat, M. Migliavacca, J. Knauer, K. Sickel, L. Šigut, O. Menzer, and M. Reichstein (2018), Basic and extensible post-processing of eddy covariance flux data with REddyProc, *Biogeosciences*, *15*(16), 5015-5030, doi:10.5194/bg-15-5015-2018.

Yang, J. C., and Z. H. Wang (2014), Land surface energy partitioning revisited: A novel approach based on single depth soil measurement, *Geophys. Res. Lett.*, *41*(23), 8348-8358, doi:10.1002/2014gl062041.

Yu, X., C. Duffy, J. Kaye, W. Crow, G. Bhatt, and Y. Shi (2014), Watershed Reanalysis of Water and Carbon Cycle Models at a Critical Zone Observatory, in *Remote Sensing of the Terrestrial Water Cycle*, edited, pp. 493-509, John Wiley & Sons, Inc, doi:10.1002/9781118872086.ch31.

Yu, X., C. Duffy, Y. Zhang, G. Bhatt, and Y. Shi (2016), Virtual Experiments Guide Calibration Strategies for a Real-World Watershed Application of Coupled Surface-Subsurface Modeling, *Journal of Hydrologic Engineering*, *21*(11), 04016043, doi:doi:10.1061/(ASCE)HE.1943-5584.0001431.

Zhang, D., and R. A. Anthes (1982), A High-Resolution Model of the Planetary Boundary Layer—Sensitivity Tests and Comparisons with SESAME-79 Data, *Journal of Applied Meteorology*, *21*(11), 1594-1609, doi:10.1175/1520-0450(1982)021<1594:ahrmot>2.0.co;2.